UNIVERSITY OF SOUTHAMPTON

Faculty of Engineering and Physical Sciences
School of Chemistry

Spectroscopic investigations of C_{60} fullerene and its endohedral derivatives

by

George Răzvan Băcanu

A thesis for the degree of
Doctor of Philosophy

May 2021

University of Southampton

Abstract

Faculty of Engineering and Physical Sciences
School of Chemistry

Doctor of Philosophy

Spectroscopic investigations of C_{60} fullerene and its endohedral derivatives

by George Răzvan Băcanu

This study presents spectroscopic investigations of C_{60} fullerenes and endofullerenes. The experimental techniques are: Nuclear Magnetic Resonance (NMR), Inelastic Neutron Scattering (INS) and far-Infrared (far-IR or THz) spectroscopy.

The ^{13}C solution NMR spectrum of C_{60} is found to display two small additional "side peaks". They arise because of the secondary NMR isotope shift effect, present for isotopomers of C_{60} with two adjacent ^{13}C nuclei. ^{13}C enriched C_{60} displays a broad peak, without the two side peaks seen for natural abundance, due to increased statistical distribution of ^{13}C nuclei in the cage. The spectra of the natural abundance and ^{13}C enriched C_{60} are simulated through a Monte-Carlo type technique, which approximates the NMR spectrum of J-coupled ^{13}C spin clusters by the second moment.

$^{3}He@C_{60}$ displays a doublet in the solution ^{13}C NMR spectrum. This is caused by a non-bonded J-coupling between ^{3}He nucleus and ^{13}C. The notation $^{0}J_{HeC}$ is adopted, in which the superscript zero symbolises the absence of a covalent bond beween ^{3}He and ^{13}C. $^{0}J_{HeC}$ increases in magnitude with increasing temperature; consistent with the ^{3}He nucleus coming closer to ^{13}C on average as temperature is increased. The ^{13}C solution NMR spectrum of $CH_4@C_{60}$ displays a significant broadening of the ^{13}C (C_{60}) peak; which is consistent with a $^{0}J_{HC}$ coupling between ^{1}H from endohedral CH_4 and ^{13}C from the confining cage.

The noble gas endofullerenes $^{3}He@C_{60}$, $^{4}He@C_{60}$ and $Ne@C_{60}$ are investigated through INS and THz spectroscopy. The atomic translational quantization is probed using these techniques. Defying the odds, $He@C_{60}$ is shown to absorb THz light which translationally excites the Helium atom. The translational transitions are interpreted using a 3D spherical oscillator model for the endohedral species. The confining potentials for $He@C_{60}$ and $Ne@C_{60}$ are obtained by simulating the experimental results. This provides valuable parameters for the non-covalent interaction between the noble gas and the confining C_{60} fullerene cage.

Dragii mei părinți, această lucrare împreună cu toată munca mea este dedicată vouă!

Declaration of Authorship

I declare that this thesis and the work presented in it is my own and has been generated by me as the result of my own original research.

I confirm that:

1. This work was done wholly or mainly while in candidature for a research degree at this University;
2. Where any part of this thesis has previously been submitted for a degree or any other qualification at this University or any other institution, this has been clearly stated;
3. Where I have consulted the published work of others, this is always clearly attributed;
4. Where I have quoted from the work of others, the source is always given. With the exception of such quotations, this thesis is entirely my own work;
5. I have acknowledged all main sources of help;
6. Where the thesis is based on work done by myself jointly with others, I have made clear exactly what was done by others and what I have contributed myself;
7. Parts of this work have been published as:
   - S. Bloodworth, G. Sitinova, S. Alom, S. Vidal, G. R. Bacanu, S. J. Elliott, M. E. Light, J. M. Herniman, G. J. Langley, M. H. Levitt and R. J. Whitby, *Angewandte Chemie International Edition*, 2019, **58**, 5038–5043.
   - G. R. Bacanu, G. Hoffman, M. Amponsah, M. Concistrè, R. J. Whitby and M. H. Levitt, *Physical Chemistry Chemical Physics*, 2020, **22**, 11850–11860.
   - G. R. Bacanu, J. Rantaharju, G. Hoffman, M. C.Walkey, S. Bloodworth, M. Concistrè, R. J. Whitby and M. H. Levitt, *Journal of the American Chemical Society*, 2020, **142**, 16926–16929.

Signed:.. Date:..................

Acknowledgements

Here I would like to show my gratitude to the people who have made this thesis possible.

Firstly, I wish to express my appreciation to Malcolm H. Levitt for being the best supervisor anyone would wish to have. He would always be extremely helpful, supportive and kind even when my questions would not stop flowing. Furthermore, I would like to thank Malcolm for allowing me to pursue even the most crazy and exotic ideas.

A special thank you goes to the organic synthesis team, Richard J. Whitby and his group, who have synthesised all the endofullerenes investigated here. I thank all group members: Gabriela Hoffman, Sally Bloodworth and Mark C. Walkey.

The Inelastic neutron scattering experiments would have not been possible without Stéphane Rolls, Anthony J. Horsewill, Mohamed Aouane and Monica Jimenez-Ruiz, for which I express my gratitude.

I am most grateful to Toomas Rõõm and his group for making the far-Infrared measurements possible. I thank all group members: Tanzeeha Jafari, Anna Shugai, Urmas Nagel, Kirill Amelin and Laur Peedu.

I am thankful to Jyrki Rantaharju for performing the quantum chemistry calculations shown in this study and for general theoretical advice.

I must thank Karel Kouřil, Benno Meier, Giuseppe Pileio and Hana Kouřilová for providing general guidance and advice whenever I needed.

I would like to thank Stuart J. Elliott and Neil J. Wells for helping with the solution state NMR measurements.

I wish to thank Jai Balachandra for being a great housemate and for help with writing up.

Finally, I wish to thank my family for the greatest support they have given me throughout the years, I would not have been able to achieve anything without them.

George Răzvan Băcanu
March 2021

Contents

List of Tables

Chapter 1

Introduction

1.1 Introduction

In 1985, a third allotropic form of Carbon was discovered, the *fullerene*.[3] The fullerene discovery was made by performing mass spectrometry on carbon species vaporized by a laser from the surface of a graphite disk. This produced very stable species with masses corresponding to 60 and 70 carbon atoms, which proved to be the C_{60} and C_{70} fullerene molecules.

The fullerene molecule is composed of carbon atoms covalently bonded into a closed structure. It is like a graphene sheet which has been folded into a spherical shape. In order for the fullerene to have curvature, it must have pentagonal as well as hexagonal faces, unlike graphite which has only hexagonal faces. Smaller faces (rings) of carbons are possible in principle but energetically unfavorable. For fullerenes, with only pentagonal and hexagonal faces, to have a closed surface there can only be 12 pentagonal faces and an arbitrary number of hexagonal faces, due to Euler's polyhedral formula.[4] Furthermore, for the carbon fullerene structure to be energetically stable, unstrained, the pentagons must not share an edge. This gives a minimum number of 20 hexagonal faces, which corresponds to the smallest stable fullerene, the C_{60} molecule.[4]

Although initially the number of carbon atoms in C_{60} was known, the exact structure was not. Due to the approximately spherical shape, C_{60} molecules by themselves do not form a long-range ordered single crystal. Thus, single crystal x-ray crystallography measurements could not be used initially to find the exact structure. Solution state NMR of C_{60} displayed a single peak in the spectrum.[5,6] This was a key piece of evidence for the structure, proving that all carbon nuclei are chemically equivalent; which was surprising since the molecule has 60 carbon atoms.

Solid state NMR was one of the experiments which proved that C_{60} has two types of C-C bonds of unequal lengths: a longer HP (Hexagon-Pentagon edge) and a shorter

HH (Hexagon-Hexagon edge).[7] Thus, the C_{60} molecule is *not* a regular truncated icosahedron, since to be regular all bonds should be of equal length. However, C_{60} does display icosahedral symmetry and all its carbon atoms are chemically equivalent. X-ray crystallography deduced the full C_{60} structure, after a single crystal was obtained for a derivative of C_{60}. It was done by chemically reacting C_{60} with an Osmium complex to break the spherical symmetry and allow for an ordered single crystal to form.[8]

Soon after the discovery of fullerenes, scientists realised there is an empty space inside the molecule which can be filled up with atoms or molecules. This way the endohedral atom/molecule is trapped in the cage mechanically and not covalently.[9] The term *endohedral* is used to describe an atom/molecule trapped inside a fullerene. Thus, the concept of endofullerene arises, where the term refers to the whole "fullerene + endohedral moeity" complex.

The first reported endofullerenes had a metallic atom inside. La@C_{60}, La@C_{70}, La@C_{74} and La@C_{84} were obtained by laser vaporization of a lanthanum oxide/graphite composite rod.[10] Noble gas endofullerenes were obtained shortly after, in low quantities through an arc discharge between graphite electrodes in an atmosphere of He or Ne to give ^{4}He@C_{60} and Ne@C_{60} endofullerenes.[11] . Another method of obtaining them is through a brute force approach, where fullerenes are kept together with noble gases under high temperature and pressure.[12] The ^{3}He@C_{60} endofullerene was also obtained through similar methods, and ^{3}He NMR was shown to be a useful tool in probing the interior of the fullerene cage through the ^{3}He chemical shift .[13–15]

Rather than relying on extreme conditions to give poor yields of endofullerenes,[10–12] organic chemists developed a technique called "molecular surgery" for the synthesis of endofullerenes. Molecular surgery consists of: firstly opening a fullerene cage through a series of reactions, secondly filling the open cage fullerene with the desired atom/-molecule through elevated temperature and pressure which should form a stable endohedral moiety-open cage fullerene complex and the final step would be to close the fullerene with the endohedral atom/molecule still inside. The first successful "molecular surgery" synthesis was done by Y. Murata *et al.*, where they enclosed a hydrogen molecule inside a C_{60} cage.[16] The ^{4}He@C_{60} and also H_2O@C_{60} were done initially by the same group.[17,18] The HF & CH_4 molecules and Argon were enclosed inside a C_{60} cage through molecular surgery by R. J. Whitby *et al.* from the University of Southampton.[19–21]

When a particle is enclosed in a small space, quantum mechanical effects come into play. Thus, endofullerenes represent a classical quantum mechanics example of a *particle in a box*. This particle in a box type behaviour leads to quantization of the translational states that a particle can have inside a fullerene cage. If a molecule with rotational and vibrational degrees of freedom is enclosed, it leads to splittings of these levels by the translational quantisation; for rotations it leads to Translational-Rotational

(TR) coupling.[22–27] This effect was observed and investigated for $H_2@C_{60}$, $H_2O@C_{60}$ and $HF@C_{60}$.[19,22–33] Such quantum systems are characterised by TR eigenstates and eigenvalues, with transitions which fall in the THz range (roughly 0-500 cm^{-1}).

Endofullerenes offer a very controlled environment to study confinement, since all fullerene cages are the same. Unlike clathrates, zeolites, etc.[34] systems, which do offer a similar confinement, but the control over each pore is not as good. One will always get a distribution of pore sizes and shapes with clathrates, whereas fullerenes will always be consistent. Furthermore, the endohedral species is always confined to the same region of space and cannot diffuse away, unless it breaks the C-C covalent bonds of the fullerene cage.

Endofullerenes offer an ideal system to study non-covalent interactions between the guest (endohedral species) and the host (fullerene cage), which can be investigated in the solid state. Molecular endofullerenes are free rotors even at cryogenic conditions, which results in sharp spectroscopic peaks even at low temperatures.[19,22–33] Studying non-covalent interactions is not an easy task to perform experimentally. Generally, experiments are done in the gas phase, where one needs specialised equipment like molecular beams, ultra high vacuum, lasers etc.[35–40] Control of temperature is difficult to do accurately for these gas phase techniques, and temperature dependent measurements are unlikely. Also, the information gained can be limited, since the analysed compounds have to be ionised for detection.[35–40] Another drawback of these gas phase type experiments is the destructive nature of the measurements, since the compounds are lost after detection. Furthermore, vibronic transitions are generally probed in these measurements, which are not easily interpreted.

In this study, C_{60} fullerenes and endofullerens are investigated through various spectroscopic methods. The techniques used are Nuclear Magnetic Resonance (NMR), Inelastic Neutron Scattering (INS) and far-Infrared (far-IR or THz) spectroscopy.

1.2 Aims and objectives

The purpose of this study is to present recent findings regarding C_{60} fullerene and its endofullerenes, together with their interpretations.

The ^{13}C solution NMR spectra of C_{60} and its endofullerene derivatives has been found to display additional side peaks, besides the well known ^{13}C peak. The aim of chapter 2 is to describe the origin of the side peaks. The interpretation of the fine structure is given using the secondary NMR isotope shift effect. Furthermore, ^{13}C enriched C_{60} fullerene is found to display a more complex spectrum than natural abundance C_{60}. A model will be presented which can accurately simulate the natural abundance and ^{13}C enriched solution NMR spectra of C_{60} fullerene, in chapter 2.

The ^{13}C solution NMR spectrum of ^{3}He@C$_{60}$ is found to present a small splitting. The aim of chapter 3 is to assign the observed splitting to a non-bonded J-coupling between ^{3}He and ^{13}C nuclei. A similar, but less clear, effect is seen for CH$_4$@C$_{60}$, which is interpreted as a non-bonded J-coupling between ^{1}H and ^{13}C.

The aim of chapter 4 is to present INS experiments on noble gas C$_{60}$ endofullerenes. The purpose of this investigation is to test whether endofullerenes of noble gases display translational quantization, if this can be detected using INS.

The purpose of chapter 5 is to present far-IR experiments on Helium C$_{60}$ endofullerenes. The adventurous aim of this investigation is to test whether Helium enclosed in C$_{60}$ fullerene displays translational quantization which can be detected using THz light. In other words if He@C$_{60}$ has a far-IR spectrum specific for the confined Helium atom.

The purpose of chapter 6 is to present a model for the confined noble gas atoms in C$_{60}$. This will use the experimental results from chapter 4 and chapter 5 to derive a non-covalent interaction potential between the endohedral noble gas atom and the C$_{60}$ carbon cage. The benefit of investigating translational quantization is to gain knowledge about the non-covalent interactions at play. Such non-bonded interactions are difficult to measure experimentally, and in general scientists have to rely on high level quantum chemistry calculations. However, without having an experimental result to compare with, the result of various quantum chemistry models have questionable validity. Thus, the main point of this chapter is to provide experimental non-covalent interaction potentials, to be used as a benchmark for quantum chemistry models.

1.3 Methods

1.3.1 Neutron scattering

The neutron is a composite particle, made up of three quarks. The neutron has spin $\frac{1}{2}$ but no electric charge. As a result, it can interact with magnetic fields and with nuclei through the strong force.

When a neutron hits a target, it can pass through or be scattered from it. The neutron can be scattered with the same energy (elastic scattering) or with a different energy (inelastic scattering) than it had before impact. For inelastic scattering, the neutron interacts with the target and losses or gains quanta of specific energy, which can give important spectroscopic information about the target.

The generic quantity used in neutron scattering is the partial differential cross section:

$$\frac{\partial^2\sigma}{\partial\Omega\partial E'} \tag{1.1}$$

which gives the fraction of neutrons, with incident energy E, being scattered with an energy between E' and $E' + dE'$ into an element of the solid angle $d\Omega$.[41] Thus, the scattering of a neutron by a target will depend on the neutron's incident energy E, on the energy of the neutron after scattering E' (for inelastic scattering), on the scattering angle $d\Omega$ with respect to the incidence direction and finally on the total cross section σ. Total scattering cross section σ, for a given energy E', has units of $barn = 10^{-24}\ cm^2$ (in general σ has units of area/energy).

Inelastic Neutron Scattering (INS) is used in this study to gain spectroscopic information about noble gas endofullerenes. By plotting the scattered neutron count against the energy lost or gained by the neutron, the INS spectrum is produced. In general the energy lost/gained by the neutron is in the meV range. Combined with the ineastic nature of these measurements it becomes clear why INS resembles Raman spectroscopy. INS does not have strict selection rules like other techniques based on light, so more information can be gained from it.[41] For example, neutrons can promote transitions between spin isomers of H_2 and H_2O, observed for $H_2@C_{60}$ and $H_2O@C_{60}$, whereas this cannot be done electromagnetically.[23–30] Further details about the INS instruments used are given in chapter 4.

1.3.2 Far-Infrared

Infrared (IR) spectroscopy is a technique used to measure electromagnetic transitions though photon absorption. The light is absorbed in discrete quanta of energy depending on the type of matter it interacts with, through the electromagnetic quantum field. When absorption occurs, the photon donates energy and angular momentum to the system; since the photon can be treated as a spin 1 particle, which donates one unit of angular momentum.[42] From this qualitative statement the well known electromagnetic selection rule of $\Delta\ell = 0, \pm 1$ arises, more details in section 6.1.1.

In general, IR is used to measure transitions between vibrational eigenstates of molecules. In the cases studied here, the energy levels arise due to translational quantization of an endohedral atom/molecule when confined inside the C_{60} cage. If the endohedral moiety is a molecule, it has additional rotational and vibrational degrees of freedom. The quantization of the rotations and translations, for endohedral species, combine according to Translational-Rotational (TR) coupling.[22–27] These transitions for endofullerenes, excluding vibrations, usually appear under 350 cm^{-1}, which corresponds to the far-IR (or THz) regime.[19,22,26,30–33]

Another condition for electromagnetic absorption to occur, is that the dipole moment associated with the transition has to be non-zero.[43–45] Higher order moments (quadrupole, etc.) can also give absorption, but display different selection rules and absorption is much reduced compared with dipole moments.[43–45] Molecules with permanent electric dipole moments give strong absorption in IR spectroscopy. Molecules with no permanent dipole, which posses induced dipole moments can also absorb light, but to a lesser extent.[32,43] For the cases studied here, the induced dipole moment is utilised, since the Helium atom does not poses a permanent dipole moment.

The experimental procedure for far-IR is rather straightforward: the light intensity as it passes through the sample is measured as a function of its wavelength. The light gets absorbed at a given wavelength if an allowed transition is present. By plotting the light absorption against wavelength, the far-IR spectrum is obtained. For the cases studied here, a Fourier transform far-IR spectrometer is used.

More information is given in chapter 5 and chapter 6.

1.3.3 Nuclear Magnetic Resonance

The spin of a particle behaves as the intrinsic angular momentum of that particle. In quantum mechanical terms, the spin angular momentum operators are defined on the eigenstate $|I, m_I\rangle$ with total spin angular momentum I and projection of the angular momentum along the z axis m_I:[46]

$$\begin{aligned}\hat{\mathbf{I}}^2 \, |I, m_I\rangle =& \hbar^2 I(I+1) \, |I, m_I\rangle \\ \hat{I}_z \, |I, m_I\rangle =& \hbar \, m_I \, |I, m_I\rangle \\ \hat{\mathbf{I}}^2 =& \hat{I}_x^2 + \hat{I}_y^2 + \hat{I}_z^2\end{aligned}$$

1.3.3.1 External magnetic interactions

Any particle with total spin angular momentum I, has $(2I+1)$ degenerate states for the projection spin angular momentum (m_I) in zero magnetic field. The degeneracy is broken into $(2I+1)$ states when a $\mathbf{B_0}$ magnetic field is applied. The energy splittings between the levels are proportional to the applied field- this is the Zeeman interaction. The Zeeman Hamiltonian is given in eq. 1.2, with usual notation of magnetic field pointing along the z axis, $\mathbf{B_0} \cdot \hat{\mathbf{I}} = (B_0 \, \mathbf{e_z} \cdot \hat{\mathbf{I}}) = B_0 \, \hat{I}_z$.[46]

$$\hat{H}^{Zeeman} = -\gamma \, \mathbf{B_0} \cdot \hat{\mathbf{I}} = -\gamma B_0 \, \hat{I}_z = \omega_0 \, \hat{I}_z \tag{1.2}$$

Where γ is the gyromagnetic ratio of the respective spin. γ and B_0 can be grouped together to give ω_0 which is the Larmor frequency of the spin. In classical terms it describes the precession frequency a spin has when experiencing a B_0 magnetic field.

In the case of spin $\frac{1}{2}$, there are only 2 states, "up"and "down"or α and β that split in energy by the amount given by eq. 1.2 when a magnetic field is applied. The spin angular momentum aligns with or against the applied static magnetic field (depending on the sign of γ), which will generate a magnetic moment $\hat{\boldsymbol{\mu}}$, eq. 1.3.

$$\hat{\boldsymbol{\mu}} = \gamma \hat{\mathbf{I}} \tag{1.3}$$

This magnetic moment precesses around a magnetic field at its Larmor frequency.

Because of the Zeeman energy splitting, at finite temperature an equilibrium governed by the Boltzman equation (eq. 6.25) is established, which gives a smaller population for the higher energy state. Thus, in an ensemble of spins experiencing a magnetic field B_0, there is a net magnetization created by the population imbalance of the spin states. A spinning magnetic moment generates current in a nearby coil. Thus, the precessing magnetization generated by the spin ensemble is used for detection in Fourier Transform NMR spectrometers.[46]

A diagram of a typical Fourier Transform (FT) NMR spectrometer is shown in fig. 1.1. The static magnetic field $\mathbf{B_0}$ points along the z axis, and is generated by the supercon-

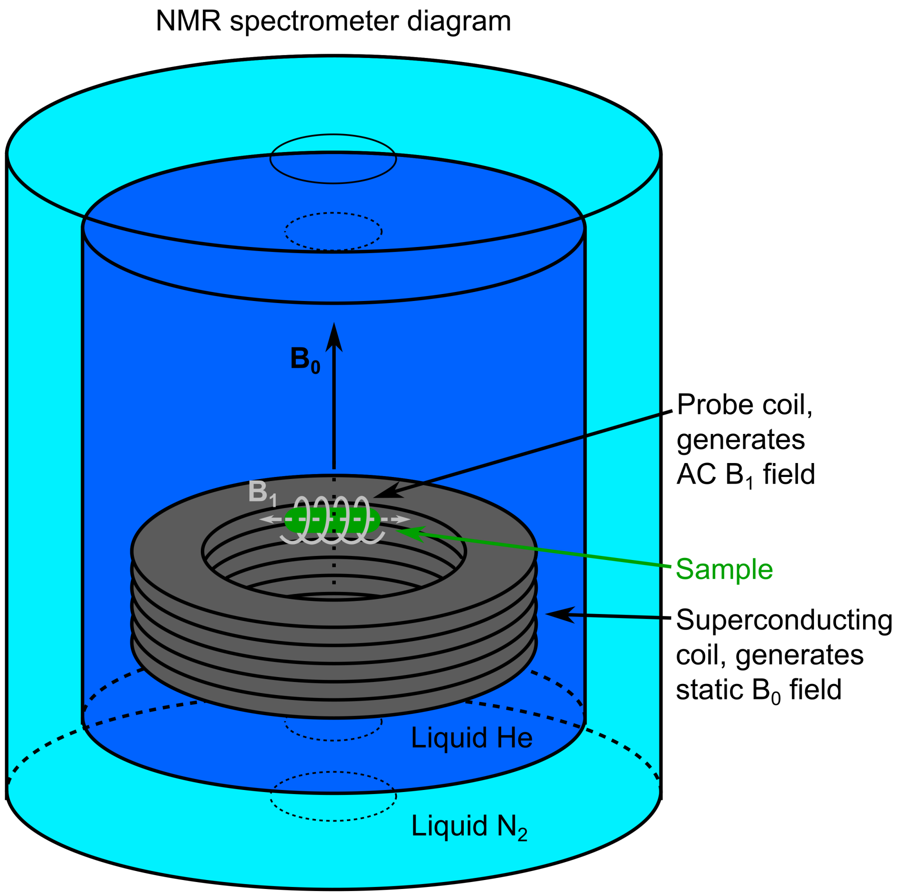

FIGURE 1.1: Diagram of a Fourier Transform NMR spectrometer. The superconducting coil is submerged liquid Helium (4 K), which itself is surrounded by liquid Nitrogen (77 K). The superdonducting coil produces the strong static $\mathbf{B_0}$ field, whereas the probe coil produces an alternating $\mathbf{B_1}$ field perpendicular to $\mathbf{B_0}$. The sample is placed inside the probe coil and experiences both $\mathbf{B_0}$ and $\mathbf{B_1}$ fields.

ducting coil placed in a liquid Helium bath (4 K), which itself is surrounded by liquid Nitrogen (77 K). In the center of the superconducting coil the NMR probe is located, containing the coil which produces the alternating $\mathbf{B_1}$ field perpendicular to $\mathbf{B_0}$. The sample is placed inside the probe coil and and experiences both $\mathbf{B_0}$ and $\mathbf{B_1}$ fields.

When the frequency of the $\mathbf{B_1}$ field matches the Larmor frequency of a given spin, magnetic resonance occurs and induces transitions between the spin states. In terms of nuclear magnetization of a sample present in the NMR spectrometer, the magnetization tilts from the z axis towards the -z axis, into the xy plane. When the magnetization has non-zero components in the xy plane, it precesses and induces a current in the probe coil nearby. Thus, the probe coil is used for excitation and for detection in NMR experiments.

1.3.3.2 Chemical shift

Matter is made up of charged particles, with spin, and their distribution around a nuclear spin change the effective magnetic field at the nucleus. This in turn changes the effective Larmor frequency of the spin. This change in the Larmor frequency ω_0 is reported relative to a reference standard (TMS for hydrogen, carbon and silicon) and is known as the chemical shift δ. In order for the chemical shift not to change with the applied magnetic field B_0, the difference $\omega_0 - \omega_0^{TMS}$ is divided by the Larmor frequency of TMS, eq. 1.4. Since chemical shifts have very small values it is usual to scale them by 10^6 and report them in ppm (parts per million) or even ppb.[46]

$$\delta = \frac{\omega_0 - \omega_0^{TMS}}{\omega_0^{TMS}} \tag{1.4}$$

In solution state NMR, due to fast tumbling of molecules the chemical shift is a scalar quantity, however, that is only the isotropic chemical shift. Because the distribution of particles (mainly electrons) around a nuclear spin is in general not spherically symmetric, the change in the Larmor frequency of the spin is dependent on the orientation of the distribution (chemical bonds, for example) with respect to the applied magnetic field $\mathbf{B_0}$. Thus, the chemical shift in the general case is a tensor quantity, see eq. 1.5 for the change in effective magnetic field $\mathbf{B^{induced}}$, rather than the change in Larmor frequency. The tensorial character of the chemical shift is only apparent in the solid state because the nearby atoms and chemical bonds are fixed. However, in liquid state, the very fast chaotic motion averages the particle distribution (atoms, bonds etc.) to a sphere on the Larmor frequency time scale. This averages the chemical shift to a scalar quantity, which equals the average of the diagonal terms in the principal axis frame of the chemical shift tensor.[46]

$$\mathbf{B}^{\mathbf{induced}} = \delta \cdot \mathbf{B_0} = \begin{pmatrix} \delta^{xx} & \delta^{xy} & \delta^{xz} \\ \delta^{yx} & \delta^{yy} & \delta^{yz} \\ \delta^{zx} & \delta^{zy} & \delta^{zz} \end{pmatrix} \cdot \begin{pmatrix} B_0^x \\ B_0^y \\ B_0^z \end{pmatrix} \tag{1.5}$$

NMR isotope shift

The NMR isotope shift is of two kinds:
- Primary, when the atom of interest is swapped with one of its isotopes (eg. replacing hydrogen with deuterium).
- Secondary, when an atom neighbouring with the atom of interest is swapped with one of its isotopes (eg. CH_4 compared with CD_4, where ^{13}C is of interest).[47]

The former induces a large change in the gyromagnetic ratio (Larmor frequency) of the nucleus (^1H NMR compared with ^2H NMR) whereas the latter induces a small change in the chemical shift (^{13}C chemical shift of CH_4 is slightly different compared with CD_4).

The change in chemical shift owed to the secondary isotope shift effect is due to a change in vibrational characteristics of the molecule.[47,48] The change in vibrational properties of the molecule results from changing the mass of the nuclei involved, and the nuclear spin does not contribute to it.

In a molecule (X-Y), the secondary NMR isotope shift effect changes the chemical shift of a nucleus (X) when its neighbour (Y) is exchanged with a different isotope (Y'). The chemical shift of nucleus (X) is shifted upfield when its neighbour (Y) is substituted with one of its heavier isotopes (Y').[48] Generally the heavier isotope (Y') is NMR active so this leads to a J-split doublet of the nucleus (X). However, the case studied here does not present a splitting because X and Y are magnetically equivalent. More details are given in chapter 2.

1.3.3.3 J-coupling

J-coupling or "*indirect dipole-dipole coupling*" between 2 nuclear spins. This is termed as indirect because the interaction is mediated by the electrons forming the chemical bonds. Because electrons have spin $\frac{1}{2}$ they can be weakly polarised by a nuclear spin. This generates a magnetic field at the location of a second nuclear spin, which depends on the nuclear spin state of the first nucleus; which changes the precession frequency (Larmor frequency) of the second nucleus. Thus, the electron mediated the interaction between the two nuclear spins. Because the spin states are quantized, J-coupling leads to discrete splitting of the energy levels, with equal splitting magnitudes for the two interacting nuclear spins. The J-coupling is independent of the applied magnetic field B_0.

As with the chemical shift, in liquid state due to chaotic molecular motion, the J-coupling becomes isotropic and averages out to a scalar quantity, eq. 1.6. However, in solid state it is a tensor quantity, $\mathbf{J}^{ab}$ which describes the J-coupling Hamiltonian between spin a and b, eq. 1.7.[46]

$$\hat{H}_{ab}^{J_{isoAB}} = 2\pi J_{ab}\,\hat{\mathbf{I}}_a \cdot \hat{\mathbf{I}}_b \tag{1.6}$$

$$\hat{H}_{ab}^{J} = 2\pi\hat{\mathbf{I}}_a \cdot \mathbf{J}_{ab} \cdot \hat{\mathbf{I}}_b = 2\pi \begin{pmatrix} \hat{I}_{ax} & \hat{I}_{ay} & \hat{I}_{az} \end{pmatrix} \cdot \begin{pmatrix} J_{ab}^{xx} & J_{ab}^{xy} & J_{ab}^{xz} \\ J_{ab}^{yx} & J_{ab}^{yy} & J_{ab}^{yz} \\ J_{ab}^{zx} & J_{ab}^{zy} & J_{ab}^{zz} \end{pmatrix} \cdot \begin{pmatrix} \hat{I}_{bx} \\ \hat{I}_{by} \\ \hat{I}_{bz} \end{pmatrix} \tag{1.7}$$

Equations shown above describe strong J-couplings between the spins, where the difference in chemical shifts of a and b is comparable to the J-coupling between them. This represents a J-coupled AB spin system which occurs for homonuclear spins.[46]

A further symplification can be done for J-couplings in high field NMR. For heteronuclear spins, or weakly coupled spins (where the chemical shift difference is much larger than their J-coupling), a J-coupled AX spin system is a good approximation of eq. 1.6. The AX J-coupling Hamiltonian is given in eq. 1.8.[46]

$$\hat{H}_{ab}^{J_{isoAX}} \simeq 2\pi J_{ab}\,\hat{I}_{az}\hat{I}_{bz} \tag{1.8}$$

The approximation is valid because off-diagonal terms are small (involving $\hat{I}_x$ and $\hat{I}_y$ in the $\hat{I}_z$ eigenbasis) and only $\hat{I}_z$ terms make a significant contribution (i.e. secular approximation[46]). Interactions defined here are based on products of spin operators, which also constitute the Zeeman product operator basis for multi-spin systems, all done within the product operator formalism.[49]

1.3.3.4 NMR propagators

In NMR, it is common to work with the "density matrix" ($\hat{\rho}$) and not with wavefunctions. The wavefunction represents the quantum state of a single spin system, whereas the density matrix represents the quantum state of the ensemble of spin systems. The density matrix $\hat{\rho} = \overline{|\psi\rangle\langle\psi|}$, where the overbar symbolises an ensemble average. A quantum system is described by the Schrödinger equation, left side of eq. 1.9. The analogous equation can be easily written in terms of the density matrix: the Liouville von Neumann equation on the right side of eq. 1.9.

$$i\hbar\frac{d}{dt}|\psi(t)\rangle = \hat{H}|\psi(t)\rangle \Longrightarrow i\hbar\frac{d}{dt}\hat{\rho} = [\hat{H}, \hat{\rho}] \tag{1.9}$$

Where $[\hat{H},\hat{\rho}]$ denotes the commutator between $\hat{H}$ and $\hat{\rho}$, $[\hat{H},\hat{\rho}] = \hat{H}\hat{\rho} - \hat{\rho}\hat{H}$.[46] If the Hamiltonian is time independent, then eq. 1.9 has a simple solution, eq. 1.10:

$$|\psi(t)\rangle = exp(-i\hat{H}t/\hbar)\,|\psi(0)\rangle \Longrightarrow \hat{\rho}(t) = exp(-i\hat{H}t/\hbar)\hat{\rho}(0)exp(i\hat{H}t/\hbar) \tag{1.10}$$

where $exp(-i\hat{H}t/\hbar)$ represents the propagator of $\hat{H}$. Thus, if the initial density matrix $\hat{\rho}(0)$ and the propagator are known, the density matrix after the propagator has acted on it, for time t, can be calculated ($\hat{\rho}(t)$). This is how NMR simulations are performed. Pulse sequences and interactions can be written in terms of their Hamiltonians, which can be transformed into propagators acting on an initial density matrix. Thus, the final density matrix is obtained, which gives rise to the observed NMR signal. This is how NMR simulations have been done in this study, using Spin Dynamica: a NMR simulation package for Mathematica.[50]

In the NMR community is common to work in Liuouville space rather than Hilbert space, which uses superoperators acting on operators.[51] In Liuouville space the hats are dropped from operators and hats are only used to refer to superoperators. This notation is used in section 2.4.4.1.

Chapter 2

Fine structure in the solution state ^{13}C-NMR spectrum of C_{60}

2.1 Introduction

Since its discovery, the C_{60} fullerene was believed to contain a single peak in its ^{13}C solution NMR spectrum, which was rather unusual due to the large size of the molecule. This observation, however, served as a piece of evidence for the icosahedral symmetry that the molecule possesses.[52,53] Since only one peak was observed and the molecule was known to consist of 60 carbon atoms, it was concluded that all 60 sites in the molecule are chemically equivalent. This is not the case for the next most common fullerene C_{70} which displays 5 peaks at significantly different chemical shifts in the ^{13}C solution NMR spectrum.[52]

A molecule with icosahedral symmetry exhibits chemical equivalence at all its sites. It was eventually proven that the mathematical shape which describes the structure of the C_{60} molecule is a truncated icosahedron,[7,54–56] see fig. 2.10 (a-c) for 3D structure of C_{60}. The carbon atoms in C_{60}, therefore are placed at the vertices of a truncated icosahedron, with 20 hexagonal faces and 12 pentagonal faces giving a total of 90 C-C bonds.

A subtle fact about the structure is that not all 90 C-C bonds are equal. There are two types of C-C bonds in C_{60}: 60 HP bonds when the bond is shared between a Hexagon-Pentagon edge and 30 HH bonds when the bond is shared between a Hexagon-Hexagon. These two types of bonds are shown in fig. 2.10 (a-c), where the HP bonds are in thin gray and the HH bonds are in thick black. It was experimentally proven that the HP bonds are longer than the HH bonds.[7,54–56] The bond lengths are measured to be: $r_{\mathrm{HH}} = 139.5 \pm 0.5\,\mathrm{pm}$ and $r_{\mathrm{HP}} = 145.2 \pm 0.2\,\mathrm{pm}$ by X-ray diffraction.[54] Similar results are obtained through solid-state NMR,[7] gas-phase electron diffraction[55] and neutron diffraction.[56] Hence the structure of the C_{60} molecule, strictly speaking, is not a regular truncated icosahedron, since all the bonds are not of equal length.[4]

This chapter is dedicated to understanding the novel fine structure observed in the ^{13}C solution NMR spectrum of C_{60}. Besides the presence of this well-known single peak (which will for the rest of this thesis be referred to as the "main C_{60} peak") in the NMR spectrum of C_{60} (which is used to prove the icosahedral symmetry), two extra side peaks are observed on the shielded side of the main C_{60} peak of weak intensity. These side peaks are shown to arise due to minor isotopomers of C_{60}, when two ^{13}C's are next to each other in the cage. The side peaks are shifted from the main C_{60} peak as a result of the secondary NMR isotope shift effect, when two ^{13}C's are adjacent in the cage.

The solution NMR spectrum of ^{13}C enriched C_{60} is presented, which exhibits widely different characteristics from that of natural abundance C_{60}. The structure of the ^{13}C enriched C_{60} spectrum is more difficult to explain, hence a model based on a Monte-Carlo type approach and a second moment approximation is presented.

Most of the contents of this chapter have been already published in a scientific journal, see ref.[1] for the publication.

2.1.1 Secondary isotope shift in NMR

In order to explain the experimental results, a description of the NMR isotope shift is required. The primary isotope shift in NMR refers to the change in the Larmor frequency when a given nucleus is replaced by one of its isotopes, for example the difference in the Larmor frequency between hydrogen and deuterium when performing NMR measurements at the same magnetic field. The change in resonance for the primary isotope shift is usually much larger than for the secondary isotope shift.

The secondary isotope shift is defined as the change in the NMR chemical shift of a given nucleus, when a neighbouring atom is exchanged with one of its isotopes.[47,48,57–59] The secondary NMR isotope shift effect stems from the vibrational dynamics of nuclei in molecules. When one of the nuclei within a molecule is replaced by an isotope with a different mass, this affects the vibrational modes (wavefunctions) of the molecule. A small introduction of the secondary NMR isotope shift effect is given below.[47,48,57–59]

The shielding of a nuclear spin, and implicitly the chemical shift, depend on the electronic wavefunction of the given atom/molecule (molecule in our case). In turn the electronic wavefunctions depend on the nuclear coordinates of all the nuclei in the molecule. Within the Born-Oppenheimer approximation the motion of the electrons is so fast that the electronic wavefunctions rapidly adjust to a change in the nuclear coordinates, such as molecular vibrations. The NMR shielding or chemical shift depends on the average over the internuclear distances explored by the nuclear vibrational wavefunction, since as the molecule vibrates the electronic wavefunctions rapidly adjust and the nuclear spins can only experience these very fast motions on average.

However, the vibrational wavefunction of the nuclei strongly depends on their mass. Nuclei with larger mass have vibrational wavefunctions more strongly localised at the minimum of the potential energy surface (PES); in other words vibrate less than lighter nuclei. As soon as the potential energy surface is asymmetric (anharmonic) with respect to the potential minimum (e.g. Morse potential), the mean expectation value of the nuclear positions depend on the masses of the nuclei. Thus for anharmonic vibrations (with asymmetric PES) the average distance between heavy nuclei is smaller compared to lighter nuclei experiencing the same vibrational PES. Molecular vibrations generally have such anharmonicity or asymmetry of the PES, since repulsion terms tend to dominate. The anharmonicity and the force constant of the bond (i.e. the shape of the PES) are expected to affect the secondary isotope shift.

In the case discussed in this study, one substitutes a ^{12}C atom with a ^{13}C which through the secondary NMR isotope shift deshields a nearby ^{13}C nucleus. Since the nucleus of interest and the one being exchanged into are both ^{13}C, they will each generate a secondary isotope shift to each other and both will have their chemical shifts changed (deshielded). Furthermore, the one-bond isotope shift for the same atomic pair will depend on the force constant and anharmonicity of the bond between the nuclei. Taking the HP and HH bonds in C_{60} discussed in the previous section into account, one would expect two different one-bond secondary isotope shifts when a ^{13}C pair is either along a HP or a HH bond.

2.2 Experimental

All NMR measurements shown in this chapter have been performed in solution state.

Fullerene C_{60} powder was purchased from Materials Technologies Research Ltd. (Cleveland, Ohio, USA) and then purified by sublimation. Natural abundance C_{60} solution was prepared by dissolving 23.4 mg of sublimed C_{60} powder in ∼1.1 mL of ortho-dichlorobenzene-d$_4$ (ODCB-d$_4$, Sigma-Aldrich). The solution was filtered to remove any undissolved impurities and degassed by bubbling O_2-free N_2 gas through the solution for 10 min.

The endofullerenes $H_2@C_{60}$ and $H_2O@C_{60}$ were prepared by the group of Richard Whitby through molecular surgery techniques.[16,18–20,60]

13-15 mg of $H_2O@C_{60}$ (79% filled) was dissolved in 0.75 mL ODCB-d$_4$ (Sigma-Aldrich). The solution was filtered to remove any undissolved impurities and degassed by bubbling O_2-free N_2 gas through the solution for 10 min.

13-15 mg of $H_2@C_{60}$ (88% filled) was dissolved in 0.75 mL ODCB-d_4 (Sigma-Aldrich). The solution was filtered to remove any undissolved impurities and degassed by bubbling O_2-free N_2 gas through the solution for 10 min.

C_{60} fullerene isotopically enriched in ^{13}C was purchased as 20-30% ^{13}C-enriched powder from MER Corporation (Tucson, Arizona, USA) and then purified by sublimation. 15.5 mg of sublimed powder was dissolved in 1 mL of ODCB-d_4, then $\sim$ 10 μL of TMS was added. The solution was filtered to remove undissolved impurities and degassed by O_2-free N_2 bubbling for 10 mins.

A mixture sample of natural abundance C_{60} and 20-30% ^{13}C-enriched C_{60} was made by adding the samples made above (in ODCB-d_4) into a 5 mm NMR tube (and $\sim$ 10 μL of TMS). The mixture ended up having a 1:0.6 mass ratio of natural abundance to ^{13}C enriched C_{60} and a volume of $\sim$0.8 mL. The solution was filtered to remove undissolved impurities and degassed by O_2-free N_2 bubbling for 10 mins.

All NMR experiments were performed at a field of 16.45 T in a Bruker Ascend 700 NB magnet fitted with a Bruker TCI prodigy 5 mm liquids cryoprobe and a Bruker AVANCE NEO console.

All NMR solution state measurements were done on 5 mm NMR tubes. In order to improve the magnetic field homogeneity and implicitly the spectral resolution, Wilmad precision NMR tubes rated for 900MHz (Sigma-Aldrich) were used in every case.

In all NMR measurements presented in this chapter, the widths of peaks at half-maximum height are between 0.128 Hz and 0.272 Hz, the bulk of measurements having line widths under 0.200 Hz.

Mass spectrometry measurements were done using a solariX (Bruker Daltonics, Bremen, Germany) FT-ICR mass spectrometer equipped with a 4.7 T superconducting magnet. Sample was infused via a syringe driver at a flow rate of 5 $\mu L/minute$. Mass spectra were recorded using positive ion atmospheric pressure photoionisation (APPI).

2.3 Results

The experimental results used to show the fine structure of the ^{13}C NMR spectrum of natural abundance C_{60} are given below. In addition, results regarding ^{13}C enriched C_{60} fullerene are also shown.

2.3.1 C_{60} Natural abundance NMR

The high resolution ^{13}C solution NMR spectrum of natural abundance C_{60} is given in fig 2.1. The spectrum displays the usual C_{60} peak at $\sim$ 142.818 ppm, referenced with respect to the ODCB-d$_4$ peak at 127.19 ppm,[61] labelled as "Main C$_{60}$ peak".[5,6,20] However, if the resolution is high enough, the spectrum reveals two small additional side peaks at a slightly lower chemical shift with respect to the main peak. In fig.2.1 c they are labelled HP and HH; the naming convention will become apparent in the following sections.

The two side peaks HP and HH have an intensity (peak area) ratio of 2:1 respectively. The HP peak is at $\Delta\delta_1 = -12.6$ ppb relative to the main ^{13}C peak and the HH is at $\Delta\delta_2 = -20.0$ ppb (at 295 K). The integrated peak areas of the side peaks, relative to the main ^{13}C peak, are $a_1/a_0 = 1.63 \pm 0.15\,\%$ and $a_2/a_0 = 0.81 \pm 0.08\,\%$ respectively; where 0 stands for the main C$_{60}$ peak, 1 for the HP peak and 2 for HH. The ratio of the integrated amplitudes for the two side peaks is given by $a_1/a_2 = 2.02 \pm 0.01$.

Since the side peak intensity is very low compared to the main C$_{60}$ peak, accurately obtaining these ratios is not so straight forward. Integration of the experimental peaks is shown in the following section (2.3.1.1) and the resuting ratios are shown at the bottom row of table 2.1.

2.3.1.1 Side peaks integration (Spectral fitting procedure)

The low intensity of the side peaks with respect to the main C$_{60}$ peak, means one needs to be careful when stating relative ratios between them. This is being exemplified in this section by using three different methods to estimate the ratios between the low intensity side peaks and the intense main C$_{60}$ peak.

In table 2.1 the integrated area of HP (a_1) and HH (a_2) peaks from fig. 2.1 2.1 are given with respect to the main C$_{60}$ peak (a_0). Three different methods were used to calculate these ratios, labelled on the left side and with the average values shown on the bottom.

TABLE 2.1: Ratios relative to the main C$_{60}$ peak (a_0/a_0=100%) for HP (a_1/a_0) and HH (a_2/a_0) (from fig. 2.1). Integration methods are defined in text. Reproduced from Ref.[1] with permission from the PCCP Owner Societies.

Method	HP (a_1/a_0)	HH (a_2/a_0)	HP/HH (a_1/a_2)
TopSpin	1.969%	0.981%	2.007
Lorentzian	1.5215%	0.754%	2.016
Interpolation	1.416%	0.688%	2.056
Average	1.63 ± 0.15 %	0.81 ± 0.08 %	2.02 ± 0.01

Firstly, the spectrum was fitted in TopSpin, where the side peaks (HP and HH) were fitted with a single Lorentzian shape and the main C$_{60}$ peak was fitted with 45% Lorentzian + 55% Gaussian. This fitting procedure is shown in fig. 2.2 where the experimental spectrum is in blue, the fitted spectrum in red and difference between the two is shown in black. The spectrum showing the difference displays just noise where the side peaks are, but it shows a significant remainder for the main C$_{60}$ peak; this remainder was

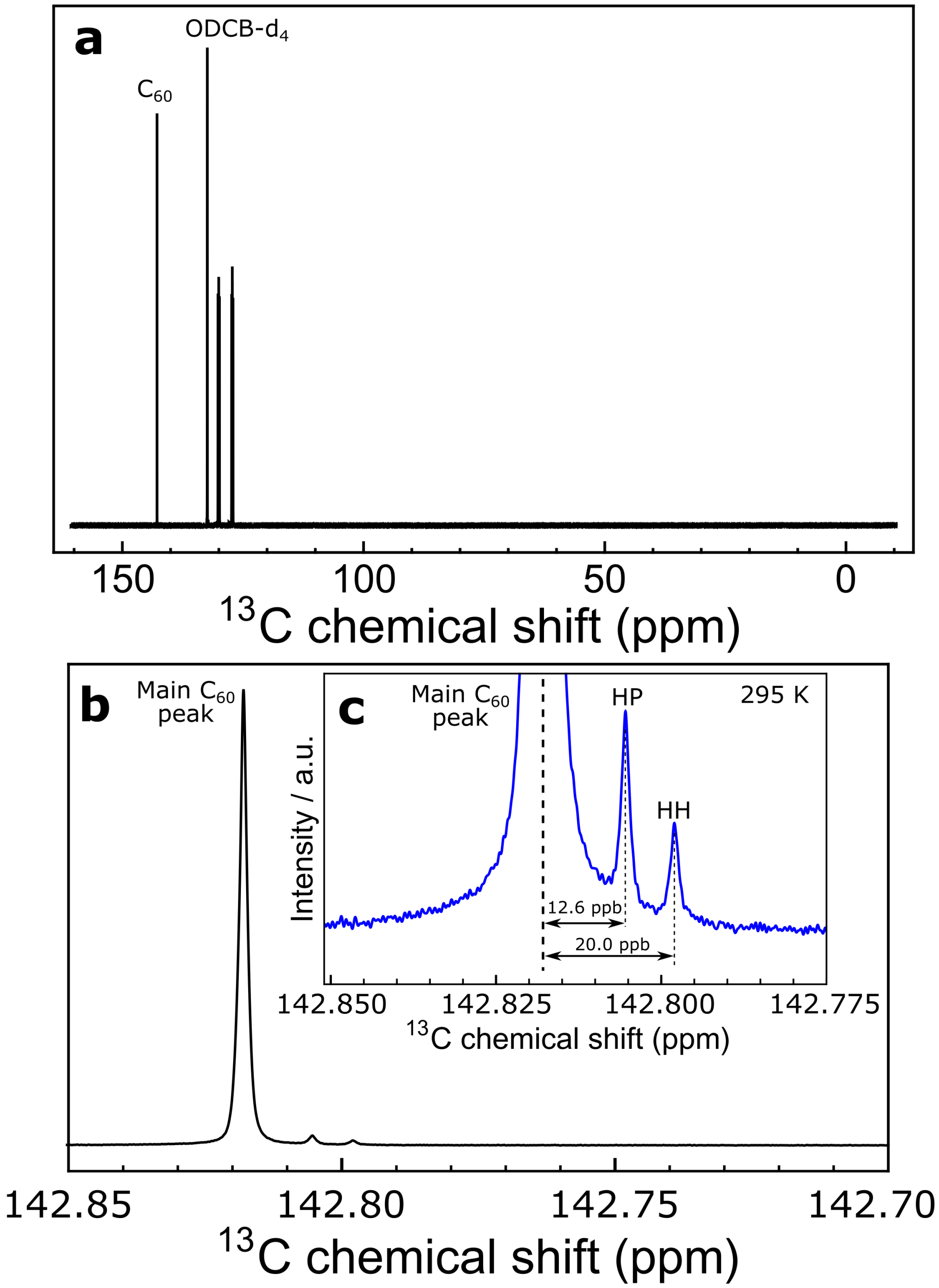

FIGURE 2.1: ^{13}C NMR spectrum of ∼25 mM C_{60} in deuterated orthodichlorobenzene (ODCB-d_4), at a magnetic field of 16.45 T and a temperature of 295 K (sum of 856 transients). (a) - full spectrum, (b) - spectrum around the C_{60} peak, (c) - focused spectrum around the main C_{60} peak showing the assignment of the side peaks to ^{13}C pairs sharing either a HP (hexagon-pentagon) or a HH (hexagon-hexagon) bond. The main C_{60} peak is at 142.818 ppm relative to TMS. The side peak shifts from the main C_{60} peak are $^{1}\Delta \simeq 12.6$ ppb for a HP $^{13}C_2$ pair and $^{1}\Delta \simeq 20.0$ ppb for a HH $^{13}C_2$ pair. Reproduced from Ref.[1] with permission from the PCCP Owner Societies.

taken into account when calculating the ratios. These results are show in table 2.1, on the "TopSPin" row.

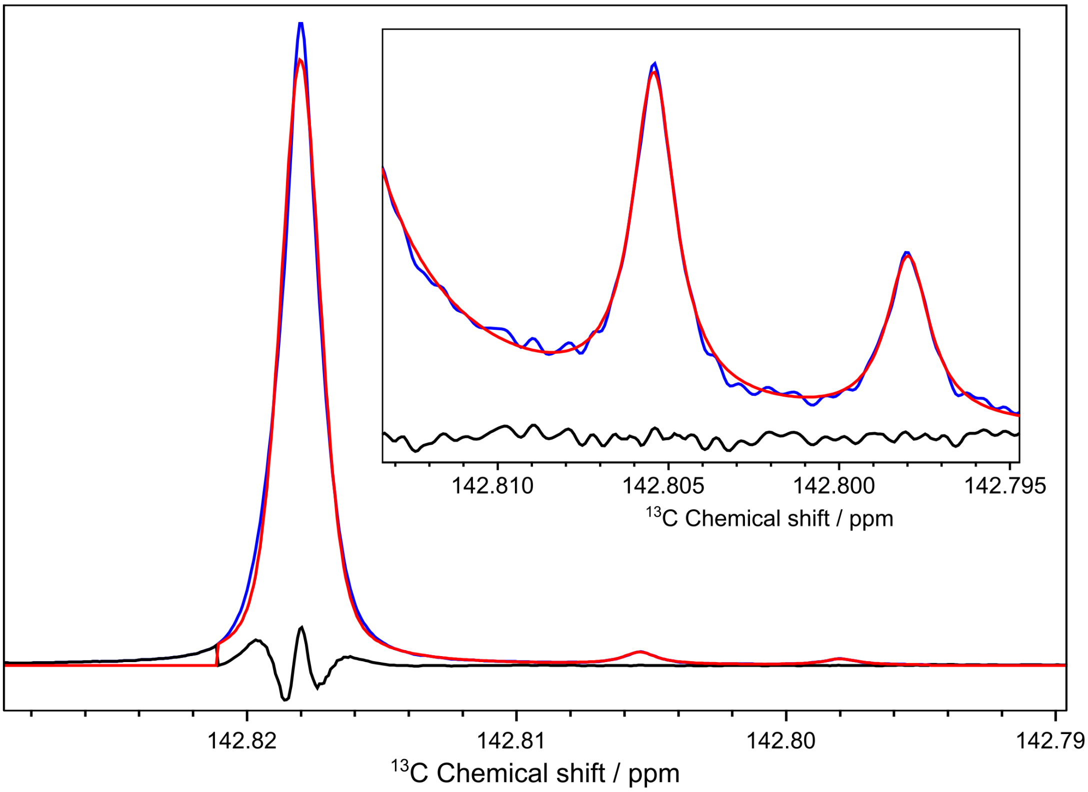

FIGURE 2.2: Blue: Experimental ^{13}C NMR spectrum from fig 2.1. Red is the fitted spectrum using the ”TopSpin” method, a single Lorentzian function was used for HP and HH, and main C_{60} peak was fitted with 45% Lorentzian and 55% Gaussian. Black is the diferece between Blue and Red. The insert is the same spectra just scaled around the side peaks for clarity. Peak integrals are found in table 2.1 on the TopSpin row. Reproduced from Ref.[1] with permission from the PCCP Owner Societies.

In table 2.1, the Lorentzian row means the HP and HH peaks were fitted with a single Lorentzian shape function and the main C_{60} was fitted with a two Lorentzian functions; each function having three free parameters. This method was carried out using the Wolfram Mathematica software.

In table 2.1, the Interpolation row signified that the peaks were interpolated with a spline function and then numerically integrated to give the area. The raised baseline under the HP/HH peaks was corrected by a double Lorentzian fit for the main C_{60} peak (from the previously mentioned ”Lorentzian” fitting). This method was carried out using the Wolfram Mathematica software.

2.3.1.2 Influence of endohedral species

The same pattern of side peaks are found in the ^{13}C solution NMR spectrum of endofullerenes, where the C_{60} cage fully encloses guest molecules such as H_2 and H_2O, see fig. 2.3.

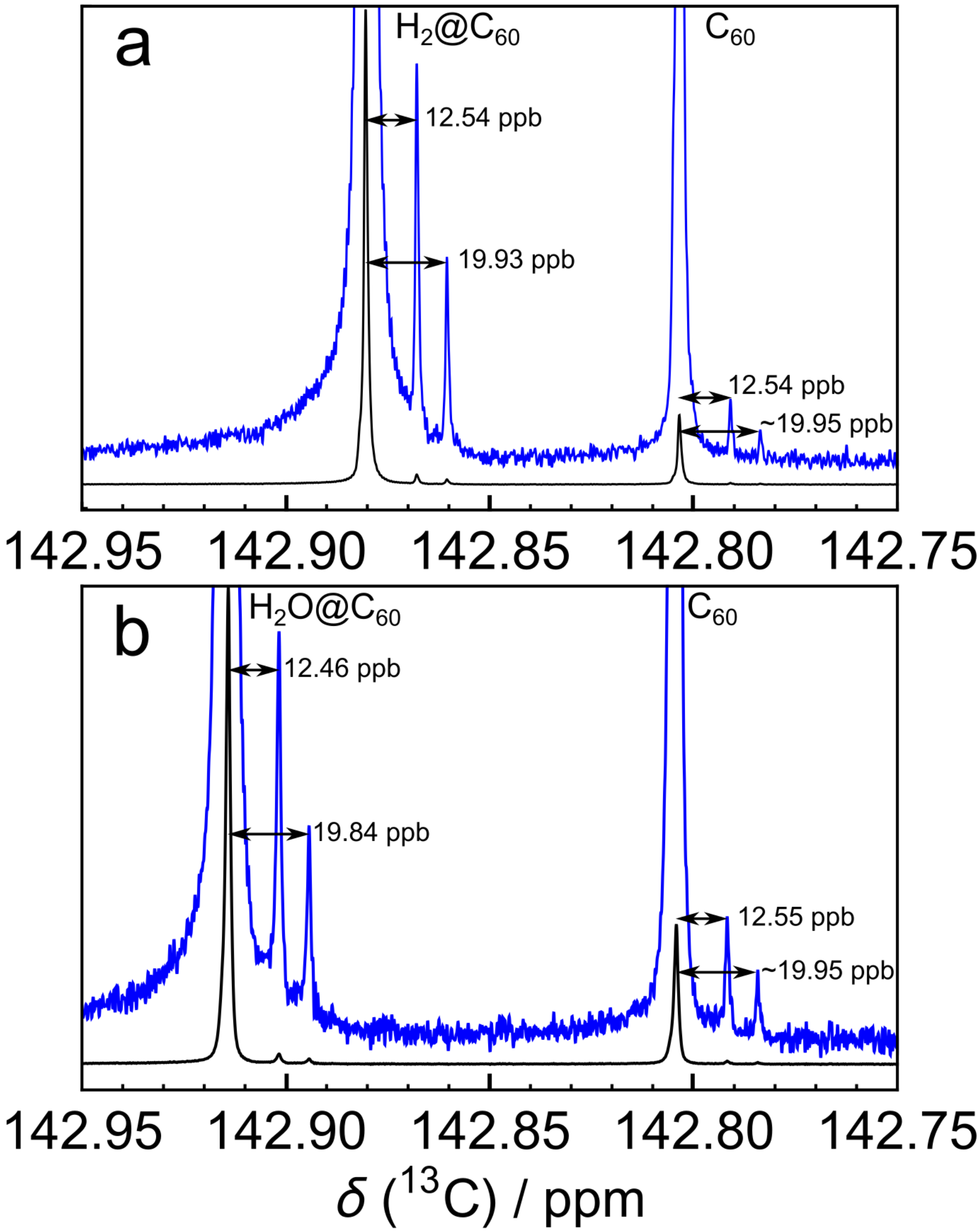

FIGURE 2.3: ^{13}C NMR spectra of ∼25 mM solutions of (a) $H_2@C_{60}$ (filling factor 87.7%, sum of 416 transients) and b) $H_2O@C_{60}$ (filling factor 78.6%, sum of 272 transients) in ODCB-d_4 at a temperature of 298 K. For each species, a pair of side peaks on the shielding side of the main ^{13}C peak is clearly visible. Reproduced from Ref.[1] with permission from the PCCP Owner Societies.

In the case of endofullerenes, the ^{13}C chemical shifts of the main peak is perturbed by the endohedral species inside of C_{60}.[16,18–21,62] This leads to two main peaks in the spectrum since the endofullerenes have a filing factor of $<$ 100 %; one main peak for empty C_{60} and one for the filled fullerene (at larger chemical shifts with respect to empty). The endofullerene main peak has the same side peaks situated at lower chemical shifts as observed for empty C_{60}. In fig. 2.3 the side peaks are seen to follow the main endofullerene peak and in the same spectrum the pattern is seen to be the same as for the empty C_{60}.

The endofullerene side peaks have the same amplitude ratio of 2:1. However, the shifts from the main peak are slightly changed by the presence of the endohedral molecule. The enclosed species seem to slightly decrease the shifts as compared to the empty C_{60}. Furthermore, the larger endohedral species seems to decrease the shifts more (fig. 2.3). The observed shift for the HH peak also seems to be affected more by the presence of the endohedral species than the HP peak. These side peak shifts are tabulated in table 2.2 at 298 K.

2.3.1.3 HP & HH side peaks temperature dependence

The shifts of the HP & HH side peaks relative to the main peak present a rather weak dependence on temperature. Both shifts decrease as temperature is increased, shown in figure 2.4, where both Y-axis scales span the same range.

The change in the shifts with respect to temperature fit well to a linear equation over the explored temperature range, with notation shown in eq. 2.1 below:

$$\Delta\delta_i = \Delta\delta_i^0 + (\mathrm{d}\Delta\delta_i/\mathrm{d}T)T \text{ with } i \in \{1,2\} \tag{2.1}$$

Where 1 and 2 stand for HP and HH respectively.

The data fitted with linear equations is shown in fig. 2.4 for C_{60}, $H_2@C_{60}$ and $H_2O@C_{60}$.

The linear fit parameters for the temperature dependence of C_{60} and two endofullerenes ($H_2@C_{60}$ and $H_2O@C_{60}$) are given in Table 2.2.

From fig. 2.4 and table 2.2 is seen that the shift pertaining to the HH side peak is more sensitive to temperature than HP. HH is also slightly more affected by the presence of an endohedral molecule than HP. In fig. 2.4 a, there is essentially no difference between the HP shifts of C_{60} and $H_2@C_{60}$. However, a measurable difference is seen between the HP shifts of C_{60} and $H_2O@C_{60}$. In comparison the HH shift shows a systematic change downwards when the size of the endohedral molecule is increased, which is consistent at all temperatures.

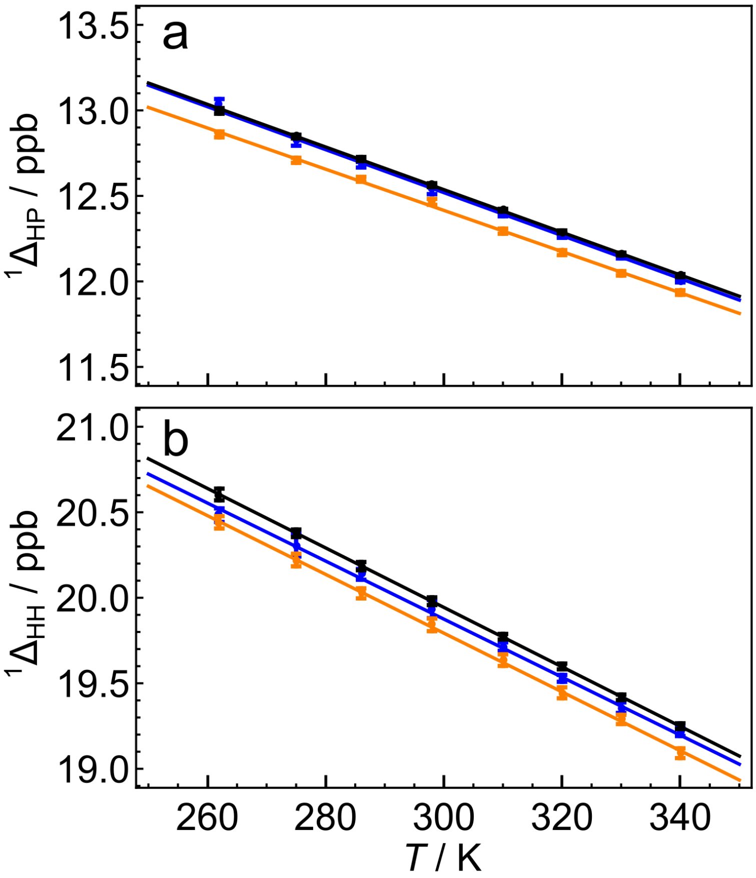

FIGURE 2.4: Temperature dependence of the side peaks shifts for C_{60} (black), $H_2@C_{60}$ (blue) and $H_2O@C_{60}$ (orange), for (a) HP the first side peak, and (b) HH the second side peak. The solid lines are best linear fits of the form $^1\Delta(T) =^1 \Delta^0 + (\mathrm{d}^1\Delta/\mathrm{d}T)T$, where the fit parameters are given in Table 2.2. The side peak shifts $\Delta\delta_1$ and $\Delta\delta_2$ are related to the isotope shifts by a sign change (see equation 2.4). Both vertical scales span the same ppb range. Reproduced from Ref.[1] with permission from the PCCP Owner Societies.

2.3.1.4 C_{60} Natural abundance, ^{13}C T_1 results

The ^{13}C spin-lattice relaxation time constant T_1 was measured. The ^{13}C T_1 of natural abundance C_{60} was measured using saturation recovery. The peak integral relaxation curve is seen in fig. 2.5. The data fits well to a mono-exponential function, which gives the natural abundance C_{60} spin-lattice ^{13}C T_1 = 16.6±0.3 s, at a field of 16.45 T.

2.3.2 C_{60} 20-30% ^{13}C enriched NMR

Since new side peaks were observed in the ^{13}C solution NMR spectrum of natural abundance C_{60}; the next natural step was to measure the same NMR spectrum of ^{13}C enriched C_{60} and observe how the spectral features vary as a result of the enrichment. In this section ^{13}C solution NMR results are shown for ^{13}C enriched C_{60}.

TABLE 2.2: Linear regression parameters for the temperature dependence of the secondary ^{13}C isotope shifts for C_{60} and the endofullerenes $H_2@C_{60}$ and $H_2O@C_{60}$ (Fig. 2.4). The side peak shifts $\Delta\delta_1$ and $\Delta\delta_2$ are related to the isotope shifts by a sign change (see equation 2.4). Reproduced from Ref.[1] with permission from the PCCP Owner Societies.

parameter	C_{60}	$H_2@C_{60}$	$H_2O@C_{60}$
$^1\Delta_{HP}$(298 K)/ppb	12.56 ± 0.01	12.54 ± 0.03	12.46 ± 0.02
$^1\Delta^0_{HP}$/ppb	16.28 ± 0.05	16.29 ± 0.11	16.03 ± 0.06
$(d^1\Delta_{HP}/dT)$ / 10^{-3} ppb K^{-1}	-12.47 ± 0.15	-12.56 ± 0.34	-12.04 ± 0.20
$^1\Delta_{HH}$(298 K)/ppb	19.98 ± 0.02	19.93 ± 0.05	19.84 ± 0.04
$^1\Delta^0_{HH}$/ppb	25.16 ± 0.10	24.96 ± 0.18	24.94 ± 0.14
$(d^1\Delta_{HH}/dT)$ / 10^{-3} ppb K^{-1}	-17.38 ± 0.30	-16.96 ± 0.58	-17.17 ± 0.44

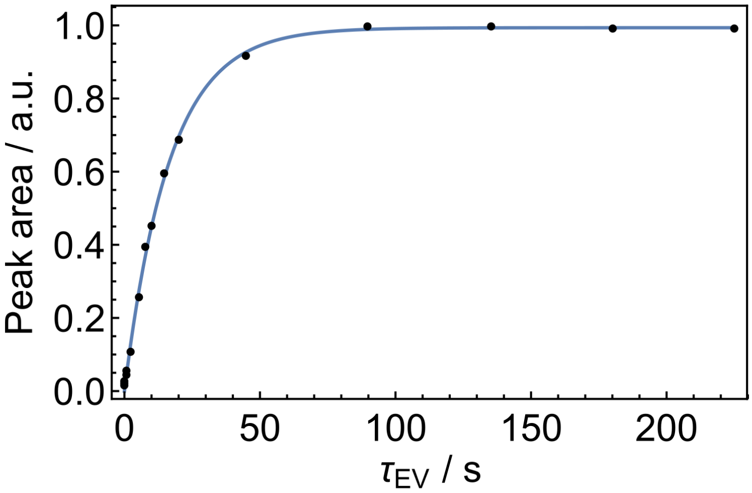

FIGURE 2.5: Saturation Recovery relaxation curve for C_{60} natural abundance 4.5 mM at 16.45 T (Ω^{13}C = 176 MHz) and 295 K with 80 transient; sample degassed by bubbling N_2 for 10 mins. ^{13}C T_1 = 16.6±0.3 s, fitted with $I_0 * (1 - exp(\frac{-t}{T_1}))$, where $I_0 = 0.994 \pm 0.005$. Reproduced from Ref.[1] with permission from the PCCP Owner Societies.

The ^{13}C NMR spectrum of a solution of 20%-30% ^{13}C enriched C_{60} in ODCB-d_4 is shown in fig. 2.6 at the top in blue. On the same figure the spectrum of the natural abundance C_{60} is shown at the bottom in black, where only the side peaks are scaled by ×80 in gray for clarity.

In the ^{13}C solution NMR spectrum of 20%-30% ^{13}C enriched C_{60} instead of three discrete peaks (one main and two side peaks), a relatively broad lineshape is observed. The total width of the feature is about 40 ppb. This broad peak is much closer to a Gaussian lineshape than a Lorentzian one. Furthermore, it shows a rather distinct shoulder on the deshielding ("downfield") side of the peak.

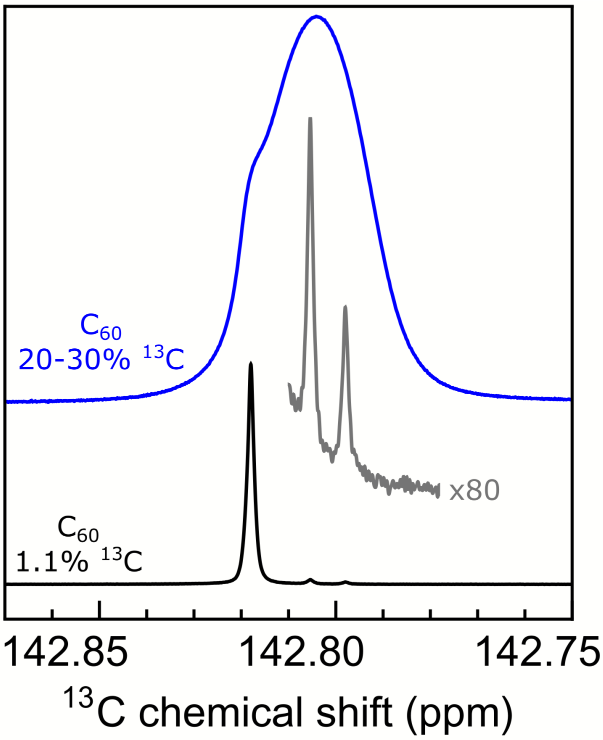

FIGURE 2.6: Blue: ~21 mM C_{60} 20-30% ^{13}C enriched in ODCB-d_4, at a magnetic field of 16.45 T and 295 K (sum of 16 transients). Black: ~25 mM natural abundance C_{60} in ODCB-d_4, at a magnetic field of 16.45 T and 295 K (sum of 856 transients). Gray is just the black spectrum scaled by 80 around the side peaks. Spectra were referenced relative to each other as described in section 2.3.2.1. The vertical scale is arbitrary for clarity.

The shoulder matches the chemical shift corresponding to the main ^{13}C peak seen in natural abundance C_{60} and the centre of the broad feature matches the side peaks much better than the main C_{60} peak (fig. 2.6). Accurate relative chemical shift referencing between ^{13}C enriched and natural abundance C_{60} is done in the next section (section 2.3.2.1), where a mixture sample of the two was measured.

From these measurements it seems that isotopically enriching C_{60} with ^{13}C obscures the side peak fine structure in the solution state ^{13}C NMR spectrum.

2.3.2.1 C_{60} 20-30% ^{13}C enriched chemical shift referencing

The ^{13}C solution NMR spectrum of 20-30% ^{13}C enriched C_{60} was shown in fig. 2.6. However, since the peaks involved are very narrow, referencing the chemical shifts of the natural abundance and ^{13}C enriched C_{60} in different samples did not give a satisfactory result.

Thus, to accurately reference the chemical shift of the ^{13}C enriched C_{60} spectrum with respect to natural abundance C_{60}, both were added to a solution and the NMR spectrum of the mixture was measured. The NMR spectrum of the mixture can be seen in blue in fig. 2.7 A. Here in green is shown the spectrum of only 20-30% ^{13}C enriched C_{60}, scaled to match the intensity of the mixture. And in black the difference between blue and green is shown, which should contain signal only from natural abundance C_{60}.

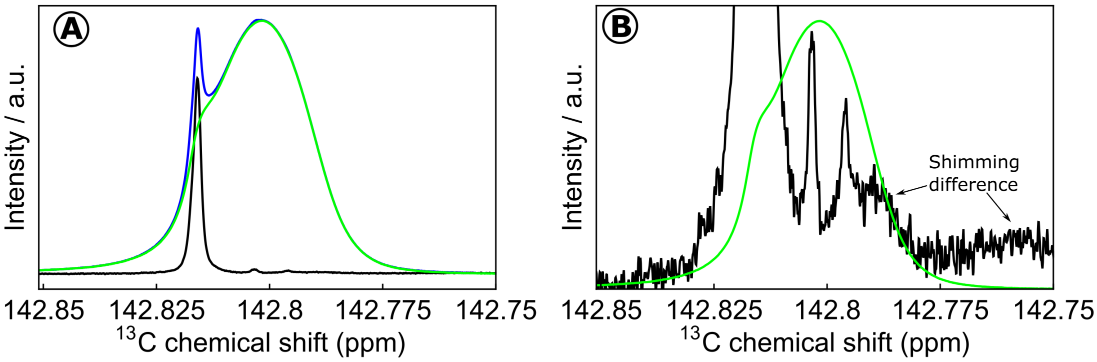

FIGURE 2.7: Experimental ^{13}C NMR spectrum of ~21 mM C_{60} dissolved in ODCB-d_4 solvent acquired at 16.45 T (^{13}C nuclear Larmor frequency = 176 MHz) and 295 K. Green- C_{60} 20-30% ^{13}C enriched (16 scans, scaled to match Blue), Blue- mixture of C_{60} natural abundance + C_{60} 20-30% ^{13}C enriched (1:0.6 mass ratio, 512 scans), Black- is Blue minus Green. B: is the same as A just without Blue and with Black scaled up to see the isotope shifted peaks match the mean chemical shift of the 20-30% ^{13}C enriched C_{60} peak. In B some broader features appear due to shimming and possibly phasing differences between the two samples. Reproduced from Ref.[1] with permission from the PCCP Owner Societies.

The spectrum changes between green (20-30% ^{13}C C_{60}) and blue (mixture). The shoulder on the deshielded side seen in the enriched sample (green) increases when natural abundance C_{60} is added to the solution. This experimentally proves that the shoulder in the 20-30% ^{13}C C_{60} is at the chemical shift of the main C_{60} peak in natural abundance. Thus, it proves that the shoulder arises from isolated ^{13}C's in the cage, since that is the origin of the main C_{60} peak in natural abundance. This referencing can be seen more clearly in the difference spectrum shown in black (blue - green), in fig. 2.7 A and B. The main peak in the black spectrum matches exactly with the shoulder of the purely ^{13}C enriched sample shown in green. In B the black spectrum was scaled up to show the overlap of the HP & HH discrete side peaks with the centre of the broad feature seen in ^{13}C enriched C_{60} (green). In B, the black line has some minor broader features arising due to shimming differences between the enriched C_{60} and the mixture. The narrowness of the peaks in the black spectrum exclude the possibility that the broad feature arises due to magnetic field inhomogeneity.

This referencing procedure experimentally proves that the ^{13}C enrichment washes away the fine structure of the natural abundance sample. It also proves that increased ^{13}C content increases the intensity in the ^{13}C spectrum where the chemical shift of the side peaks are, a fact which is used in the analysis later on.

2.3.2.2 C_{60} 20-30% ^{13}C enriched ^{13}C T_1 results

The ^{13}C spin-lattice relaxation time constant (T_1) was measured for the 20-30% ^{13}C enriched C_{60} sample. The ^{13}C T_1 was measured using inversion recovery and the relaxation curve is seen in fig. 2.8. The data is fitted well by a mono-exponential function, which gives the 20-30% ^{13}C enriched C_{60} ^{13}C T_1 = 14.8±0.2 s, at a field of 16.45 T.

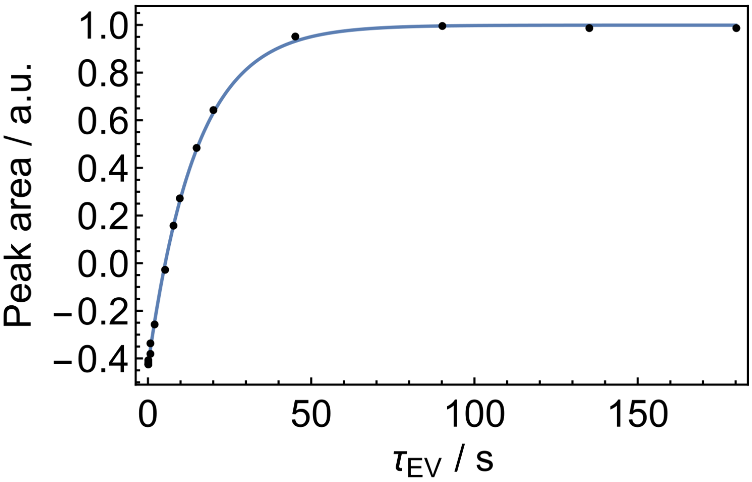

FIGURE 2.8: Inversion Recovery relaxation curve for C_{60} 20-30% ^{13}C ~21 mM at 16.45 T (Ω^{13}C = 176 MHz) and 295 K with 32 transients; sample degassed by bubbling N_2 for 10 mins. ^{13}C T_1 = 14.8±0.2 s, fitted with $I_0 * (1 - A * exp(\frac{-t}{T_1}))$, where $I_0 = 0.999 \pm 0.005$ and A=1.431 $\pm$ 0.004. Reproduced from Ref.[1] with permission from the PCCP Owner Societies.

The ^{13}C T_1 for 20-30% ^{13}C C_{60}, at the same field of 16.45 T, is only a little by shorter than the natural abundance C_{60}. The 20-30% ^{13}C enriched C_{60} ^{13}C T_1 = 14.8±0.2 s whereas the natural abundance C_{60} ^{13}C T_1 = 16.6±0.3 s (from section 2.3.1.4). The slightly shorter T_1 for the enriched C_{60} is expected since it contains a lot more ^{13}C's giving rise to dipolar relaxation.

The small difference between the T_1 's of the enriched and natural abundance C_{60} excludes the possibility that the broad feature seen in the ^{13}C solution NMR spectrum of 20-30% ^{13}C C_{60} spectrum (fig. 2.6 and fig. 2.7 green) arises due to homogeneous broadening (i.e. very fast relaxation). Thus in order to explain the observed spectrum of 20-30% ^{13}C enriched C_{60} one needs a model for inhomogeneous broadening, most likely involving distributions of chemical shifts and J-couplings.

2.3.3 Mass Spectrometry

The mass spectrum of 20-30% ^{13}C enriched C_{60} sample was acquired and it is seen in fig. 2.9. This was done to more accurately probe the ^{13}C isotopomers of the ^{13}C enriched C_{60} sample, since the range of 20-30% ^{13}C specified by MER Corporation is fairly large.

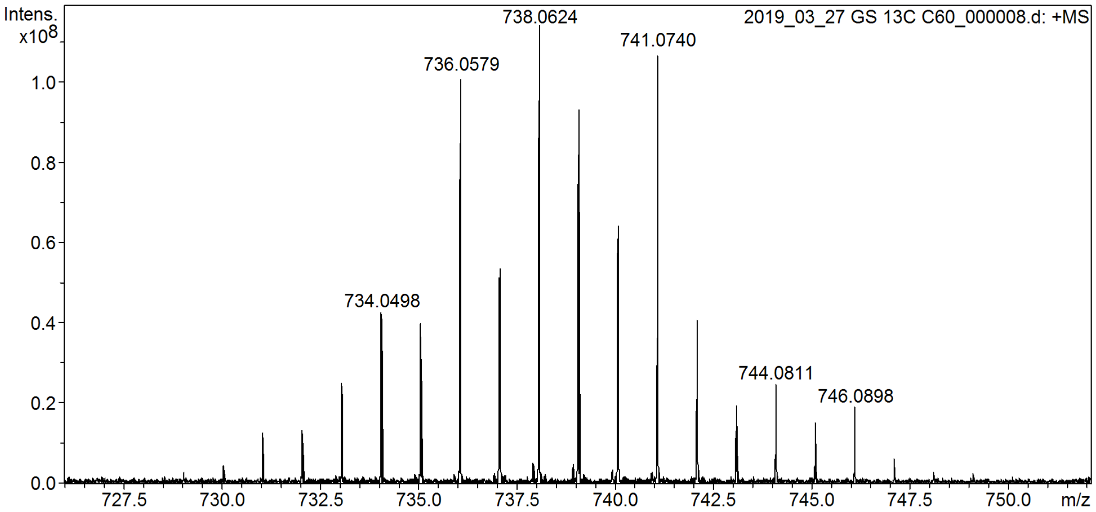

FIGURE 2.9: Experimental FT-Mass Spectrometry spectrum of C_{60} 20-30% ^{13}C enriched. It serves to show the rather non-binomial distribution of ^{13}C's substituted in the cage for this sample. The centre of this distribution is at 18×^{13}C's in the cage, which matches fairly well with the theoretical statistical distribution of 30% (where the distribution is predicted to be peaked at 19×^{13}C). Reproduced from Ref.[1] with permission from the PCCP Owner Societies.

The mass spectrum shows a nearly binomial distribution of ^{13}C's isotopomers of C_{60} centred at 738 m/z, which corresponds to 18×^{13}C's present in the isotopically enriched cage.

The distribution of the peaks seen in the mass spectrum of 20-30% ^{13}C enriched C_{60} deviate from a binomial distribution. We do not know the reason why these variations occur, they might be due to some details of the enrichment procedure implemented in the synthesis of the enriched C_{60}, of which we are not informed.

2.4 Discussion

This section is dedicated to the analysis and discussion of the experimental observations made in section 2.3. It encompasses assignment of the discrete side peaks seen in the ^{13}C solution NMR spectrum of natural abundance C_{60} through a purely statistical approach and a Monte-Carlo type simulation. The Monte-Carlo type model for the simulation of the broad feature in the 20-30% ^{13}C enriched C_{60} NMR spectrum based on the second moment[63] is presented. The prediction made by the model is in agreement with the mass spectrometry results of the ^{13}C enriched C_{60}. It will be shown that the same Monte-Carlo approach can be used to correctly simulate the natural abundance C_{60} spectrum as well.

2.4.1 C_{60} natural abundance discussion

The ^{13}C solution NMR spectrum of C_{60} fullerene is well known in literature to be composed of a single peak, reflecting the high symmetry of this molecule.[52,53] With 60 carbon atoms in its composition but a single NMR peak, it proved that all 60 sites in the molecule are chemically equivalent. The mathematical shape that the C_{60} molecule classifies as is a truncated icosahedron, see fig. 2.10 (a-c). Since the natural abundance of ^{13}C is only 1.108% the majority of the cages that are NMR active have a single ^{13}C present and the other 59 are ^{12}C. Thus, the well-known main C_{60} peak from fig. 2.10 (d,e) arises (mainly as it is shown later) from cages with only one ^{13}C, as sketched in fig. 2.10 (a) where the black circle represents a ^{13}C atom.

Despite the fact that only one peak was known in the ^{13}C solution NMR spectrum of C_{60},[5,6] the high resolution spectrum of natural abundance C_{60} shown in fig. 2.1 and fig. 2.10 (d,e) is clearly composed of three peaks, one major one (main C_{60} peak) and two weak side peaks (HP & HH). The main C_{60} peak is easily assigned to cages with only one ^{13}C, as mentioned above. However, the two side peaks need more investigation to assign them.

The side peaks HP and HH have a relative amplitude area ratio of 2:1 respectively. Their amplitude with respect to the main C_{60} peak are $a_1/a_0 = 1.63 \pm 0.15\,\%$ for HP and $a_2/a_0 = 0.81 \pm 0.08\,\%$ for HH (see table 2.1). In order to gain some insight into the origin of these peaks, a closer look at the exact structure of C_{60} is needed.

The carbon atoms in C_{60} are placed at the vertices of a truncated icosahedron, with 20 hexagonal faces and 12 pentagonal faces giving a total of 90 C-C bonds (fig. 2.10 (a-c)). A rather subtle fact is that not all C-C bonds are equal, which was proved experimentally by a variety of methods.[7,54–56] Because of this fact, the structure of C_{60} seen in nature is *not* a regular truncated icosahedron.

As seen in fig. 2.10 (a-c) the two types of bonds in C_{60} are called HP and HH depending if the bond is shared between a Hexagon-Pentagon (HP) or Hexagon-Hexagon (HH).[64,65] The HP bonds are shown as thin gray lines and HH bonds as thick black lines. Due to the nature of the C_{60} structure there are 60 HP bonds and 30 HH bonds, in abundance ratio 2:1.

It was experimentally proven that the HP C-C bonds are longer than the HH bonds. The bond lengths for the two types are measured to be: $r_{\mathrm{HH}} = 139.5 \pm 0.5\,\mathrm{pm}$ and $r_{\mathrm{HP}} = 145.2 \pm 0.2\,\mathrm{pm}$ by X-ray diffraction.[54] Similar results have been obtained through solid-state NMR,[7] gas-phase electron diffraction[55] and neutron diffraction.[56]

The relative abundance of HP bonds to HH bonds of 2:1 provides the first piece of evidence for the assignment of the side peaks. One may suggest that the observed side peaks in ratio 2:1 arise when two ^{13}C atoms are adjacent along a HP bond or

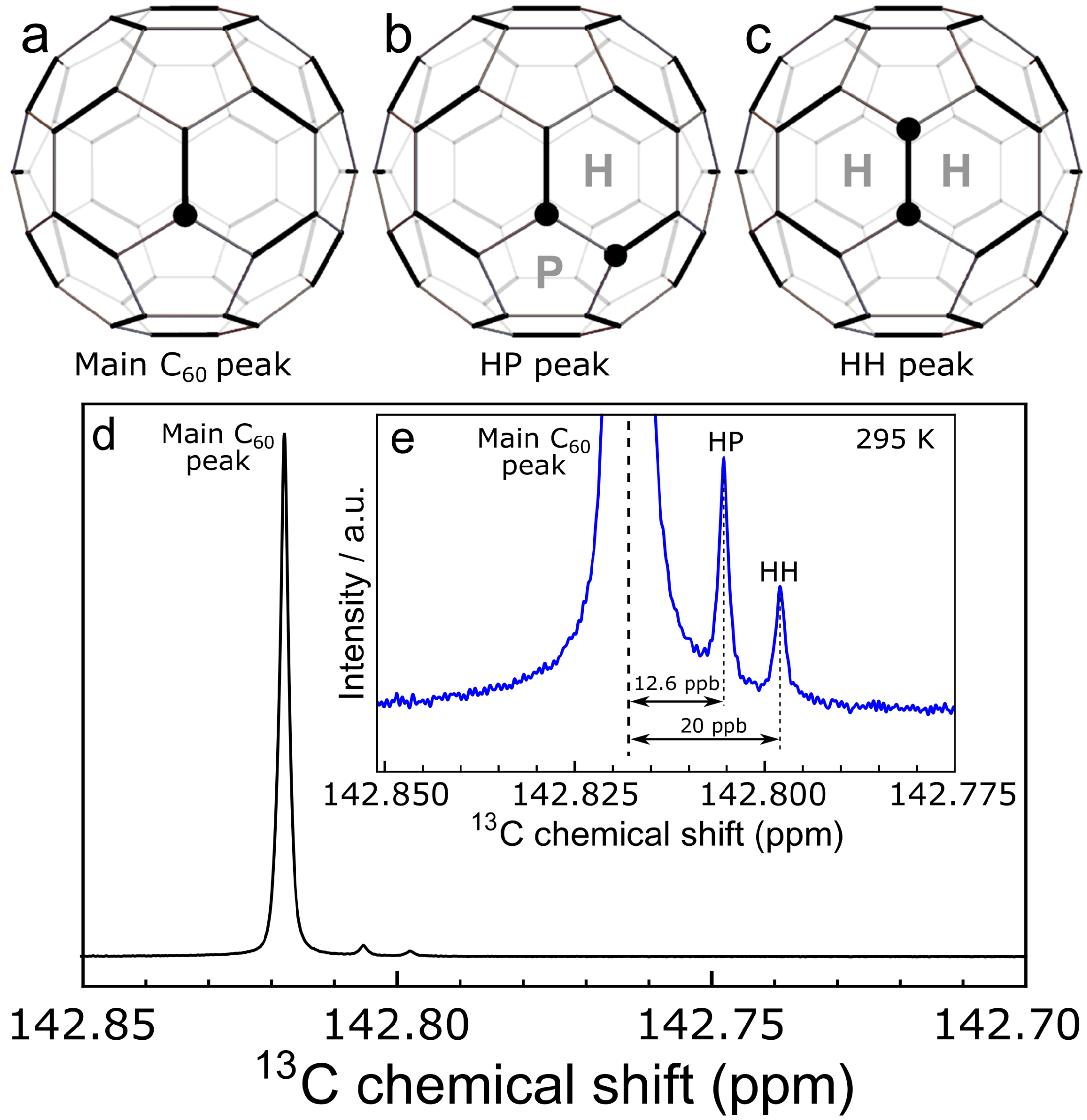

FIGURE 2.10: (a) 3D structure of [$^{13}C_1$]-C_{60}; (b) 3D structure of [HP-$^{13}C_2$]-C_{60}; (c) 3D structure of [HH-$^{13}C_2$]-C_{60}. The ^{13}C's are represented by filled circles and the hexagonal faces (H) and pentagonal faces (P) are indicated. (d) :∼25 mM natural abundance C_{60} in ODCB-d_4, at a magnetic field of 16.45 T and 295 K (sum of 856 transients). (e) is the spectrum in (d) scaled around the side peaks. Note: The C_{60} configurations from (a-c) are not the only ones contributing to the discrete NMR peaks in (d,e), further description is given in section 2.4.1. Reproduced from Ref.[1] with permission from the PCCP Owner Societies.

HH bond, since the probability of being along HP is twice that of being along HH. Thus an interpretation of the natural abundance C_{60} ^{13}C spectrum is given, in terms of the components with the majority of NMR intensity. The main C_{60} peak arises from [$^{13}C_1$]-C_{60} molecules where the ^{13}C is isolated with no ^{13}C's as close neighbours. The HP peak comes from [HP-$^{13}C_2$]-C_{60} molecules where two ^{13}C's are adjacent along a HP bond with no other ^{13}C's nearby and similarly the HH peak comes from [HH-$^{13}C_2$]-C_{60} molecules where two ^{13}C's are adjacent along a HP bond with no other ^{13}C's nearby. Now the naming of the side peaks from fig. 2.1 and fig. 2.10 (d,e) becomes apparent.

As mentioned above, the assignment of the observed side peaks is due to isotopomers of C_{60} when more than one ^{13}C is present in the cage. Depending where the two ^{13}C's are present in the cage they give rise to different NMR peaks. In order to explain the different resonances of the peaks one needs to use the NMR secondary isotope shift effect.[47,48,57–59,66] The secondary isotope shift arises when a neighbouring atom is substituted by one of its isotopes of a different mass and this causes a shift in the NMR resonance of the nucleus in question. In our case, the resonance of [$^{13}C_1$]-C_{60} is different compared to [HP-$^{13}C_2$]-C_{60} or [HH-$^{13}C_2$]-C_{60} since one of the ^{12}C's adjacent to the ^{13}C (of [$^{13}C_1$]-C_{60}) has been substituted by a heavier ^{13}C.

The NMR secondary isotope shift has origins in the vibrational properties of the given molecule, general theory of the secondary isotope shift was shown in section 2.1.1. In short: the vibrational wavefunction of the nucleus of interest is perturbed by the substitution of a nearby nucleus by one of its isotopes with a different mass; causing a change in the average bond lengths which affects the chemical shift (shielding) of the nucleus in question. This leads to different chemical shifts when discussing isotopomers of a given molecule. In our case, the C_{60} molecule possess two different types of C-C bonds, HP & HH, with different bond lengths and different vibrational characteristics. Thus, it is not surprising that in the ^{13}C NMR spectrum of C_{60} two side peaks are observed since the isotope shift is expected to be different for the two types of bonds. Generally, for secondary isotope shifts, substituting a neighbouring atom for its heavier isotope will result in a shielding of the chemical shift of the nucleus of interest. This is what is being observed in the spectra; the side peaks are shifted to lower chemical shifts (shielded) compared with the main C_{60} peak, since an adjacent ^{12}C is swapped for ^{13}C. The experimental results suggest a larger secondary isotope shift for two ^{13}C's along a HH bond (19.98 ± 0.02 ppb at 298 K) compared to a HP bond (12.56 ± 0.01 ppb at 298 K). This is likely due to the HH bond being stronger than the HP bond, since it is shorter and has a larger force constant. Thus, it seems the stronger bond is more affected by the change in mass than the weaker bond.

As shown above, the 2:1 ratio of the HP & HH side peaks in the NMR spectrum is due to the relative abundance of the two types of C-C bonds in C_{60}. In each case, [HP-$^{13}C_2$]-C_{60} and [HH-$^{13}C_2$]-C_{60}, the two^{13}C's are related by a symmetry operation; hence, they are magnetically equivalent. Due to the magnetic equivalence, the ^{13}C-^{13}C J-coupling between the spins has no direct effect on the NMR spectrum in an isotropic solution.[46] It must, therefore, be noted that the fine structure seen in the ^{13}C solution NMR spectrum of natural abundance C_{60} is not caused by ^{13}C-^{13}C J-couplings, but rather by the secondary isotope shift when substituting an adjacent ^{12}C with a ^{13}C and the intensities are caused by the relative abundance of the HP & HH bonds. Similar ^{13}C side peaks have also observed for other symmetrical molecules, such as ferrocene.[67]

A more complicated pattern of side peaks is seen for the natural abundance C_{70} fullerene. In this case many peaks are seen around the main C_{70} peaks, both on the shielded and deshielded side. For C_{70}, there are cases of chemical non-equivalence between the carbon sites in the molecule.[52] Similar isotope shifted peaks arising when two ^{13}C's along a bond are chemically (and magnetically) equivalent overlap with peaks split by the ^{13}C-^{13}C J-coupling when the ^{13}C's are not equivalent. This arises since the ^{13}C-^{13}C J-coupling, when the ^{13}C's are more than one bond away, has similar magnitude to the one bond isotope shifts. This is not the case for C_{60} since any two ^{13}C's in the cage would be at least chemically equivalent. Further investigation is needed to understand the C_{70} spectrum, involving 2D NMR techniques.

The general definition of the secondary isotope shift[48] has a rather counter-intuitive sign convention. The secondary isotope shift of a ^{13}C site induced by swapping the "lighter" isotope ^{L}A of a neighbouring atom A with a "heavier" isotope ^{H}A is defined as follows:[48]

$$^{1}\Delta^{13}\mathrm{C}(\mathrm{A}) = \delta^{13}\mathrm{C}(^{\mathrm{L}}\mathrm{A}) - \delta^{13}\mathrm{C}(^{\mathrm{H}}\mathrm{A}) \tag{2.2}$$

The condensed notation used here is introduced below for the one-bond secondary isotope shifts in C_{60}:

$$\begin{aligned} ^{1}\Delta_{\mathrm{HP}} &= \delta^{13}\mathrm{C}([^{13}\mathrm{C}_1]\text{-}\mathrm{C}_{60}) - \delta^{13}\mathrm{C}([\mathrm{HP}\text{-}^{13}\mathrm{C}_2]\text{-}\mathrm{C}_{60}) \\ ^{1}\Delta_{\mathrm{HH}} &= \delta^{13}\mathrm{C}([^{13}\mathrm{C}_1]\text{-}\mathrm{C}_{60}) - \delta^{13}\mathrm{C}([\mathrm{HH}\text{-}^{13}\mathrm{C}_2]\text{-}\mathrm{C}_{60}) \end{aligned} \tag{2.3}$$

The chemical shifts of the two side peaks, relative to the main ^{13}C peak, are given by

$$\begin{aligned} \Delta\delta_1 &= -^{1}\Delta_{\mathrm{HP}} \\ \Delta\delta_2 &= -^{1}\Delta_{\mathrm{HH}} \end{aligned} \tag{2.4}$$

The discussion so far gives an interpretation of the natural-abundance ^{13}C spectrum of C_{60}. The main C_{60} peak is a result of $^{13}C_1$ isotopomers of C_{60} ($[^{13}C_1]$-C_{60}), whereas the side peaks come from the two different types of $^{13}C_2$ isotopomers, [HP-$^{13}C_2$]-C_{60} and [HH-$^{13}C_2$]-C_{60}. The 2:1 ratio of the side peaks matches the abundance of HP:HH bonds in C_{60}, however the amplitude ratios of side peaks to the main C_{60} peak ($a_1/a_0 = 1.63 \pm 0.15\,\%$ and $a_2/a_0 = 0.81 \pm 0.08\,\%$) are not explained.

Considering a simplified approach of two sites in the C_{60} molecule, with ^{13}C abundance of $x = 1.108\,\%$, along an HH bond. The probability to have one ^{13}C and one ^{12}C is $2x(1-x)$, since the two sites are indistinguishable. Now the probability to have both ^{13}C's is x^2, and the NMR signal is doubled since there are two ^{13}C's. The ratio of the NMR signal in this case of the HH bond to the main C_{60} peak is $\frac{2x^2}{2x(1-x)} = \frac{x}{1-x} = 1.121\,\%$. This prediction for the ratio is quite different to the experimental one of $0.81 \pm 0.08\,\%$. This simplified approach does not correctly account for the experimental amplitude ratios of side peaks to the main C_{60} peak. For a more accurate treatment and a more substantial agreement with experiment see the statistical approach in section 2.4.2.

2.4.1.1 Endofullerene $^{13}C_2$ isotope shifts discussion

When the C_{60} molecule is filled with an atom/molecule, it deshields the ^{13}C chemical shift of the filled cage. It was shown in fig. 2.3 that the side peaks are present for endofullerenes ($H_2@C_{60}$ and $H_2O@C_{60}$) as well as empty C_{60} and that they follow the change in chemical shift of the main endofullerene peak. The secondary isotope shifts for endofullerenes are now measured with respected to the main peak of the filled cage.

It was found that the $^{13}C_2$ isotope shifts of endofullerenes are slightly smaller in magnitude than for the empty C_{60}. Furthermore, they get smaller in magnitude with increasing size of the endohedral molecule, as shown in fig. 2.3 and table 2.2 for $H_2@C_{60}$ and $H_2O@C_{60}$. The reason for this change in the isotope shifts with endohedral moiety is currently unknown but is under investigation. A possible explanation is that the endohedral molecule pushes on the cage forcing it to expand, similar to a pressure exerted by a gas on its container. This explanation is appealing if one looks at the temperature dependence of the isotope shifts for both the empty and filled C_{60}, which decrease in magnitude with an increase in temperature. Since increasing the temperature should expand the empty C_{60} cage (if one speaks in terms of average internuclear distances at a given temperature), and this decreases the magnitude of the isotope shifts; then inserting a molecule inside the cage might force it to expand and similarly decreases the magnitude of the isotope shifts. This evidence is not strong enough to classify as an experimental proof but it aids the analysis of this effect which is being investigated further.

A related (possibly identical) explanation is that the endohedral molecule changes the vibrational modes of the cage which in turn affects the $^{13}C_2$ isotope shifts. This effect of changes in the vibrational modes of the cage has been detected in Raman spectroscopy for noble gas endofullerenes.[68] However, to make such a connection and to understand it in detail further in-depth investigation is essential.

Ideally, one would like to simulate the values of the isotope shifts from ab initio calculations and compare them with the experimental results. Unfortunately, these require very difficult and time consuming calculations which may not be feasible with current computing facilities.

2.4.1.2 Temperature dependence of the isotope shifts

The dependence on temperature of the isotope shifts $^1\Delta_{\mathrm{HP}}$ and $^1\Delta_{\mathrm{HH}}$ was measured for C_{60}, $H_2@C_{60}$ and $H_2O@C_{60}$ and it is shown in fig. 2.4. The magnitude of the isotope shifts decrease with increasing temperature in a linear fashion over the studied temperature range. Linear fit parameters are found in table 2.2. The $^1\Delta_{\mathrm{HH}}$ isotope shift has a stronger change with temperature than $^1\Delta_{\mathrm{HP}}$.

Since the vibrational modes of C_{60} are rather complicated, in this discussion the HP and HH bonds will be treated analogous to diatomic molecules for clarity. The reason why the isotope shifts decrease with temperature may be explained by increased populations of excited vibrational states with increased temperature. The mass of the vibrating particles has less of an effect on excited vibrational wavefunctions than it does on the ground vibrational state.[47] Thus, increasing the temperature makes the populated vibrational eigenstates more immune to the $^{13}C/^{12}C$ mass difference and the secondary isotope shift is reduced.

The reason why the $^{1}\Delta_{HH}$ has a stronger temperature dependence than $^{1}\Delta_{HP}$ is not fully understood yet. It might be because the HH bond is shorter and it has a stronger force constant. A stronger force constant means the vibrational eigenstates are further apart in energy and are less accessible at a given temperature than the HP bond with a weaker force constant. At a given temperature the HH bond would have higher population of the vibrational states close to the ground state than the HP bond would have. Thus, a further change in temperature should affect the HH bond more, and implicitly the $^{1}\Delta_{HH}$ isotope shift would be more sensitive to temperature.

2.4.2 Statistical analysis of the C_{60} natural abundance side peaks

This section aims to give an explanation for the unusual ratio of the side peak amplitudes relative to the main C_{60} peak of $1.63 \pm 0.15\,\%$ for HP and $0.81 \pm 0.08\,\%$ for HH, in the natural abundance sample. The approach used here is purely based on the statistics on how ^{13}C is being substituted in C_{60} when all 60 sites are indistinguishable.

2.4.2.1 Statistics for $m\times{}^{13}$C's substituted in C_{60}

The probability for a number of $m\times{}^{13}C$ to be substituted *anywhere* in the C_{60} cage needs to be computed. For this a statistical equation implementing the total number of carbon sites "n_C" = 60, the number of ^{13}C's substituted in the cage "m" and the ^{13}C (natural) abundance "$x = 0.01108$" is needed, eq. 2.5.[4] The binomial coefficient $\binom{n_c}{m} = \frac{n_c!}{(n_c-m)!m!}$ is needed to take into account equivalent configurations, since all ^{12}C's and ^{13}C's are indistinguishable amongst themselves. This probability is written as $P^{x}_{m,\,n_c}$ and it its shown in equation 2.5.[4]

$$P^{x}_{m,\,n_c} = \binom{n_c}{m} x^{m}(1-x)^{n_c-m} \tag{2.5}$$

The probabilities for $m\times{}^{13}C$'s to be substituted in the natural abundance C_{60} are shown in table 2.3, up to m=5.

TABLE 2.3: Probability for $m \times ^{13}$C's to be substituted anywhere in the C_{60} cage, $P^{x}_{m,\, n_c}$ where x= 0.01108 (natural abundance), $n_C = 60$ and $m = 0, 1, 2, 3, 4, 5$. The ^{13}C NMR signal is just $m \times P^{x}_{m,n_c}$ and in brackets is shown the relative contribution to the total ^{13}C NMR signal. Reproduced from Ref.[1] with permission from the PCCP Owner Societies.

m	0	1	2	3	4	5
$P^{0.01108}_{m,\,60}$	0.512471	0.344508	0.113868	0.0246652	0.00393803	0.000494169
^{13}C NMR signal	0 (0%)	0.344508 (51.8%)	0.227735 (34.3%)	0.0739957 (11.1 %)	0.0157521 (2.4 %)	0.00247085 (0.4%)

The probability for a number (m) of ^{13}C's to be substituted in the C_{60} cage can be calculated using eq. 2.5 if the ^{13}C abundance (x) is know (where n_C=60). Thus eq. 2.5 is plotted in fig. 2.11 for different ^{13}C abundances (x): black- natural abundance (1.108% ^{13}C), orange- 20% ^{13}C, green- 25% ^{13}C and blue- 30% ^{13}C. These plots essentially represent the pattern an ideal mass spectrum would look like for C_{60} with a given ^{13}C abundance (x).

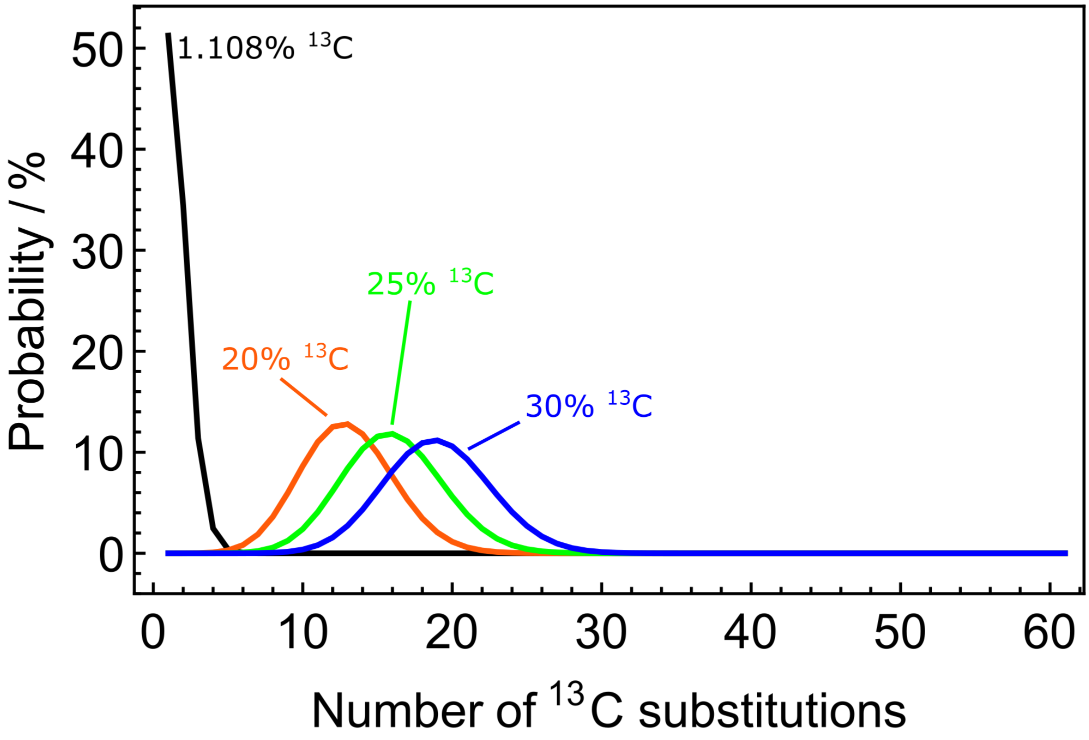

FIGURE 2.11: Probability for a number (m) of ^{13}C's to substituted anywhere in the C_{60} cage given the ^{13}C abundance (x). Essentially eq. 2.5 plotted against m for different values of x. Black- natural abundance (x = 1.108% ^{13}C), Orange- 20% ^{13}C, Green- 25% ^{13}C, Blue- 30% ^{13}C. The centres of the distributions are found at: $13 \times ^{13}$C for 20% ^{13}C, $16 \times ^{13}$C for 25% ^{13}C and $19 \times ^{13}$C for 30% ^{13}C. Reproduced from Ref.[1] with permission from the PCCP Owner Societies.

2.4.2.2 C_{60} isotope shift natural abundance statistical analysis, up to three ^{13}C substitutions

From the HP and HH peak integral ratio of 2:1 it seems that they arise from the HP and HH bonds. But the relative ratios with respect to the main C_{60} peak are needed to fully elucidate the origin of these peaks. For this the statistical substitutions of ^{13}C's in the C_{60} cage are required. In the section below, this was done statistically by considering up to maximum three ^{13}C's being substituted in the cage at one time.

It must be noted that an approximation has been made, such that if two ^{13}C's are more than 3 bonds apart, they are treated as fully decoupled. This is because if the ^{13}C's are more than 3 bonds apart the ^{13}C-^{13}C J-couplings drop to under 1 Hz ($\sim$ 6 ppb for ^{13}C at 16.45 T)[69] which is smaller than the observed isotope shifts, see section 2.4.4 for more details. Thus, if two ^{13}C's are more than 3 bonds apart we assume each one contributes to the main C_{60} peak and not the HP or HH peaks. This applies to three ^{13}C's such that if all three are connected by more than 3 bonds, each one contributes to the main C_{60} peak. When all three are connected together (by maximum 3 bonds) we ignore this contribution because the chemical shift of the cluster would end up somewhere else on the spectrum, not within the three discrete peaks (main C_{60}, HP or HH). The contribution is also so small that it does not make much of difference for natural abundance C_{60}. Importantly for the HP and HH peaks in the spectrum when three ^{13}C's are present, for a configuration to contribute to the isotope shifted peaks firstly two ^{13}C's need to be adjacent (along a HP or HH bond) and the third one must be more than 3 bonds away from any of the two adjacent ^{13}C's.

However, when only two ^{13}C's are substituted in the cage, if they are not adjacent we assume that both contribute to the main C_{60} peak. This is because, even if they were 2-3 bonds away and considered as coupled spins, they would still be magnetically equivalent and with a negligible 2-3 bonds away isotope shift they contribute to the main C_{60} peak and not the isotope shifted peaks.

From table 2.3 it can be seen that the main contribution to the ^{13}C NMR signal comes from substitutions up to m=3 and it represents 97.2% of the total signal arising from natural abundance C_{60}. In the analytic prediction of the NMR peak intensities below, only substitutions up to m=3 will be considered, accounting for most of the signal.

Mathematica has a feature called Chemical Data in which it has chemical information about the C_{60}, physico-chemical properties such as bond lengths, structure etc. Most importantly it provides atom connectivities as a list of rules, showing which carbon atom is directly bonded to another, for example, if atom 1 is directly bonded to atom 2 is shown as "$1 \rightarrow 2$". It seems that the bond types corresponding to the connectivities Mathematica provided were wrong, this has been corrected for in these calculations and Wolfram has been informed about the error.

To find out which C$_{60}$ configuration, with its ^{13}C's substituted, contributes to the main C$_{60}$ or HP or HH NMR peak a Mathematica code has been implemented to count all of the configurations. In order to achieve this, all inequivalent C$_{60}$ configurations corresponding to m ^{13}C's randomly substituted were generated. The number of configurations for a given m equals the binomial coefficient $\binom{n_c}{m} = \frac{n_c!}{(n_c-m)!m!}$ above. Now each configuration is a list of $''m''$ numbers, each number is between 1-60 and it represents the location of the ^{13}C's, since the ^{12}C's are the rest and are not important for this analysis. Then the Mathematica code essentially goes through all of these configurations checking the ^{13}C's connectivities by comparing with the list of rules provided for the C$_{60}$ connectivities. Each time the configurations are read, a pattern check is done by Mathematica. When the pattern check is true, that particular configuration is counted and added to the total number of satisfactory configurations. Then the ratio between satisfactory configurations and total configurations represents how much of the percentage given in the columns of table 2.3 contributes to the main C$_{60}$ or HP or HH peak in the ^{13}C NMR spectrum. This has been done for all configurations up to $m = 3$ below.

m=0

The probability for all carbons to be ^{12}C is $P_{0,\,60}^{0.01108} = 0.512471$ but it does not contribute to the ^{13}C NMR spectrum. Its contribution to the ^{13}C NMR spectrum is denoted as $\{0\}$ and:
$\{0\} = 0$.

m=1

The probability for one carbon to be ^{13}C and the rest ^{12}C is $P_{1,\,60}^{0.01108} = 0.344508$ and all of it contributes to the main C$_{60}$ peak in the ^{13}C NMR spectrum. Its contribution to the ^{13}C NMR spectrum is denoted as $\{1\}$ and:
$\{1\} = 0.344508$.

m=2

The probability for two carbons to be ^{13}C and the rest ^{12}C is $P_{2,\,60}^{0.01108} = 0.113868$ and it contributes to all peaks in the ^{13}C NMR spectrum. There are 1770 (= $\binom{60}{2}$)) total configurations with m=3, but the configurations need to be classified as follows:

m=2, all ^{13}C's remote

When both ^{13}C's are not directly connected in a configuration, this will makes a contribution to the main C$_{60}$ peak. There are 1680 configurations (out of 1770 = $\binom{60}{2}$)) with this property and to get the contribution to the main C$_{60}$ peak an additional factor of 2 is need (the number of ^{13}C's). Its contribution to the ^{13}C NMR spectrum is denoted as $\{2, \text{remote}\}$.

$$\{2, \text{remote}\} = 2 * \frac{1680}{1770} * P_{2,\,60}^{0.01108} = 0.216155$$

m=2, HP

When both ^{13}C's are directly connected along a HP bond in a configuration, it will make a contribution to the HP peak. There are 60 configurations (out of 1770 = $\binom{60}{2}$) with this property and to get the contribution to the HP peak an additional factor of 2 is need (the number of ^{13}C's). Its contribution to the ^{13}C NMR spectrum is denoted as $\{2, \mathrm{HP}\}$.

$$\{2, \mathrm{HP}\} = 2 * \frac{60}{1770} * \mathrm{P}^{0.01108}_{2,\,60} = 0.00771984$$

m=2, HH

When both ^{13}C's are directly connected along a HH bond in a configuration, this will make a contribution to the HH peak. There are 30 configurations (out of 1770 = $\binom{60}{2}$) with this property and to get the contribution to the HH peak an additional factor of 2 is need (the number of ^{13}C's). Its contribution to the ^{13}C NMR spectrum is denoted as $\{2, \mathrm{HH}\}$.

$$\{2, \mathrm{HH}\} = 2 * \frac{30}{1770} * \mathrm{P}^{0.01108}_{2,\,60} = 0.00385992$$

When adding all the cases together 1680 + 60 + 30 = 1770 the total number of m=2 configurations (i.e. $\binom{60}{2}$).

m=3

The probability for three carbons to be ^{13}C and the rest ^{12}C is $\mathrm{P}^{0.01108}_{3,\,60} = 0.0246652$ and it contributes to all peaks in the ^{13}C NMR spectrum. There are 34220 (= $\binom{60}{3}$) total configurations with m=3, but the configurations need to be classified as follows:

m=3, all ^{13}C's in a cluster

When all three ^{13}C's are connected by 3 bonds or less in a configuration we consider it will not make a contribution to the NMR signal. The spectrum of the cluster will be broadened and will in most cases overlap with all peaks (main C$_{60}$, HP and HH), contributing to all equally. There are 5080 configurations (out of 34220 = $\binom{60}{3}$) with this property and to get the contribution to the NMR signal, an additional factor of 0 is needed (because of the approximation made). Its contribution to the ^{13}C NMR spectrum is denoted as $\{3, \mathrm{cluster}\}$.

$$\{3, \mathrm{cluster}\} = 0 * \frac{5085}{34220} * \mathrm{P}^{0.01108}_{3,\,60} = 0 * 0.00366159 = 0$$

m=3, all ^{13}C's remote

When all three ^{13}C's are more than 3 bonds apart from each other in a configuration, this will make a contribution to the main C$_{60}$ peak. There are 11260 configurations (out of 34220 = $\binom{60}{3}$) with this property and to get the contribution to the main C$_{60}$ peak an additional factor of 3 is needed (the number of ^{13}C's). Its contribution to the ^{13}C NMR spectrum is denoted as $\{3, \text{all remote}\}$.

$$\{3, \text{all remote}\} = 3 * \frac{11260}{34220} * P^{0.01108}_{3,\,60} = 0.0243481$$

m=3, two ^{13}C's in a cluster and one remote

When two ^{13}C's are in a cluster (1-3 bonds away) and the third far away (more than 3 bonds away from both) in a configuration that will make a contribution to the main C_{60} peak (from the remote ^{13}C) and some contribution to the HP or HH peak (when the two ^{13}C's are adjacent in the cluster) or the main C60 peak (when the two ^{13}C's are not adjacent in the cluster). There are 17880 configurations (from the Mathematica code), out of 34220= $\binom{60}{3}$ with this property. When adding all three cases above (for m=3) we get: 5080 + 11260 + 17880 = 34220 (i.e. $\binom{60}{3}$)). The 17880 cases in this section need to be further divided into 3 classes:

- "HP + remote" when two ^{13}C's are adjacent along HP bond and the third ^{13}C is remote.
- "HH + remote" when two ^{13}C's are adjacent along HH bond and the third ^{13}C is remote.
- "cluster (not adj.) + remote" when two ^{13}C's are 2-3 bonds away in a cluster and the third ^{13}C is remote from either of them.

- m=3, HP + remote

When two ^{13}C's are adjacent along a HP bond and the third is remote in a configuration, this will make a contribution to the main C_{60} peak (from the remote ^{13}C) and a double contribution to the HP peak (from the two adjacent ^{13}'s). There are 2280 configurations (from the Mathematica code), out of 34220 = $\binom{60}{3}$, with this property and their contribution to the ^{13}C NMR spectrum is denoted as $\{3, \text{HP + remote}\}$.

$$\begin{aligned}\{3, \text{HP } + \text{ remote}\} &\to \text{main } C_{60} \text{ peak} = 1 * \frac{2280}{34220} * P^{0.01108}_{3,\,60} = 0.00164339\\ &\to \text{HP peak} = 2 * \frac{2280}{34220} * P^{0.01108}_{3,\,60} = 0.00328678\end{aligned}$$

- m=3, HH + remote

When two ^{13}C's are adjacent along a HH bond and the third is remote in a configuration, this will make a contribution to the main C_{60} peak (from the remote ^{13}C) and a double contribution to the HH peak (from the two adjacent ^{13}C's). There are 1140 configurations (from the Mathematica code), out of 34220 = $\binom{60}{3}$, with this property and their contribution to the ^{13}C NMR spectrum is denoted as $\{3, \text{HH + remote}\}$.

$$\{3, \text{HH} + \text{remote}\} \rightarrow \text{main C}_{60}\text{ peak} = 1 * \frac{1140}{34220} * \text{P}^{0.01108}_{3,\,60} = 0.000821694$$

$$\rightarrow \text{HH peak} = 2 * \frac{1140}{34220} * \text{P}^{0.01108}_{3,\,60} = 0.00164339$$

- m=3, cluster (not adj.) + remote

Two ^{13}C's are 2-3 bonds away from each other in a cluster and the third one is remote in a configuration. The remote ^{13}C will make a contribution to the main C_{60} peak. The two ^{13}C's 2-3 bonds away will also contribute to the main C_{60} peak. Since the third ^{13}C is far enough to make the other two nearly equivalent and they are not adjacent, the isotope shift is assumed to be negligible in this case. There are 14460 (17880 - (2280 + 1140)) configurations, out of 34220 = $\binom{60}{3}$, with this property. Their contribution to the ^{13}C NMR spectrum is denoted as {3, cluster (not adj.) + remote} and a factor of 3 is needed because all 3 spins contribute to the main C_{60} peak.

$$\{3, \text{cluster (not adj.)} + \text{remote}\} \rightarrow \text{main C}_{60}\text{ peak} = 3 * \frac{14460}{34220} * \text{P}^{0.01108}_{3,\,60} = 0.0312676$$

2.4.2.3 Statistical ^{13}C NMR stick spectrum of natural abundance C_{60} considering up to m=3 ^{13}C substitutions

All the cases presented above are shown as a histogram in fig. 2.12 where all the contributions to the NMR peaks (main C_{60}, HP and HH) from the configurations above are summarised.

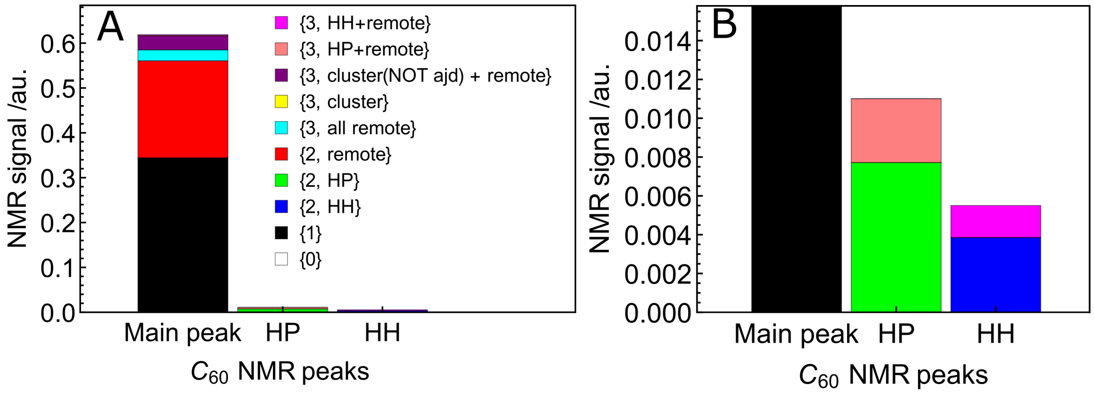

FIGURE 2.12: Statistically predicted ^{13}C NMR intensities of natural abundance C_{60} considering up to m=3 ^{13}C substitutions, A- full size and B- zoomed to see HP and HP. All contributions discussed previously are presented in the legend and the histogram shows how they build up the ^{13}C NMR peaks.{0} and {3, cluster} are assumed to have zero contribution. Reproduced from Ref.[1] with permission from the PCCP Owner Societies.

From these, the predicted ratios of the peaks were obtained and shown in table 2.4 together with the experimentally measured ratios; where the ratios are given as a percentage from the total NMR signal = main C_{60} peak + HP peak + HH peak.

TABLE 2.4: Predicted (from fig. 2.12) and experimental ^{13}C NMR peak ratios for natural abundance C_{60}. Here main C_{60} peak + HP + HH = 100%. Reproduced from Ref.[1] with permission from the PCCP Owner Societies.

Peak	Predicted ratios (up to m = 3)	Experimental ratios
Main C_{60}	97.401 %	$97.62 \pm 0.21\%$
HP	1.733%	$1.59 \pm 0.14\%$
HH	0.866%	$0.79 \pm 0.07\%$

From the table it can be seen that the predicted ratios are close to the experimental ones but not exactly the same. The reason for this could be that only substitutions up to m=3 were considered, these account for 97.2% of the total NMR signal and the mismatch could be due to the leftover 2.8%. This 2.8% would have intensity distributed among all three peaks and in between them due to the clustering effect on the isotope shift (see section 2.4.4). Thus, final intensities when all ^{13}C substitutions in natural abundance C_{60} are considered would be close to the ones shown in table 2.4. Other possible reasons for the discrepancies would be the assumptions and approximations made when building up the arguments above. Furthermore, the leftover 2.8% and the {3, cluster} configurations could contribute to inhomogeneous broadening of the main C_{60} peak, as seen in fig. 2.2 where the main C_{60} peak is not a perfect Lorentzian/Gaussian shape.

2.4.3 ^{13}C enriched C_{60}

This section discusses the NMR spectrum of ^{13}C enriched C_{60}, highlighting differences with natural abundance C_{60}. A Monte-Carlo type method is presented which under suitable assumptions correctly predicts the NMR spectra of both ^{13}C enriched and natural abundance C_{60}.

The ^{13}C solution NMR spectrum of 20-30% ^{13}C enriched C_{60} shown in fig. 2.6, displayed a rather broad lineshape compared with the discrete peaks of natural abundance C_{60} shown at the bottom of the figure. The width of the enriched C_{60} peak was $\sim$40 ppb and it covered the natural abundance C_{60} sharp peaks entirely. The broad peak was close to a Gaussian lineshape with a shoulder on the deshielded side; the shoulder corresponded exactly with the chemical shift of the main peak in natural abundance C_{60} and the centre of the Gaussian was roughly corresponding with the discrete side peaks. This increase in NMR intensity with ^{13}C enrichment, where the chemical shifts of the side peaks are, hints towards an explanation which involves clustering of the ^{13}C's within the C_{60} cage. The exact chemical shift referencing was shown in section 2.3.2.1, where the possibility of the broad peak arising from magnetic field inhomogeneity was also excluded.

Another possible explanation for the broadening of the ^{13}C enriched spectrum is fast relaxation rate. To check, the T_1 spin-lattice relaxation times were measured in both cases: 16.6±0.3 s (295 K and 16.45 T) for natural abundance C_{60} in fig. 2.5 and 14.8±0.2 s (295 K and 16.45 T) for 20-30% ^{13}C enriched C_{60} in fig. 2.9. This small difference in the relaxation time constants is not enough to explain the significant increase in broadening seen for the enriched C_{60}. The small decrease in T_1 of the enriched C_{60} is presumably due to increased number of ^{13}C's increasing the ^{13}C-^{13}C dipolar relaxation rates. Thus, to explain the broad spectrum one needs an inhomogeneous broadening model, which should include coherent interactions like secondary isotope shifts and ^{13}C-^{13}C J-couplings.

The mass spectrum of 20-30% ^{13}C enriched C_{60} was shown in fig. 2.9 to contain on average ∼18 ^{13}C's per cage. Accurate spin dynamics simulation of a spin system this large is at the limit of current computations. For such a system one would need to simulate an enormous number of C_{60} configurations where the 18 ^{13}C's would be randomly distributed in the cage with widely different isotope shifts and J-couplings. However, the lack of fine structure seen in the NMR spectrum of enriched C_{60} suggests one may not need such detailed and heavy computations and that under suitable approximations one may be able to simulate the experimental spectrum more easily.

2.4.4 Monte-Carlo approach to simulate C_{60} lineshape of arbitrary ^{13}C enrichement

In this section a model is presented which can simulated the solution ^{13}C spectrum of C_{60} with an arbitrary content of ^{13}C. This model is based on a Monte-Carlo type simulation where one computes the second moment[63] of a large number of different C_{60} configurations, with ^{13}C's are distributed randomly in the cage, and then sums together all the spectra which were approximated by the second moment.

The technique is divided in the following steps: (1) Generation of an ensemble of ^{13}C configurations (depending on the ^{13}C abundance); (2) Identification of distinct ^{13}*C clusters* (within each configuration); (3) Prediction of spin interaction parameters (chemical shifts and J-couplings for each ^{13}C cluster); (4) Calculation of the approximate spectral lineshape for a ^{13}C cluster (with the predicted interaction parameters); (5) Summation of the simulated lineshapes (over all ^{13}C clusters, leading to the total NMR spectrum).

The details of the individual steps are as follows:

1. *Generation of an ensemble of ^{13}C configurations.*
   The bonding network for C_{60} are set up in the *Mathematica* symbolic software platform[70] based on the C_{60} adjacency matrices. A ^{13}C or ^{12}C nucleus is randomly assigned to each of the 60 carbon sites using a stochastic function with probability x for ^{13}C and $1 - x$ for ^{12}C, to create a distinct C_{60} configuration. Calculations presented here involve 10000 random configurations ($N_{\text{config}} = 10000$). This is by no means equal to the total number of possible configurations in C_{60}, but is sufficient to simulate the main experimental features observed in the NMR spectra.

2. *Identification of distinct ^{13}C clusters.*
   One needs to identify ^{13}C clusters within each computer-generated C_{60} configuration. A cluster means a group of ^{13}C's spins which interact with sufficient strength with each other to be treated as distinct spin systems; while interactions between ^{13}C's spins from different clusters are weak enough to treat the two clusters as completely separate spin systems. Quantum chemistry calculations have been done on C_{60} to simulate all the ^{13}C-^{13}C J-couplings,[69,71] where they predict that J_{CC} couplings between pairs of ^{13}C nuclei separated by more than 3 bonds are smaller than 1 Hz.[69,71] Since 1 Hz at a magnetic field of 16.45 T corresponds to $\sim$ 6 ppb for ^{13}C, which is smaller in magnitude than the one-bond secondary isotope shifts, we define a ^{13}C cluster as follows:
   A group of ^{13}C nuclei for which (i) each nucleus is connected to at least one other member of the cluster by at most 3 bonds, and (ii) for which every nucleus is at least 4 bonds away from any ^{13}C which is part of a different cluster.
   For example, all C_{60} configurations shown in fig. 2.13 (a-c) contain a single cluster. Additionally, the C_{60} configurations shown in fig. 2.14 (a,b) contain one ^{13}C cluster (containing 3 and 4 ^{13}C nuclei respectively), whereas the configuration from fig. 2.14 (c) contains two clusters: one composed of 2 ^{13}C nuclei and a second cluster of 4 ^{13}C nuclei. One should take note of fig. 2.14 (b) which shows that a cluster can contain ^{13}C atoms which are not directly bonded to each other. The number of ^{13}C nuclei in an individual cluster c is denoted N_c.

3. *Spin interaction parameters for a ^{13}C cluster.*
   Simulating the NMR spectrum of a ^{13}C cluster requires the spin interaction parameters to be known, i.e chemical shifts and J-couplings for solution state NMR. For the ^{13}C-^{13}C J-couplings, we made use of the results from published quantum chemistry calculations.[69]

   For chemical shifts, we make use of the experimentally measured one-bond secondary isotope shifts shown previously, $^{1}\Delta_{\text{HP}}$ and $^{1}\Delta_{\text{HH}}$. If less than three ^{13}C's are present in a cluster the chemical shifts are zero or $^{1}\Delta_{\text{HP}}$ or $^{1}\Delta_{\text{HH}}$. If one ^{13}C is in a cluster its chemical shift is zero since this corresponds to the main C_{60} peak, and we define everything with respect to it, see fig. 2.13 (a,d) for structure and simulated spectra. If two ^{13}C's are adjacent in a cluster, their chemical shift is just $^1\Delta_{\mathrm{HP}}$ or $^1\Delta_{\mathrm{HH}}$ since they can be along an HP or HH bond, see fig. 2.13 (b,c,e,f) for structure and simulated spectra. If two ^{13}C's are further than one bond away within a cluster, then we assume this generates a negligible isotope shift and the two ^{13}C's have zero chemical shift. We make use of the fact that only two isotope shifted peaks were observed in the NMR spectrum of natural abundance C_{60}; and if higher order isotope shifts were present, they are too small to be measured and fall within the main C_{60} peak.

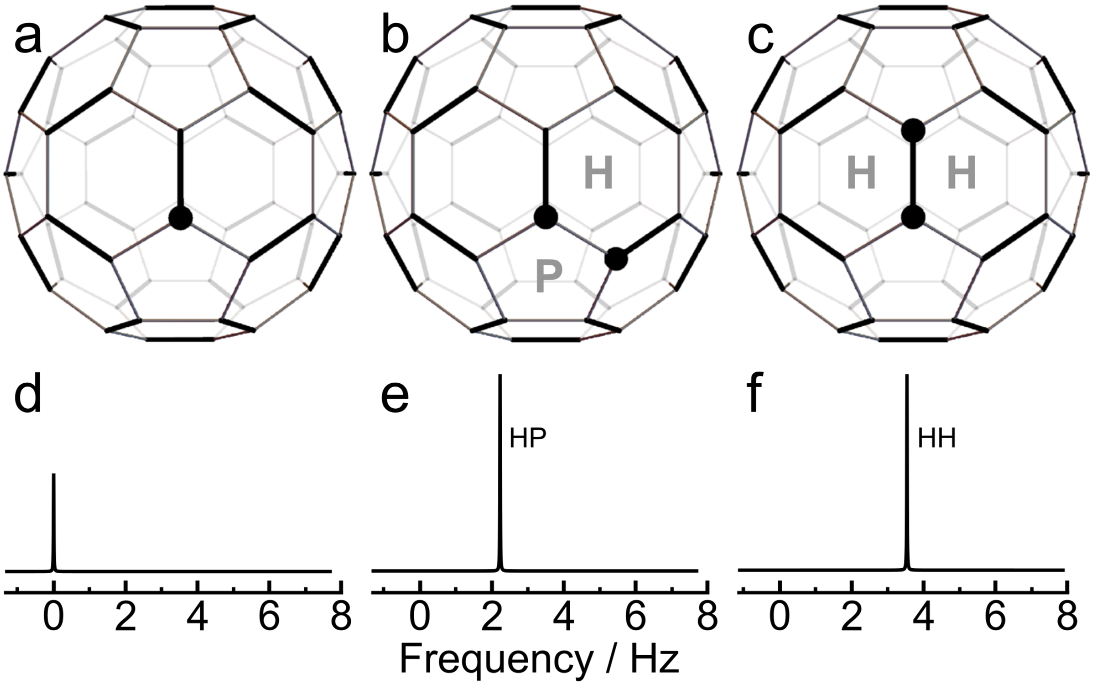

FIGURE 2.13: Three isotopomers of C_{60}, with the positions of ^{13}C sites marked by a filled circle: (a) [$^{13}C_1$]-C_{60}; (b) [HP-$^{13}C_2$]-C_{60}; (c) [HH-$^{13}C_2$]-C_{60}. The hexagonal and pentagonal carbon rings are marked; HP bonds are in thin gray and HH bonds are in thick black. (d-e) Simulations of the associated ^{13}C spectra at a magnetic field of 16.45 T: (d) [$^{13}C_1$]-C_{60}; (e) [HP-$^{13}C_2$]-C_{60}; (f) [HH-$^{13}C_2$]-C_{60}. Artificial Lorentzian lineshapes were used and secondary isotope shifts were taken from experiment (Fig. 2.1). The spectral amplitudes contributed by each $^{13}C_2$ molecule is twice as large as for each $^{13}C_1$ molecule. The ^{13}C-^{13}C J-coupling does not influence the spectra of the $^{13}C_2$ isotopomers, since the ^{13}C nuclei are in magnetically equivalent sites. Reproduced from Ref.[1] with permission from the PCCP Owner Societies.

For more complicated clusters containing adjacent ^{13}C's, an additive model is assumed for the one-bond secondary isotope shifts. Suppose that a ^{13}C site i has $n_{\mathrm{HP}}(i)$ ^{13}C nearest neighbours separated by a HP bond, where $n_{\mathrm{HP}}(i) \in \{0,1,2\}$, and $n_{\mathrm{HH}}(i)$ ^{13}C neighbours separated by a HH bond, where $n_{\mathrm{HH}}(i) \in \{0,1\}$. The total one-bond secondary isotope shift of the i ^{13}C site is assumed to be given by:

$$^1\Delta_i \simeq n_{\mathrm{HP}}(i)^1\Delta_{\mathrm{HP}} + n_{\mathrm{HH}}(i)^1\Delta_{\mathrm{HH}} \tag{2.6}$$

where the values $^{1}\Delta_{\mathrm{HP}} = 12.6$ ppb and $^{1}\Delta_{\mathrm{HH}} = 20.0$ ppb are assumed in the calculations. Again, the higher order secondary isotope shifts are ignored. The isotope shift has a maximum value of $2^{1}\Delta_{\mathrm{HP}} +^{1} \Delta_{\mathrm{HH}} = 45.2$ ppb, and a minimum value of 0 ppb, these approximately bound the broad lineshape of the ^{13}C enriched C_{60} spectrum, shown in fig. 2.6.

The isotope shift of each i ^{13}C may be converted into a frequency shift relative to the main C_{60} peak by using the relationship

$$\Omega_i = -^{1}\Delta_i \times \omega^0 \tag{2.7}$$

where the ^{13}C Larmor frequency is $\omega^0 = -\gamma B^0$, γ is the magnetogyric ratio of ^{13}C and B^0 is the magnetic field.[46] Equation 2.7 takes into account the sign convention for the secondary isotope shift (equation 2.4).[48]

4. *Approximate lineshape for a ^{13}C cluster.*
After identifying a ^{13}C cluster and estimating all spin interactions, the ^{13}C spectrum can be simulated. In the case of small number of ^{13}C's in the cluster (small N_c), it is possible to analytically simulate the spectrum, using software packages like *SpinDynamica*.[50] Some analytically simulated spectra are shown in the middle row of fig. 2.14. Each of the simulations show a complicated spectrum composed of many individual peaks.

   Accurate simulations like these are not feasible for large values of N_c. Furthermore, the fine structure seen in the simulations is washed away in the experimental NMR spectrum of ^{13}C enriched C_{60}. Hence, the analytical spectrum $S_c(\omega)$ for each individual cluster are replaced by the second moment[63] giving an approximated spectrum $S_c^\star(\omega)$. This results from a moment analysis of the NMR spectrum, as described in detail in section 2.4.4.1, where it is also shown that J-couplings do not affect the second moment at all. The spectrum for each individual cluster is approximated by the following $S_c^\star(\omega)$ Gaussian function:

$$S_c^\star(\omega) = N_c(2\pi\sigma_c)^{-1/2} \exp\left\{-\frac{(\omega - \overline{\Omega}_c)^2}{2\sigma_c}\right\} \tag{2.8}$$

   where the standard deviation σ_c of the Gaussian function is as follows:

$$\sigma_c = N_c^{-1} \sum_{i=1}^{N_c} (\Omega_i - \overline{\Omega}_c)^2 \tag{2.9}$$

   and the mean resonance offset frequency of a cluster $\overline{\Omega}_c$ is given by

$$\overline{\Omega}_c = N_c^{-1} \sum_{i=1}^{N_c} \Omega_i \tag{2.10}$$

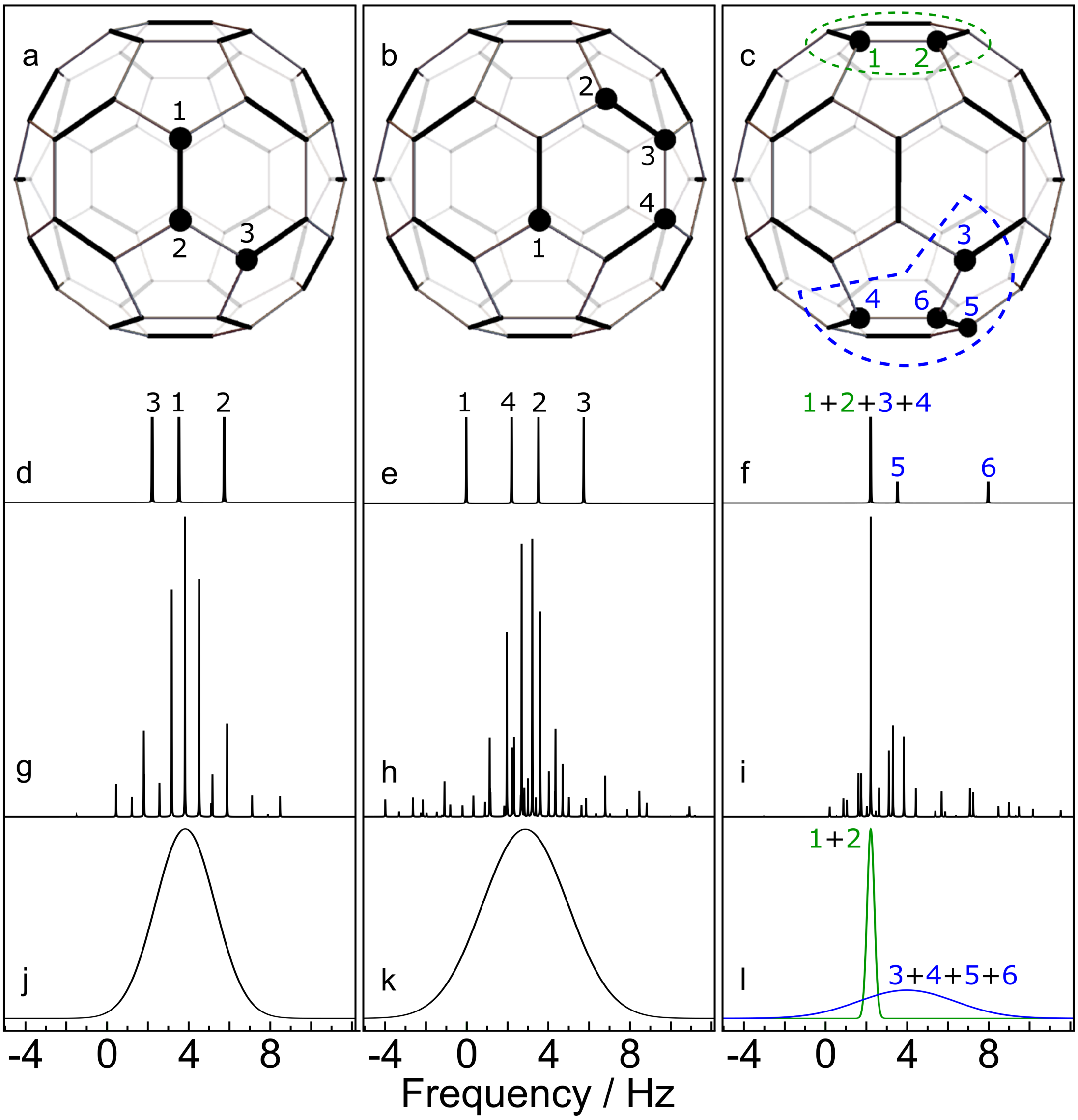

FIGURE 2.14: Simulated NMR spectra for three selected C_{60} configurations, at a magnetic field of 16.45 T. ^{13}C nuclei are shown by filled circles. Cases (a) and (b) contain a single ^{13}C cluster. Case (c) contains two ^{13}C clusters. (d-f) Stick spectra showing the predicted ^{13}C chemical shifts, perturbed by the one-bond secondary isotope shifts from neighbouring ^{13}C nuclei; (g-h) Accurate spin dynamical computations of the NMR spectra, including the predicted chemical shifts and J-couplings from quantum chemistry calculations.[69,71] (i-l) Approximate simulations of the NMR spectra for each cluster using equation 2.8. All vertical scales are arbitrary. Reproduced from Ref.[1] with permission from the PCCP Owner Societies.

Note that the standard deviation σ_c shown here is actually the normalised second moment $\mathcal{M}_c^{(2)}$ from eq. 2.45 which was derived in section 2.4.4.1. Furthermore, eq. 2.8 above is the same as eq. 2.46 at the end of the derivation from section 2.4.4.1, with the only addition being the mean resonance offset of the cluster $\overline{\Omega}_c$.

Therefore, rather than computing spectra for large spin systems, one can just use eq. 2.8 which evaluates very rapidly even for large cluster dimension N_c.

Different panels of fig 2.14 compare some simulated spectra of clusters using eq. 2.8 in (j-l) (bottom row) with analytical spin-dynamical simulations in (g-i) (middle row). The second moment approximation of the spectra omits the fine structure of the spectra but reproduces the average centre frequency and width of the cluster spectra accurately. The big advantage of using such approximated spectra is the speed with which one can compute spectra for a large number of distinct C_{60} configurations.

Equation 2.9 predicts a Gaussian function with zero width when all ^{13}C nuclei in the cluster have identical chemical shifts (magnetic equivalence). A line-broadening term is included when this is the case, which matches the experimental linewidth of the natural-abundance C_{60} peak.

5. *Summation of the simulated lineshapes.*

The final NMR spectrum $S(\omega)$ can be obtained after summing all the analytically simulated spectra for each individual cluster $S_c(\omega)$:

$$S(\omega) = N_{\text{config}}^{-1} \sum_{c=1}^{M} S_c(\omega) \tag{2.11}$$

Where M is the total number of clusters and the total number of configurations is denoted by N_{config}.

As said before, this procedure would be extremely computationally demanding, therefore, we use spectra approximated by the second moment $S_c^{\star}(\omega)$ for each cluster to give the approximated final NMR spectrum $S^{\star}(\omega)$:

$$S^{\star}(\omega) = N_{\text{config}}^{-1} \sum_{c=1}^{M} S_c^{\star}(\omega) \tag{2.12}$$

where cluster spectral contributions $S_c^{\star}(\omega)$ were defined in eq. 2.8.

Therefore, the ^{13}C NMR spectrum of C_{60} can be simulated using such a Monte-Carlo type method by generating large number of random configurations and summing the approximate spectra of each cluster.

The Monte-Carlo approach described above can be done for an arbitrary ^{13}C content x. Simulated spectra using this method with 10000 different configurations are shown in fig. 2.15 (a) for natural abundance C_{60} ($x = 1.108\%$) and fig. 2.15 (b) for 30% ^{13}C enriched C_{60}, where they are compared with the experimental NMR spectra of natural abundance and 20-30% ^{13}C enriched C_{60}, with good correspondence. For the natural abundance, it shows the two discrete side peaks HP & HH away from the main C_{60} peak with approximately correct amplitudes. Small variations are seen due to the nature of the Monte-Carlo approach, more than 10000 configurations are expected to

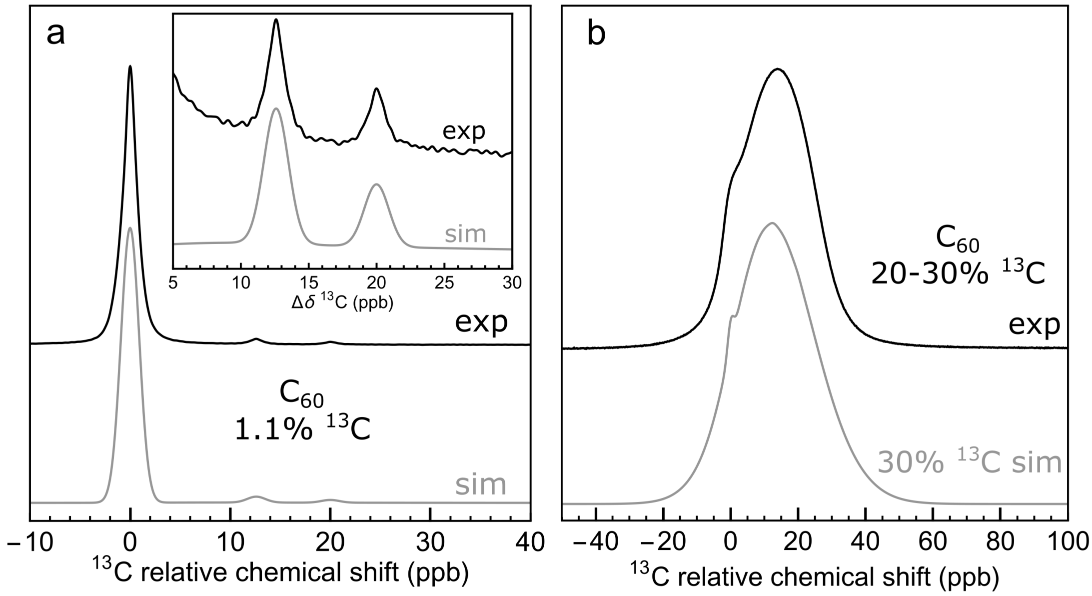

FIGURE 2.15: (a) ^{13}C NMR spectrum of 25 mM solution of C_{60} in ODCB-d_4 (sum of 856 transients); (b) ^{13}C NMR spectrum of ∼21 mM of ^{13}C-enriched C_{60} (20-30% ^{13}C) in ODCB-d_4 (sum of 16 transients). Spectra are taken at 16.45 T and 295 K. Black lines show experimental data. The grey lines show the results of Monte Carlo simulations using a ^{13}C abundance of (a) 1.1% and (b) 30%. The horizontal axes depict the ^{13}C chemical shift relative to that of the main C_{60} peak. Reproduced from Ref.[1] with permission from the PCCP Owner Societies.

be needed to converge on the exact experimental result for natural abundance C_{60}. This is probably because the intensity of the side peaks comes from a very small number of configurations compared to the total and a very large number of configurations (> 10000) seems to be needed for convergence.

For the 20-30% ^{13}C enriched C_{60} NMR spectrum, the simulation which best matched the experimental result was that of 30% ^{13}C content, see fig. 2.15 (b) for a good fit between the shape of the simulated and experimental spectrum. This reproduced the broad peak observed at the correct average chemical shift together with the shoulder on the deshielded side which corresponds to isolated $^{13}C_1$ (i.e. the chemical shift of the main C_{60} peak). This is also in agreement with the mass spectrometry measurement done on the same 20-30% ^{13}C enriched C_{60} sample, fig. 2.9. From the mass spectrum the binomial distribution was centred around $18\times^{13}$C, so on average the cages had 18 ^{13}C present. The statistical prediction for how many ^{13}C's are present anywhere in a C_{60} cage with a given ^{13}C abundance is given in fig. 2.11; these are shown for 1.108% ^{13}C, 20% ^{13}C, 25% ^{13}C and 30% ^{13}C. From this purely statistical prediction the distributions were centred around: $13\times^{13}$C for 20% ^{13}C, 16 $\times^{13}$C for 25% ^{13}C and 19 $\times^{13}$C for 30% ^{13}C; hence the studied sample of 20-30% ^{13}C enriched C_{60} had a ^{13}C content very close to 30%. This is in agreement with the result of the Monte-Carlo type simulation, where the 30% ^{13}C abundance also matched best with the experimental spectra. A point worth noting is that without identifying a ^{13}C cluster to be consisted of ^{13}C's within 1-3 bonds

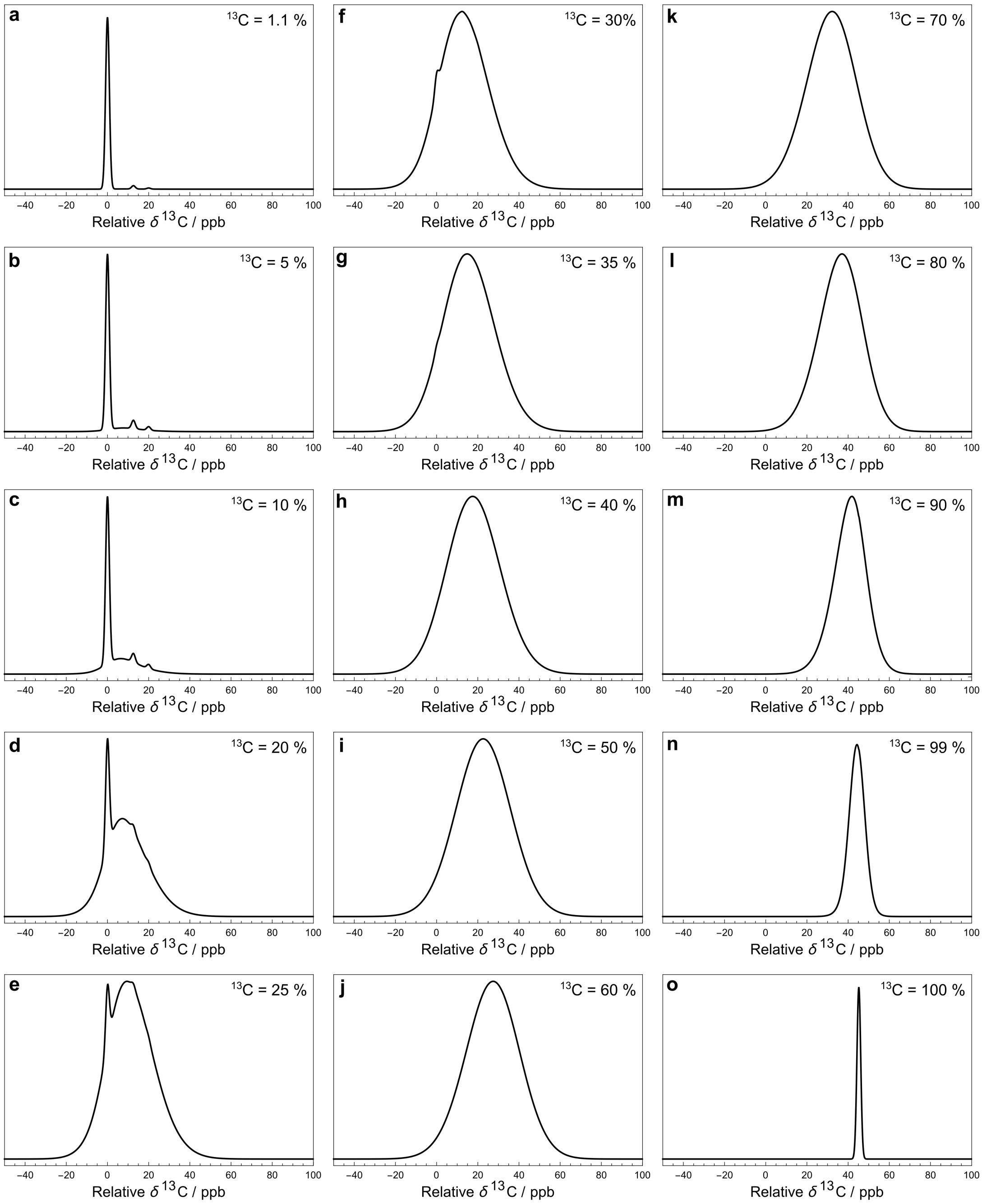

FIGURE 2.16: Monte Carlo simulations of the ^{13}C NMR spectra of C_{60} with different ^{13}C abundances. Considering spins to be coupled if they are within 3 bonds or less away from each other. Simulations done by averaging the spectra of 10000 random C_{60} configurations. Spectra were normalised for clarity. Reproduced from Ref.[1] with permission from the PCCP Owner Societies.

of each other, the Monte-Carlo type simulation would not give such a good match with the experimental ^{13}C NMR spectrum of the 20-30% ^{13}C enriched C_{60} sample, nor would the ^{13}C content from the simulation match the one obtained from the mass spectrum.

The Monte-Carlo type calculation was repeated for a series of different ^{13}C abundances, being presented in fig. 2.16 with increasing ^{13}C probability from 1.1% up to 100%. The simulations show that as the ^{13}C probability is increased from natural abundance the broad feature starts rising and shifting towards shielded chemical shifts. The discrete side peaks seen for natural abundance are distinguishable up until about 20% ^{13}C enrichment, then the clustering of ^{13}C's is too strong and the side peaks arising from isolated adjacent $^{13}C_2$ have lost their intensity. The sharp main C_{60} peak is still visible in the spectrum until about 30% ^{13}C when it becomes clear that it turned into the shoulder seen in the experimental spectrum of the enriched C_{60}. Past 30% ^{13}C only the broad feature is observable and it moves towards more shielded chemical shifts. Interestingly the width of the broad feature is somewhat constant until the ^{13}C content is increased past 50-60%, then the width starts steadily decreasing until reaching the extreme of 100% ^{13}C content; this is because the isotope shifts of the ^{13}C sites become more uniform when most carbon sites in C_{60} are occupied by ^{13}C. In the extreme case of $x = 100\%$, the simulated spectrum is very sharp, since all ^{13}C sites have three ^{13}C neighbours and experience the same secondary isotope shift of $2^1\Delta_{\mathrm{HP}} +^1 \Delta_{\mathrm{HH}} = 45.2$ ppb. All sixty ^{13}C nuclei are magnetically equivalent in this case and the spectrum is composed of a single sharp peak.

2.4.4.1 Moments of NMR spectra containing chemical shifts & J-couplings

This section shows the derivation of equation 2.8, which approximates the NMR spectrum of a given spin system by the second moment $M_c^{(2)}$. In the case discussed here for solution state NMR, the spins experience chemical shifts and J-couplings interactions.

Consider a cluster c containing N_c J-coupled spins-1/2, with chemical shifts δ_i and J-couplings J_{ij}, where $i, j \in \{1 \ldots N_c\}$. The rotating-frame spin Hamiltonian in isotropic solution is given by

$$H = H_{CS} + H_J \tag{2.13}$$

where the chemical shift and J-coupling terms are given by

$$H_{CS} = \sum_{i=1}^{N_c} \Omega_i \, I_{iz} \; ; \quad H_J = \sum_{i<j}^{N_c} 2\pi J_{ij} \, \mathbf{I}_i \cdot \mathbf{I}_j \tag{2.14}$$

The resonance offset frequencies are given by

$$\Omega_i = -\gamma B^0 (\delta_i - \delta_{\mathrm{ref}}) \tag{2.15}$$

Therefore, the Hamiltonian may be written as:

$$H = H_0 + H_1 \tag{2.16}$$

where H_0 is defined as follows:

$$H_0 = \overline{\Omega}_c I_z \tag{2.17}$$

and the mean offset frequency for the cluster $\overline{\Omega}_c$ is shown below (also defined in equation 2.10).

$$\overline{\Omega}_c = N_c^{-1} \sum_{i=1}^{N_c} \Omega_i \tag{2.18}$$

The term H_1 is given by

$$H_1 = H_J + \sum_{i=1}^{N_c} \Delta\Omega_i \, I_{iz} \tag{2.19}$$

where $\Delta\Omega_i$ are resonance offsets with respect to the mean cluster frequency:

$$\Delta\Omega_i = \Omega_i - \overline{\Omega}_c \tag{2.20}$$

The NMR signal for the cluster (free-induction decay) is given by

$$s_c(t) = \big(Q_{\text{obs}} \big| \exp(-i\hat{H}t)\rho(0)\big) \tag{2.21}$$

where $\hat{H}$ is the commutation superoperator of the Hamiltonian H, and the Liouville bracket is defined:[51]

$$\big(A\big|B\big) = \text{Tr}\big\{A^\dagger B\big\} \tag{2.22}$$

Since the Hamiltonian terms H_0 and H_1 commute, the cluster NMR signal may be written

$$s_c(t) = \big(Q_{\text{obs}}\exp(+i\hat{H}_0 t) \big| \exp(-i\hat{H}_1 t)\rho(0)\big) \tag{2.23}$$

The spin density operator at the start of signal detection is denoted $\rho(0)$ and the observable operator is denoted Q_{obs}. In an ordinary single-pulse NMR experiment, using quadrature detection, it is convenient to define these operators as follows:[46]

$$\begin{aligned} \rho(0) &= -I_y \\ Q_{\text{obs}} &= -iI^- \end{aligned} \tag{2.24}$$

With this choice of observable operator, the following commutation relationship holds:

$$\hat{H}_0 \big| Q_{\text{obs}}\big) = -\overline{\Omega}_c \big| Q_{\text{obs}}\big) \tag{2.25}$$

and hence

$$\exp(-i\hat{H}_1 t)\big|Q_{\text{obs}}\big) = \exp(+i\overline{\Omega}_c t)\big|Q_{\text{obs}}\big) \tag{2.26}$$

This leads to the following expression for the cluster NMR signal:

$$s_c(t) = g_c(t)\exp(i\overline{\Omega}_c t) \tag{2.27}$$

where the function $g_c(t)$ is defined as follows:

$$g_c(t) = \left(Q_{\text{obs}}\middle|\exp(-i\hat{H}_1 t)\rho(0)\right) \tag{2.28}$$

The NMR spectrum of the cluster is given by the one-sided Fourier transform of the NMR signal:

$$S_c(\omega) = \int_0^\infty s_c(t)\exp(-i\omega t)\mathrm{d}t \tag{2.29}$$

which may be written as follows:

$$S_c(\omega) = G_c(\omega - \overline{\Omega}_c) \tag{2.30}$$

where the function $G_c(\omega)$ is the Fourier transform of $g_c(t)$:

$$G_c(\omega) = \int_0^\infty g_c(t)\exp(-i\omega t)\mathrm{d}t \tag{2.31}$$

Equation 2.30 shows that the cluster spectrum $S_c(\omega)$ may be derived from the function $G_c(\omega)$ by a simple frequency shift. The function $G_c(\omega)$ is centred around $\omega = 0$, while the spectrum $S_c(\omega)$ is centred around the mean resonance offset $\overline{\Omega}_c$.

An approximate expression for $G_c(\omega)$ is developed by a moment analysis. The use of spectral moments is a powerful technique in broad-line solid-state NMR,[63] but has rarely been used for solution NMR. The nth moment $M_c^{(n)}$ of the real part of the function $G_c(\omega)$ is defined as follows:

$$M_c^{(n)} = \int_{-\infty}^{\infty} \mathrm{Re}\{G_c(\omega)\}\omega^n \,\mathrm{d}\omega \tag{2.32}$$

From the properties of the Fourier transform,[72] the nth moment of the real part of the spectrum is proportional to the nth derivative of the time-domain signal at the time origin:

$$M_c^{(n)} = (-i)^n \left(\frac{\mathrm{d}^n}{\mathrm{d}t^n} g_c(t)\right)_{t=0} \tag{2.33}$$

Repeated differentiation of equation 2.28 leads to the expression

$$\frac{\mathrm{d}^n}{\mathrm{d}t^n} g_c(t) = (-i)^n \left(Q_{\text{obs}}\middle|\hat{H}_1^n \rho(t)\right) \tag{2.34}$$

and hence a compact form for the nth spectral moment of $G_c(\omega)$:

$$M_c^{(n)} = -i(-1)^n \big(I^- \big| \hat{H}_1^n I_y\big) \tag{2.35}$$

For example, the $n = 0$ moment, which is equal to the integral of the spectrum, evaluates to:

$$M_c^{(0)} = -i(+i)\big(I_y\big|I_y\big) = N_c\, 2^{N_c-2} \tag{2.36}$$

using equation 2.28.

The expression for the first moment of $G_c(\omega)$ involves the following terms:

$$\hat{H}_1\big|I_y\big) = \hat{H}_J\big|I_y\big) + \sum_{i=1}^{N_c} \Delta\Omega_i \hat{I}_{iz}\big|I_y\big) \tag{2.37}$$

The first term vanishes since the J-coupling Hamiltonian commutes with the total angular momentum operator along an arbitrary axis:

$$\big[\mathbf{I}_i \cdot \mathbf{I}_j, I_{iy} + I_{jy}\big] = 0 \tag{2.38}$$

The commutation properties of the angular momentum operators lead to the following expression for the second term:

$$\hat{H}_1\big|I_y\big) = \sum_{i=1}^{N_c} \Delta\Omega_i \hat{I}_{iz}\big|I_y\big) = -i \sum_{i=1}^{N_c} \Delta\Omega_i \big|I_{ix}\big) \tag{2.39}$$

Hence the first spectral moment is given by

$$M_c^{(1)} = \sum_{i=1}^{N_c} \Delta\Omega_i \big(I^-\big|I_{ix}\big) = 0 \tag{2.40}$$

The first moment of $G_c(\omega)$ vanishes since each bracketed term is identical, and the sum of the resonance offsets, relative to the mean frequency of the cluster, is zero by definition:

$$\sum_{i=1}^{N_c} \Delta\Omega_i = 0 \tag{2.41}$$

The second moment is conveniently evaluated by rearranging equation 2.35 for $n = 2$:

$$M_c^{(2)} = -i\big(I^- \hat{H}_1\big|\hat{H}_1 I_y\big) \tag{2.42}$$

All terms involving the J-coupling term H_J vanish through the commutation relationship in equation 2.38. This leads through equation 2.39 to the expression

$$M_c^{(2)} = \sum_{i,j=1}^{N_c} \Delta\Omega_i \Delta\Omega_j \big(I_{ix}\big|I_{jx}\big) \tag{2.43}$$

Since the angular momentum operators of different spins are orthogonal, we get

$$M_c^{(2)} = 2^{N_c-2} \sum_{i=1}^{N_c} \Delta\Omega_i^2 \tag{2.44}$$

The normalized second moment, defined as the ratio of the second and zeroth moments, is given by

$$\mathcal{M}_c^{(2)} = \frac{M_c^{(2)}}{M_c^{(0)}} = N_c^{-1} \sum_{i=1}^{N_c} \Delta\Omega_i^2 \tag{2.45}$$

which is equal to the mean-sum-square of the resonance offsets for all spins in the cluster, relative to the mean resonance offset.

Note that the J-couplings do not appear in the expression for the second moment. The second moment of the NMR spectrum of a given J-coupled spin cluster may, therefore, be calculated extremely rapidly using only the chemical shift values for all spins in the cluster and ignoring the J-couplings. The situation is different for the case of dipole-dipole coupling in solids,[63] since a commutation relationship of the type given in equation 2.38 does not apply for the dipole-dipole Hamiltonian.

The algorithm used in this paper uses the following Gaussian function as an approximation to the function $G_c(\omega)$:

$$G_c^{\star}(\omega) = N_c(2\pi\mathcal{M}_c^{(2)})^{-1/2} \exp\left\{-\frac{\omega^2}{2\mathcal{M}_c^{(2)}}\right\} \tag{2.46}$$

where the normalized second moment is given by equation 2.45. This expression omits the fine details of the NMR spectrum but has correct values for the zeroth, first, and second moments. The approximate form of the spectral function $S_c(\omega)$ for a cluster of ^{13}C spins, given in equation 2.8, is derived from equation 2.46 by using the expression for the second moment in equation 2.45, and the frequency-shift relationship in equation 2.30.

2.5 Conclusion

To conclude, this chapter was dedicated to the presentation and analysis of the fine structure seen in the solution ^{13}C NMR of C_{60} fullerene, with significant differences seen between samples with different ^{13}C content.

Natural abundance C_{60} displays two extra peaks in the ^{13}C solution NMR spectrum, of weak intensity in relative ratio 2:1. These are labelled HP with amplitude $1.63 \pm 0.15\,\%$ of the main C_{60} peak and HH with amplitude $0.81 \pm 0.08\,\%$ of the main C_{60} peak. These side peaks are on the deshielded side of the main C_{60} peak, shifted by $^{1}\Delta_{\mathrm{HP}} = 12.56 \pm 0.01$ ppb and $^{1}\Delta_{\mathrm{HH}} = 19.98 \pm 0.02$ ppb with respect to the main peak at 298 K. These shifts decrease linearly in magnitude as temperature is increased, with the HH peak being more strongly influenced by a change in temperature. The side peaks are also present for endofullerene samples with the same pattern. The only difference being the shifts are slightly decreased in magnitude by the presence of an endohedral molecule and this effect scales with the size of the endohedral molecule. The HH shift seems to be more strongly affected by the presence of an endohedral molecule than the HP shift. The origin of the shifts is shown to be due to the one-bond secondary NMR isotope shift; these arise when $^{13}C_2$ isotopomers of C_{60} have the ^{13}C's adjacent along a HP bond ([HP-$^{13}C_2$]-C_{60}) or a HH bond ([HH-$^{13}C_2$]-C_{60}). The fine structure seen in the natural abundance C_{60} ^{13}C NMR spectrum is *not* due to ^{13}C-^{13}C J-couplings. The relative amplitudes of the two side peaks is 2:1, identical to the HP:HH bond ratio in C_{60} of 2:1. The amplitudes of the side peaks with respect to the main C_{60} peak are described through a purely statistical argument and a Monte-Carlo type simulation.

The solution ^{13}C NMR spectrum of 20-30% ^{13}C enriched C_{60} is broader than that of natural abundance C_{60}, and the fine structure is lost. An algorithm was developed, based on a Monte-Carlo type approach, to simulate C_{60} spectra of arbitrary levels of ^{13}C. Firstly the ^{13}C spin systems in C_{60} are decoupled based on a cluster identification method which uses the magnitudes of ^{13}C-^{13}C J-couplings relative to the experimentally observed isotope shifts in C_{60}. Then the spectra of each cluster are approximated by their second moment and added up in a Monte-Carlo fashion to simulate the C_{60} spectrum. The simulation using this method matches quite well with the experimental result, even for natural abundance C_{60}. Multiple spectra of C_{60} with various ^{13}C contents were shown after being computed using this method.

The broader feature of the ^{13}C enriched C_{60} solution NMR spectrum can be connected to that of NMR spectra of solid powders, where the spectrum is broadened by a statistical distribution of orientations; in our case, the spectrum is broadened by a statistical distribution of ^{13}C's relative to each other among the C_{60} sites, but in a solution and not a solid. This method of approximating the spectrum evaluates rapidly for a large number of J-coupled spins and may be adapted to other problems in solution and solid-state NMR.

2.5.1 Future work

One could perform a similar study on the C_{70} molecule. It was attempted but the ^{13}C spectrum around each main C_{70} peak is composed of many overlapping peaks. This arises because the ^{13}C-^{13}C J-coupling when the ^{13}C's are more than one bond away has similar magnitude to the one-bond isotope shifts, and gives rise to peaks split by J-coupling overlapping with one-bond isotope shifted peaks (when the two ^{13}C's are equivalent). Further investigation, using 2D NMR techniques, is needed to understand the fine structure in the C_{70} ^{13}C spectrum.

A computational study can be done to deeply understand and quantify why the isotope shifts are different for the two types of bonds (HP & HH) in the C_{60} molecule. Maybe one could deduce the force constant and/or the anharmonicity of the HP & HH bonds from the NMR isotope shifts ($^1\Delta_{HP}$ & $^1\Delta_{HH}$). However, such simulations would require large amounts of computational power, which may not be feasible on such a large molecule like C_{60}.

After the isotope shifts for the C_{60} are more deeply understood, one can attempt to explain why these shifts change slightly when an atom/molecule is encapsulated in the cage. Further measurement of these isotope shifts for endofullerenes are ongoing.

Chapter 3

^{0}J-coupling induced by molecular confinement

3.1 Introduction

Among the nuclear spin-spin interactions, the J-coupling is probably the most used in high-resolution nuclear magnetic resonance (NMR). J-couplings make use of the electrons present in chemical bonds to mediate the dipolar interaction between nuclei, which represents the reason why sometimes is called *indirect dipole-dipole coupling*.[46] J-couplings tend to get weaker as the number of chemical bonds between the nuclei increases. It is the only spin-spin NMR interaction which is not averaged out in isotropic liquids (solutions). Because of this, J-couplings generate very characteristic splittings of the NMR peaks, which are crucial for molecular structure elucidation.[73] Furthermore, the development of 2D NMR techniques in liquids make extensive use of J-couplings.[74] Through such 2D NMR techniques, finding the structure of large bio-molecules in solution is now well established method.

J-couplings depend on how the electron wavefunctions (orbitals) overlap to make up chemical bonds. For example, the three-bond J-coupling ^{3}J, where the superscript 3 marks the number of bonds between the participating nuclei, depends on torsional angles between the chemical bonds, which can be used to determine molecular conformations.[75,76]

Due to the dependence on the covalent bonds between interacting nuclei, J-couplings are generally believed to be a signature of covalent chemical bonding. However, cases are known in which J-couplings are induced by the electron overlap and are not a direct consequence of covalent molecular bonding. Thus, J-couplings are known to be transmitted through hydrogen bonds,[77–80] a non-covalent type of chemical bonding.

J-couplings are known to be quite strongly influenced by steric constraints, which induce electronic overlap. Such interactions are called ”through-space” or ”non-bonded” J-couplings.[81–83] Since steric effects can influence J-couplings, this can be used for structure determination of constrained molecules.[82,84] Generally such ”non-bonded” J-couplings are disentangled by quantum chemistry calculations.[85–90]

Some experimental evidence exists for really small J-couplings between species in van der Waals complexes. This was shown indirectly from noble gas magnetometry (^{3}He and ^{129}Xe) for atoms and molecules associated by van der Waals forces, with support from computational studies.[90–92]

Confining atoms/molecules to the same region of space generates electronic overlap, since repulsive surface interactions force electrons to overlap. In principle, this should induce internuclear J-couplings between spatially confined, but not chemically bonded, nuclei. Usually, such an interaction would be strongly attenuated by the rapid spatial diffusion of the two species. Thus, it seems necessary to keep the species in close proximity for extended periods of time for such confinement induced J-coupling to be observed. To our knowledge only one example is known for confinement induced J-couplings, from ^{129}Xe adsorbed in microporous solids.[93] Where double-quantum ^{129}Xe NMR data[93] was interpreted in terms of anisotropic ^{129}Xe-^{129}Xe J-couplings through quantum chemistry calculations.[89]

A suitable confined system is provided by endofullerenes, in which small molecules or atoms are completely encapsulated in the interior space of a closed carbon cage.[94] In this case the carbon cage completely restricts the endohedral moiety to a well defined region of space. Direct spectroscopic evidence will be provided in this chapter for a ”confinement-induced” J-coupling between ^{3}He and ^{13}C nuclei in the noble gas endofullerene ^{3}He@C$_{60}$. The naming convention ^{0}J$_{\mathrm{HeC}}$ will be used, where the superscript zero represents the absence of a chemical bond between ^{3}He and ^{13}C atoms. The ^{3}He nucleus is a good candidate for such a J-coupling, since it has spin $I = 1/2$ and a rather large magnetogyric ratio ($\sim 3/4$ of ^{1}H). Also, the ^{3}He spin lattice relaxation time is long, which allows the observation of a weak J-coupling. This ^{0}J$_{\mathrm{HeC}}$-coupling is supported by quantum chemistry calculations.

Furthermore, a similar type of ^{0}J-coupling is observed between ^{1}H and ^{13}C in CH$_4$@C$_{60}$. However, this system is not as well suited as ^{3}He@C$_{60}$ for observing weak J-couplings. Experimental evidence is shown which infers the presence of ^{0}J$_{\mathrm{HC}}$ in CH$_4$@C$_{60}$.

Most of the contents of this chapter have been already published in a scientific journal, see ref. 95 for the publication.

3.2 Experimental

The endofullerenes $^{3}He@C_{60}$ and $^{4}He@C_{60}$ were prepared by the group of Richard Whitby through molecular surgery, as described in reference 96.

$\sim$15 mg of $^{3}He@C_{60}$ (43% filled) was dissolved in 0.75 mL ODCB-d_4 (Sigma-Aldrich). The solution was filtered to remove any undissolved impurities and degassed by bubbling O_2-free N_2 gas through the solution for 10 min.

$\sim$15 mg of $^{4}He@C_{60}$ (41% filled) was dissolved in 0.8 mL ODCB-d_4 (Sigma-Aldrich). The solution was filtered to remove any undissolved impurities and degassed by bubbling O_2-free N_2 gas through the solution for 10 min.

8-9 mg of $CH_4@C_{60}$ (41% filled) was dissolved in 0.6 mL ODCB-d_4 (Sigma-Aldrich). The solution was filtered to remove any undissolved impurities and degassed by bubbling O_2-free N_2 gas through the solution for 10 min. A similar sample of 4.5 mM $CH_4@C_{60}$ (100% filled) in degassed ODCB-d_4 (Sigma-Aldrich) was also prepared.

All ^{13}C and ^{1}H NMR experiments were performed at a field of 16.45 T on a Bruker Ascend 700 NB magnet fitted with a Bruker TCI prodigy 5 mm liquids cryoprobe and a Bruker AVANCE NEO console.

The ^{3}He NMR measurements were performed at a field of 11.7 T on a Bruker Ascend 500 magnet fitted with a Bruker 5 mm liquids SmartProbe and a Bruker AVIIIHD500 console.

All NMR solution state measurements were done on 5 mm NMR tubes. In order to improve the magnetic field homogeneity and implicitly the spectral resolution, Wilmad precision NMR tubes rated for 900MHz (Sigma-Aldrich) were used in every case.

3.3 Results

The experimental solution NMR results which show the new splitting of the ^{13}C peak of $^{3}He@C_{60}$ are given below. The splitting is shown to be present for the HP & HH side peaks of $^{3}He@C_{60}$; HP & HH side peaks are described in chapter 2.

Some $CH_4@C_{60}$ ^{13}C solution NMR results are presented. A broadening is observed for the solution NMR ^{13}C (C_{60}) peak of $CH_4@C_{60}$, which disappears when ^{1}H decoupling is applied on endohedral CH_4.

3.3.1 ^{3}He@C$_{60}$ results

3.3.1.1 Main ^{13}C peak splitting

The ^{13}C solution NMR spectrum of ^{3}He@C$_{60}$ (filling factor $f = 0.43$) ∼27 mM in *ortho*-dichlorobenzene-d$_4$ (ODCB-d$_4$) was measured at 16.45 T and 340 K and it is shown in fig. 3.1 (a, b), together with a 3D sketch of the ^{3}He@C$_{60}$ structure which is observable by ^{13}C NMR. The same measurement was repeated for ^{4}He@C$_{60}$ (filling factor $f = 0.41$) ∼25 mM in ODCB-d$_4$, under the same conditions, and it is shown in fig. 3.1 (c, d), together with a 3D sketch of the ^{4}He@C$_{60}$ structure which is observable by ^{13}C NMR.

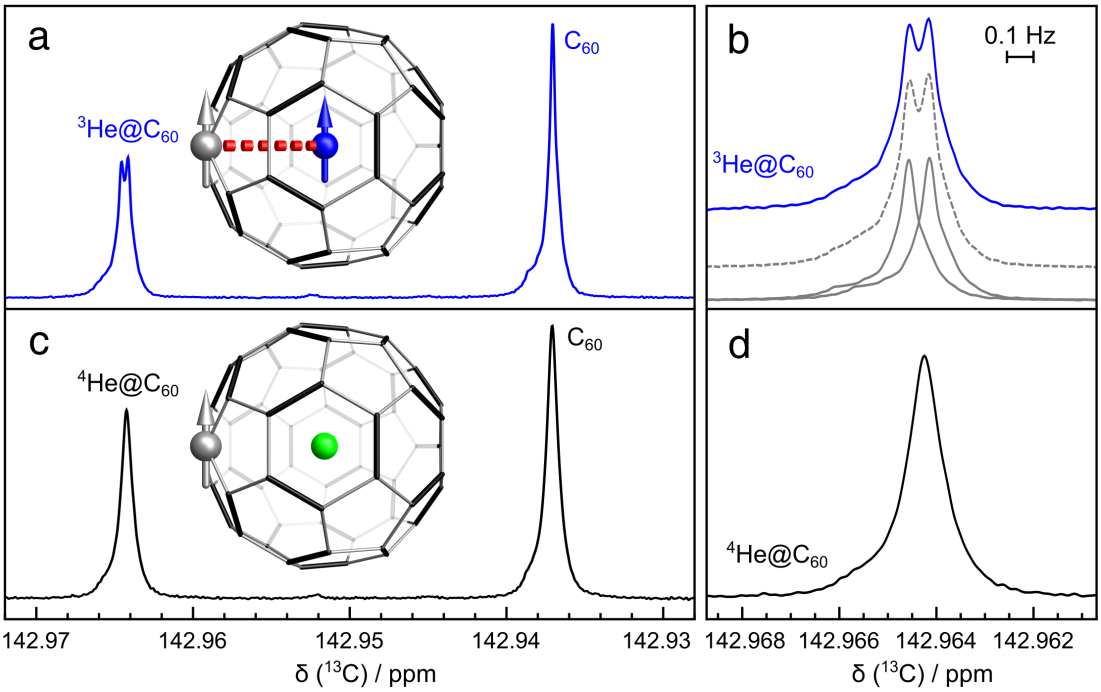

FIGURE 3.1: **(a)** ^{13}C solution NMR spectra of a ∼27 mM solution of ^{3}He@C$_{60}$ (43% filling factor) in ODCB-d$_4$ at 340 K and 16.45 T (average of 40 transients); **(b)** Blue line: expansion of the ^{13}C peak of ^{3}He@C$_{60}$; Dashed grey line: Best fit to two shifted spectral components, each with a shape matching the ^{13}C peak of C$_{60}$; Solid gray lines: individual spectral components. **(c)** ^{13}C solution NMR spectra of a ∼25 mM solution of ^{4}He@C$_{60}$ (41% filling factor) in ODCB-d$_4$ (average of 32 transients). All other conditions are the same as in **(a)**. **(d)** Expansion of the ^{13}C peak of ^{4}He@C$_{60}$. 3D sketches show the structures of endofullerenes giving rise to the ^{13}C peaks; non-zero nuclear spins are represented as arrows. Reprinted (adapted) with permission from (95). Copyright (2020) American Chemical Society.

Both ^{13}C spectra show discrete peaks for C$_{60}$, ^{3}He@C$_{60}$ and ^{4}He@C$_{60}$. The C$_{60}$ cages with an encapsulated ^{3}He or ^{4}He atom have a change of +0.027 ppm in their chemical shift, consistent with previous measurements.[17] The ^{3}He@C$_{60}$ chemical shift difference with respect to C$_{60}$ seems to be 0.2 ppb larger than for ^{4}He@C$_{60}$, but this could be due to experimental error since the measurements were done separately on different samples.

A clear splitting is observed for the ^{13}C peak of ^{3}He@C$_{60}$. The splitting is absent for ^{4}He@C$_{60}$ as seen by comparing panels a-c and b-d from fig. 3.1. The splitting is absent for C$_{60}$ in both samples, which indicates that the magnetic field inhomogeneity is not the cause of the ^{3}He@C$_{60}$ splitting.

The spectra from fig. 3.1 were obtained after extensive optimization of the magnetic field homogeneity, giving sharp ^{13}C peaks with a rather non-Lorentzian shape as seen by the small shoulders at the base of the peaks. The linewidth-at-half-height of the C$_{60}$ peak from the ^{3}He@C$_{60}$ sample was 96 mHz (fig. 3.1 (a)).

Since the observed splitting is really small, the following procedure was used to estimate the splitting between the doublet components of the ^{3}He@C$_{60}$ peak. The lineshape of the unsplit ^{13}C peak of empty C$_{60}$ present in the same spectrum (fig. 3.1 (a)) was interpolated by a spline type function in the region ±6 ppb (or ±1 Hz) with respect to the centre of the peak. This interpolated lineshape represents the reference spectrum which was used to match the doublet structure in the spectrum by fitting a superposition of two mutually shifted reference lineshapes. The result of such fitting of the ^{3}He@C$_{60}$ doublet with an interpolated reference C$_{60}$ peak is shown in fig. 3.1 (b), where the two components are in a ratio of 1:1 exactly. From this fitting the splitting is estimated to be 77.5 ± 0.2 mHz at 340 K. The same estimate of the splitting is obtained through reference deconvolution methods[97] by using the same C$_{60}$ peak as reference.

3.3.1.2 HP & HH side peaks splitting

Both C$_{60}$ fullerene and endofullerenes of C$_{60}$ in their ^{13}C solution NMR spectrum show two additional side peaks shifted towards deshielded chemical shifts. They are labelled HP & HH based on the C-C bonds present in C$_{60}$, HP = Hexagon-Pentagon bond and HH = Hexagon-Hexagon bond. The origin of these side peaks is described in detail in chapter 2.

The high resolution ^{13}C solution NMR spectra of ^{3}He@C$_{60}$ $\sim$27 mM and ^{4}He@C$_{60}$ $\sim$25 mM in ODCB-d$_4$ are shown in fig. 3.2 (a,d). In the spectra discrete peaks are seen for C$_{60}$, ^{3}He@C$_{60}$ and ^{4}He@C$_{60}$. Besides the main ^{13}C peaks, additional side peaks HP & HH are observed for each of them, when scaling the region around them by a factor of 40. The 3D structures of the endofullerenes giving rise to the ^{13}C side peaks are shown in fig. 3.2 (b,c) for ^{3}He@C$_{60}$ and (e,f) for ^{4}He@C$_{60}$.

The side peak structure for C$_{60}$ and ^{4}He@C$_{60}$ is the same as seen in chapter 2. However, the structure of the side peaks is different for ^{3}He@C$_{60}$, both the HP and HH peaks have a small visible splitting associated with them. Due to the difficulty associated with keeping a high enough homogeneity of the magnetic field for a long period of time to enable the acquisition of such long measurements, the spectrum in fig. 3.2 (a) is the finest one obtained so far, in which the splitting of the side peaks is rather clear

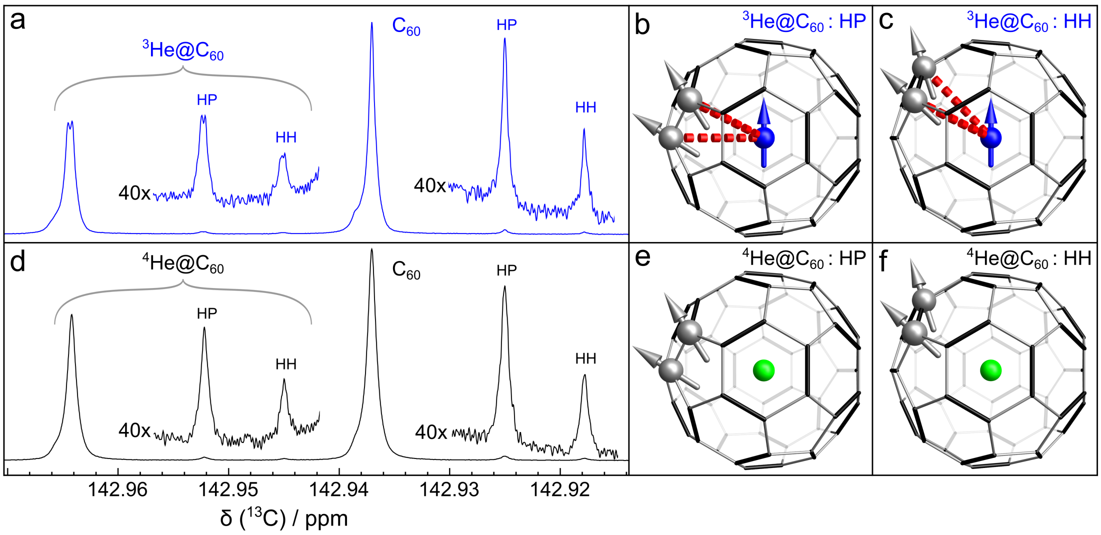

FIGURE 3.2: **(a)** ^{13}C solution NMR spectrum of ~27 mM ^{3}He@C$_{60}$ (f=0.43) in ODCB-d$_4$ at 340 K and 16.45 T (average of 512 transients). The HP & HH side peaks are scaled by 40 for clarity; showing only the ^{3}He@C$_{60}$ side peaks split due to ^{0}J$_{HeC}$. Fullerene 3D structures are shown for HP ^{3}He@C$_{60}$ **(b)** and HH ^{3}He@C$_{60}$ **(c)**, with: HP bond in thin gray, HH bond in thick black and ^{0}J$_{HeC}$ shown in red dashed. **(d)** ^{13}C solution NMR spectrum of ~25 mM ^{4}He@C$_{60}$ (f=0.41) in ODCB-d$_4$ (average of 888 transients), all other conditions are the same as in **(a)**. The HP & HH side peaks are scaled by 40 for clarity; showing no peak splitting. Fullerene 3D structures are shown for HP ^{4}He@C$_{60}$ **(e)** and HH ^{4}He@C$_{60}$ **(f)**, with: HP bond in thin gray, HH bond in thick black and with no ^{0}J$_{HeC}$ present. Non-zero nuclear spins are represented as arrows. Reprinted (adapted) with permission from (95). Copyright (2020) American Chemical Society.

but not ideal. Adding transients with ever so slightly different homogeneities washes away the small splitting, as seen in the difference between the main ^{13}C peak splitting of ^{3}He@C$_{60}$ from fig. 3.1 (a) and fig 3.2 (a), the former has a much clear doublet acquired with 40 transients, whereas the latter was acquired with 512 transients and the doublet is less clear. Unfortunately, due to the weak intensity of the ^{3}He@C$_{60}$ side peaks and the not so well defined doublets, an estimate of the splitting using the interpolation method from section 3.3.1.1 was not possible. However, the spitting of the side peaks can be seen to be of the same magnitude as for the main peak, in fig 3.2 (a) and previously in fig. 3.1 (a)

There is a negligible difference (within experimental error) between the side peak shifts, with respect to the main, of empty C$_{60}$ compared with ^{3}He@C$_{60}$ or ^{4}He@C$_{60}$.

3.3.1.3 Temperature dependence

The ^{13}C solution NMR spectra of ^{3}He@C$_{60}$ was measured at a range of temperatures. The splitting observed for the ^{3}He@C$_{60}$ peak depends slightly on temperature. The ^{3}He@C$_{60}$ ^{13}C doublet at each temperature was fitted with a superposition of two identical spline functions, which originate from the interpolation of the C$_{60}$ peak lineshape from within the same NMR spectrum (as in section 3.3.1.1). The resulting estimates of the splitting at each temperature are plotted in fig. 3.3.

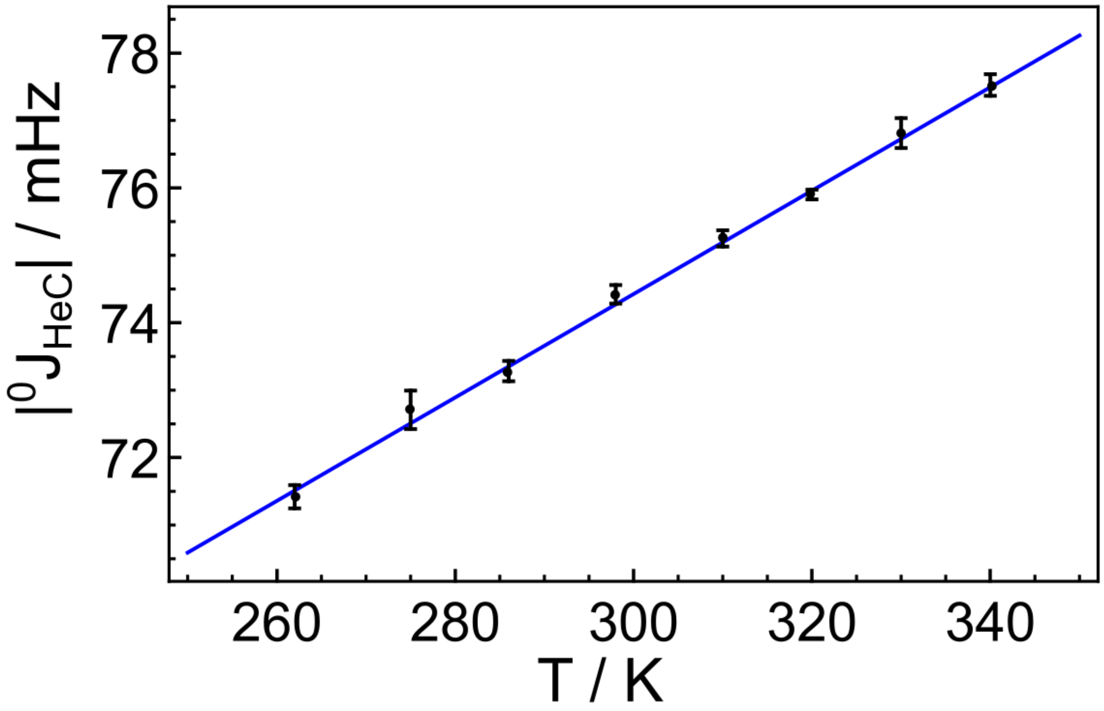

FIGURE 3.3: Temperature dependence of the ^{3}He-^{13}C spin-spin coupling $^0J_{HeC}$, for a ∼27 mM solution of ^{3}He@C$_{60}$ (filling factor $f = 0.43$) in *ortho*-dichlorobenzene-d$_4$. The solid blue line shows the best linear fit, $|^0J_{HeC}| = mT + c$, with $c = 51.4$ mHz and $m = 76.7 \times 10^{-3}$ mHz K^{-1}. Reprinted (adapted) with permission from (95). Copyright (2020) American Chemical Society.

From fig. 3.3 the splitting of the ^{3}He@C$_{60}$ ^{13}C peak is seen to slightly increase with increasing temperature. The splitting has an approximately linear dependence on temperature, over the measured temperatures (262 K - 340 K). The data fits well to a linear function of the form:

$$|^0J_{HeC}| = mT + c \tag{3.1}$$

Where the observed ^{3}He@C$_{60}$ splitting is labelled as $|^0J_{HeC}|$.

The result of the linear fit are:
- The intercept is $c = 51.4 \pm 0.7\,$mHz.
- The slope is $m = (76.7 \pm 2.3) \times 10^{-3}$ mHz K^{-1}.

3.3.1.4 ^{3}He@C$_{60}$ ^{3}He T_1

The ^{3}He NMR measurments were done by Dr. N. Wells from the School of Chemistry NMR facility, since our equipment at the time did not allow ^{3}He NMR experiments.

The ^{3}He T_1 spin lattice relaxation time for a solution of ~25 mM ^{3}He@C$_{60}$ in ODCB-d$_4$ has been measured at a field of 11.7 T by saturation recovery. The saturation recovery relaxation curve is shown in fig. 3.4. The data fits well to a monoexponential function, of the form $I_0 * (1 - exp(\frac{-t}{T_1}))$, with the decay constant:

- ^{3}He@C$_{60}$ ^{3}He T_1 = 365 ± 41 s.

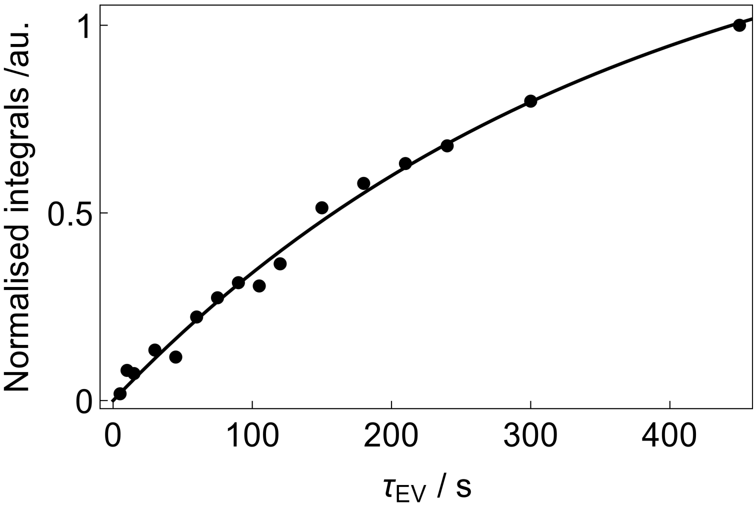

FIGURE 3.4: Saturation Recovery relaxation curve for ^{3}He T_1 of ^{3}He@C$_{60}$ ~25 mM in ODCB-d$_4$ (f = 0.05) at 11.7 T (Larmor frequency ^{3}He = 380.99 MHz) and 298 K with 16 transients and degassed by bubbling N$_2$ for 10 mins. Data fits well to a monoexponential function, of the form $I_0 * (1 - exp(\frac{-t}{T_1}))$, with the decay constant ^{3}He T_1 = 365 ± 41 s. Reprinted (adapted) with permission from (95). Copyright (2020) American Chemical Society.

3.3.1.5 ^{3}He@C$_{60}$ ^{13}C T_1

The ^{13}C T_1 spin lattice relaxation times have been measured for a solution of ^{3}He@C$_{60}$ and C$_{60}$ in ODCB-d$_4$, by inversion recovery at a field of 16.45 T. The inversion recovery relaxation curves are shown in fig. 3.5. The measurement was done on both compounds at the same time, since C$_{60}$ is already present in the ^{3}He@C$_{60}$ sample because of the 43% filling factor.

Both data sets are well fitted by a monoexponential function, of the form $I_0 * (1 - A * exp(\frac{-t}{T_1}))$, with $A \simeq 2$. The inversion recovery fittings give the following decay constants:

- ^{3}He@C$_{60}$ ^{13}C T_1 = 16.83 ± 0.04 s.
- C$_{60}$ ^{13}C T_1 = 16.87 ± 0.04 s.

These results for the ^{13}C T_1 's of ^{3}He@C$_{60}$ and C$_{60}$ show there is no measurable difference between the two. The presence of the ^{3}He inside the C$_{60}$ cage appears to not affect the T_1 of a ^{13}C within the cage. This is valid at the field of 16.45 T at which the measurement was done.

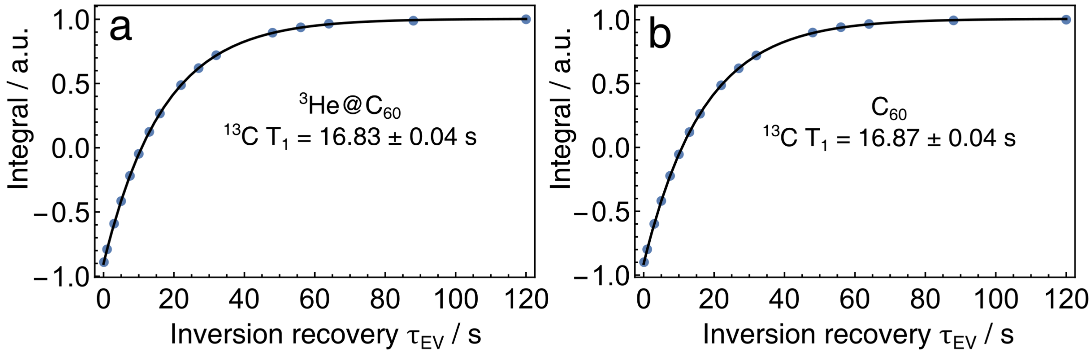

FIGURE 3.5: ^{13}C T_1 Inversion Recovery relaxation curves for: (a) ^{3}He@C$_{60}$ and (b) C$_{60}$. Both within the same sample, ∼27 mM ^{3}He@C$_{60}$ (f = 0.43) in ODCB-d$_4$ at 298 K and 16.45 T, average of 16 transients. Data sets fit to a monoexponential function, of the form $I_0 * (1 - A * exp(\frac{-t}{T_1}))$. The decay constants are: ^{3}He@C$_{60}$ ^{13}C T_1 = 16.83 ± 0.04 s and the C$_{60}$ ^{13}C T_1 = 16.87 ± 0.04 s. Reprinted (adapted) with permission from (95). Copyright (2020) American Chemical Society.

3.3.2 CH$_4$@C$_{60}$ results

^{13}C solution NMR measurements have been performed on CH$_4$@C$_{60}$. The full ^{13}C{^{1}H} spectrum of a 4.5 mM solution of CH$_4$@C$_{60}$ (f=1.0), acquired with ^{1}H WALTZ16 decoupling (nutation frequency = 14.2 kHz) is shown in fig. 3.6. In the ^{13}C{^{1}H} spectrum,

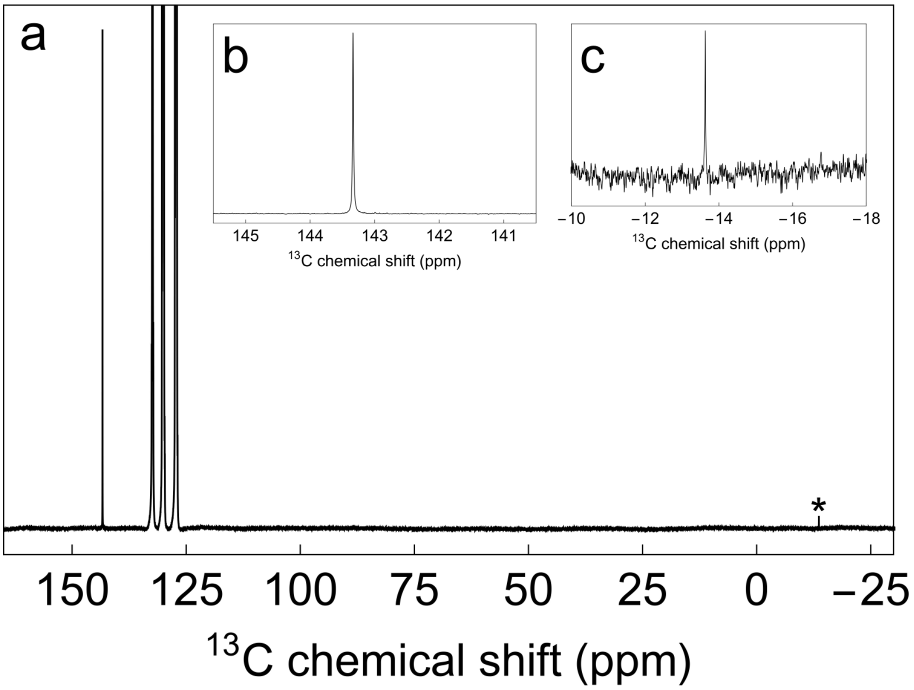

FIGURE 3.6: **(a)** Full ^{13}C{^{1}H} NMR spectrum of CH$_4$@C$_{60}$ (f=1.0) with ^{1}H WALTZ16 decoupling (nutation frequency = 14.2 kHz) of CH$_4$@C$_{60}$ (4.5 mM in degassed ODCB-d$_4$) acquired at 16.45 T, 295 K with 4928 transients (with 10 s delay between scans). The three solvent peaks are found around 130 ppm. The CH$_4$@C$_{60}$ ^{13}C (C$_{60}$) peak is found at 143.34 ppm and the CH$_4$@C$_{60}$ ^{13}C (CH$_4$) peak at -13.63 ppm (marked with an asterisk). Expansions of the (a) spectrum are shown for the ^{13}C (C$_{60}$) peak in **(b)** and for the ^{13}C (CH$_4$) peak in **(c)**. Reprinted with permission from Ref. 20.

there are two peaks for $CH_4@C_{60}$:
- ^{13}C (C_{60}) peak is at 143.3 ppm, also shown in fig. 3.6 (b).
- ^{13}C (CH_4) peak at -13.6 ppm marked with an asterisk, also shown in fig. 3.6 (c).

The ODCB-d_4 solvent peaks are seen around 130 ppm. No ^{13}C (C_{60}) peak is seen for empty C_{60} here since the $CH_4@C_{60}$ filling factor was 100% (f=1.0) for this sample.

3.3.2.1 $CH_4@C_{60}$ ^{13}C (CH_4)

The solution ^{13}C (CH_4) peak of $CH_4@C_{60}$ was shown for the $^{13}C\{^1H\}$ spectrum in fig. 3.6 (a) and (c). The peak is a singlet since ^1H WALTZ16 decoupling was applied. The solution ^{13}C NMR spectrum (with no ^1H decoupling) is shown in fig. 3.7 (b) for the ^{13}C (CH_4) resonance of $CH_4@C_{60}$. The spectrum displays a quintet in a $1:4:6:4:1$ ratio, with a splitting of 124.3 ± 0.2 Hz. The outer peaks of the quintet are barely visible, but are confirmed by the INEPT[98] spectrum from fig. 3.7 (a) acquired on the same sample. The interpulse delay, specific for INEPT,[98] τ was set to 2.012 ms since $\tau = \frac{1}{4\,^1J_{HC}}$ where $^1J_{HC} = 124.3$ Hz from above.

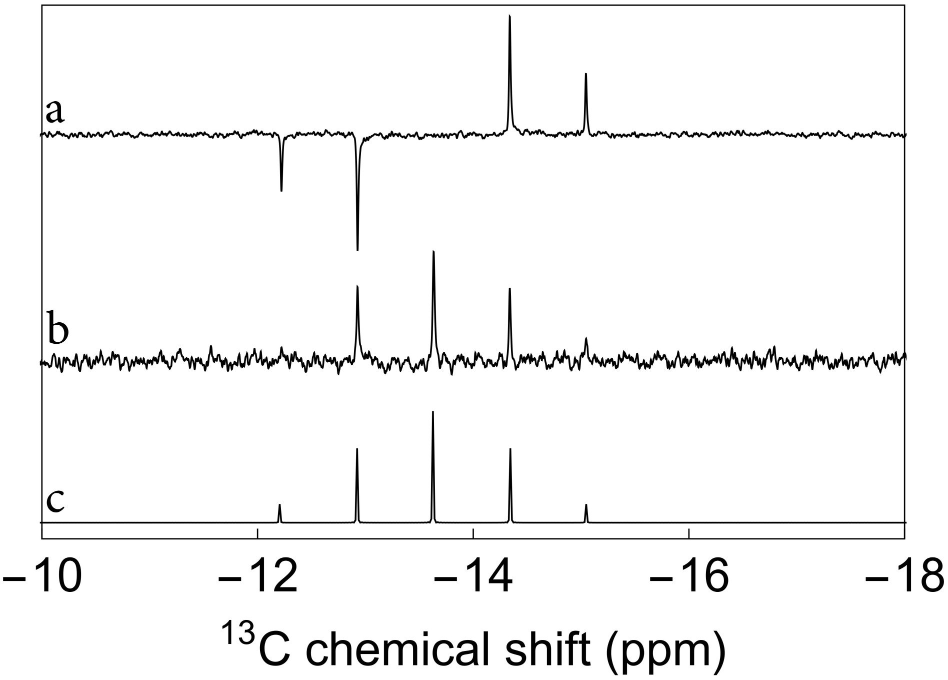

FIGURE 3.7: ^{13}C solution NMR resonances for endohedral CH_4 in $CH_4@C_{60}$ (f=1.0) 4.5 mM in degassed ODCB-d_4 acquired at 16.45 T, 295 K. **(a)** INEPT[98] spectrum acquired with 35840 transients and with $\tau = \frac{1}{4\,^1J_{HC}}$ with $^1J_{HC} = 124.3$ Hz. **(b)** ^{13}C spectrum acquired with 35840 transients. **(c)** Spectral simulation of (b) using SpinDynamica[50] with $^1J_{HC} = 124.3$ Hz. Reprinted with permission from Ref. 20.

A simulation is shown for the ^{13}C (CH_4) quintet, performed with a 5 spin system for $^{13}CH_4$, using SpinDynamica.[50] In the simulation a J-coupling between ^{13}C and ^1H of $^1J_{HC} = 124.3$ Hz was used.

3.3.2.2 $CH_4@C_{60}$ ^{13}C (C_{60})

The ^{13}C solution NMR spectra of $CH_4@C_{60}$ (f=0.41) have been measured with and without ^{1}H decoupling. This was done below, where the focus is only on the (endo)fullerene cage ^{13}C peak. A different sample from above was used in these measurements, since a filling factor of $<$ 100% is needed to compare the ^{13}C peaks of empty C_{60} and $CH_4@C_{60}$ in the same sample.

The ^{13}C spectrum of $CH_4@C_{60}$ at 298 K and 16.45 T is shown in fig 3.8 (a) in red. The $^{13}C\{^1H\}$ spectrum of $CH_4@C_{60}$ at 298 K and 16.45 T is shown in fig 3.8 (b) in blue. The ^{1}H carrier frequency was set to the centre of the ^{1}H peak of $CH_4@C_{60}$ (at about -5.7 ppm[20]), to be used for $^{13}C\{^1H\}$ Waltz16 decoupling with a ^{1}H nutation frequency of 1.15 kHz (low pulse power of 0.02 W was used due to the long acquisition time of 13 s). Fig 3.8 (c, d) has the two spectra show in (a) and (b) overlaid and on the same vertical scale. The spectra were acquired one after the other to ensure the peak lineshapes were as similar as possible, i.e. the magnetic field homogeneity did not change substantially in between the scans.

The ^{13}C (C_{60}) peak of $CH_4@C_{60}$ is significantly broader than the ^{13}C (C_{60}) peak of empty C_{60} when no ^{1}H decoupling is applied; the full-width-at-half-maximum (FWHM) are 212.9 ± 0.6 mHz and 144.0 ± 0.3 mHz respectively, found in table 3.1. There is a considerable narrowing of the ^{13}C (C_{60}) peak of $CH_4@C_{60}$ down to 142.6 ± 0.4 mHz FWHM once ^{1}H decoupling is applied, whereas the ^{13}C (C_{60}) peak of empty C_{60} is not affected at all, see table 3.1 and fig. 3.8 (c, d).

TABLE 3.1: Lorentzian full-width-at-half-maximum (FWHM) of the ^{13}C (C_{60}) peaks of empty C_{60} and $CH_4@C_{60}$ spectra, from fig. 3.8. FWHM of the ^{13}C (C_{60}) peaks are shown for the ^{13}C and $^{13}C\{^1H\}$ spectra, together with the difference between them (in mHz).

species	^{13}C FWHM (/ mHz)	$^{13}C\{^1H\}$ FWHM (/ mHz)	Δ FWHM = $^{13}C - {}^{13}C\{^1H\}$ (/ mHz)
C_{60}	144.0 ± 0.3	144.3 ± 0.3	-0.3 ± 0.4
$CH_4@C_{60}$	212.9 ± 0.6	142.6 ± 0.4	70.3 ± 0.8

Applying ^{1}H waltz16 decoupling on the $CH_4@C_{60}$ protons, produced a narrowing of the ^{13}C (C_{60}) peak of $CH_4@C_{60}$. The difference in the FWHM of the peaks was of 70.3 ± 0.8 mHz between the ^{13}C and $^{13}C\{^1H\}$ spectra, all linewidths are tabulated in table 3.1. This experiment shows a clear change in the solution ^{13}C (C_{60}) peak of $CH_4@C_{60}$ when decoupling the ^{1}H of the endohedral CH_4.

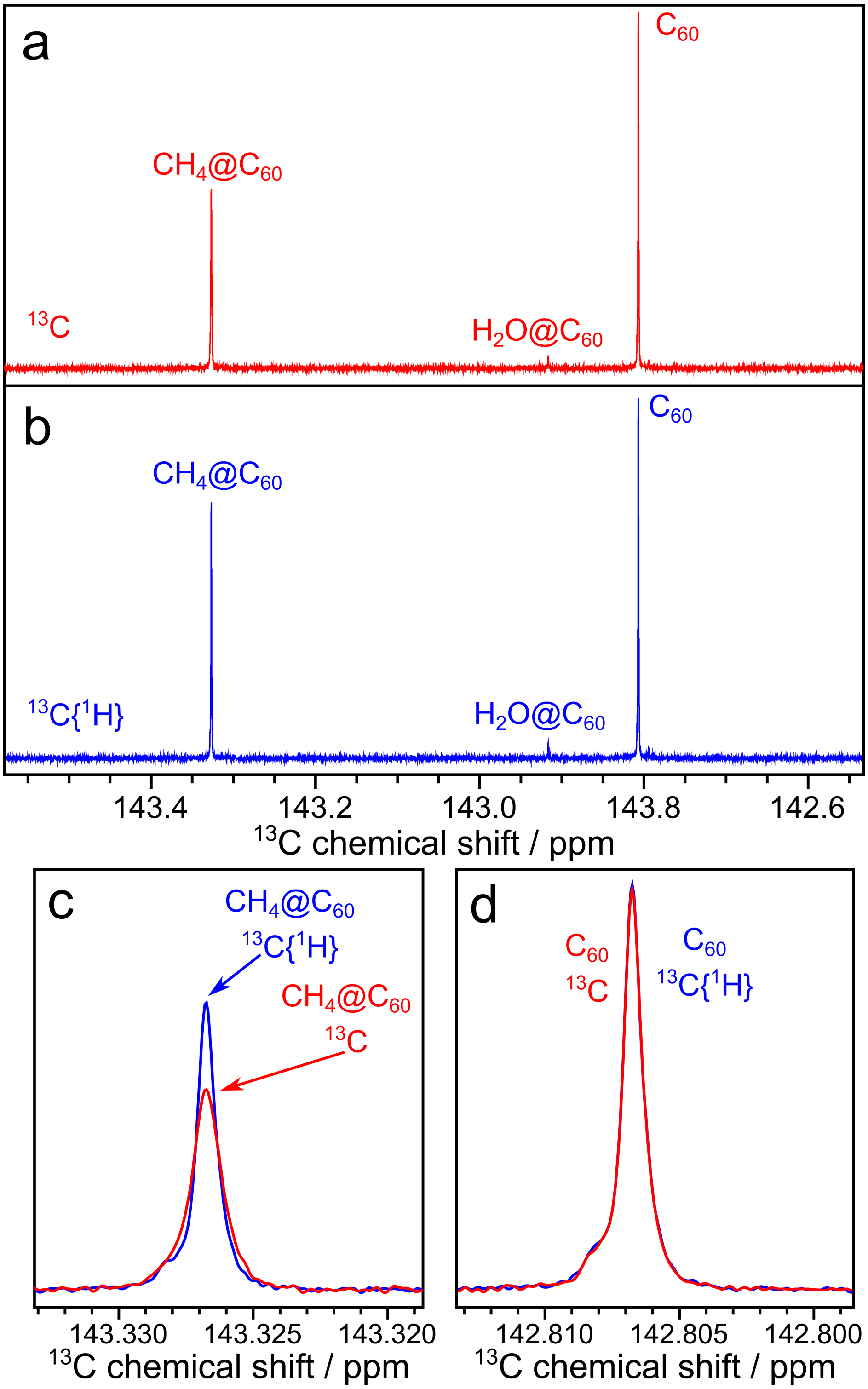

FIGURE 3.8: ^{13}C solution NMR spectra of ∼20 mM $CH_4@C_{60}$ (f=0.41) in ODCB-d_4 at 298 K and 16.45 T; $H_2O@C_{60}$ traces are annotated. (a) ^{13}C spectrum with 8 transients. (b) $^{13}C\{^1H\}$ spectrum using waltz16 decoupling (^1H nutation frequency 1.15 kHz) with 8 transients. (c) has both (a) and (b) overlaid around the $CH_4@C_{60}$ cage peak. (d) has both (a) and (b) overlaid around the C_{60} peak. (a) and (b) share the same vertical axis; same for (c) and (d).

A similar narrowing is observed for the ^{13}C (C_{60}) peaks of $H_2@C_{60}$ and $H_2O@C_{60}$ when decoupling the ^{1}H of the endohedral species. However, in these cases the peak narrowing was much less pronounced, being at the limit of detection, hence spectra are not shown. More experimental investigation will be done on these systems.

3.3.2.3 $CH_4@C_{60}$ ^{1}H T_1

The ^{1}H T_1 spin lattice relaxation time for a solution of ~20 mM $CH_4@C_{60}$ in ODCB-d_4 has been measured at a field of 16.45 T by inversion recovery. The inversion recovery relaxation curve is shown in fig. 3.9. The data fits well to a monoexponential function, of the form $I_0 * (1 - A * exp(\frac{-t}{T_1}))$, with $A \simeq 2$. The inversion recovery fitting gives the following decay constant:

- $CH_4@C_{60}$ ^{3}He T_1 = 1.465 ± 0.001 s.

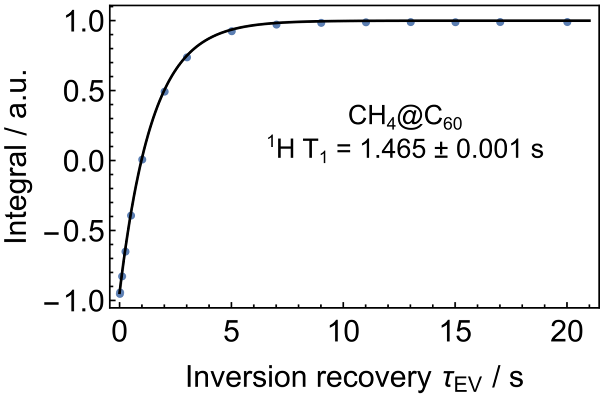

FIGURE 3.9: ^{1}H T_1 Inversion Recovery relaxation curve for ~20 mM $CH_4@C_{60}$ (f = 0.41) in ODCB-d_4 at 298 K and 16.45 T, average of 8 transients. Data is fitted with a monoexponential function, of the form $I_0 * (1 - A * exp(\frac{-t}{T_1}))$. The decay constant $CH_4@C_{60}$ ^{1}H T_1 = 1.465 ± 0.001 s.

3.3.2.4 $CH_4@C_{60}$ ^{13}C (C_{60}) T_1

The ^{13}C T_1 spin lattice relaxation times have been measured for a solution of $CH_4@C_{60}$ and C_{60} in ODCB-d_4, by inversion recovery at a field of 16.45 T. The inversion recovery relaxation curves are shown in fig. 3.10. The measurement was done on both compounds at the same time, since C_{60} is already present in the $CH_4@C_{60}$ sample because of the 41% filling factor.

Both data sets are well fitted by a monoexponential function, of the form $I_0 * (1 - A * exp(\frac{-t}{T_1}))$, with $A \simeq 2$. The inversion recovery fittings give the following decay constants:

- $CH_4@C_{60}$ (cage) ^{13}C T_1 = 17.12 ± 0.05 s.
- C_{60} ^{13}C T_1 = 17.64 ± 0.04 s.

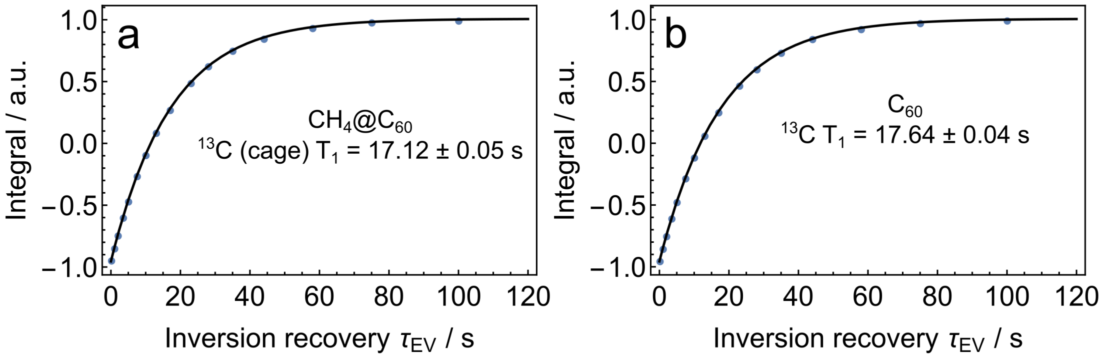

FIGURE 3.10: ^{13}C T_1 Inversion Recovery relaxation curves for: (a) $CH_4@C_{60}$ (cage ^{13}C) and (b) C_{60}. Both within the same sample, ∼20 mM $CH_4@C_{60}$ (f = 0.41) in ODCB-d_4 at 298 K and 16.45 T, average of 24 transients. Data sets fit to a monoexponential function, of the form $I_0 * (1 - A * exp(\frac{-t}{T_1}))$. The decay constants are: $CH_4@C_{60}$ cage ^{13}C T_1 = 17.64 ± 0.04 s and the C_{60} ^{13}C T_1 = 17.12 ± 0.05 s.

These results show a slightly shorter T_1 for the ^{13}C in the cage of $CH_4@C_{60}$ as compared with the empty C_{60} present in the same sample. The presence of CH_4 inside the C_{60} slightly affects the relaxation time of a ^{13}C within the cage.

3.4 Discussion

This section is dedicated to the discussion and analysis of the NMR experimental results shown in section 3.3. It assigns the splitting seen in the ^{13}C solution NMR spectra of $^3He@C_{60}$ to an internuclear J-coupling between the ^{3}He and ^{13}C nuclei, named $^0J_{HeC}$. A similar ^{0}J-coupling is shown to produce a broadening for ^{13}C the peak of the cage in $CH_4@C_{60}$, interpreted as a $^0J_{HC}$-coupling between the ^{1}H and ^{13}C nuclei.

3.4.1 $^3He@C_{60}$ discussion

The main ^{13}C solution NMR peak of $^3He@C_{60}$ was shown in fig. 3.1 (a) to be a doublet split by 77.5 ± 0.2 mHz at 340 K. The splitting is absent for C_{60} within the same spectrum and the peak is sharp with a linewidth-at-half-height of 96 mHz. Thus, proving that the splitting is not due to magnetic field inhomogeneity. The splitting is also absent in the $^4He@C_{60}$ ^{13}C solution NMR spectrum, where both $^4He@C_{60}$ and C_{60} display sharp singlets of similar linewidth to the C_{60} peak from the $^3He@C_{60}$ sample, see fig. 3.1.

The ^{13}C peak of $^4He@C_{60}$ is a singlet, whereas $^3He@C_{60}$ is a doublet which strongly suggest that an internuclear spin-spin coupling is responsible for the observed splitting; since measurements were done on a solution and ^{3}He has nuclear spin $I = 1/2$, whereas ^{4}He has zero nuclear spin $I = 0$. There is no conceivable type of NMR interaction, like chemical shift for example, which would differentiate between the ^{3}He and ^{4}He nuclei in this way, other than a spin-spin interaction (since there are no quadrupolar nuclei present). The very unlikely possibility that there are two distinct compounds each giving a singlet separated by an isotropic chemical shift which equals the splitting is eliminated because the two doublet components are in 1:1 ratio exactly. Also, the 1:1 splitting is observed in another distinct sample of ^{3}He@C$_{60}$.

The splitting being observed in solution and arising due to a spin-spin interaction, the only explanation for it is the presence of an internuclear J-coupling; since it is not averaged out in isotropic liquids.[46] The only non-zero nuclear spins present in ^{3}He@C$_{60}$ are ^{13}C and ^{3}He; therefore, we assign the splitting seen in the ^{13}C solution NMR spectrum of ^{3}He@C$_{60}$ to a J-coupling between ^{3}He and ^{13}C.

We ascribe the observed splitting in the ^{13}C NMR spectrum of ^{3}He@C$_{60}$ (fig. 3.1 (a)) to a *"through-space"* or *"non-covalent"* or *"non-bonded"* J-coupling between the endohedral ^{3}He nucleus ($I = 1/2$) and a ^{13}C nucleus ($I = 1/2$) present in the cage. We adopt the nomenclature ^{0}J$_{\mathrm{HeC}}$ for the spin-spin interaction. The superscript *"0"* indicates that no formal chemical bond is present between ^{3}He and ^{13}C, since the Helium atom is *mechanically* confined to the interior of the C$_{60}$ cage and it is not bonded to the enclosing carbon surface.[99] The ^{0}J$_{\mathrm{HeC}}$ interaction is depicted in fig. 3.1 (a) by the red dashed line on the ^{3}He@C$_{60}$ structure. After accounting for the gyromagnetic ratios, the observed ^{0}J$_{\mathrm{HeC}}$ of $77.5 \pm 0.2\,$mHz is roughly consistent with reported values for "non-bonded" J-couplings in proteins.[84]

J-couplings in NMR are generally perceived as intramolecular spin-spin interactions, emerging as a consequence of chemical bonding, which are transmitted through the molecular bonds. However, it has been known that J-couplings can be induced (or increased) by the overlap of electron wavefunctions even when the participating nuclei are separated by a large number chemical bonds (n), so large that the corresponding ^{n}J-couplings would be essentially negligible. Spin-spin couplings of these types are referred to as "through-space" or "non-bonded" J-couplings.[81–83] The electronic overlap is in general forced by some constraints (e.g. steric constraints) and the resulting "through-space" J-couplings can provide useful information about the molecular geometry.[82,84] Such J-couplings are commonly disentangled by quantum chemistry calculations.[85–90]

Following the same idea, J-couplings across molecular surfaces seem possible, since surface interactions, even when mainly repulsive, involve the overlap of electron wavefunctions. Thus, confining atoms or molecules to a well defined region of space, might induce internuclear ^{0}J-couplings simply due to the overlap of electron clouds; even when no formal type of chemical bonding is present. In the absence of confinement, an interaction of this type would be attenuated by the rapid spatial diffusion of the given species. In order to detect such a coupling, it seems necessary to confine the interacting species in close proximity for a significant amount of time. The endofullerene compounds are ideal for observing such ^{0}J-couplings, due to their increased stability even over geological timescales.[100] To our knowledge, there is only one experimental evidence for J-couplings induced by confinement, from double-quantum NMR measurement on ^{129}Xe in microporous solids.[93] These have been interpreted in terms of anisotropic ^{129}Xe-^{129}Xe J-couplings through quantum chemistry calculations.[89]

This is, to our knowledge, the first *direct* spectroscopic observation of a J-coupling involving the ^{3}He nucleus. However, there is *indirect* experimental evidence for very small internuclear J-couplings between species in van der Waals complexes.[90–92] For ^{3}He they were observed as scalar ^{3}He-^{129}Xe collisional frequency shifts from low-field magnetometry measurements on noble gases (^{3}He and ^{129}Xe), supported by computational studies, in ref. 90,92.

Another noble gas endofullerene which in principle may present the same type of ^{0}J-coupling is ^{129}Xe@C$_{60}$. Detecting such a ^{0}J-coupling was attempted in the ^{13}C and ^{129}Xe solution NMR of ^{129}Xe@C$_{60}$, in ref. 62. However, no splitting was observed in the spectra and an upper bound was set for it of $< 2\,\mathrm{Hz}$.[62]

From the presented spectrum (fig. 3.1 (a)) only the magnitude of $^0\mathrm{J}_{\mathrm{HeC}}$ can be measured experimentally. Although, quantum chemistry calculations predict $^0\mathrm{J}_{\mathrm{HeC}}$ to be negative, see section 3.4.1.3. Experiments have been planned to use cross-correlated relaxation effects to experimentally determine the sign of $^0\mathrm{J}_{\mathrm{HeC}}$.[101]

^{3}He@C$_{60}$ spin lattice relaxation times

To observe ^{0}J-couplings, the nuclei have to be confined to the same region of space for a long period of time. Besides this requirement, the spin lattice relaxation times of the two nuclei need to be long enough to allow such a weak ^{0}J-coupling to be detectable.

Fortunately for the ^{3}He@C$_{60}$ system the spin lattice relaxation times are long enough. The ^{3}He T_1 of ^{3}He@C$_{60}$ in solution was measured to be 365 ± 41 s at a field of 11.7 T, see fig. 3.4. The ^{13}C T_1 of ^{3}He@C$_{60}$ in solution was measured to be 16.83 ± 0.04 s at a field of 16.45 T, see fig. 3.5. These T_1 parameters allow the small $^0\mathrm{J}_{\mathrm{HeC}}$ to be detectable as a splitting in the NMR spectrum. The long ^{13}C T_1 allows for high resolution spectra and the long ^{3}He T_1 ensures the splitting is observable and not decoupled from the spectrum by relaxation.

The presence of the ^{3}He inside the cage seems to not affect the spin lattice relaxation time of the ^{13}C for ^{3}He@C$_{60}$. As seen by the negligible difference in the T_1 's of C$_{60}$ and ^{3}He@C$_{60}$ from fig. 3.5. However, these were measured only at 16.45 T, and this might not be the case at different magnetic fields. The influence of the ^{3}He on the ^{13}C T_1 should increase as the field is decreased: since the CSA contribution to relaxation should decrease with the field (found to be dominant for C_{60}[102]) and the ^{3}He-^{13}C dipolar contribution should be field invariant.

3.4.1.1 ^{3}He@C_{60} HP & HH peak splitting

C_{60} fullerene in natural abundance displays in its ^{13}C solution NMR spectrum, besides the main peak, two additional side peaks shifted towards deshielded chemical shifts (with respect to the main). They are called HP & HH based on the C-C bonds present in C_{60}, HP = Hexagon-Pentagon bond and HH = Hexagon-Hexagon bond. There are 60 HP bonds and 30 HH bonds in the structure of C_{60}, so the HP:HH abundance ratio is 2:1; the same as the relative ratio of the two side peaks. They are shifted from the main C_{60} peak by the secondary isotope shift that arises when two ^{13}C's are adjacent along a HP or HH bond. The side peaks are also present for endofullerene samples and they are shifted with respect to the main peak of the filled C_{60} cage, which is itself shifted from the main peak of empty C_{60} (see fig. 3.2). The side peaks and their origin are discussed in detail in chapter 2.

The side peaks of ^{3}He@C_{60} and ^{4}He@C_{60} have their shifts from the main ^{13}C peak essentially the same as the side peaks of empty C_{60} (within experimental error). This is probably because the enclosed Helium atom does not affect the C_{60} cage that much. This is in contrast with the side peaks shifts of H_2@C_{60} and H_2O@C_{60}, which were shown in chapter 2 to be smaller in magnitude (within experimental error) than for the empty C_{60}; and the effect was scaling with the size of the endohedral molecule.

Fig. 3.2 shows the main ^{13}C and side peaks of ^{3}He@C_{60}, ^{4}He@C_{60} and the corresponding C_{60} from the $\sim$ 40% filling factors. A small splitting is observed *only* for the peaks corresponding to ^{3}He@C_{60}. Since the main ^{13}C peak was split by $^0J_{HeC}$, the side peaks are also split into doublets by $^0J_{HeC}$. The ^{3}He@C_{60} HP & HH peaks are only split into doublets since the ^{3}He does not break the magnetic equivalence of the two adjacent ^{13}C's contributing to the side peaks. The $^0J_{HeC}$ coupling for the ^{3}He@C_{60} side peaks is shown as dashed red lines on the molecular structures in fig. 3.2 (b,c); the same is shown for ^{4}He@C_{60} in fig. 3.2 (e,f), but here $^0J_{HeC}$ is absent because ^{4}He has zero nuclear spin.

The splitting of the ^{3}He@C_{60} ^{13}C side peaks provide further evidence to the existence of the $^0J_{HeC}$ coupling, between the endohedral ^{3}He and a ^{13}C part of the enclosing surface, even in the absence of a chemical bond. Furthermore, fig. 3.2 (a) now shows that the ^{13}C solution NMR spectrum of ^{3}He@C_{60}, previously thought to contain a single peak, is actually made up of 6 peaks: 3 peaks (main ^{13}C, HP and HH) each split into a doublet by $^0J_{HeC}$.

3.4.1.2 $^0\mathrm{J}_{\mathrm{HeC}}$ temperature dependence

The magnitude of the $^0\mathrm{J}_{\mathrm{HeC}}$ coupling in ^{3}He@C$_{60}$ has been measured at a range of temperatures (262 K- 340 K) and the result is shown in fig. 3.3. This shows an increase of the $^0\mathrm{J}_{\mathrm{HeC}}$ coupling with temperature, well fitted by a linear equation: $|^0\mathrm{J}_{\mathrm{HeC}}| = mT + c$, with $c = 51.4 \pm 0.7\,\mathrm{mHz}$ and $m = (76.7 \pm 2.3) \times 10^{-3}$ mHz K^{-1}. An interpretation of this behaviour is given below in terms of the ^{3}He - ^{13}C distance, since a shorter distance is expected to give a larger magnitude of $^0\mathrm{J}_{\mathrm{HeC}}$ due to the increased overlap of the electron clouds.

Using a classical mechanics approach, one speaks about kinetic energies of the atoms involved. Increasing the temperature makes the average kinetic energy of the enclosed Helium atom to increase, making the Helium bounce more often and more strongly inside the C$_{60}$ cage. This means the Helium will penetrate more into the cage,[103] increasing the overlap of the electron clouds; which in turn will make the magnitude of $^0\mathrm{J}_{\mathrm{HeC}}$ increase.

A quantum mechanical approach involves the translational quantization of the enclosed Helium atom, see other endofullerene examples in literature[19,22,23,30] or chapter 6 which is dedicated to this. One can think of the confined He atom as a ″particle-in-a-box″ or more accurately as a quantum an-Harmonic oscillator with a symmetric potential (see chapter 6), yet both predict very similar wavefunctions.[42] The translational ground state is strongly localised at the centre of the box (C$_{60}$ cage), whereas the excited states have increasingly more probability amplitude towards the edge of the box (inner surface of the C$_{60}$ cage). As temperature is increased, the population of excited translational states increases. This will make the mean expectation value for the position of the Helium atom be closer to the edge of the box at elevated temperatures. Thus, this argument also predicts a shorter ^{3}He - ^{13}C distance on average as temperature is increased, which in turn would increase the magnitude of the $^0\mathrm{J}_{\mathrm{HeC}}$ coupling due to the increased overlap of the electron clouds.

To our knowledge only one other study presented temperature dependencies of ″non-bonded″ J-couplings, those mediated by hydrogen bonds in proteins. They have shown in general a decrease in magnitude of the J-couplings with increasing temperature;[104] opposite trend to $^0\mathrm{J}_{\mathrm{HeC}}$. This example serves to show the diverse behaviour of ″non-bonded″ J-couplings with temperature.

3.4.1.3 $^0\mathrm{J}_{\mathrm{HeC}}$ simulation by quantum chemistry

An attempt was made to simulate the observed $^0\mathrm{J}_{\mathrm{HeC}}$ coupling though quantum chemistry techniques.[105] The simulations were done by Jyrki Rantaharju from University of

Southamton, more details in reference 95. The calculations were done by treating the ^{13}C and ^{3}He nuclei as localised points, with no delocalisation.

Calculating the $^{3}He@C_{60}$ system by *ab initio* methods is computationally very demanding. Thus, test computations were done on the simpler system of a ^{3}He atom positioned on the six-fold symmetry axis of a C_6H_6 molecule,[106] see fig.3.11 for structure.

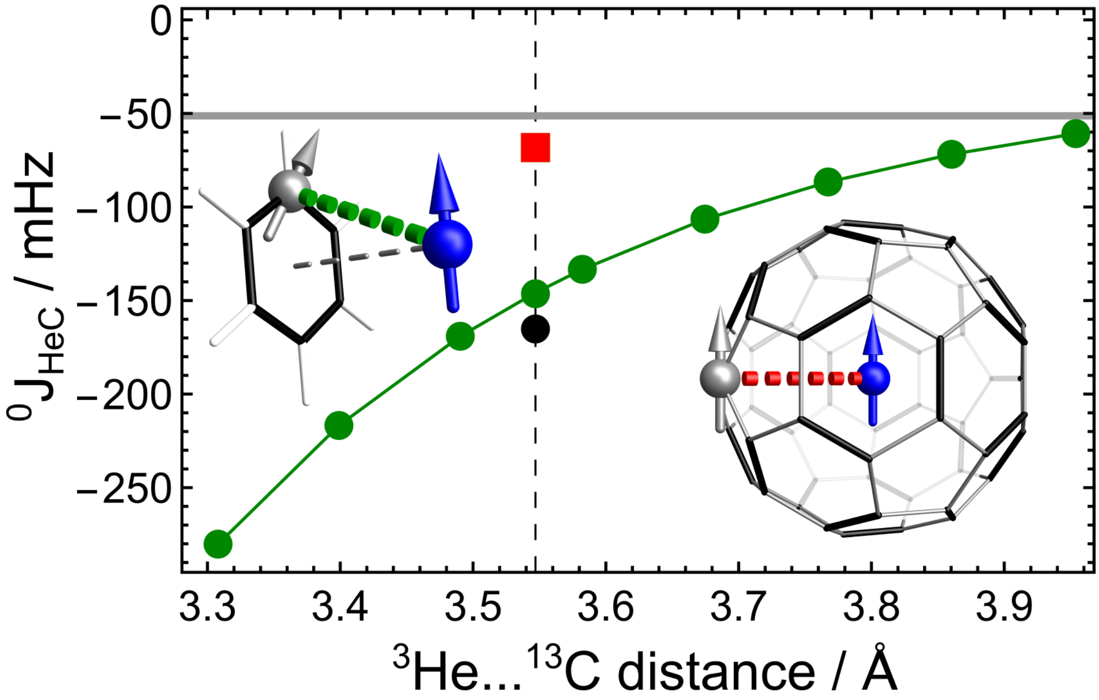

FIGURE 3.11: ^{3}He-^{13}C J-couplings calculated by quantum chemistry techniques. Green circles: Results of the *ab initio* CCSD calculations on the $^{3}He...C_6H_6$ model system. The solid green line is a guide for the eye. Black circle: DFT benchmark calculation of the $^{3}He...C_6H_6$ model system. Red square: DFT-calculated J-coupling of the $^{3}He@C_{60}$ endofullerene. The horizontal gray band shows the confidence limits of the zero-Kelvin intercept of the linear temperature-dependence of $|^{0}J_{HeC}|$, as shown in figure 3.3. The vertical dashed line shows the internuclear distance of 3.547Å between the ^{3}He and ^{13}C nuclei in $^{3}He@C_{60}$. Reprinted (adapted) with permission from (95). Copyright (2020) American Chemical Society.

Computations of the J-coupling were done at different positions of the ^{3}He nucleus away from the C_6H_6 ring and are shown as green circles in fig. 3.11. Each point was calculated using Coupled-Cluster (CC) theory at the CCSD level, using the ccJ-pVDZ basis.[107] The calculated J-coupling is predicted to be negative, with an increasing magnitude as the $^{3}He \ldots ^{13}C$ distance decreases. The trend is as expected since the overlap of the electron clouds would increase as the $^{3}He \ldots ^{13}C$ distance decreases.

The CCSD calculations done on the $^{3}He \ldots C_6H_6$ system were used to benchmark DFT-functionals with the pcJ-X (X=0-4) basis sets.[108] The DFT calculation of the $^{3}He \ldots C_6H_6$ system when using the PBE0 functional with 75% of exact exchange[109,110] were similar to the CCSD ones, as seen by the black circle in fig. 3.11.

Using the pcJ-3 basis and the functional which was benchmarked by the CCSD calculations of the ^{3}He ... C_6H_6 system, the $^0J_{HeC}$ coupling in ^{3}He@C$_{60}$ was simulated using DFT. This is shown in fig. 3.11 by the red square, where the $^0J_{HeC}$ is predicted to be negative and to = -68.3 mHz. This value is compared with the magnitude of the experimental $^0J_{HeC}$ coupling extrapolated at zero Kelvin, $|^0J_{HeC}|(0\,K) \simeq 51.4$ mHz, shown by the gray band in fig. 3.11. The simulated $^0J_{HeC}$ is in rather good agreement with the experimental result.

3.4.2 CH$_4$@C$_{60}$ discussion

Discussion below is dedicated to the broadening observed for the ^{13}C (C$_{60}$) peak of CH$_4$@C$_{60}$. The ^{13}C (CH$_4$) resonance of CH$_4$@C$_{60}$ was presented in section 3.3.2.1 for completion and are not discussed further.

Solution ^{13}C NMR spectra of CH$_4$@C$_{60}$ were shown in fig 3.8, in the region around the fullerene cage peaks. The ^{13}C measurements were done with and without ^{1}H waltz16 decoupling, fig 3.8 (b) and (a) respectively. For the ^{13}C{^{1}H} spectrum, the ^{1}H carrier frequency was set to the ^{1}H resonance of the CH$_4$@C$_{60}$ (at about -5.7 ppm[20]) and the protons were decoupled using waltz16 with a ^{1}H nutation frequency of 1.15 kHz.

In the ^{13}C spectrum (no ^{1}H decoupling) the ^{13}C (C$_{60}$) peak of CH$_4$@C$_{60}$ was considerably broader than the ^{13}C (C$_{60}$) peak of empty C$_{60}$, Lorentzian FWHM of 212.9 ± 0.6 mHz and 144.0 ± 0.3 mHz respectively. When ^{1}H decoupling was applied on the CH$_4$@C$_{60}$ protons, the ^{13}C (C$_{60}$) peak of CH$_4$@C$_{60}$ got narrower by 70.3 ± 0.8 mHz (33%), whereas the ^{13}C (C$_{60}$) peak of empty C$_{60}$ was not affected. This is best seen in fig 3.8 (c, d); all peak linewidths are tabulated in table 3.1.

The solution NMR result demonstrates how the ^{13}C (C$_{60}$) peak linewidth of CH$_4$@C$_{60}$ is appreciably narrowed down by decoupling the protons present on the endohedral CH$_4$ molecule. This suggests that an internuclear spin-spin $^0J_{HC}$-coupling exist in CH$_4$@C$_{60}$, between ^{1}H and a cage ^{13}C. As for the $^0J_{HeC}$-coupling there is no formal chemical bond between the endohedral CH$_4$ and the C$_{60}$ cage.

Unfortunately, there is no visible splitting in the ^{13}C spectrum of CH$_4$@C$_{60}$ to allow further verification and measurement of such $^0J_{HC}$-coupling. However, this can be explained by the short ^{1}H T_1 of CH$_4$@C$_{60}$; which was shown to be 1.465 ± 0.001 s in ODCB-d$_4$ at 298 K in fig. 3.9. Comparing it with the CH$_4$@C$_{60}$ ^{13}C (C$_{60}$) T_1 of 17.12 ± 0.05 s (fig. 3.10) and the ^{3}He@C$_{60}$ ^{3}He T_1 of ∼365 s (fig. 3.4), one sees at least an order of magnitude difference with the ^{1}H T_1 of CH$_4$@C$_{60}$. One would expect a $^0J_{HC}$ of similar magnitude to $^0J_{HeC}$ ($\sim$ 75 mHz), and $1/^0J_{HeC} \simeq 13.5$ s at room temperature. Thus, the fast spin-lattice relaxation of the CH$_4$@C$_{60}$ protons of 1.465 ± 0.001 s explains why the $^0J_{HC}$-coupling is not observable as a splitting in the ^{13}C spectrum of CH$_4$@C$_{60}$, as opposed to $^0J_{HeC}$ in ^{3}He@C$_{60}$. Nonetheless, there is a measurable effect of the protons in $CH_4@C_{60}$ on the enclosing cage ^{13}C peak, which can be understood in terms of a $^{0}J_{HC}$-coupling.

The broadening of the ^{13}C (C_{60}) peak of $CH_4@C_{60}$ could also be due to faster relaxation caused by the presence of CH_4 inside the cage. Since the 4 protons could give rise to ^{1}H-^{13}C dipolar relaxation. Faster spin lattice relaxation of the ^{13}C (C_{60}) of $CH_4@C_{60}$ as compared with empty C_{60} is actually observed in fig. 3.10. However, the difference is small: ^{13}C (C_{60}) T_1 of $CH_4@C_{60}$ is 17.12 ± 0.05 s and ^{13}C (C_{60}) T_1 of empty C_{60} is 17.64 ± 0.04 s. This small difference in the relaxation rates is not enough to explain the rather significant broadening seen in fig. 3.8 for the ^{13}C (C_{60}) peak of $CH_4@C_{60}$. Thus, the presence of a $^{0}J_{HC}$-coupling is postulated. The small difference in the spin lattice relaxation times indicates a relaxation mechanism is generated by the endohedral CH_4, probably ^{1}H-^{13}C dipolar relaxation with the carbon nuclei in the cage.

The ^{13}C spin lattice relaxation times for empty C_{60} were measured at the same time as for $^{3}He@C_{60}$ and $CH_4@C_{60}$, since they were present in the same solution due to the filling factors of $\sim$40% . However, the two empty C_{60} ^{13}C T_1 's obtained from fig. 3.5 and fig. 3.10 are rather different: 16.87 ± 0.04 s and 17.64 ± 0.04 s respectively. The difference is not large and it arises because two different samples were used, which were prepared separately. Concentrations were different, exact O_2 content could differ and the fullerene powders themselves might have had different amounts of impurities in them slightly affecting the T_1 measurements. Thus, one should quantitatively compare the relaxation parameters obtained from compounds within the same sample tube; empty and filled C_{60} cages, with ^{3}He and CH_4 separately.

A similar narrowing of the ^{13}C (C_{60}) peak is observed when decoupling the ^{1}H of the endohedral species for $H_2@C_{60}$ and $H_2O@C_{60}$. The FWHM difference was much less pronounced in these cases, being at the limit of detection, hence spectra are not shown. This is probably due to the number of ^{1}H's in the endohedral species available for the $^{0}J_{HC}$ interaction; CH_4 having double the number of protons, it is expected to generate a stronger effect in the spectrum. More investigation will be done on these systems to further understand ^{0}J-couplings in endofullerenes.

3.5 Conclusion

To conclude, this chapter was dedicated to the newly observed ^{0}J-couplings in C_{60} endofullerenes, between a ^{13}C within the cage and the endohedral moiety. The confinement seems to induce an overlap of the electron clouds between the endohedral species and the C_{60} cage, which is strong enough to lead to a detectable ^{0}J-coupling even when no chemical bonds connect the participating nuclei.

The ^{13}C solution NMR spectrum of ^{3}He@C$_{60}$ presents a small peak splitting into a 1:1 doublet, of 77.5 ± 0.2 mHz at 340 K. The HP & HH side peaks, described in chapter 2, of ^{3}He@C$_{60}$ show the same splitting as the main ^{13}C peak. This splitting is used as *direct* evidence for a J-coupling type of spin-spin interaction, in which there are *"zero"* formal chemical bonds between the participating nuclei. This leads to the notation ^{0}J$_{\mathrm{HeC}}$, where the superscript zero indicates the number of bonds between ^{3}He and ^{13}C. The ^{0}J$_{\mathrm{HeC}}$-coupling displays an increase in magnitude as temperature is increased. This is consistent with the ^{3}He nucleus coming closer to ^{13}C on average at elevated temperatures, which can be understood from a quantum *"particle-in-a-box"* or classical mechanics perspective. Quantum chemistry DFT calculations predict a negative ^{0}J$_{\mathrm{HeC}}$, with a magnitude close to the experimental ^{0}J$_{\mathrm{HeC}}$ extrapolated at 0 K.

This is, to our knowledge, the first *direct* experimental evidence for a J-coupling of the ^{3}He nucleus. The simple confinement of nuclear spins to a region of space is enough to induce such ^{0}J-couplings across molecular surfaces. Since the coupling strength is really small, directly observing the splitting is only possible if the NMR relaxation times are long enough; in order to allow high spectra resolution and to ensure the interaction lives long enough to be observable. This applies to ^{3}He@C$_{60}$ for both ^{3}He and ^{13}C, which have long spin lattice relaxation times of tens of seconds.

A similar type of ^{0}J-coupling is observed between ^{1}H and a ^{13}C (C$_{60}$) in the cage of CH$_4$@C$_{60}$. Unfortunately, the ^{1}H spin lattice relaxation time is short ($\sim$1.5 s), so direct observation of the ^{0}J$_{\mathrm{HC}}$ splitting was not possible. However, ^{0}J$_{\mathrm{HC}}$ leads to a significant broadening of the ^{13}C (C$_{60}$) peak of CH$_4$@C$_{60}$, as compared with empty C$_{60}$. This is not due to faster relaxation of the ^{13}C spin in the cage induced by the endohedral CH$_4$ (e.g. ^{1}H $-$ ^{13}C dipolar relaxation), since there is too little difference between the ^{13}C (C$_{60}$) T_1 's of empty C$_{60}$ cages and cages filled with CH$_4$. The broadening was shown to disappear when applying ^{1}H decoupling. For CH$_4$@C$_{60}$ all is consistent with a ^{0}J$_{\mathrm{HC}}$-coupling between endohedral ^{1}H and a ^{13}C within the enclosing C$_{60}$ cage.

Such ^{0}J-couplings across molecular surfaces might help investigating mechanically interlocked molecules.[99] ^{0}J-couplings also might enable the transfer of hyperpolarization from optically-pumped noble gases, as in biosensor applications.[111]

Further work is under way to estimate the sign and accurate magnitude of the ^{0}J$_{\mathrm{HeC}}$ coupling using double-resonance techniques, and to detect similar internuclear couplings in other spatially confined systems, such as molecular endofullerenes.[16,18–20]

3.5.1 Future work

A new solution state NMR probe was ordered from Bruker, capable of doing ^{3}He NMR experiments. This will enable a more accurate measurement of the ^{0}J$_{\mathrm{HeC}}$-coupling, though double resonance ^{3}He-^{13}C NMR experiments.[112] Experiments have also been planned to use cross-correlated relaxation effects to experimentally determine the sign of ${}^{0}J_{HeC}$.[101]

Further measurements are planned to gain a better understanding of the ${}^{0}J_{HC}$-coupling in molecular endofullerenes: $CH_4@C_{60}$, $H_2@C_{60}$, $H_2O@C_{60}$ etc.

Chapter 4

Inelastic neutron scattering on noble gas C_{60} endofullerenes

4.1 Introduction

Inelastic Neutron Scattering (INS) makes use of the energy lost or gained by a scattered neutron, in order to obtain spectroscopic information. This produces an INS spectrum, which is similar to the electromagnetic spectroscopic techniques (IR, Raman, etc.) where one uses light rather than neutrons.

INS has been used to study molecular endofullerenes such as $H_2@C_{60}$, $H_2O@C_{60}$, $HF@C_{60}$, and isotopomers.[19,23–30] Confining the small molecules in fullerene cages slightly changes the ro-vibrational properties, yet they are essentially free rotors even at cryogenic conditions.[19,22–33] Besides the perturbation of the ro-vibrational states, translational quantization was observed for the endohedral molecule, caused by the confinement. This amounts to rotational levels being split into multiple states due to the Translational-Rotational (TR) coupling.[22–27] Furthermore, pure translational transitions have been observed for the endohedral molecules, in which the translational quantum number changes but the rotational quantum number does not.[19,22–33] Making the same observations for noble gas endofullerenes is the aim of this chapter.

There are almost no selection rules for INS, so in principle any transitions can be observed. This is very useful at the lowest temperatures, since only the ground state is populated and all transitions originate from it. This can give an overview of the whole landscape of energy levels. The INS experiments were done at the Institut Laue-Langevin (ILL) in Grenoble France, which has a nuclear reactor as a neutron source.

The noble gas endofullerenes $^3He@C_{60}$, $^4He@C_{60}$ and $Ne@C_{60}$ were measured using inelastic neutron scattering. These experiments were performed on the solid pure samples at cryogenic temperatures. The confinement gives rise to peaks specific for the noble gas atom in the INS spectra. The INS transitions correspond to the confined Helium atom, since the energy of the observed peaks are rather strongly dependent on the mass of the He isotope.

The INS instruments used in this study probe relatively low energies, 0-200 meV, which correspond to lattice phonon modes and molecular vibrations. We are interested in the dynamics of the Helium and Neon atoms inside the C_{60} cage, and the corresponding energies are in this energy range, as discussed below.

The INS instruments used are IN4c and IN1 LAGRANGE, both located at the ILL. IN4c is a time of flight (TOF) type spectrometer, which uses the time when neutrons arrive at the detectors to generate an INS spectrum. IN4c uses a single incident neutron energy, from which energy is lost or gained, and the scattered neutrons of different energies are detected in a TOF fashion. IN1 LAGRANGE uses multiple incident neutron energies (Ei) and detects scattered neutrons of a single energy (4.5 meV). By scanning the energy of the incident beam and only detecting 4.5 meV neutrons, the INS spectrum of the difference $Ei - 4.5$ meV is generated. An advantage of IN4c is that the INS spectrum is generated all at once, whereas for IN1 LAGRANGE each data point has to be measured separately.

There were two sets of INS measurements: (1) on IN4c and (2) on IN1 LAGRANGE. The first set of measurements was made on IN4c, where the sample preparation was not ideal and the second set was made on IN1 LAGRANGE, where sample preparation was improved.

4.2 INS measurements of He@C_{60} using IN4c

All INS experiments in this section were performed at the ILL (Institut Laue-Langevin) in Grenoble France, on the IN4c instrument together with the instrument chief Stéphane Rolls and Anthony Horsewill from University of Nottingham. The ILL proposal number is 7-04-156 with doi:10.5291/ILL-DATA.7-04-156.

The data presented here represent our first attempts to perform INS measurements on the Helium C_{60} endofullerenes. As shown below, much of the data is of rather poor quality, in part due to instrumental problems, and in part because of interference from contamination of the sample with traces of the water C_{60} endofullerene $H_2O@C_{60}$, incorporated as a by-product of the sample synthesis.

4.2.1 Experimental

The IN4c is a time of flight type of spectrometer working in a pulsed fashion, fig. 4.1 shows a diagram of the IN4c detector at the ILL.

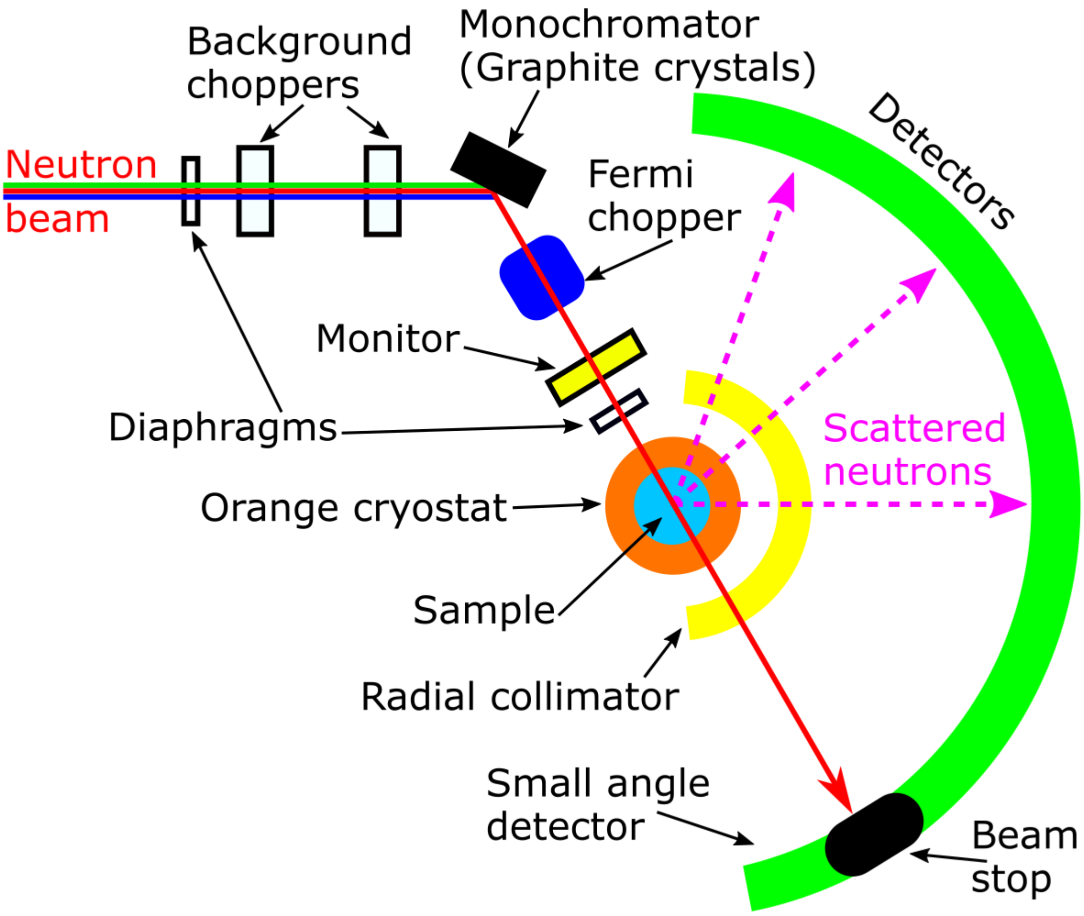

FIGURE 4.1: Diagram of the time-of-flight (TOF) neutron scattering spectrometer IN4c at the ILL. Description of how it works found in text.

The diaphragms act as a beam stop which can be turned on or off, the background choppers chop a continuous beam of neutrons into broad pulses in the time domain. The monochromator then (Bragg) diffracts neutrons of the desired wavelength towards the Fermi chopper which makes the pulse of neutrons very narrow in the time domain. The monitor is an ”inefficient detector” to give an estimate for the total number of neutrons in the pulsed beam. The beam enters the orange cryostat which keeps the sample at a constant temperature using liquid helium and then is scattered radially from the sample point to be detected by the circular (^{3}He) detectors as shown, the radial collimator ensures that no double scattered neutrons reach the detectors. The green circular detectors give the angle at which the neutrons scatter and, implicitly, the momentum transfer(Q). Because IN4c is a time of flight spectrometer, the time at which the neutrons arrive is recorded to give a 3D plot with time and angle (Q) on the X and Y axes and neutron count on the Z axis. By integrating over all angles, a plot of neutron count against time is obtained and by transforming the time axis into energy transfer, with respect to the elastically scattered beam, the inelastic neutron scattering spectrum is obtained.

4.2.1.1 Sample preparation

Both $^3He@C_{60}$ and $^4He@C_{60}$ were synthesised by the group of Prof. R. Whitby through "molecular surgery".[96] The solid $He@C_{60}$ powder is the same as the one used in the NMR experimental, section 4.2.3.1.

224 mg of $^3He@C_{60}$ (4.4% filling factor) was transferred to a thin rectangular (∼ 1cm x 1cm) aluminium foil cell and then put in the orange cryostat for measuring.

175 mg of $^4He@C_{60}$ (26.1% filling factor) was transferred to a thin rectangular (∼ 1cm x 1cm) aluminium foil cell and then put in the orange cryostat for measuring.

The same procedure was done for 739 mg of empty C_{60}.

As discussed below, the $He@C_{60}$ samples contained traces of $H_2O@C_{60}$: 0.2% for $^3He@C_{60}$ and 0.1% for $^4He@C_{60}$. The traces were generated as a by-product of the endofullerene synthesis. The $H_2O@C_{60}$ impurity caused additional features in the INS spectra, which complicated the analysis.

4.2.1.2 Data processing

The baseline subtraction was performed using LAMP, a dedicated software for neutron scattering at the ILL and it was carried out in the following way: first an empty cell (Ecell) made of aluminium foil was subtracted from both $He@C_{60}$ and C_{60}, then the new C_{60} spectrum was scaled (due to sample mass differences) by a factor a and subtracted from the new $He@C_{60}$ ($He@C_{60}$ - empty aluminium cell). The scaling factor was chosen based on best resulting pure $He@C_{60}$ spectrum. Example of notation for a scaling factor "a" for the 2.2 Å $^3He@C_{60}$ spectrum: Incident neutron wavelength 2.2 Å, 1.6 K, (($He@C_{60}$ - Ecell) - $a*$(C_{60}- Ecell)). The scaling factor helps in generating the best spectrum, because some features scale up or down with the scaling factor applied to the C_{60}. The peaks shown in this section were quite invariant to the scaling factor so we are confident they are real and not random noise.

4.2.2 Results

For the INS spectra, 3 different wavelengths were chosen for the incident neutron to see different regions of the energy transfer spectra, the wavelengths were: 1.6 Å, 2.2 Å and 3.2 Å. The faster neutrons (smaller wavelength) give a broader range for the energy transfer (up to about 26 meV), however the resolution gets worse because the interval between data points gets larger. Unfortunately, the ball bearings of the background choppers on IN4 crashed when we were acquiring the empty cell background for 1.6 Å and 3.2 Å so the background subtraction for these wavelengths was faulty.

3.2 Å empty cell measurement was completely unusable; 1.6 Å was acceptable in the lower energy part of the spectrum but quite poor in the high energy transfer regime. However, it seemed to work rather well for ^{4}He@C$_{60}$ even in the high energy part but not for ^{3}He@C$_{60}$ (due to neutron absorption by the ^{3}He nucleus). Thus, for 1.6 Å the focus should be in the lower energy regime up to about 20 meV.

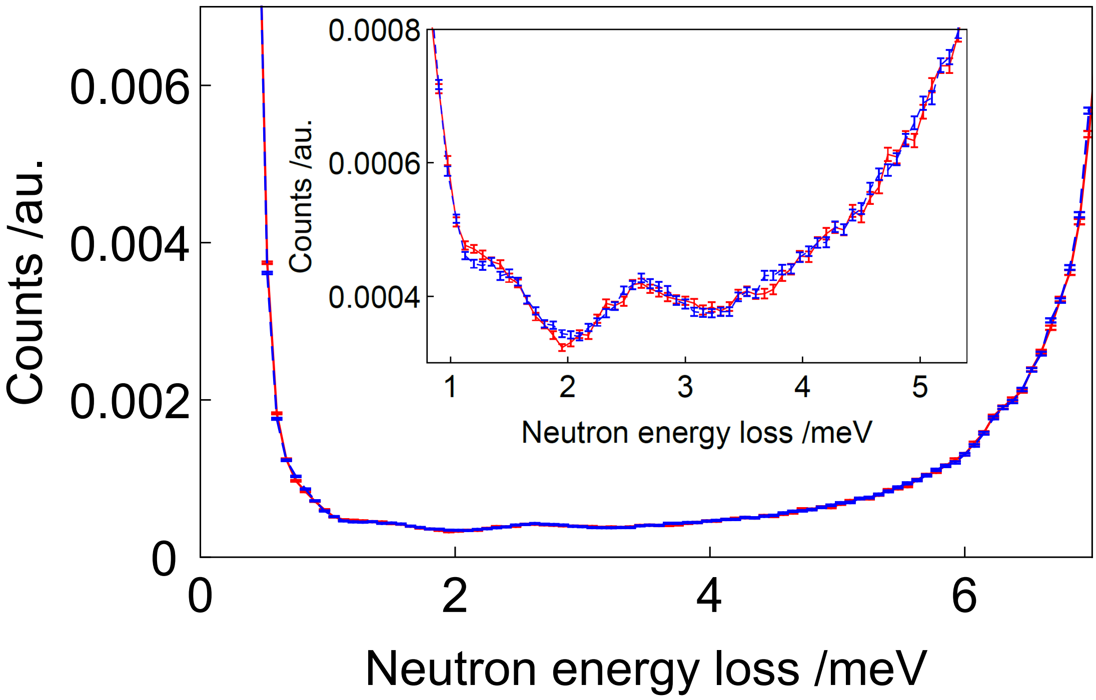

FIGURE 4.2: Raw INS spectra of ^{3}He@C$_{60}$ (red) and ^{4}He@C$_{60}$ (blue dashed), with no subtraction of the C$_{60}$ or empty cell. Incident neutron wavelength 3.2 Å at 1.6 K acquiring for 16 h ^{3}He@C$_{60}$ and 22 h ^{4}He@C$_{60}$. ^{4}He@C$_{60}$ spectrum was scaled by 1.1 to reach the same intensity level as ^{3}He@C$_{60}$ (due to sample mass differences). The insert is the scaled up version of the main spectra showing the similarity of the ^{3}He@C$_{60}$ and ^{4}He@C$_{60}$ spectra.

The 3.2 Å wavelength measurements make visible the low energy part of the spectrum, ~0-7 meV. Because a good background subtraction was not possible, the pure ^{3}He@C$_{60}$ and ^{4}He@C$_{60}$ INS spectra are shown in fig. 4.2, where it can be seen that there is almost no difference between the two spectra. The 3.2 Å measurements conclude that there are no peaks from either ^{3}He@C$_{60}$ or ^{4}He@C$_{60}$ in this energy range (0-7 meV).

4.2.2.1 ^{3}He@C$_{60}$ results

Fig. 4.3 contains the INS spectrum of ^{3}He@C$_{60}$ recorded with a wavelength for the incident neutron of 2.2 Å at 1.6 K acquiring for 41 h. There are a number of peaks in the spectrum, most of which could not be assigned to ^{3}He@C$_{60}$. At this point the presence of H$_2$O@C$_{60}$ traces in the sample was postulated, which was later on verified by NMR measurements.

The peak at 3.3 meV has a stable shape but its intensity is very sensitive to the background subtraction (specifically sensitive to the scaling factor given to empty C_{60} before subtracting from He@C60) so its intensity and width should not be taken seriously, only the peak position should be considered. The rest of the peaks in the spectrum seem to be invariant to the scaling factor of empty C_{60}, except the higher energy part which is quite unusable in all cases due to some malfunctioning detectors and in this case due to the absorption by the ^{3}He nucleus.

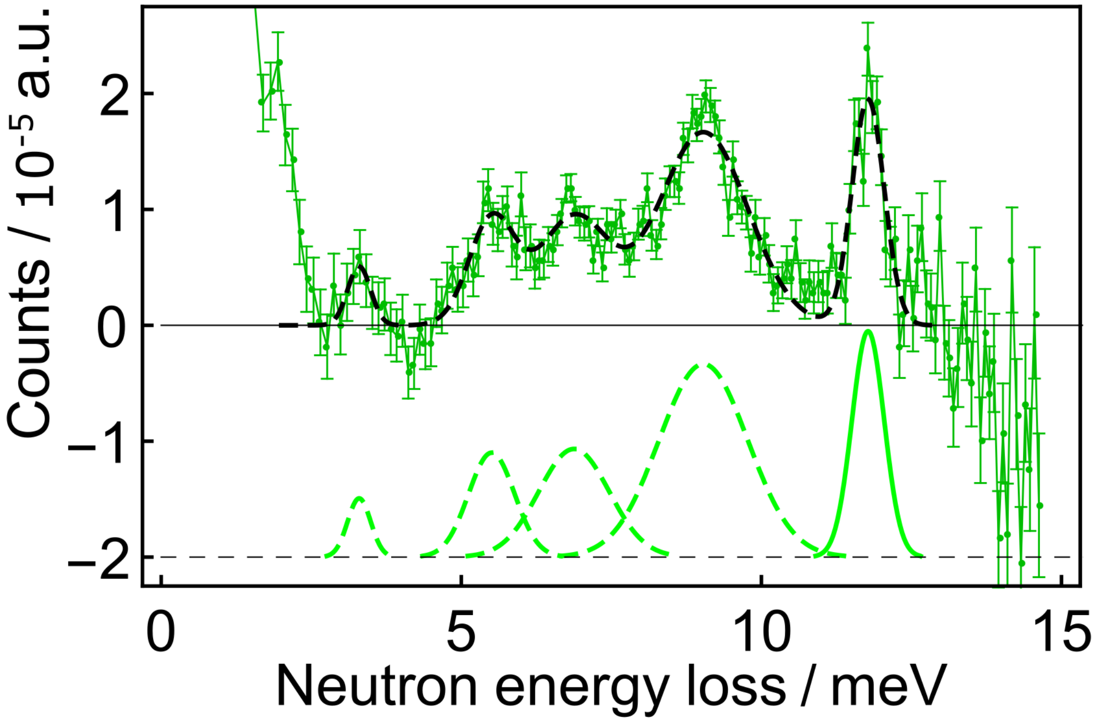

FIGURE 4.3: Relevant INS spectrum of $^3He@C_{60}$, scattered intensity against neutron energy loss. Incident neutron wavelength 2.2 Å at 1.6 K acquiring for 41 h, ((He@C_{60} - Ecell) - 1*(C_{60}- Ecell)). Fitted with 5 gaussian peaks: green dashed peaks come from $H_2O@C_{60}$ and the green solid peak comes from $^3He@C_{60}$. The black dashed line is the sum of the gaussian peaks. Fitting parameters found in table 4.1.

The spectrum was fitted with 5 Gaussian peaks, 4 of them come from $H_2O@C_{60}$ (green dashed peaks) and one comes from the $^3He@C_{60}$ at 11.77 meV (green solid peak), parameters for the fit are found in table 4.1.

The $H_2O@C_{60}$ peak at 9.03 ± 0.03 meV can be seen from fig. 4.3 that the experimental data points have the peak slightly shifted to a higher energy, which would probably match well with the 9.20 ± 0.05 meV value from ref.[29] The fits from our measurements are not within experimental error with the values from ref.[29] but in our case the $H_2O@C_{60}$ filling is 0.2% whereas in ref.[29] the $H_2O@C_{60}$ filling is about 90%. The C_{60} cages filled with H_2O are expected to be different than empty C_{60} and to display different lattice dynamics, since the geometry of the cages is slightly different. Changes in the lattice is expected to affect the energies of the transitions for endohedral H_2O,

TABLE 4.1: ^{3}He@C$_{60}$ INS 2.2 Å fitting parameters for the 5 gaussian peaks from fig. 4.3.

Species	Energy transfer /meV	Energy transfer / meV (ref.[29])	FWHM / meV
$H_2O@C_{60}$	3.3 ± 0.07	3.02 ± 0.05	0.45 ± 0.17
	5.5 ± 0.06	5.68 ± 0.05	0.9 ± 0.13
	6.88 ± 0.06	6.51 ± 0.05	1.38 ± 0.2
	9.03 ± 0.03	9.20 ± 0.05	1.74 ± 0.08
$^3He@C_{60}$	11.77 ± 0.02		0.63 ± 0.04

depending if the nearest neighbours of a H$_2$@C$_{60}$ cage are C$_{60}$ or H$_2$O@C$_{60}$, which depends on the filling factor.

The same experiment was repeated using a neutron wavelength of 1.6 Å in order to explore the higher energy transfer regions of the spectrum, see fig. 4.4; temperature was 1.6 K and acquisition time 8 h. The figure has the 2.2 Å spectrum underneath it to confirm the peaks seen around 10 meV, and fitted gaussian peaks are shown, with parameters in table 4.2.

TABLE 4.2: ^{3}He@C$_{60}$ INS 1.6 Å fitting parameters for the 2 gaussian peaks from fig. 4.4.

Species	Energy transfer / meV	Energy transfer / meV (ref.[29])	FWHM /meV
$H_2O@C_{60}$	8.7 ± 0.14	9.20 ± 0.05	1.3 ± 0.19
$^3He@C_{60}$	11.8 ± 0.08		0.7 ± 0.08

On the figure there is another very broad feature centred around 20 meV but no obvious structure can be seen here and a fit with gaussian peaks was unsuccessful, we expect this feature to arise from a combination of H$_2$O@C$_{60}$ and ^{3}He@C$_{60}$ peaks. The broadness comes from overlap with other H$_2$O@C$_{60}$ peaks in this region and the very small ratio of it in the sample buries the peaks under the noise. The big drop in intensity after 25 meV occurs because of the fault in the empty cell measurement when the background choppers crashed which made the background subtraction problematic. The absorption of ^{3}He is expected to affect the background subtraction as well.

4.2.2.2 ^{4}He@C$_{60}$ results

The INS spectrum was measured for ^{4}He@C$_{60}$ on the IN4c instrument at the ILL, using incident neutrons of 2.2 Å, at 1.6 K and acquiring for 40 h. The spectrum is shown in fig. 4.5, where the empty cell and C$_{60}$ contributions were subtracted, ((^{4}He@C$_{60}$ - Ecell) - 1.3*(C$_{60}$- Ecell)).

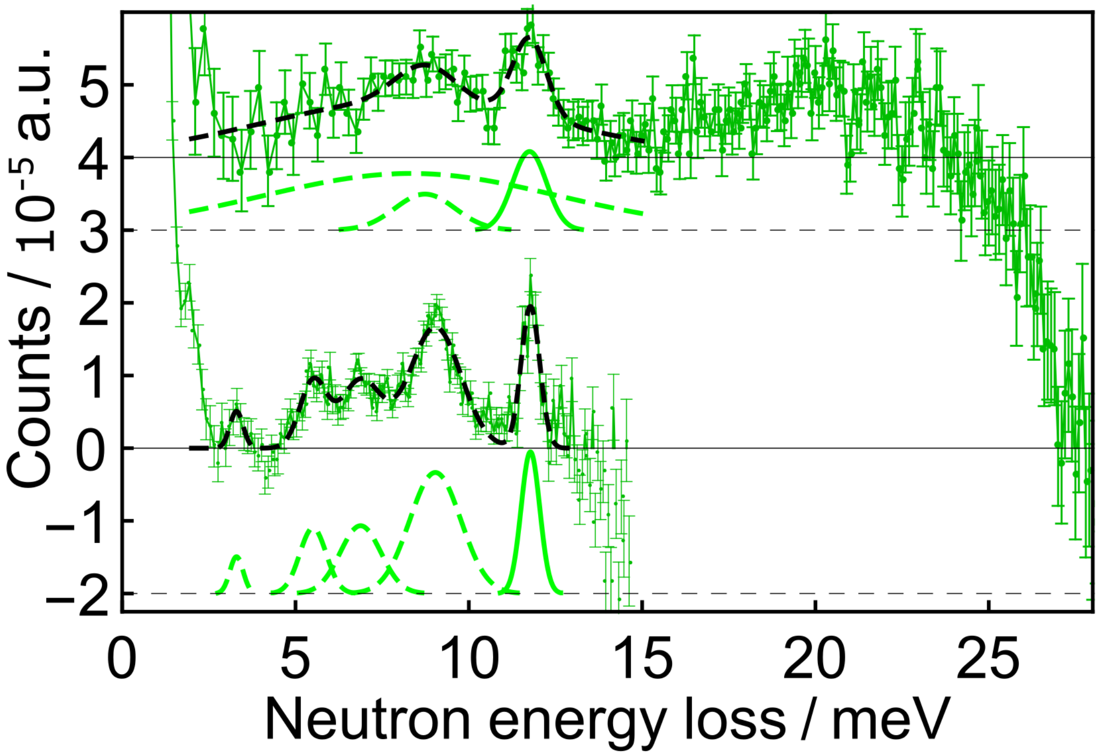

FIGURE 4.4: Relevant INS spectra of $^3He@C_{60}$, scattered intensity against neutron energy loss. Top spectrum: Incident neutron wavelength 1.6 Å at 1.6 K acquiring for 8 h, (($^3He@C_{60}$ - Ecell) - 0.97*(C_{60}- Ecell)). Bottom spectrum: Incident neutron wavelength 2.2 Å at 1.6 K acquiring for 41 h, (($^3He@C_{60}$ - Ecell) - 1*(C_{60}- Ecell)), from fig 4.3. The black dashed lines are the sum of the fitted gaussian peaks underneath. Green dashed curves are fits for $H_2O@C_{60}$ and green solid are for $^3He@C_{60}$. Fitting parameters for the 1.6 Å spectrum are found in table 4.2. Straight horizontal lines represents the zero line for the respective spectrum.

Only the region with the most intense peaks was possible to be fitted with 2 gaussian peaks, one for $H_2O@C_{60}$ (blue dashed line) and one for $^3He@C_{60}$ (blue solid line), see fig. 4.5. A straight line was fitted for the region around the peaks to account for the raised and tilted baseline with a line equation of : $0.00003244 - 1.926 * 10^-6x$. Fitting parameters for the gaussian peaks are found in table 4.3.

TABLE 4.3: $^4He@C_{60}$ INS 2.2 Å fitting parameters for the 2 gaussian peaks from fig. 4.5.

Species	Energy transfer / meV	Energy transfer / meV (ref[29])	FWHM / meV
$H_2O@C_{60}$	8.94 ± 0.05	9.20 ± 0.05	0.68 ± 0.11
$^4He@C_{60}$	9.85 ± 0.02		0.71 ± 0.05

The same experiment was repeated using a neutron wavelength of 1.6 Å in order to explore the higher energy transfer regions of the spectrum, see fig. 4.6, temperature was 1.6 K and acquisition time 8 h.

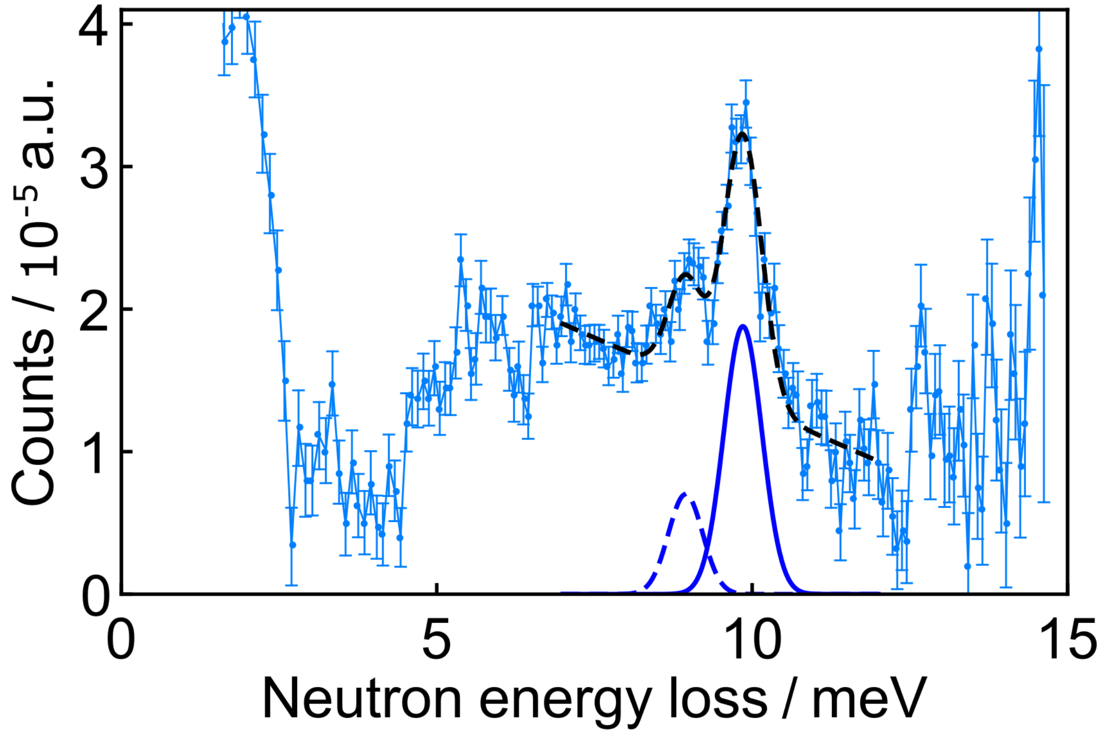

FIGURE 4.5: Relevant INS spectrum of ^{4}He@C_{60}, scattered intensity against neutron energy loss. Incident neutron wavelength 2.2 Å at 1.6 K acquiring for 40 h, ((^{4}He@C_{60} - Ecell) - 1.3*(C_{60}- Ecell)). Fitted with 2 gaussian peaks: blue dashed peak comes from H_2O@C_{60} and the blue solid peak comes from ^{4}He@C_{60}. The black dashed line is the sum of the gaussian peaks. Fitting parameters found in table 4.3.

Fig. 4.6 has the 1.6 Å neutrons spectrum at the top with the 2.2 Å spectrum underneath it to confirm the peaks seen around 10 meV. The fairly broad feature seen at 10 meV with 1.6 Å neutrons matched very well with the 10 meV peak seen with 2.2 Å neutrons. Unfortunately, due to the low signal to noise ratio the peak from the 1.6 Å spectrum could not be fitted. On the figure there is another very broad feature centred around 20 meV but no obvious structure can be seen here and a fit with gaussian peaks was unsuccessful. The broadness comes from overlap with other H_2O@C_{60} peaks in this region and the very small ratio of it in the sample buries the peaks in the noise.

4.2.3 Discussion

4.2.3.1 Quantification of the H_2O@C_{60} impurity by ^{13}C NMR

In the INS spectra of both ^{3}He@C_{60} and ^{4}He@C_{60} some extra peaks were observed. They were around the energies for H_2O@C_{60} known from previous INS studies.[29] In order to check the H_2O@C_{60} content in the samples, solution state ^{13}C NMR was done on the ^{3}He@C_{60} and ^{4}He@C_{60} samples, used in the INS measurements.

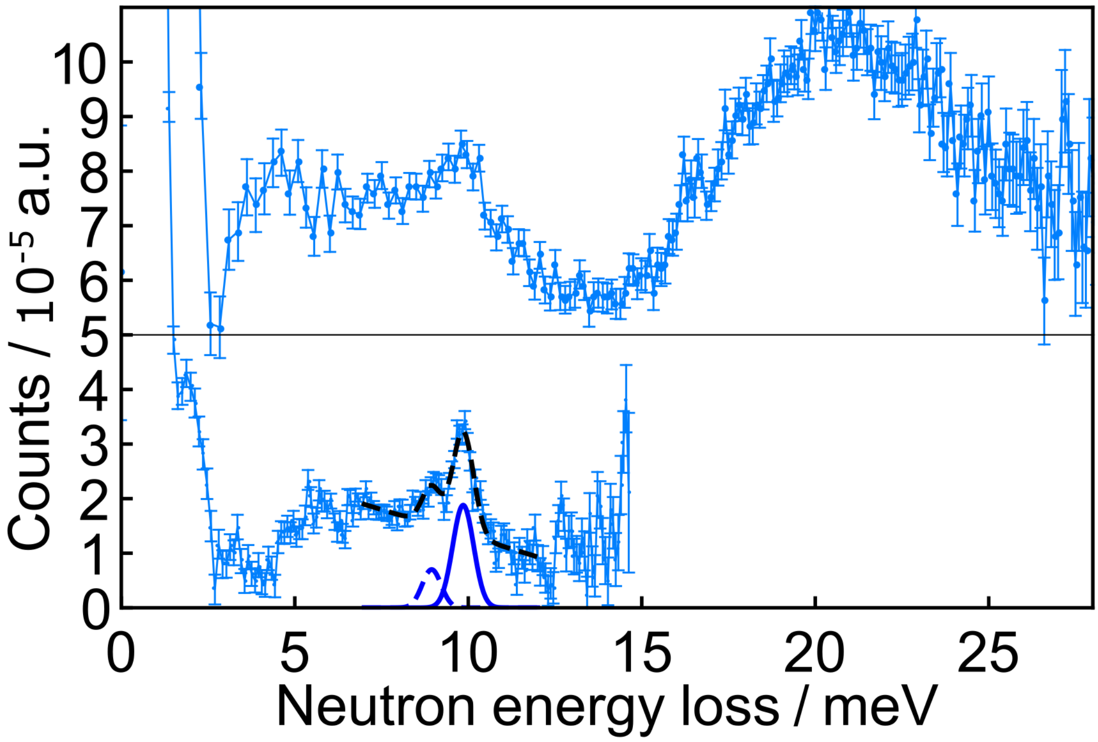

FIGURE 4.6: Relevant INS spectra of $^4He@C_{60}$, scattered intensity against neutron energy loss. Top spectrum: Incident neutron wavelength 1.6 Å at 1.6 K acquiring for 8 h, (($^4He@C_{60}$ - Ecell) - 1.15*(C_{60}- Ecell)). Bottom spectrum: Incident neutron wavelength 2.2 Å at 1.6 K acquiring for 40 h, (($^4He@C_{60}$ - Ecell) - 1.3*(C_{60}- Ecell)), from fig 4.5. The black dashed line is the sum of the gaussian peaks underneath. Straight horizontal lines represents the zero line for the respective spectrum. $H_2O@C_{60}$ peaks are blue dashed and $^4He@C_{60}$ peaks are blue solid.

Sample preparation For the $^3He@C_{60}$ solution state sample 18.4 mg of $^3He@C_{60}$ powder was dissolved in 0.86 mL of o-DCB-*d*4 to give a 29.67 mM solution. The sample was then degassed by bubbling N_2 through the sample for 5 mins.

For the $^4He@C_{60}$ liquid state sample 16.6 mg of $^4He@C_{60}$ powder was dissolved in 0.775 mL of ODCB-d_4 to give a 29.7 mM solution. The sample was then degassed by bubbling N_2 through the sample for 6 mins

$^3He@C_{60}$, ^{13}C NMR results

The ^{13}C NMR spectrum of $^3He@C_{60}$ around the C_{60} peak is shown in fig. 4.7. The smaller downfield peak is the ^{13}C peak of a C_{60} cage which has ^{3}He enclosed inside and the other one comes from empty C_{60}. At 142.93 ppm another small peak can be seen for $H_2O@C_{60}$. The ^{13}C chemical shifts and filling percentages are given in table 4.4.

Besides the main ^{13}C peaks of C_{60}, $^3He@C_{60}$ and $H_2O@C_{60}$, some small side peaks are observed in the NMR spectrum in fig. 4.7, annotated by blue and red arrows. These are due to $^{13}C_2$ isotopomers of C_{60} and $^3He@C_{60}$, see chapter 2 for more details. Figure 4.7 is one of the spectra where the C_{60} fullerene side peaks were first observed.

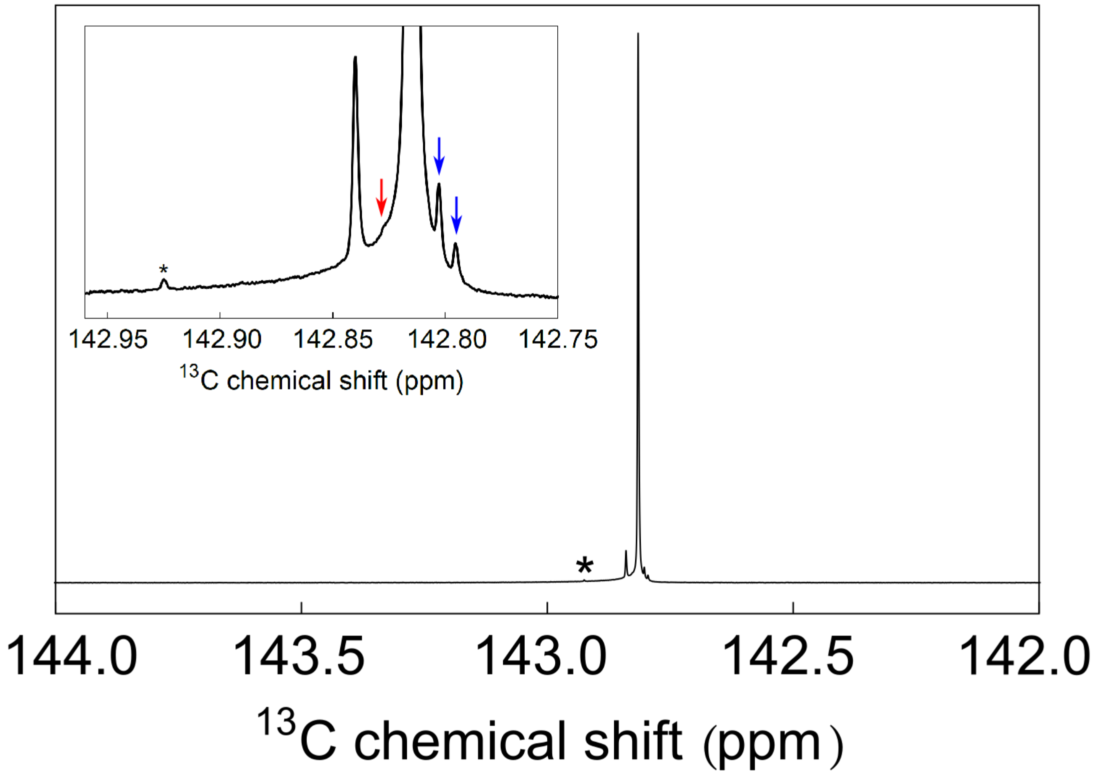

FIGURE 4.7: Relevant part of the experimental ^{13}C NMR spectrum of 29.67 mM ^{3}He@C_{60} (4.4% filling factor) dissolved in 4 solvent acquired at 16.45 T (^{13}C nuclear Larmor frequency = 176 MHz) and 21.85°C with 2560 transients. The spectrum was processed using Lorentzian line broadening (full width at half maximum = 0.1 Hz). The main peak is empty C_{60} and on the left is the ^{3}He@C_{60} one. The insert is a zoomed version of the shown spectrum and the asterisk marks the H_2O@C_{60} peak. The arrows mark the HP & HH side peaks, blue for C_{60} and red for ^{3}He@C_{60} (see chapter 2).

TABLE 4.4: ^{3}He@C_{60} sample ^{13}C chemical shifts and filling percentage, from fig. 4.7.

Species	chemical shift /ppm	ratio
H_2O@C_{60}	142.93	0.2 %
^{3}He@C_{60}	142.84	4.4 %
C_{60}	142.82	95.4 %

^{4}He@C_{60}, ^{13}C NMR Results

The ^{13}C NMR spectrum of ^{4}He@C_{60} around the C_{60} peak is shown in fig. 4.8, the smaller downfield peak is the ^{13}C peak of a C_{60} cage which has ^{4}He enclosed inside and the other one comes from empty C_{60}. At 142.93 ppm another small peak can be seen for H_2O@C_{60}. The ^{13}C chemical shifts and filling percentages are given in table 4.5.

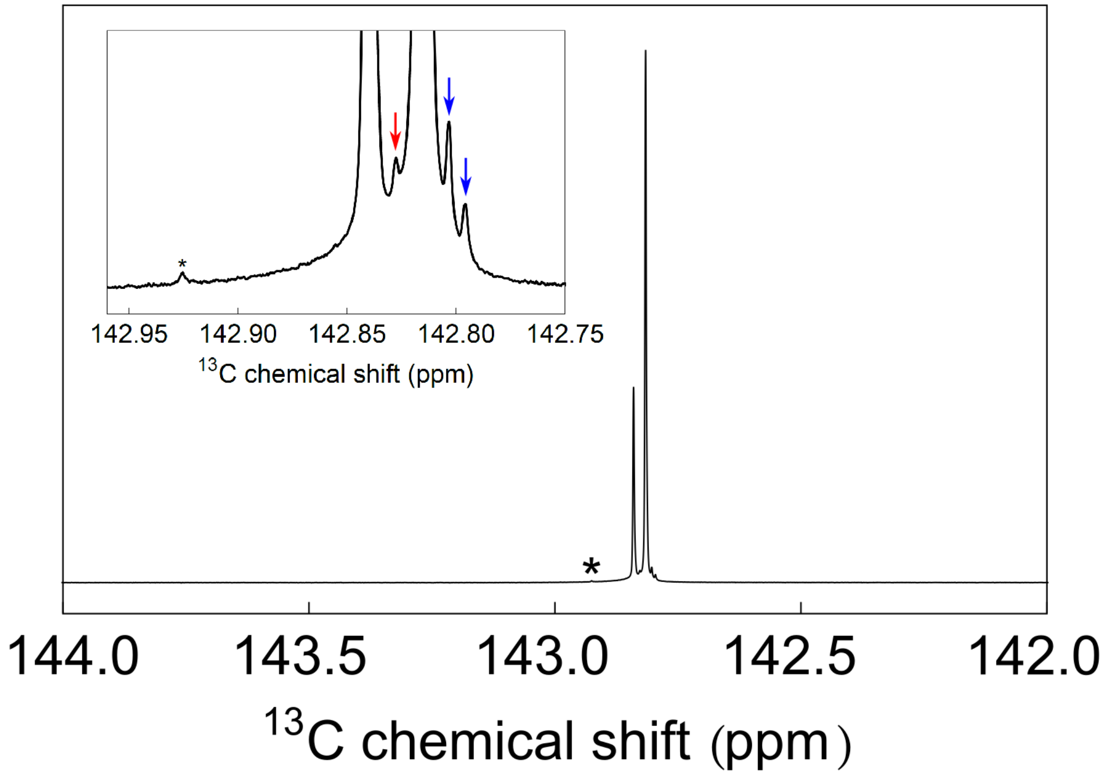

FIGURE 4.8: Relevant part of the experimental ^{13}C NMR spectrum of 29.7 mM $^{4}He@C_{60}$ (26.1% filling factor) dissolved in 4 solvent acquired at 16.45 T (^{13}C nuclear Larmor frequency = 176 MHz) and 21.85°C with 2048 transients. The spectrum was processed using Lorentzian line broadening (full width at half maximum = 0.1 Hz). The main peak is empty C_{60} and on the left is the $^{4}He@\underline{C}_{60}$ one. The insert is a zoomed version of the shown spectrum and the asterisk marks the $H_2O@C_{60}$ peak. The arrows mark the HP & HH side peaks, blue for C_{60} and red for $^{4}He@C_{60}$ (see chapter 2).

TABLE 4.5: $^{4}He@C_{60}$ sample ^{13}C chemical shifts and filling percentage, from fig. 4.8.

Species	chemical shift /ppm	ratio
$H_2O@C_{60}$	142.93	0.1 %
$^{3}He@C_{60}$	142.84	26.1 %
C_{60}	142.82	73.8 %

$H_2O@C_{60}$ neutron scattering quantification

This section aims to prove that most of the peaks observed in the INS spectra actually arise from small traces of $H_2O@C_{60}$ leftover from the synthesis of $^{3}He@C_{60}$ and $^{4}He@C_{60}$. Even small traces of hydrogen containing compounds are undesirable for INS measurements, since the neutron scattering cross section for ^{1}H is one of the largest amongst all elements in the periodic table.[41]

We used neutrons of wavelengths 3.2-1.6 Å which translates into energy 8-32 meV. In ref. 113 the H_2O total neutron cross-section starts to level off at temperatures under 0°C, at any neutron energies. For neutron energies of 32 meV and 2.7 meV the total scattering cross sections are around 100 barn and 175 barn (at temperatures between -100 to 0°C). For 32 meV neutron energies, the scattering stays rather constant with temperature and for 2.7 meV the total scattering cross section does not go beyond 220 barn (this maximum reached at 100°C).

From ref. 41 the total scattering cross sections for "thermal" neutrons (10-100 meV) are: $\sigma_{^1\mathrm{H}} = 81.7$ barn, $\sigma_{^3\mathrm{He}} = 5.6$ barn, $\sigma_{^4\mathrm{He}} = 1.2$ barn and $\sigma_{^{16}\mathrm{O}} = 4.2$ barn. With those values the total scattering cross section for H$_2$O would be $\sigma_{\mathrm{H_2O}} = 167.6$ barn, which is close to the values from ref. 113 above. With these values in mind and the relative ratios of ^{3}He@C$_{60}$:H$_2$O@C$_{60}$ and ^{4}He@C$_{60}$:H$_2$O@C$_{60}$ above, the following ratios of scattering power were obtained:

$$\frac{\sigma_{^3\mathrm{He}} \cdot \mathrm{ratio}_{^3\mathrm{He}}}{\sigma_{\mathrm{H_2O}} \cdot \mathrm{ratio}_{\mathrm{H_2O}}} = \frac{5.6 \cdot 4.4\%}{167.6 \cdot 0.2\%} = \frac{24.64}{33.52} = \frac{1}{1.36}$$

$$\frac{\sigma_{^4\mathrm{He}} \cdot \mathrm{ratio}_{^4\mathrm{He}}}{\sigma_{\mathrm{H_2O}} \cdot \mathrm{ratio}_{\mathrm{H_2O}}} = \frac{1.2 \cdot 26.1\%}{167.6 \cdot 0.1\%} = \frac{31.32}{16.76} = \frac{1}{0.53}$$

We see that the ^{3}He@C$_{60}$ should scatter almost as much as H$_2$O@C$_{60}$, whereas ^{4}He@C$_{60}$ should scatter about twice as much as H$_2$O@C$_{60}$. This is what is observed in the INS spectra in section 4.2.2.

4.2.3.2 He@C$_{60}$ INS discussion

The INS spectra of ^{3}He@C$_{60}$ and ^{4}He@C$_{60}$ displayed a number of peaks (section 4.2.2). However, as shown above, most of the peaks were due to traces of H$_2$O@C$_{60}$ being present in the samples. Nonetheless, for each endofullerene (^{3}He@C$_{60}$ and ^{4}He@C$_{60}$) one peak was identified with high degree of certainty.

For ^{3}He@C$_{60}$ a peak at 11.77 ± 0.02 meV and for ^{4}He@C$_{60}$ a peak at 9.85 ± 0.02 meV were identified. These peaks were found in the INS spectra acquired with 2.2 Å neutrons. The same features were also present at the same energies in the INS spectra acquired with 1.6 Å neutrons; this reassures us of the validity of the 2.2 Å results. All measurements were performed at really low temperature (of 1.6 K), which indicates that the observed transitions originated in the ground state of the confined Helium atom (since transitions are on the order of $\sim$ 10 meV). Thus, the observed peaks are assigned to the fundamental translational transitions of the confined Helium atom in ^{3}He@C$_{60}$ and ^{4}He@C$_{60}$. The mass of the confined Helium atom influences the energy of the observed peak, the lighter ^{3}He atom having a larger transition energy.

Endofullerenes translationally confine atoms/molecules to the inside of fullerene cages. This is reminiscent of the well known quantum mechanics example of a "particle in a box" or the quantum harmonic oscillator, where the potential confines a quantum particle to a region of space. These models should at least partially describe the confined Helium isotopes in fullerene cages.

To support the above argument, we need to take into account the isotope effect between ^{3}He and ^{4}He and consider the 2 extreme models which can represent our system. From INS measurements the ratio between the ^{3}He and ^{4}He transition energy is $\frac{11.77\pm0.02\ \text{meV}}{9.85\pm0.02\ \text{meV}} = 1.195 \pm 0.003$. An isotropic harmonic oscillator would have this ratio equal to the inverse square root of the masses = $\frac{\sqrt{4}}{\sqrt{3}} = 1.155$; whereas a particle in a box model, which has no interaction with the boundaries until the particle reaches them (and then potential energy becomes infinite), would have the ratio equal to the inverse of the masses = $\frac{4}{3} = 1.333$.[42] We can see from this very simple argument that our system is closer to a harmonic oscillator model than a particle in a box model; ergo, Helium has some degree of interaction with the cage carbons and cannot be described just by a "particle in a box" model. A detailed theoretical description and analysis of the He@C_{60} system is given in section 6.2 where the potential is more realistically described by even power polynomials.

4.2.4 Final remarks and future work

The INS measurements done on ^{3}He@C_{60} and ^{4}He@C_{60} at the ILL using the IN4c instrument successfully detected one transition, the fundamental, of the translationally confined Helium atom. The energy for the transition was dependent on the isotopic mass, with ^{3}He@C_{60} having a higher energy for the transition. Unfortunately, no other transitions were detected and the traces of H_2O@C_{60} in the samples leftover from the synthesis obscured the spectra quite a lot making the analysis rather difficult.

By learning that any trace of H_2O@C_{60} in the samples are problematic and that the amount of sample used in these measurements was on the low limit of detection, new INS measurements were planned on ^{3}He@C_{60} and ^{4}He@C_{60}. The instrument used was different, IN1 LAGRANGE as compared to IN4c, and the sample amount was increased with effectively no traces of H_2O@C_{60}, this is presented in section 4.3.

4.3 INS measurements of He@C_{60} using IN1 LAGRANGE

All INS experiments were performed at the ILL (Institut Laue-Langevin) in Grenoble France, on the IN1 LAGRANGE instrument with the help of Stéphane Rolls and the instrument chief Mónica Jiménez-Ruiz. The measured endofullerenes are ^{3}He@C_{60}, ^{4}He@C_{60} and Ne@C_{60}. The ^{3}He@C_{60} INS experiments were affected by the COVID-19 pandemic, so users could not participate in the measurements; these were done by Stéphane Rolls, Mohamed Aouane and Mónica Jiménez-Ruiz from the ILL. For the ^{4}He@C$_{60}$ and Ne@C$_{60}$ measurements the ILL proposal number is 7-04-169 with doi:10.5291/ILL-DATA.7-04-169. For the ^{3}He@C$_{60}$ measurements the ILL proposal number is 7-04-176 with doi:10.5291/ILL-DATA.7-04-176.

4.3.1 Experimental

LAGRANGE stands for: LArge GRaphite ANalyser for Genuine Excitations.

IN1 is an instrument with a high flux neutron beam, since the neutrons are provided by the "hot source" moderator of the reactor. The moderator slows down the fast neutrons produced by the nuclear reaction, to be used for spectroscopic measurements.

A main difference between IN4c and IN1 is that IN4c produces the spectrum all at once and IN1 does it one data point at a time. Therefore, when statistics are improved in IN4c the number or runs (transients) was increased, whereas for IN1 one needs to make sure they measure all the data points in the same way.

Each data point in IN1 measurements is normalised with respect to the incoming neutron flux as measured by the monitor. The measurement is done in such a way to ensure the same total neutron flux was used for each data point.

Fig. 4.9 contains a diagram of IN1 Lagrange spectrometer.

The nuclear reactor produces a beam of hot neutrons which is directed onto one of the three monochromators, Si111, Si311 or Cu220. The monochromators diffract (reflect) neutrons of a given energy (wavelength) based on the 2θ Bragg angle from fig. 4.9. The monochromators reflect neutrons within a certain energy range as follows: Si111 5.5-20 meV, Si311 16.5-31.5 meV and Cu220 26-500 meV. By rotating the whole setup with respect to the monochromators and synchronising their rotation as well to change the 2θ angle, a different energy (wavelength) can be selected for the incident neutron beam.

Once the energy of the neutron beam has been selected based on the Bragg diffraction angle, the beam passes through the spectrometer: firstly passing through the Monitor, secondly through the Diaphragm, thirdly it enters the spectrometer passing through the sample and finally it is stopped by the beam stop. The Monitor is an "inefficient detector" to give an estimate for the total number of neutrons in the beam and the diaphragm just completely stops the neutron beam. The Displex cryostat keeps the sample at the desired temperature.

When the beam hits the sample it scatters neutrons, elastically and inelastically, in all directions. The neutrons scattered downwards, between 33.73° and 69.36°, from the main beam direction are refocused by the highly oriented pyrolytic graphite (PG) crystals into the neutron detector (^{3}He gas). The PG crystals are arranged in a parabola

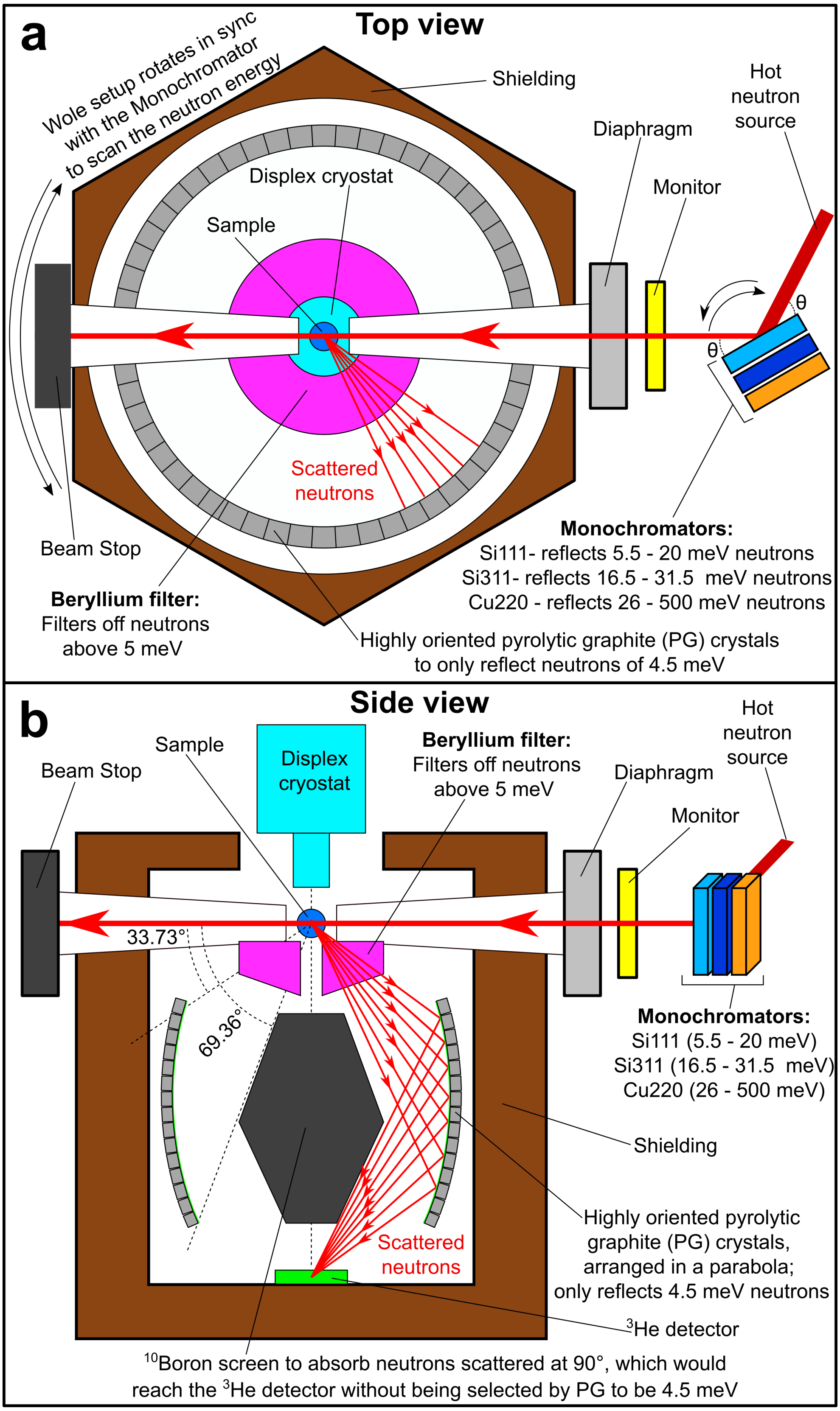

FIGURE 4.9: Diagram of the IN1 Lagrange spectrometer at the ILL. (a) Viewed from the top and (b) viewed from the side. See text for details.

(similar to a wooden barrel) to focus all incoming neutrons from the sample into the ^{3}He detector. The PG crystals also conform to a geometry which only reflects 4.5 meV neutrons towards the detector, thus the ^{3}He detector can only detect 4.5 meV neutrons. In principle the ^{3}He detector can detect neutrons of any energy, however, the PG crystals only select the 4.5 meV ones. To avoid any neutrons scattered off the sample at an angle $>69.36°$ reaching the detector, a ^{10}Boron screen is present in the middle to absorb such neutrons. Also to avoid higher order reflections from reaching the detector, the Beryllium filter only lets through neutrons of <5 meV, further ensuring that only 4.5 meV neutrons reach the detector.

Thus, the Y-axis of the INS spectrum is constructed by measuring the neutron count from the ^{3}He detector, normalised by the monitor flux, at a given incident energy. The X-axis is made up from the neutron's incident energy minus 4.5 meV, since only 4.5 meV neutrons scattered inelastically by the sample are being detected. This way the INS spectrum using the IN1 LAGRANGE instrument is constructed point by point, by scanning the incident energy.

4.3.1.1 Sample preparation

The ^{3}He@C_{60}, ^{4}He@C_{60} and Ne@C_{60} samples were synthesised by the group of Richard Whitby at the University of Southampton, through molecular surgery as described in ref 96. All endofullerene samples were purified by HPLC to eliminate any H_2O@C_{60} traces; proven to be problematic, in section 4.2, for low scattering samples such as these. Afterwards, samples (empty C_{60} included) were sublimed and then transported to the ILL for the experiments.

294 mg of ^{4}He@C_{60} ($\sim$ 40% filling factor) was transferred to a thin cylindrical annulus made up of aluminium foil cell and then put in the dysplex cryostat for measuring. The same procedure was applied to a mass matched (293 mg) sample of C_{60} to be used for background subtraction.

174 mg of Ne@C_{60} ($\sim$ 70% filling factor) was transferred to a thin cylindrical annulus made up of aluminium foil cell and then put in the dysplex cryostat for measuring. The same procedure was applied to 293 mg sample of C_{60} to be used for background subtraction, which was mass matched with the ^{4}He@C_{60} sample above.

1067 mg of ^{3}He@C_{60} ($\sim$ 45% filling factor) was transferred to a thin cylindrical annulus made up of aluminium foil cell and then put in the dysplex cryostat for measuring. The same procedure was applied to a mass matched (1067 mg) sample of C_{60} to be used for background subtraction. For the ^{3}He@C_{60} sample, the Cadmium shield was also measured to account for the neutron absorption by the ^{3}He nucleus. The Cd shield is always present on the sample holder, its use is to restrict the neutron beam within the sample space.

An empty aluminium cell, thin cylindrical annulus with no sample inside, was also measured to improve the background subtraction procedure for all compounds.

4.3.2 Results

This section presents the INS experimental results from the IN1 LAGRANGE instrument at the ILL. Samples measured were $^{3}He@C_{60}$, $^{4}He@C_{60}$ and $Ne@C_{60}$.

$^{3}He@C_{60}$ INS spectra were recorded in the energy transfer range [5, 200] meV. $^{4}He@C_{60}$ spectra were recorded in the energy range [5, 60] meV

4.3.2.1 $^{3}He@C_{60}$ results

The INS measurements of $^{3}He@C_{60}$ were done using the IN1 LAGRANGE instrument at the ILL, with proposal number 7-04-176 with doi:10.5291/ILL-DATA.7-04-176. Unfortunately, due to the COVID19 pandemic I could not take part in these measurements, they were performed by Stéphane Roll, Mohamed Aouane and Mónica Jiménez-Ruiz from the ILL.

The INS spectrum of 1067 mg of $^{3}He@C_{60}$ (f = 0.45) was measured at cryogenic temperatures (2.7 K) using the IN1 LAGRANGE instrument. The same spectrum was acquired for 1067 mg of C_{60}, the empty Aluminium sample holder (Ecell) and the Cadmium shield which restricts the neutron beam to the sample space. The Cadmium shield is always present on the sample holder, even for the empty Aluminium sample holder (Ecell).

Since the ^{3}He nucleus absorbs neutrons rather strongly, this needs to be corrected in the INS spectrum:
- Firstly, the Cd shield was subtracted from all measurements, resulting in Cd free spectra denoted $\underline{^{3}He@C_{60}}$, $\underline{C_{60}}$ and $\underline{\text{Ecell}}$.
- Secondly, the Cd free empty Aluminium cell ($\underline{\text{Ecell}}$) is subtracted from the $\underline{\text{fullerene}}$ spectra. Before subtraction, the $\underline{\text{Ecell}}$ needs to be scaled for the neutron absorption. This scaling α is $\propto \sqrt{E}$ (where E is the neutron incident energy), because the absorption cross section is $\propto \frac{1}{\sqrt{E}}$.[41] Now $\alpha = t * \sqrt{E}$, where t is the transmission through the sample. For $\underline{C_{60}}$ the transmission was assumed to be 95% ($t = 0.95$). For $\underline{^{3}He@C_{60}}$ the transmission was deduced by comparing with the $\underline{C_{60}}$ spectrum at 11 meV, which was found to be ∼4 times more intense than $\underline{^{3}He@C_{60}}$. Thus, the $\underline{^{3}He@C_{60}}$ transmission was chosen to be ~ 0.25; spectra shown actually used $t = 0.275$ for $\underline{^{3}He@C_{60}}$ which gave the best subtraction. The transmission corrected spectra are found in fig. 4.10 (a) red for $^{3}He@C_{60}$ and black for C_{60}, where $t = 0.275$ and $t = 0.95$ respectively; these are denoted $\underline{^{3}He@C_{60}}^{t}$ and $\underline{C_{60}}^{t}$. The overall intensity of the $\underline{^{3}He@C_{60}}^{t}$ spectrum was still weaker than the $\underline{C_{60}}^{t}$, so an extra scaling was done to the $\underline{C_{60}}^{t}$ spectrum: $a * \underline{C_{60}}^{t}$ where

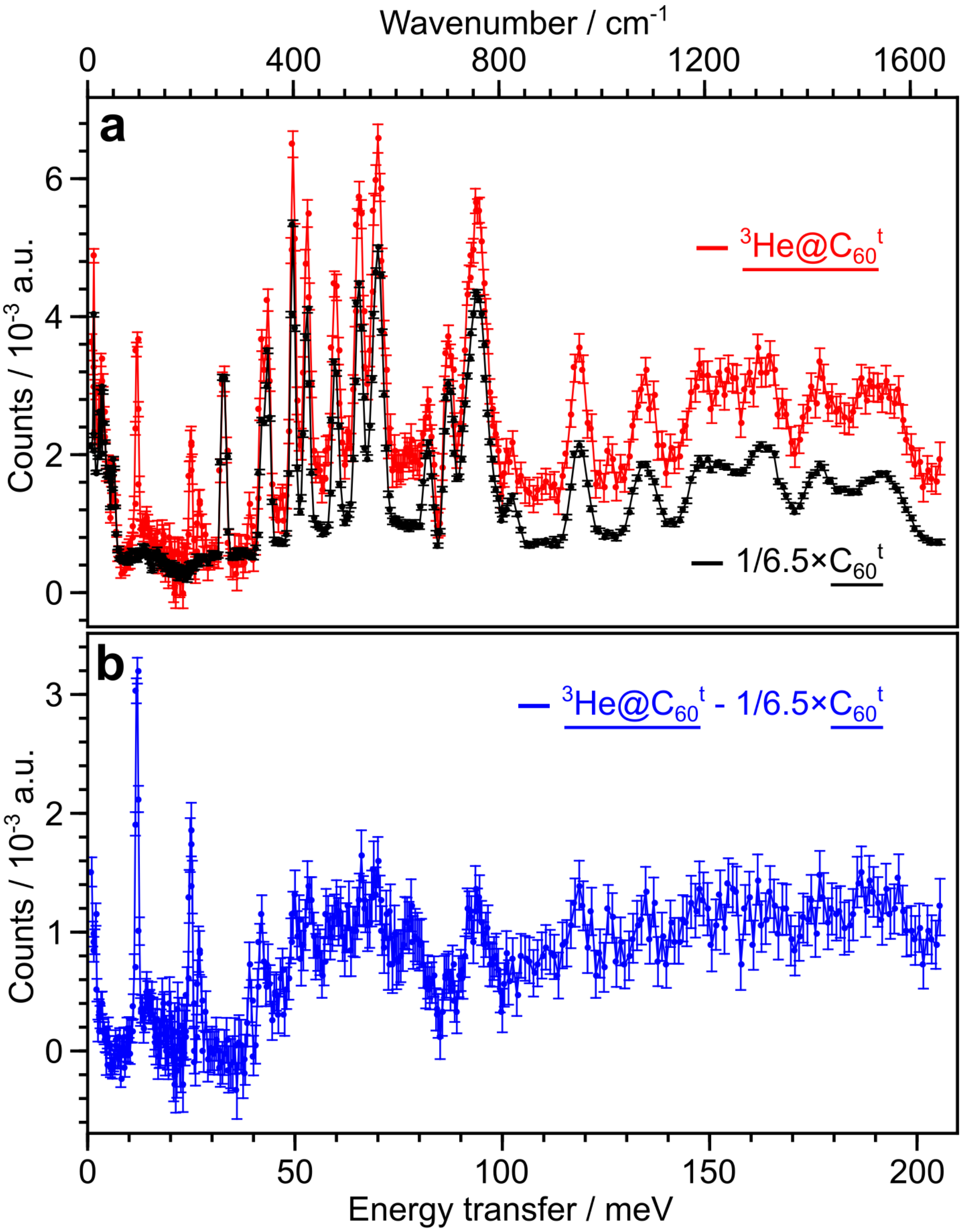

FIGURE 4.10: **(a)** IN1 LAGRANGE INS (transmission corrected) spectra of: 1067 mg $\underline{^{3}He@C_{60}}^{t}$ (f=0.45) in red and 1067 mg $a{*}\underline{C_{60}}^{t}$ ($a = \frac{1}{6.5}$) in black, at 2.7 K. **(b)** in blue the difference red−black from (a) is shown.

$a = 1/6.5$ in the black spectrum from fig 4.10 (a). This extra scaling with a was done in order to match the intensities of the 33 meV peak in both $\underline{^{3}He@C_{60}}^{t}$ and $\underline{C_{60}}^{t}$ spectra; this is shown in fig 4.10 (a) in red and black respectively.

Finally to isolate the spectrum of the confined Helium atom, the difference between the pure contributions is needed, $\underline{^{3}\mathrm{He@C}_{60}}^{t}$ - $a*\underline{\mathrm{C}_{60}}^{t}$, and it is shown in fig. 4.10 (b) in blue for a = 1/6.5.

Some extra peaks are seen for ^{3}He@C$_{60}$ compared with the C$_{60}$ spectra, as seen in the difference spectrum in fig. 4.10 (b), where some peaks are observed in the lower energy part of the spectrum. The cage vibrations peaks of ^{3}He@C$_{60}$ are cancelled to some extent in the mid energy region, by subtracting the empty C$_{60}$ peaks, but still a raised baseline is present continuing up to higher energies.

These extra peaks of ^{3}He@C$_{60}$ are shown more clearly in fig. 4.11 (a) where only the lower energy part of the difference spectrum is shown. The spectrum was fitted in this region with Gaussian lineshapes to extract information about the peaks position, area and width. The baseline was fitted with a rank 5 polynomial function to account for imperfect background subtraction. Peak fitting parameters are found in table 4.6.

There seem to be 5 peaks in the spectrum in fig. 4.11 (a) which could be fitted with Gaussian lineshapes. The most prominent peak is at 11.90 ± 0.01 meV which we assign as being the fundamental transition of the confined ^{3}He atom, from the ground state to the first excited state. The other observed peaks should also be originating in the translational ground state, since the spectra were measured at really low temperature (2.7 K).

TABLE 4.6: Parameters for the peak fitting of the ^{3}He@C$_{60}$ INS difference spectrum from fig. 4.11 (a)

Peak	Energy transfer / meV	Area / a.u.	FWHM / meV
a	11.90 ± 0.01	2.81	0.85 ± 0.03
b	24.87 ± 0.04	1.87	0.92 ± 0.09
c	26.98 ± 0.08	0.97	0.96 ± 0.18
d	39.07 ± 0.14	0.52	0.75 ± 0.27
e	41.93 ± 0.11	1.29	1.44 ± 0.26

For the spectra in fig. 4.10, the scalling factor $a = 1/6.5$ because this ensured the intensities of the 33 meV peak in the ^{3}He@C$_{60}$ and C$_{60}$ spectra matched. This gave the best subtraction ($\underline{^{3}\mathrm{He@C}_{60}}^{t}$ - $a*\underline{\mathrm{C}_{60}}^{t}$) in the low energy region seen in fig. 4.10 (b) and more clearly in fig. 4.11 (a). However, when $a = 1/6.5$ the other vibrational peaks of the $\underline{\mathrm{C}_{60}}^{t}$ did not match with $\underline{^{3}\mathrm{He@C}_{60}}^{t}$, as seen in fig. 4.11 (b) where only the 33 meV peak is matched between the two spectra. This gave a non-ideal subtraction (in blue) for the cage peaks, with a raised baseline continuing up to high energies.

In order to better compare the cage vibrational peaks of ^{3}He@C$_{60}$ and C$_{60}$, a different scaling was used ($a = 1/5$) for the $\underline{\mathrm{C}_{60}}^{t}$ spectrum and this is shown in fig. 4.11 (c), where

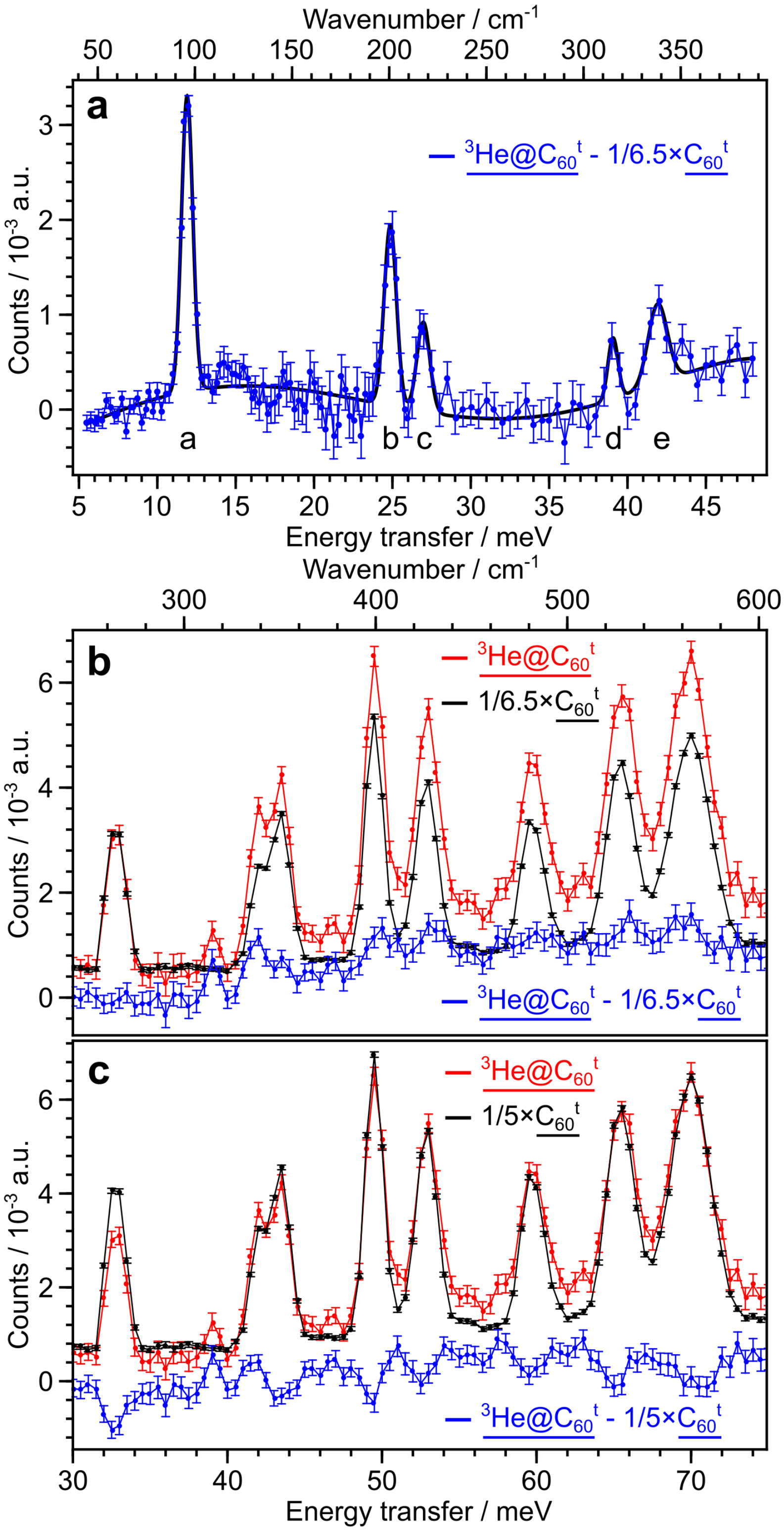

FIGURE 4.11: **(a)** IN1 LAGRANGE INS spectrum, 4-48 meV, of the difference $\underline{^3\mathrm{He@C}_{60}}^t - a * \underline{\mathrm{C}_{60}}^t$ ($a = 1/6.5$), from fig. 4.10 (b). Spectrum fitted with Gaussian lineshapes, with parameters in table 4.6. **(b)** INS spectra, 30-74 meV of: $\underline{^3\mathrm{He@C}_{60}}^t$ in red, $a * \underline{\mathrm{C}_{60}}^t$ ($a = 1/6.5$) in black and their difference in blue, from fig. 4.10. **(c)** is the same as (b) just with $a = 1/5$.

the peaks match much better (except for the 33 meV peak). Now the difference spectrum (in blue) is almost zero, with some small variations. Some very weak dispersion peak shapes are seen in the blue difference spectrum from fig. 4.11 (c), where the vibrational peaks for the cage should be present. The dispersion shape arises because the vibrational peaks of the cage filled with ^{3}He have a frequency very slightly shifted from that of the empty C_{60}; the endohedral noble gas atom slightly changes the vibrational frequency of the cage peaks. Thus, subtracting the empty C_{60} peaks with a slightly different frequency results in a dispersion shape for the cage peaks in the difference spectrum. However, the dispersion peak shapes are rather weak for $^3He@C_{60}$.

4.3.2.2 $^4He@C_{60}$ results

The INS measurements of $^4He@C_{60}$ were done using the IN1 LAGRANGE instrument at the ILL, with proposal number 7-04-169 with doi:10.5291/ILL-DATA.7-04-169.

The INS spectrum of 294 mg of $^4He@C_{60}$ (f = 0.4) was measured at cryogenic temperatures (2.7 K) using the IN1 LAGRANGE instrument. The same spectrum was acquired for 293 mg of C_{60} and for an empty sample holder made of aluminium foil (Ecell). The empty sample holder contribution was subtracted from $^4He@C_{60}$ and C_{60}, and the resulting spectra containing the pure contributions from $^4He@C_{60}$ and C_{60} are shown in fig. 4.12 (a) in green and black respectively.

To isolate the spectrum of the confined Helium atom, the difference between the pure contributions is needed, denoted (($^4He@C_{60}$ - Ecell)-$a*$(C_{60}- Ecell)), and it is shown in fig. 4.12 (b) for $a = 0.92$ in dark green. The factor a is an extra parameter needed to perform the best possible subtraction of the C_{60} background.

Some extra peaks are seen for $^4He@C_{60}$ compared with the C_{60} spectra, as seen in the difference spectrum in fig. 4.12 (b), where some peaks are observed in the lower energy part of the spectrum. Furthermore, some dispersion type peaks are observed in the higher energy part of the difference spectrum at 30-55 meV, where the C_{60} cage peaks should be (fig. 4.12 (a) black). At $\sim$26 meV an experimental artifact is marked with an asterisk in fig. 4.12 (a) and (b), since this feature was present in both the $^4He@C_{60}$ and C_{60} spectra. This artifact is also seen in the $Ne@C_{60}$ spectrum from fig 4.14, which was acquired in the same experimental run as $^4He@C_{60}$.

These extra peaks of $^4He@C_{60}$ are shown more clearly in fig. 4.13 (a), where only the lower energy part of the difference spectrum is shown. The spectrum was fitted in this region with Gaussian lineshapes to extract information about the peaks position, area and width. The baseline was fitted with a rank 5 polynomial function to account for imperfect background subtraction. Peak fitting parameters are found in table 4.7.

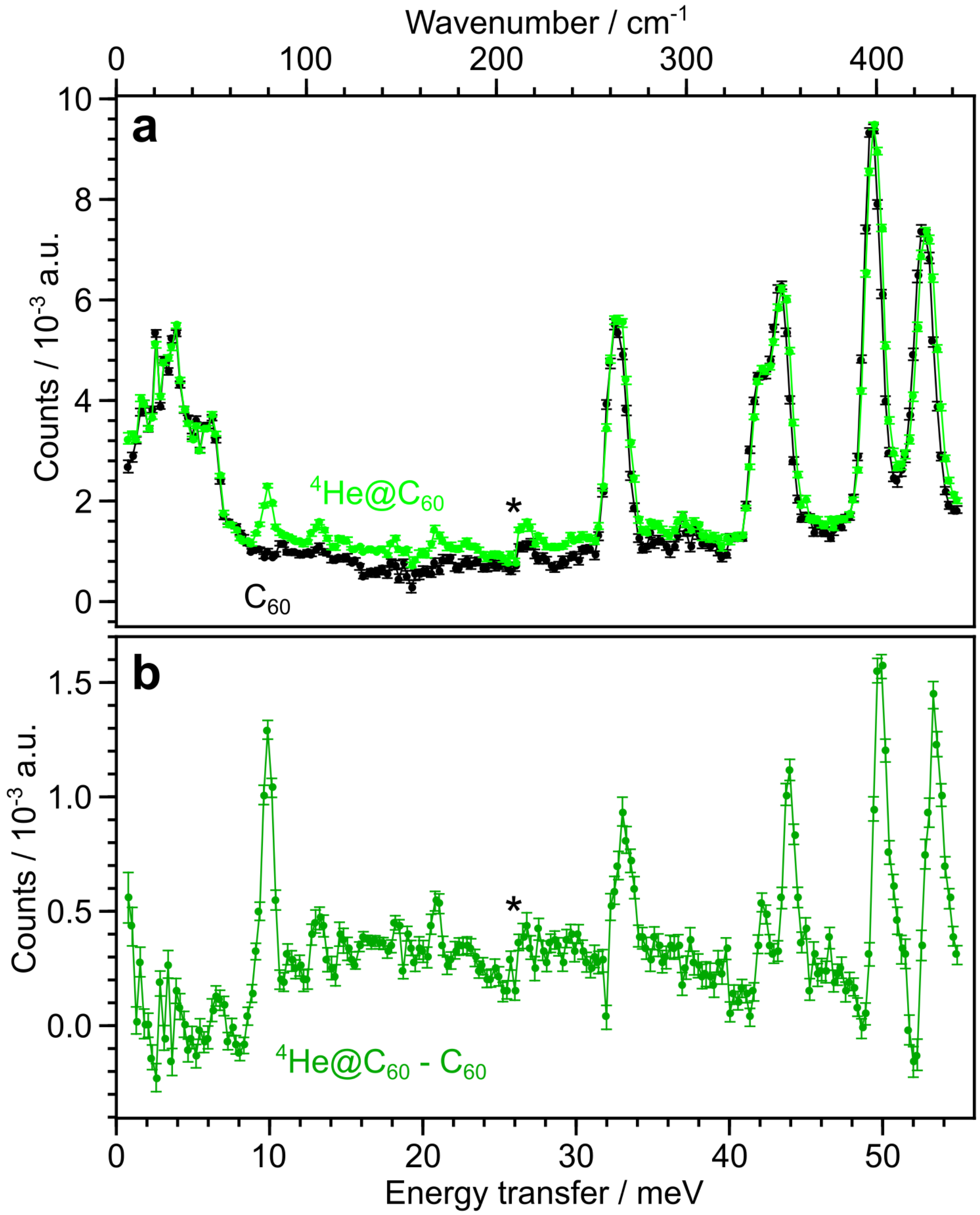

FIGURE 4.12: **(a)** IN1 LAGRANGE INS spectra of: 294 mg ^{4}He@C$_{60}$ (f=0.40) in green and 293 mg a∗C$_{60}$ (a = 0.92) in black, at 2.7 K after empty cell (Ecell) subtraction. **(b)** in dark green the difference green−black from (a) is shown. At ∼26 meV an experimental artifact is marked with an asterisk.

There seem to be 4 peaks in the spectrum in fig. 4.13 (a) which could be fitted with Gaussian lineshapes. The most prominent peak is at 9.86 ± 0.01 meV which we assign as being the fundamental transition of the confined ^{4}He atom, from the ground state to the first excited state. The other observed peaks should also be originating in the translational ground state, since the spectra were measured at really low temperature (2.7 K). The peaks at 6.60±0.07 meV and 13.14±0.06 meV are most likely experimental

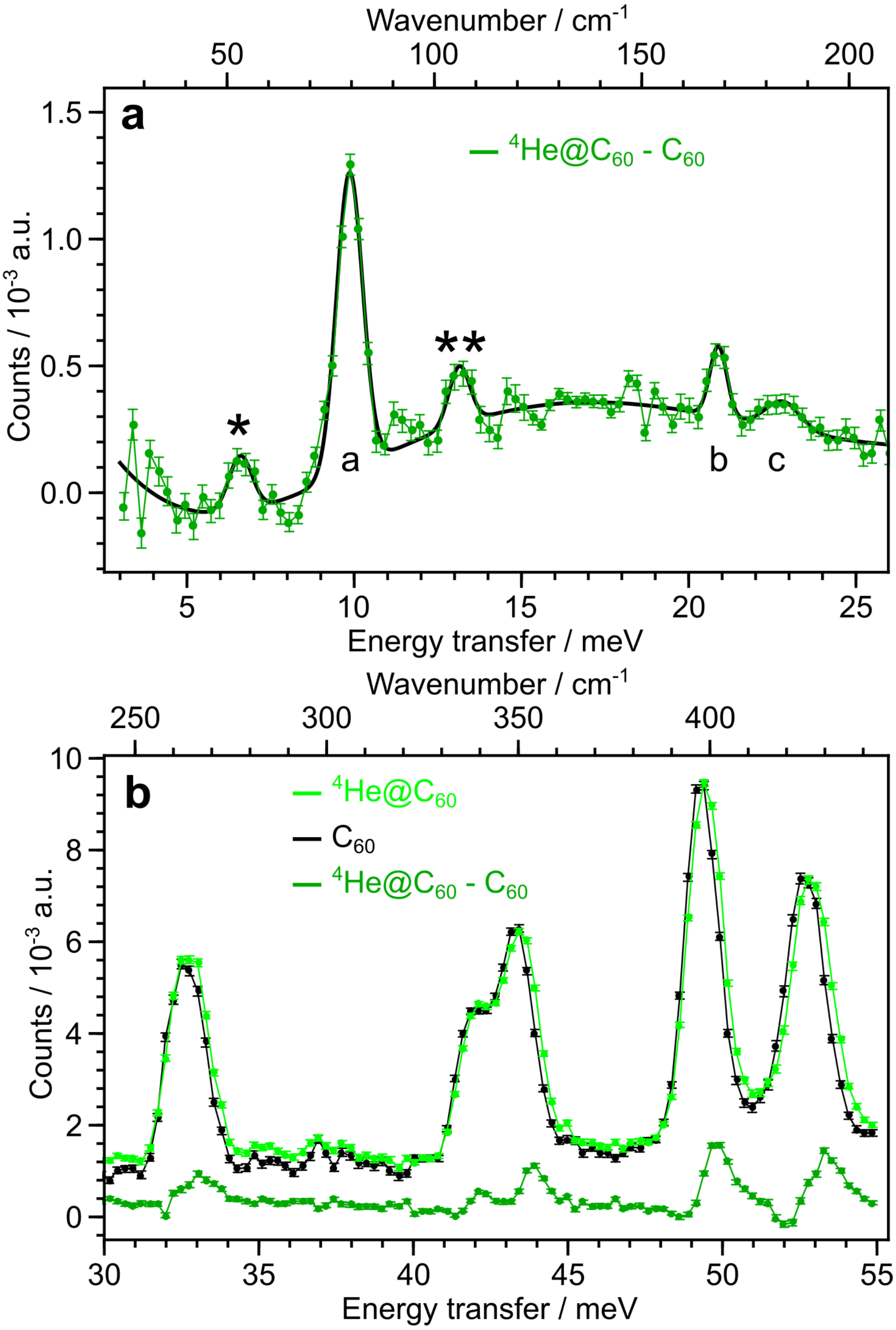

FIGURE 4.13: **(a)** IN1 LAGRANGE INS spectrum, 3-25 meV, of the difference $^4He@C_{60} - a * C_{60}$ ($a = 0.92$), from fig. 4.12 (b). Spectrum fitted with Gaussian lineshapes, with parameters in table 4.7. **(b)** INS spectra, 30-55 meV of: $^4He@C_{60}$ in green, $a{*}C_{60}$ ($a = 0.92$) in black and their difference in dark green, from fig. 4.12.

artifacts from, since they could not be assigned to the confined ^{4}He transitions (see section 6.2).

The origin of the dispersion peaks at high energies in the difference spectrum is shown

TABLE 4.7: Parameters for the peak fitting of the ^{4}He@C$_{60}$ INS difference spectrum from fig. 4.13 (a)

Peak	Energy transfer / meV	Area / 10^{-3} a.u.	FWHM / meV
$*$	6.60$\pm$ 0.07	0.19	0.82 $\pm$ 0.15
a	9.86$\pm$ 0.01	0.92	0.92 $\pm$ 0.03
$**$	13.14 $\pm$ 0.06	0.18	0.73 $\pm$ 0.15
b	20.89 $\pm$ 0.04	0.17	0.60 $\pm$ 0.10
c	22.82 $\pm$ 0.13	0.14	1.22 $\pm$ 0.32

more clearly in fig. 4.13 (b), where the spectra are shown for ^{4}He@C$_{60}$, C$_{60}$ and the difference between them on the same Y-axis scale. The dispersion shape arises because the vibrational peaks of the cage filled with ^{4}He have a frequency slightly shifted from that of the empty C$_{60}$; the endohedral noble gas atom slightly changes the vibrational frequency of the cage peaks. Thus, subtracting the empty C$_{60}$ peaks with a slightly different frequency results in a dispersion shape for the cage peaks in the difference spectrum.

4.3.2.3 Ne@C$_{60}$ results

The INS measurements of Ne@C$_{60}$ were done using the IN1 LAGRANGE instrument at the ILL, with proposal number 7-04-169 with doi:10.5291/ILL-DATA.7-04-169.

The INS spectrum of 174 mg of Ne@C$_{60}$ (f = 0.7) was measured at cryogenic temperatures (2.7 K) using the IN1 LAGRANGE instrument. The same spectrum was acquired for 293 mg of C$_{60}$ and for an empty sample holder made of aluminium foil (Ecell). The empty sample holder contribution was subtracted from Ne@C$_{60}$ and C$_{60}$, and the resulting spectra containing the pure contributions from Ne@C$_{60}$ and C$_{60}$ are shown in fig. 4.14 (a) in orange and black respectively.

To isolate the spectrum of the confined Helium atom, the difference between the pure contributions is needed, denoted ((Ne@C$_{60}$- Ecell)-$a*$(C$_{60}$- Ecell)), and it is shown in fig. 4.14 (b) for $a = 0.56$ in brown. The factor a is an extra parameter needed to perform the best possible subtraction of the C$_{60}$ background.

Some extra peaks are seen for Ne@C$_{60}$ compared with the C$_{60}$ spectra, as seen in the difference spectrum in fig. 4.14 (b), where some peaks are observed in the lower energy part of the spectrum. Furthermore, some dispersion type peaks are observed in the higher energy part of the difference spectrum at 30-55 meV, where the C$_{60}$ cage peaks should be (fig. 4.14 (a) black). At $\sim$26 meV an experimental artifact is marked with an asterisk in fig. 4.14 (a) and (b), since this feature was present in both the Ne@C$_{60}$ and

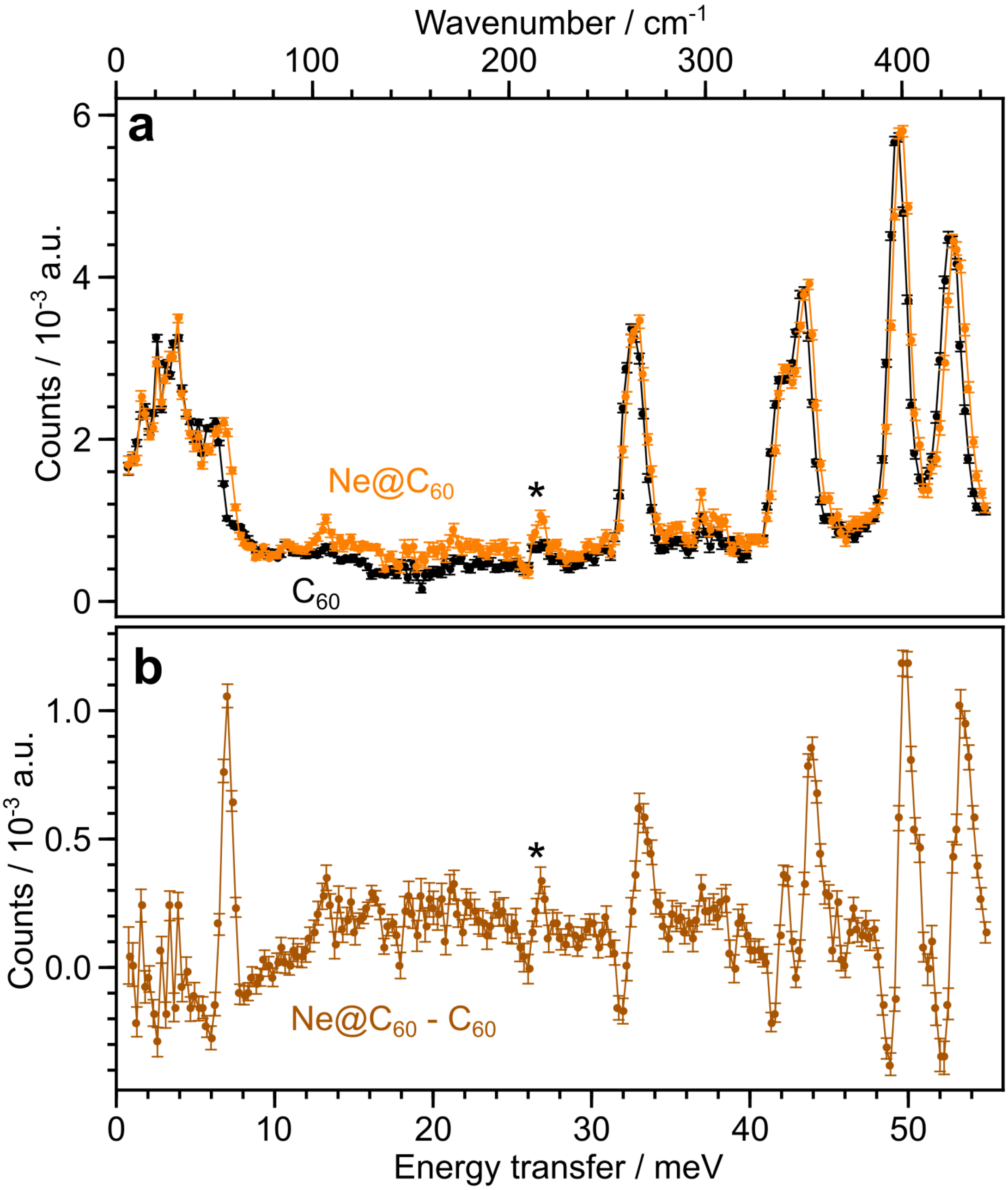

FIGURE 4.14: **(a)** IN1 LAGRANGE INS spectra of: 174 mg Ne@C_{60} (f=0.70) in orange and 293 mg $a{*}C_{60}$ ($a = 0.56$) in black, at 2.7 K after empty cell (Ecell) subtraction. **(b)** in dark orange the difference orange−black from (a) is shown. At ~26 meV an experimental artifact is marked with an asterisk.

C_{60} spectra. This artifact also is seen in the ^{4}He@C_{60} spectrum from fig 4.12, which was acquired in the same experimental run as Ne@C_{60}.

These extra peaks of Ne@C_{60} are shown more clearly in fig. 4.15 (a), where only the lower energy part of the difference spectrum is shown. The spectrum was fitted in this region with Gaussian lineshapes to extract information about position, area and width of the peak. The baseline was fitted with a rank 5 polynomial function to account for imperfect background subtraction. Peak fitting parameters are found in table 4.8.

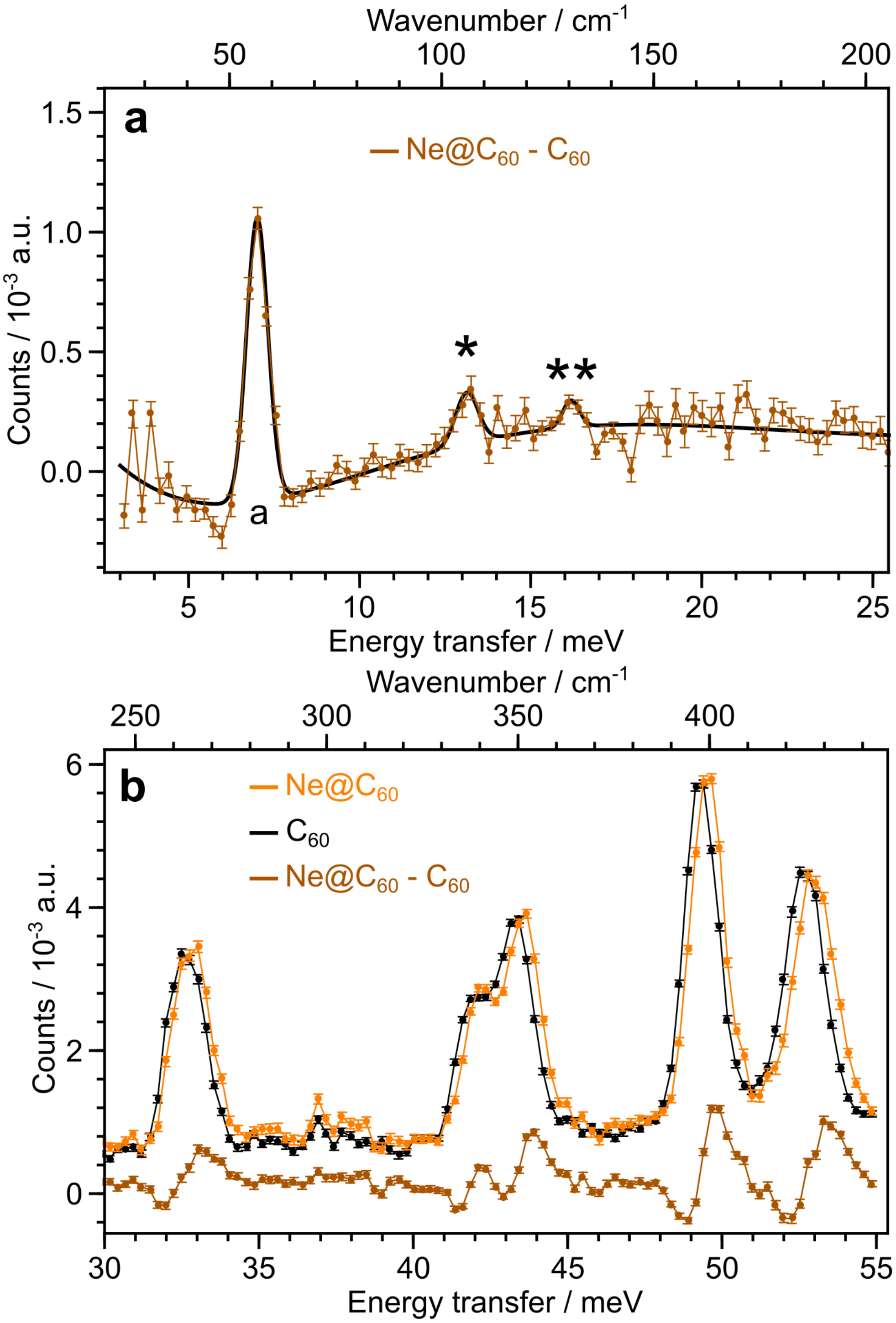

FIGURE 4.15: **(a)** IN1 LAGRANGE INS spectrum, 3-25 meV, of the difference Ne@$C_{60} - a * C_{60}$ ($a = 0.56$), from fig. 4.14 (b). Spectrum fitted with Gaussian lineshapes, with parameters in table 4.8. **(b)** INS spectra, 30-55 meV of: Ne@C_{60} in orange, $a{*}C_{60}$ ($a = 0.56$) in black and their difference in dark orange, from fig. 4.14.

There seem to be 3 peaks in the spectrum in fig. 4.15 (a) which could be fitted with Gaussian lineshapes. The most prominent peak is at 7.01 ± 0.01 meV which we assign as being the fundamental transition of the confined atom, from the ground state to the first excited state.

TABLE 4.8: Parameters for the peak fitting of the Ne@C_{60} INS difference spectrum from fig. 4.15 (a)

Peak	Energy transfer / meV	Area / 10^{-3} a.u.	FWHM / meV
a	7.01 ± 0.01	0.92	0.73 ± 0.02
$*$	13.13 ± 0.07	0.18	0.77 ± 0.16
$**$	16.18 ± 0.07	0.07	0.57± 0.16

The origin of the dispersion peaks at high energies in the difference spectrum is shown more clearly in fig. 4.15 (b). Where the spectra are shown for Ne@C_{60}, C_{60} and the differecen between them on the same Y-axis scale. The dispersion shape arises because the vibrational peaks of the cage filled with Ne have a frequency slightly shifted from that of the empty C_{60}; the endohedral noble gas atom slightly changes the vibrational frequency of the cage peaks. Thus, subtracting the empty C_{60} peaks with a slightly different frequency results in a dispersion shape for the cage peaks in the difference spectrum.

4.3.3 Discussion

INS measurements were done on ^{3}He@C_{60}, ^{4}He@C_{60} and Ne@C_{60} using the IN1 LAGRANGE instrument at the ILL. Some discussion of the results is shown below. In each sample two set of observations are made: 1) for the endohedral atom and 2) for the fullerene cage. In other words, peaks corresponding to the endohedral noble gas atom and changes to the vibrational peaks of the cages are observed.

Further theoretical description of the He@C_{60} system is given in section 6.2.

4.3.3.1 ^{3}He@C_{60} discussion

The ^{3}He@C_{60} INS results using the IN1 LAGRANGE instrument were shown in section 4.3.2.1. It shows the ^{3}He@C_{60} INS spectra, H_2O@C_{60} free due to the HLPC purification step in the sample preparation.

In the lower energy part of the spectrum (<50 meV) clear peaks are seen for the endohedral noble gas atom, see fig. 4.10 (b) and fig. 4.11 (a). The peaks were fitted with Gaussian lineshapes and the parameters are given in table 4.6. The measurement was done at 2.7 K so all transitions should be originating in the ground state (since transitions are on the order of $\sim$ 10 meV). The most intense peak is at 11.90±0.01 meV and this is assigned as the fundamental ^{3}He transition. This value is essentially the same as the one obtained in section 4.2.2.1, where a different instrument (IN4c) was used to acquire the INS spectra of a different sample of ^{3}He@C_{60} with lower filling factor.

The other observed peaks are also assigned to be originating in the translational ground state. The other peaks (besides the 11.90±0.01 meV fundamental) are overtone transitions, originating in the ground state and ending up in excited states (2nd, 3rd, etc.). The overtones appear at roughly double and triple the energy of the 11.90±0.01 meV fundamental. The only peak which is ambiguous is the one at ∼42 meV, because this is found at the same energy as a cage vibration (fig. 4.11 (b) and (c)), so it could be arising due to imperfect subtraction of the C_{60} background. Further interpretation of these peaks is given in section 6.2.

Subtracting the C_{60} contribution from the ^{3}He@C_{60} spectrum generated *very small* dispersion type lineshapes at the energies where the vibrational peaks of the cage are, fig. 4.10 (a) and fig. 4.11 (b) & (c)). The dispersion shape arises because the vibrational peaks of the cage filled with ^{3}He have an energy very slightly shifted from that of the empty cage. This is seen by looking at the ^{3}He@C_{60} peaks in green from fig. 4.13 (b), which are shifted very slightly compared with the spectrum of C_{60} in black. This is different from what is being observed for ^{4}He@C_{60} in section 4.3.2.2 and for Ne@C_{60} in section 4.3.2.3; where the cage vibrational peaks for the endofullerene were shifted more significantly, generating more obvious dispersion peak shapes. However, the experimental resolution was worse for the ^{3}He@C_{60} measurements in the high energy regime, which makes the accurate detection of such shifts more difficult.

These kind of shifts have been previously reported in the Raman spectra of noble gas endofullerenes;[68] where they generally observe an increase in the cage vibrational shift when the size of the noble gas atom is increased. A possible explanation for why the dispersion lineshape is much weaker for ^{3}He@C_{60} is that the mass of ^{3}He is too small compared with ^{4}He and Ne to change the vibrational frequencies of the cage enough to be detectable by INS.

4.3.3.2 ^{4}He@C_{60} discussion

The ^{4}He@C_{60} INS results using the IN1 LAGRANGE instrument were shown in section 4.3.2.2. It shows the ^{4}He@C_{60} INS spectra, H_2O@C_{60} free due to the HLPC purification step in the sample preparation.

In the lower energy part of the spectrum (<25 meV) clear peaks are seen for the endohedral noble gas atom, see fig. 4.12 (b) and fig. 4.13 (a). The peaks were fitted with Gaussian lineshapes and the parameters are given in table 4.7. The measurement was done at 2.7 K so all transitions should be originating in the ground state. The most intense peak is at 9.86±0.01 meV and this is assigned as the fundamental ^{4}He transition. This value is essentially the same as the one obtained in section 4.2.2.2, where a different instrument (IN4c) was used to acquire the INS spectra of a different sample of $^4He@C_{60}$ with lower filling factor.

The other observed peaks are also assigned to be originating in the translational ground state. However, as shown later on in section 6.2, only the peaks at 20.89±0.04 meV and 22.82±0.13 meV could be assigned to the ^4He transitions. The others probably are just experimental artifacts from the data treatment, marked with asterisk in fig. 4.13 (a). The peaks at 20.89±0.04 meV and 22.82±0.13 meV are roughly at double the energy of the fundamental transition. Thus, they are assigned as overtone transitions from the ground state to the second and third excited states respectively.

Subtracting the C_{60} contribution from the $^4He@C_{60}$ spectrum generated dispersion type lineshapes at the energies where the vibrational peaks of the cage are (fig. 4.12). The dispersion shape arises because the vibrational peaks of the cage filled with ^4He have an energy slightly shifted from that of the empty cage. This is seen by looking at the shifted $^4He@C_{60}$ peaks in green from fig. 4.13 (b), comparing with the spectrum of C_{60} in black. These kinds of shifts have been previously reported in the Raman spectra of noble gas endofullerenes.[68] Note the shift in the cage vibrations (the dip of the dispersion shape) seems to be smaller for $^4He@C_{60}$ than for, $Ne@C_{60}$ seen in section 4.3.2.3. This is in agreement with ref 68, where they generally observe an increase in the cage vibrational shift when the size of the noble gas atom is increased. Furthermore, almost no detectable dispersion shapes were seen for the cage peaks of the $^3He@C_{60}$ - C_{60} difference in section 4.3.2.1. A possible explanation is that the mass of ^3He is too small compared with ^4He and Ne to change the vibrational frequencies of the cage enough to be detectable by INS.

4.3.3.3 $Ne@C_{60}$ discussion

The $Ne@C_{60}$ INS results using the IN1 LAGRANGE instrument were shown in section 4.3.2.3. It shows the $Ne@C_{60}$ INS spectra, $H_2O@C_{60}$ free due to the HLPC purification step in the sample preparation.

In the lower energy part of the spectrum (<25 meV), clear peaks are seen for the endohedral noble gas atom, see fig. 4.14 (b) and fig. 4.15 (a). The peaks were fitted with Gaussian lineshapes and the parameters are given in table 4.7. The measurement was done at 2.7 K so all transitions should be originating in the ground state. The most intense peak is at 7.01±0.01 meV and this is assigned as the fundamental Ne transition. The peak at 13.13±0.07 meV seems to be at roughly double the energy of the fundamental peak, so it could be the overtone transition from the ground state to the second excited state. However, without having another experimental result to compare with the confidence in this assignment is limited. The peak at 16.18±0.07 meV could be just an experimental artifact or coming from the data treatment.

Subtracting the C_{60} contribution from the Ne@C_{60} spectrum generated dispersion type lineshapes at the energies where the vibrational peaks of the cage are (fig. 4.14). The dispersion shape arises because the vibrational peaks of the cage filled with Ne have an energy slightly shifted from that of the empty cage. This is seen by looking at the shifted Ne@C_{60} peaks in orange from fig. 4.15 (b), comparing with the spectrum of C_{60} in black. These kinds of shifts have been previously reported in the Raman spectra of noble gas endofullerenes.[68] Note the shift in the cage vibrations (the dip of the dispersion shape) seems to be larger for Ne@C_{60} than for ^{4}He@C_{60}, seen in section 4.3.2.2. This is in agreement with ref 68, where they generally observe an increase in the cage vibrational shift when the size of the noble gas atom is increased. Furthermore, almost no detectable dispersion shapes were seen for the cage peaks of the ^{3}He@C_{60} - C_{60} difference in section 4.3.2.1. A possible explanation is that the mass of ^{3}He is too small compared with ^{4}He and Ne to change the vibrational frequencies of the cage enough to be detectable by INS.

4.4 Conclusion

INS measurements of ^{3}He@C_{60} and ^{4}He@C_{60} revealed some peaks in the spectra due to the confined Helium atoms. The transitions are sensitive to the mass of the He isotope, the lighter ^{3}He has a higher energy for the transitions than ^{4}He. Two different INS instruments were used to measure He@C_{60} endofullernes, IN4c and IN1 LAGRANGE, both at the Institut Laue-Langevin (ILL) in Grenoble France. Both instruments successfully detected the same fundamental peaks of ^{3}He@C_{60} and ^{4}He@C_{60}. The INS spectra acquired with the IN1 instrument revealed some extra overtone transitions, not observed with IN4c. This was possible since the sample preparation was vastly improved from the initial IN4c measurements: the sample amounts and filling factors were increased, and traces of H_2O@C_{60} were removed by HPLC prior to the INS measurements.

The most intense INS peaks at 11.90 ± 0.01 meV for ^{3}He@C_{60} and 9.86 ± 0.01 meV for ^{4}He@C_{60} were assigned to fundamental translational transitions of the confined He isotopes. Furthermore, overtone transitions were observed for the two isotopes. This offers an outline of the energy level structure, which is used to accurately define the potential energy surface (PES) that the Helium atom experiences when enclosed inside C_{60} fullerenes, in section 6.2.2.

INS measurements of Ne@C_{60} revealed three peaks in the spectrum. However, due to the lack of extra experimental data, only the fundamental transition at 7.01 ± 0.01 meV was identified. This is used to estimate the harmonic confining potential of Ne@C_{60}, in section 6.2.1.

The vibrational peaks of the cages filled with the noble gases are shifted compared with empty C_{60}, as seen from the dispersion lineshapes in the difference spectra. The effect seems to scale with the mass and the size of the endohedral noble gas atom. The smallest shifts detected were for ^{3}He@C_{60} and the largest ones for Ne@C_{60}. This agreed with ref 68, where the increase in the cage vibrational shift scaled with the size of the endohedral noble gas atom.

4.4.1 Future work

For the Ne@C_{60} only the fundamental translational transition could be accurately identified. In order to assign other transitions, further INS experiments are being planned. This will attempt to complete the story of noble gas C_{60} endofullerenes, where other compounds such as Ar@C_{60}, Kr@C_{60}, etc. might be studied using INS.

The origin of the shift seen for the vibrational modes of the C_{60} cage, when a noble gas is encapsulated, was not investigated in this study. This has been investigated in reference 68 for Ar@C_{60} and Kr@C_{60}, where shifts of the cage vibrational modes were observed in the Raman spectra. Future analysis will be done to understand the cage vibrational shifts for ^{3}He@C_{60}, ^{4}He@C_{60} and Ne@C_{60}; similar to the work from reference 68.

Chapter 5

THz spectroscopy of ^{3}He@C$_{60}$ and ^{4}He@C$_{60}$

5.1 Introduction

Far-Infrared (far-IR) is an electromagnetic type of spectroscopy, which uses low energy light, 0-500 cm^{-1}, to probe matter. Since the technique uses light with frequencies in the THz range, is also called THz spectroscopy. Far-IR and THz is used interchangeably throughout the chapter. Far-IR spectroscopy has well-known selection rules associated with electromagnetic radiation, $\Delta\ell = 0, \pm 1$ and $\Delta m = 0, \pm 1$, where ℓ and m are the usual angular momentum quantum numbers.[43–45] These experiments were performed on the solid pure endofullerene samples at cryogenic temperatures. The far-IR measurements were done with the group of Toomas Rõõm, at the National Institute of Chemical Physics and Biophysics (KFBI) in Tallinn Estonia.

Molecular endofullerenes, H_2O@C$_{60}$, HF@C$_{60}$, etc., have been studied using far-IR spectroscopy, since they absorb electromagnetic radiation quite strongly due to their permanent electric dipole moments. The peaks in the THz spectra were shown to be rotations and translations of the endohedral molecule; with the added Translational-Rotational (TR) coupling.[22–27,114] Since molecular endofullerenes display observable pure translational peaks in the THz spectrum,[19,22,26,30–33] detecting such analogous transitions was attempted for atomic endofullerenes of noble gases. There are only translational degrees of freedom for noble gases, which should generate clean experimental spectra; compared with molecular endofullerenes in which the TR coupling complicates the spectrum. The information gained from such spectra provides valuable insight into the non-covalent interaction between the endohedral noble gas and the C$_{60}$ carbon cage. This chapter is dedicated to the study of atomic translational quantization of noble gases trapped inside C$_{60}$ fullerenes, where ^{3}He@C$_{60}$ and ^{4}He@C$_{60}$ are investigated using far-IR spectroscopy.

The He@C$_{60}$ THz measurements were a gamble, because inherently the Helium atom does not possesses a dipole moment and an induced dipole moment could easily be too small to be detectable. Fortunately, this was not the case, and the first far-IR spectrum of confined Helium inside C$_{60}$ was measured. It really is astounding that the first noble gas atom from the periodic table, Helium, acquires an induced dipole moment when encapsulated in the cavity of a C$_{60}$ molecule. Beyond all expectations, the He@C$_{60}$ molecule absorbs THz light which translationally excites the confined Helium atom.

There were two sets of far-IR measurements performed on He@C$_{60}$. An initial series of far-IR experiments, which gave rise to the THz spectrum of ^{4}He@C$_{60}$. ^{3}He@C$_{60}$ was also measured, but nothing was detected since the filling factor was too low. Magnetic field dependent measurements were performed as well, yet there was no observable effect on the THz spectrum of ^{4}He@C$_{60}$. A second series of far-IR measurements were performed, where the sample preparation was vastly improved. This time the filling factors of both ^{3}He@C$_{60}$ and ^{4}He@C$_{60}$ were increased, and this resulted in observing a THz spectrum for both compounds.

5.1.1 IR transmission and differential absorbance

For IR spectroscopy two notions are important, the transmission $T(\omega)$ and the differential absorbance $A(\omega)$ defined in eq. 5.1 and eq. 5.2.

$$T(\omega) = \frac{I(\omega)}{I_0(\omega)} \tag{5.1}$$

$$A(\omega) = -\frac{1}{d} ln \left(\frac{sT(\omega)}{(1-R)^2} \right) \tag{5.2}$$

$I(\omega)$ represents the IR signal being transmitted through the sample at frequency ω, and $I_0(\omega)$ the transmitted signal for the reference. The term $s = \frac{\text{Reference cross section}}{\text{Sample cross section}}$, yet in our cases they are the same so $s = 1$. The factor $R = (\frac{1-\eta}{1+\eta})^2$ accounts for the double reflection at the interfaces of the sample pellet. η is the refractive index of C$_{60}$ (for C$_{60}$ $\eta = 2$[115]) and d is the thickness of the sample pellet in cm. In eq. 5.2 there is a minus sign because the transmission $T(\omega)$ shows how much light passes through, so absorption peaks would be negative, the minus sign ensured absorption peaks are positive in the THz spectrum. Absorption and absorbance are used interchangeably in the chapter.

5.2 THz experiments on He@C_{60} (first series)

THz (or far-Infrared) spectroscopy was attempted, in the lab of Toomas Rõõm and coworkers at KFBI in Tallinn, Estonia. Against all odds, a far-IR signal was observed for ^{4}He@C_{60}.

5.2.1 Experimental

5.2.1.1 Sample preparation

The ^{3}He@C_{60} and ^{4}He@C_{60} were synthesised by the group of Richard Whitby and coworkers, at the University of Southampton, through molecular surgery as described in ref. 96. Before the far-IR measurements were attempted, the ^{3}He@C_{60} and ^{4}He@C_{60} samples were purified by HPLC to try and remove the H_2O@C_{60} traces. Then the samples were sublimed in Southampton and transported to Tallinn Estonia for measuring.

The sublimed endofullerene (or C_{60} fullerene reference) powders were put into a brass cylindrical sample holder, with a round hole in the centre along its height, of 3 mm inner diameter. The powder was put under vacuum ($\sim 1.5 * 10^{-2}$ mBar), then pressed into a cylindrical pellet of 3 mm diameter and a sample dependent thickness (height). The THz radiation passes through the hollow part of the sample holder and the (endo)fullerene pellet before reaching the detector. If the sample absorbs any radiation the spectrometer signal drops at that frequency.

For C_{60}, 25.4 mg were pressed into a pellet 2.106 mm thick.

For ^{3}He@C_{60}, 24.6 mg (4.4% filling factor) were pressed into a pellet 2.33 mm thick.

For ^{4}He@C_{60}, 25.1 mg (26.1% filling factor) were pressed into a pellet 2.39 mm thick.

5.2.1.2 Far-IR experimental setup

A diagram of the far-IR FT spectrometer in Tallinn is shown in fig. 5.1. It contains a Fourier-Transform interferometer (SPS-300 FTIR) and a home-built cryostat with a superconducting magnet. The FT interferometer modulates the light intensity (at specific frequencies) passing through the sample based on the distances ”d1” and ”d2”, similar to a Michelson interferometer.[116]

Firstly, a Hg lamp at 5000 K produces black-body radiation in all directions. Some of this light is directed through an initial linear polariser (A), which polarises the light as shown in fig. 5.1 by the blue (magnetic field polarisation) and green (electric field polarisation) double headed arrows. The light then goes through a polarising beam splitter

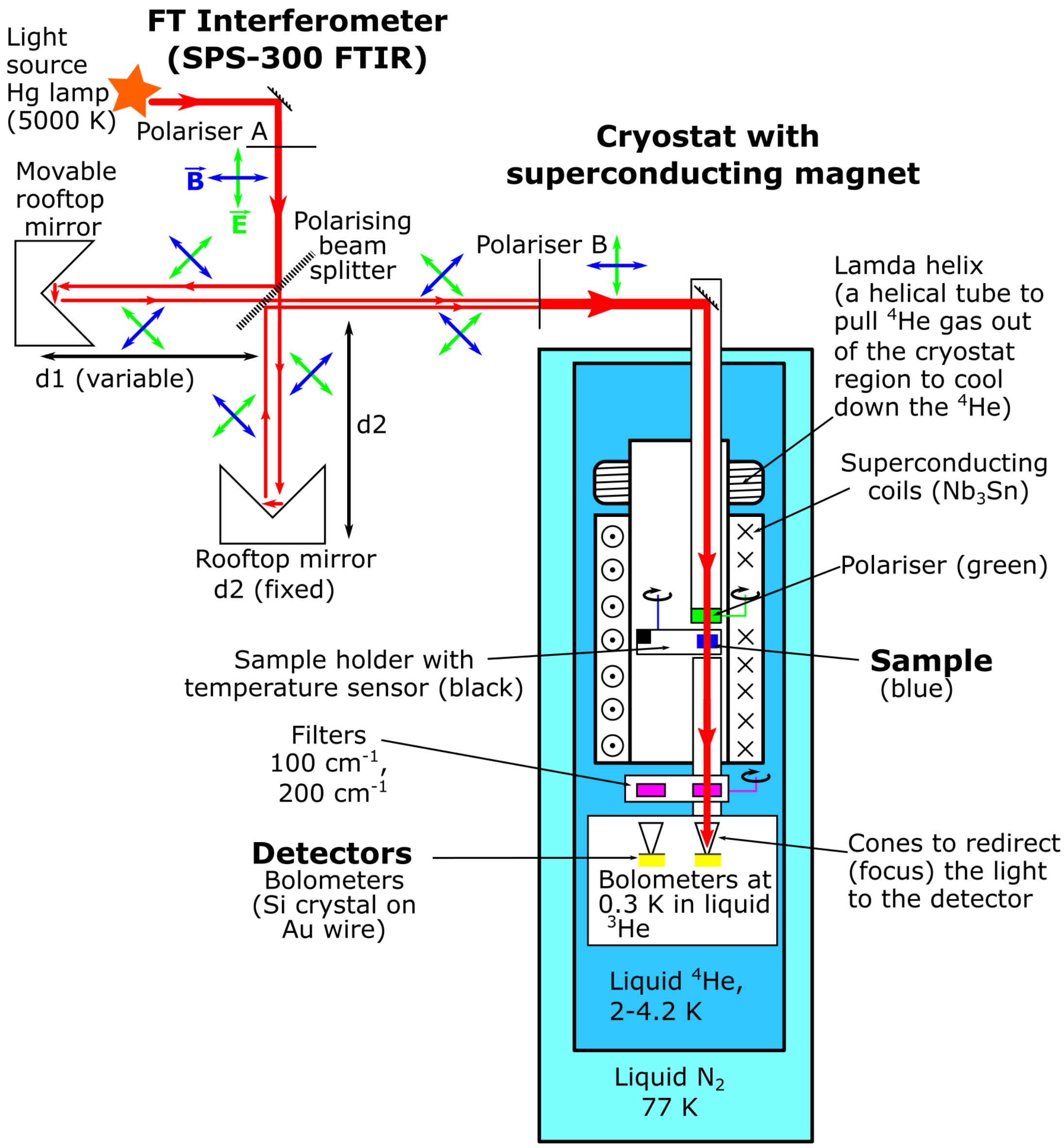

FIGURE 5.1: Diagram of the far-IR FT spectrometer in Tallinn. SPS-300 FTIR is the FT interferometer and the cryostat with the superconducting magnet are home buit. See text for further details.

which splits the incident light in two. The polarising beam splitter transmits light polarised in only one direction and it reflects the light with polarisation perpendicular to the transmitted one. The beam splitter is positioned such that it splits the incident beam in two equal parts with perpendicular polarisations, both resulting polarisations are shifted by ± 45°with respect to the incident beam. The double reflection with the rooftop mirrors then induce a 90°phase shift of the polarisation for the two beams which are then transmitted (reflected) with unchanged polarisation through (by) the polarising beam splitter. The beams then overlap and pass through a second polariser (B) which combines the two perpendicular polarisations into a singular linear one as shown in fig. 5.1. The light is then introduced in the cryostat and passes through a variable linear polariser, which can be used to do polarisation dependent measurements. Afterwards, it passes through the sample, getting absorbed at some wavelengths, and then through the filters- which stop light passing through if it is beyond a given energy (e.g. a 100 cm^{-1} filter only lets through light under 100 cm^{-1} as seen in fig. 5.2). The light is then focused by the cones and it reaches the detectors (bolometers). The bolometer is made up of a silicon crystal which absorbs incoming far-IR radiation and heats up. The silicon is in thermal contact with a gold wire which changes its resistance with temperature, based on how much radiation the silicon crystal has absorbed. If one then plots the resistance of the bolometer against the variable distance "d1", an interferogram is obtained and its Fourier transformation gives the raw far-IR spectrum, seen in fig. 5.2.

Measurements using this procedure have been done on C$_{60}$, ^{3}He@C$_{60}$ and ^{4}He@C$_{60}$ at different temperatures. There are two options for acquiring signal averaged data: averaging spectra or averaging interferograms. For these measurements, the interferograms have been averaged, which improves the signal-to-noise but leads to a loss of the statistical errors from the spectrum.

Measurements were done with static magnetic fields as well, from 0-14 T. This was done hoping that the magnetic field would split the degeneracies of the first excited state ($n = 1$ and $\ell = 1$), similar to the Zeeman splitting seen for the hydrogen atom. No detectable splitting was seen for ^{4}He@C$_{60}$ between 0-14 T and these spectra are not shown.

5.2.2 Results

Firstly, the raw far-IR transmission spectra of the samples at 4 K were measured and are seen in fig. 5.2. In the figure C$_{60}$ and ^{4}He@C$_{60}$ show interference fringes arising due to reflections at the pellet's surface. ^{3}He@C$_{60}$ does not show fringes and it is believed that the pellet's surface was too rough to have clean reflections. Initially from this raw spectrum it can be seen that ^{4}He@C$_{60}$ absorbs some radiation around 80 cm^{-1}.

Signals above 100 cm^{-1} were attenuated by the 100 cm^{-1} filter used for this measurement.

5.2.2.1 Differential absorbance far-IR spectra for C$_{60}$, ^{3}He@C$_{60}$ and ^{4}He@C$_{60}$

For IR spectroscopy the transmission $T(\omega)$ and the differential absorbance $A(\omega)$ were defined in eq. 5.1 and eq. 5.2. In eq. 5.2 there is a minus sign to ensure absorption peaks are positive, since transmission peaks are negative.

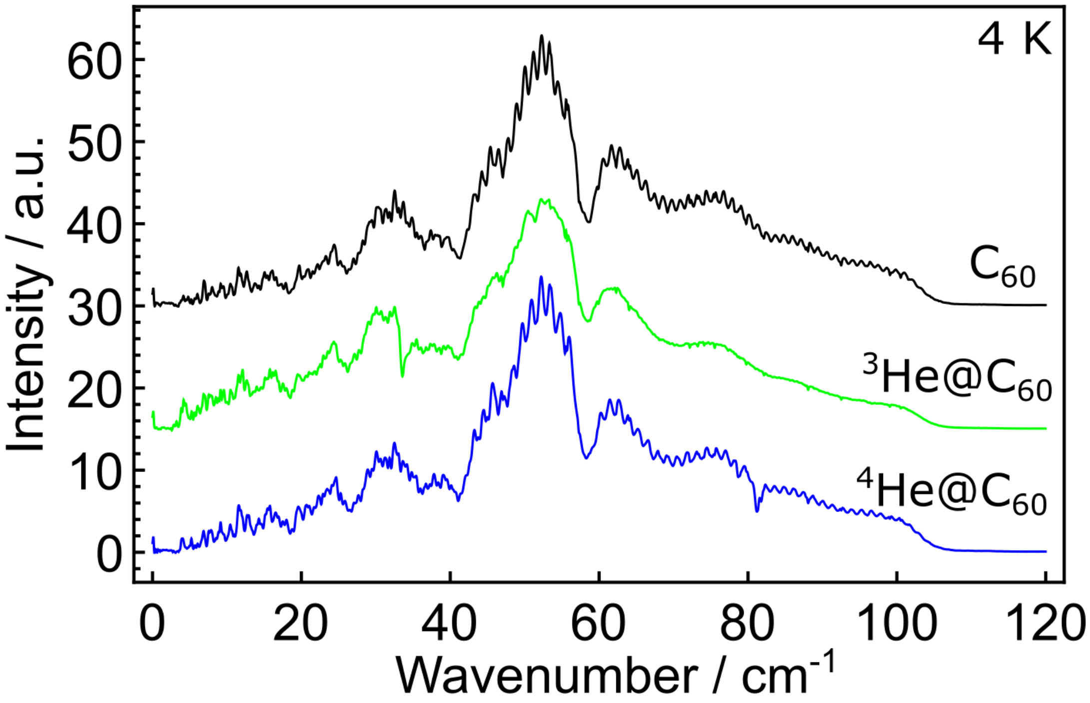

FIGURE 5.2: Far-IR spectrometer raw signal (transmission) response at 4 K with a 100 cm^{-1} filter for C_{60}, $^3He@C_{60}$ and $^4He@C_{60}$. In the $^4He@C_{60}$ spectrum some negative peaks are seen around 80 cm^{-1} where the THz intensity drops, due to the quantised translational transitions of the confined ^4He atom.

After the raw far-IR spectra were obtained for all samples at 4 K, the differential absorbance was done for $^3He@C_{60}$ and $^4He@C_{60}$ by taking C_{60} as the reference. However, this did not help much since each sample has different interference fringes, fig. 5.2, when taking the ratio (difference of logarithms) it produces beats in the spectrum due to differences in the fringe spacing (the "fringe wavelength"). Thus, the same sample at a different temperature was used as its own reference when plotting the differential absorbance. This was done in fig. 5.3 for C_{60}, $^3He@C_{60}$ and $^4He@C_{60}$ where the raw far-IR signal at 4 K was taken as the sample and the raw far-IR signal at 100 K was the reference. In the figure they are all plotted for comparison.

Quite a lot of peaks are seen below 60 cm^{-1}, however they are present in all samples, even C_{60}, thus they cannot be from the confined helium atom. For $^3He@C_{60}$ some extra peaks are seen at 33 cm^{-1} and 51 cm^{-1} but these turn out to be from $H_2O@C_{60}$ traces,[30,31] since the $^3He@C_{60}$ sample had most traces present (section 4.2.3.1) and HPLC probably did not get rid of it all.

Finally in the $^4He@C_{60}$ spectrum some clear peaks are seen between 75-100 cm^{-1}, marked with a dashed semicircle in fig. 5.3 and they turn out to arise from the confined ^4He atom.

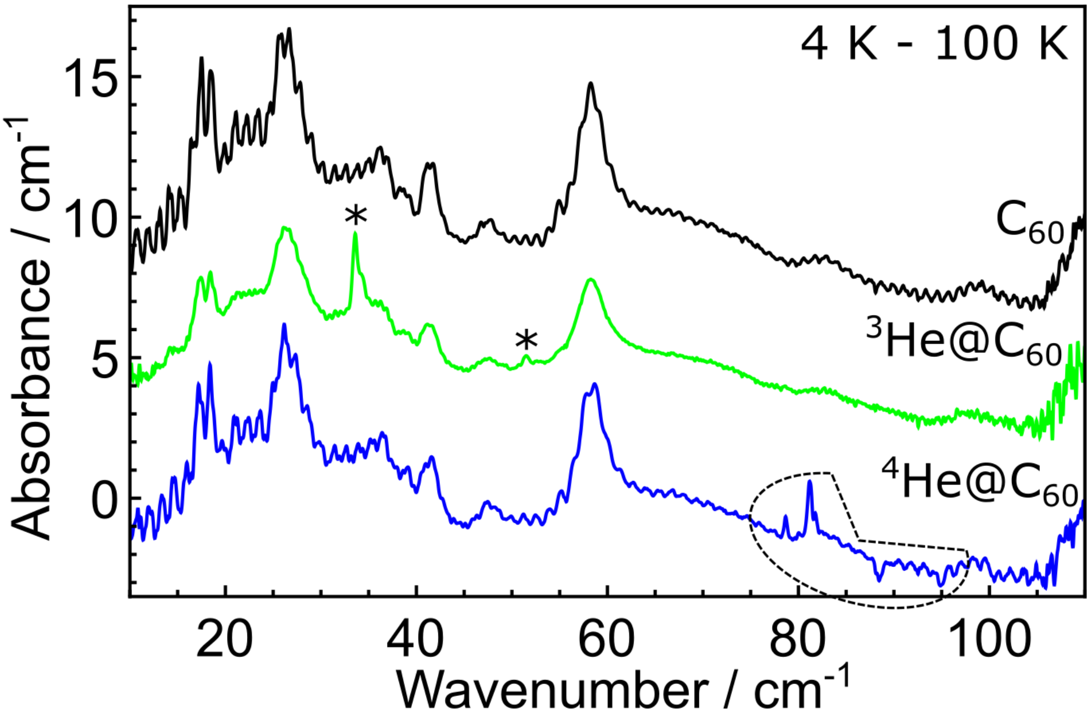

FIGURE 5.3: Far-IR differential absorbance spectra for C$_{60}$, ^{3}He@C$_{60}$ and ^{4}He@C$_{60}$. Obtained from the difference (differential absorbance) between the signal at 4 K and at 100 K, using the same sample as reference (i.e. C$_{60}$ at 4 K is the sample and C$_{60}$ at 100 K is the reference). An asterisk marks the signals arising fromH$_2$O@C$_{60}$. The dashed semicircle marks the ^{4}He@C$_{60}$ translational peaks.

5.2.2.2 Differential absorbance spectra for ^{4}He@C$_{60}$ at different temperatures

After the peaks for ^{4}He@C$_{60}$ in fig. 5.3 were confirmed, the far-IR spectra were acquired at multiple temperatures. These are plotted as differential absorbance in fig. 5.4 by using the spectrum at 100 K as reference. The raw spectrum at 4 K only shows the 81 cm^{-1} peak (and the 79 cm^{-1} impurity marked with an asterisk in fig. 5.4) and no peaks at 88 cm^{-1} or 95 cm^{-1}.

A preliminary assignment of the transitions is shown in fig. 5.4. The peaks were fitted with Gaussian lineshapes and the parameters are given in table. 5.1.

TABLE 5.1: ^{4}He@C$_{60}$ 4 K- 100 K far-IR peaks from fig. 5.4

Wavenumber	78.7 cm^{-1}	81.2 cm^{-1}	81.8 cm^{-1}	88.5 cm^{-1}	95 cm^{-1}
Area	0.26 cm^{-2}	1 cm^{-2}	0.2 cm^{-2}	–	–
Transition n=i → f	?	$0 \rightarrow 1$	$0 \rightarrow 1'$	$1 \rightarrow 2$	$2 \rightarrow 3$

The peaks beyond 85 cm^{-1} were not fitted because they are suspected to be composed of overlapping peaks and the presence of the peak at 95 cm^{-1} is not 100% certain since

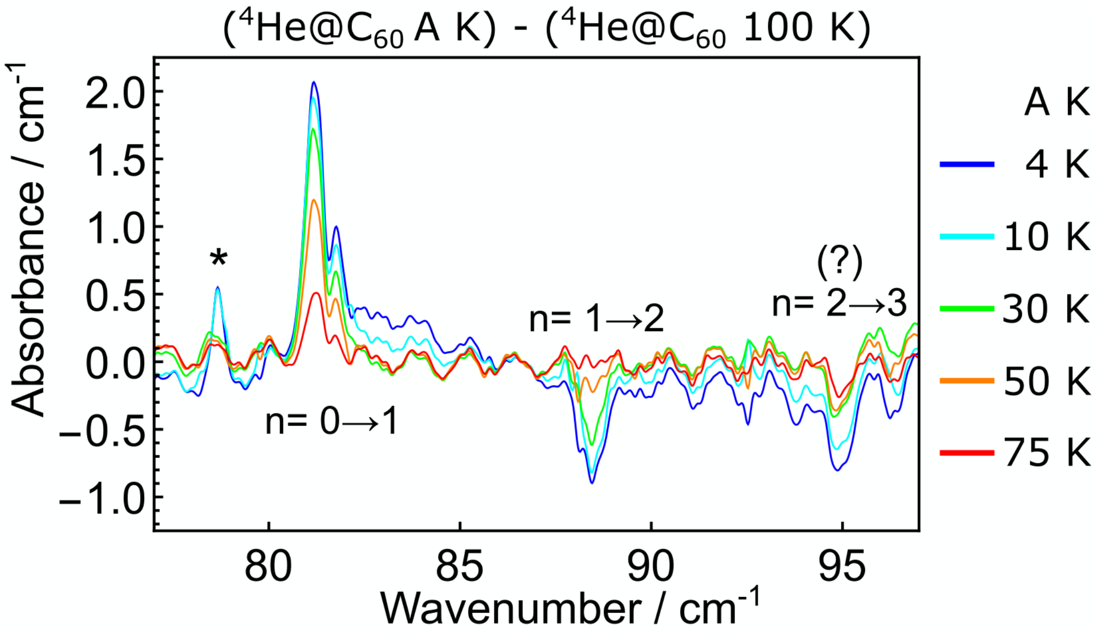

FIGURE 5.4: Far-IR differential absorbance spectra for ^{4}He@C$_{60}$ at different temperatures using the 100 K signal as reference. Peak positions and area for the 4 K spectra are found in table 5.1. The n stands for the translational quantum number for a harmonic oscillator. The asterisk marks an unknown impurity peak which disappeared in future measurements.

its intensity is quite low. To confirm this last peak, the same measurements were repeated with higher filling factor to improve the signal to noise ratio and detect a similar spectrum but shifted to higher energies for ^{3}He@C$_{60}$ (see section 5.3).

5.2.3 Discussion

The first THz spectrum of ^{4}He@C$_{60}$ was shown to contain some peaks from the confined ^{4}He atom in the range 80-100 cm^{-1} (fig. 5.3). Unfortunately, the ^{3}He@C$_{60}$ sample did not display any observable peaks in the THz spectrum. This was due to the low filling factor of ^{3}He@C$_{60}$ (4.4%), compared with the 26.1% filling factor of ^{4}He@C$_{60}$.

The variable temperature THz measurements of ^{4}He@C$_{60}$ from fig. 5.4 shows the peaks more clearly. From the figure, all peaks are seen to increase in magnitude with decreasing temperature but some peaks are positive and some are negative. This happens because of the initial state for the transition: if the initial eigenstate of a ^{4}He@C$_{60}$ peak is the ground state then the peak decreases in intensity as temperature is increased because the population of ground state decreases. Since fig. 5.4 essentially shows the difference between the spectrum at A K ($A < 100$) and at 100 K as A increases, this predicts that peaks originating in the ground state are positive and decrease in intensity as temperature is increased. This is because the difference between a peak's intensity at 4 K and 100 K is larger than the difference between 50 K and 100 K. Now if a transition has its initial eigenstate as an excited state of ^{4}He@C$_{60}$, the peak intensity increases as the temperature is increased, because the population of this excited state increases with temperature. Thus, a peak at 100 K would always be more intense than at lower temperatures, so the peaks originating in excited states would appear as negative in the differential absorbance plot from fig. 5.4 and would increase in magnitude as temperature is lowered. Thus, the *doublet* peak at 81 cm^{-1} is assigned as the fundamental transition for the confined ^{4}He atom and the two peaks at 88 cm^{-1} and 95 cm^{-1} are assigned as hot-band transitions originating in excited states.

The peak at 79 cm^{-1} is assigned to an impurity, or experimental artifact, since after repeating the measurements with higher filling factors the peak disappeared, see section 5.3. These measurements were repeated, to ensure validity of the observed peaks, shown in section 5.3.

A detailed theoretical description and analysis of the He@C$_{60}$ system is given in section 6.2.

5.2.4 Final remarks and future work

The measurements presented here show the first THz (far-IR) spectrum of ^{4}He@C$_{60}$. As surprising as this may sound, the Helium atom with no permanent dipole moment once confined inside C$_{60}$ can absorb electromagnetic radiation in the THz regime.

Some peaks were observed for ^{4}He@C$_{60}$ and these were assigned to the confined ^{4}He atom. The fundamental transition was seen at 81 cm^{-1} and two hot-band transitions were seen at 88 cm^{-1} and 95 cm^{-1}. Measurements were also done in the presence of a magnetic field, 0-14 T; however, this did not have any effect on the ^{4}He@C$_{60}$ spectra. The fundamental and hot-band transitions were unaffected, within the accuracy of the experiment.

The hot-band peaks had weak intensity and their validity is questionable. To ensure these peaks are real and not experimental artifacts, new far-IR experiments were planned. The THz measurements were repeated on samples of ^{3}He@C$_{60}$ and ^{4}He@C$_{60}$ with higher filling factors, these results are shown in section 5.3

5.3 THz experiments ^{3}He@C$_{60}$ and ^{4}He@C$_{60}$ (second series)

Further THz experiments were planned on these samples to detect the far-IR spectrum of ^{3}He@C$_{60}$ and get better quallity data on ^{4}He@C$_{60}$. The experiments were done in the same lab of Toomas Rõõm and coworkers at KFBI in Tallinn, Estonia. Unfortunately, due to the COVID-19 pandemic I could not participate in the acquisition of these measurements. The samples were shipped and the measurements were done by Tanzeeha

Jafari *et al.* from the group of Toomas Rõõm. Data processing and analysis was done in collaboration with the group of Toomas Rõõm.

5.3.1 Experimental

The THz (far-IR) experiments shown in this section (5.3) were performed on a similar spectrometer to the one shown in fig. 5.1. The main difference is that the previous setup enabled static magnetic fields to be applied on the sample.

The working principle of this spectrometer is essentially the same as described in section 5.2.1.2. A Michelson interferometer (Bruker Vertex 80v) modulates the THz light, which passes through the sample holder placed in a cryostat (Konti cold finger cryostat 5-400 K), after which it reaches the detector (4 K bolometer). Spectral resolution was $\leq 0.3\ \mathrm{cm}^{-1}$ in all THz measurements.

5.3.1.1 Sample preparation

The ^{3}He@C$_{60}$ and ^{4}He@C$_{60}$ were synthesised by the group of Richard Whitby, at the University of Southampton, as described in ref 96.

After synthesis the filling factors of ^{3}He@C$_{60}$ and ^{4}He@C$_{60}$ endofullerenes were enriched to ~90% through recycling HPLC. The HPLC purification was also used to remove any H_2O@C$_{60}$ traces. Then the endofullerenes were sublimed to obtain high purity material.

The sublimed endofullerene powders were put under vacuum, then pressed into a cylindrical pellet of 3 mm diameter and a sample dependent thickness (height). The brass sample holder has a cylindrical shape, with a round hole in the centre along its height, of 3 mm inner diameter.

^{3}He@C$_{60}$ (95.1±0.7% filled) was pressed into a pellet 2.16 mm thick with a 3 mm diameter.

^{4}He@C$_{60}$ (84.3±0.6% filled) was pressed into a pellet 1.72 mm thick with a 3 mm diameter.

5.3.2 Results

The experimental results of THz (far-IR) measurements on ^{3}He@C$_{60}$ and ^{4}He@C$_{60}$ are presented below.

5.3.2.1 ^{4}He@C$_{60}$ results

The THz (far-IR) spectra at cryogenic temperatures were measured on ^{4}He@C$_{60}$ (84.3±0.6% filled) sublimed powder. In fig. 5.5 (a) the wide THz spectrum of ^{4}He@C$_{60}$ is shown at 5 K and 100 K (with 0.1 cm^{-1} resolution).

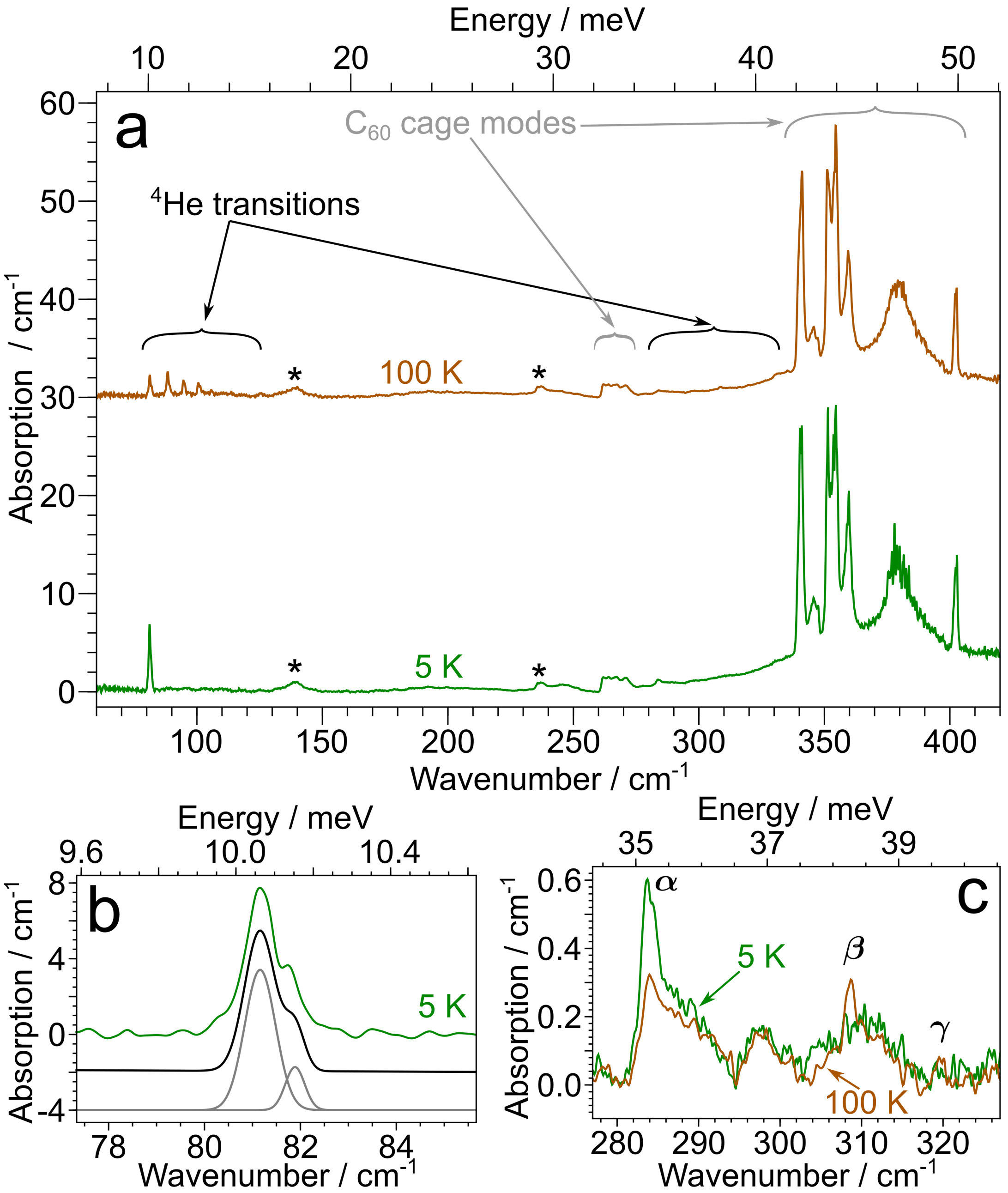

FIGURE 5.5: THz absorption spectra of ^{4}He@C$_{60}$ (f=0.843) at 5 K and 100 K. **(a)** displays the full spectra: green for 5 K and dark orange for 100 K. **(b)** shows the fundamental peak at 5 K in green (from (a)), with Gaussian lineshape fitting in black and the two fitted components in gray (fitting parameters in table 5.2). **(c)** shows the spectrum from (a) in the 280-320 cm^{-1} region; α, β, γ peaks fitted with Gaussian lineshapes and the parameters are found in table 5.3. Baseline corrected (c) spectra are found in fig. 6.4. Background peaks are marked with an asterisk.

The spectra present discrete peaks for the endohedral ^{4}He and for the C$_{60}$ cage, annotated in fig. 5.5 (a). C$_{60}$ cage modes are seen at ∼265 cm^{-1} and past 330 cm^{-1}.
At 140 cm^{-1} and 240 cm^{-1} there are broad background features, marked with an asterisk, which are rather unaffected by temperature (this is used later for background subtraction). Transitions corresponding to ^{4}He are seen between 80-150 cm^{-1} and between 280-320 cm^{-1}.

• ^{4}He **transitions between 80-150** cm^{-1}**:**
At 5 K the fundamental transition of ^{4}He is observed at ∼81 cm^{-1} (fig. 5.5 (a)). A closer look actually reveals two peaks corresponding to this transition, split apart by 0.727 ± 0.011 cm^{-1}, in intensity ratio of approximately 8:2; this fine structure is seen in fig. 5.5 (b) together with fitted Gaussian lineshapes and the peak fitting parameters are found in table 5.2. At high temperature (100 K) the ∼81 cm^{-1} transition decreases in intensity and many hot-band transitions appear at 100-150 cm^{-1} (fig. 5.5 (a) and fig. 5.6). The decrease in intensity with increase in temperature indicates that the ∼81 cm^{-1} transition originates in the ground state. The opposite behaviour for the other peaks indicate they are hot-band transitions, originating in excited states only populated at elevated temperatures.

TABLE 5.2: Parameters for the observed splitting (0.727 ± 0.011 cm^{-1}) of the fundamental ^{4}He@C$_{60}$ transition ∼81 cm^{-1}, at 5 K from fig. 5.5 (b). Fitting done using Gaussian lineshapes.

Peak	Wavenumber / cm^{-1}	Area / cm^{-2}	Ratio	FWHM / cm^{-1}
1a	81.160 ± 0.004	5.984	83.872%	0.758 ± 0.011
1b	81.887 ± 0.011	1.151	16.128%	0.474± 0.022

• ^{4}He **transitions between 280-320** cm^{-1}**:**
For ^{4}He at 5 K in the region 280-320 cm^{-1}, a relatively weak transition is seen at 283.9 cm^{-1} (fig. 5.5 (c)). This peak decreases in intensity at 100 K, indicating it originates in the ground state; peak fitting parameters are found in table 5.3, where the background has been accounted for. At 100 K another two peaks appears at 308.6 cm^{-1} and 319.6 cm^{-1} which were not present at 5 K, indicating they are hot-band transitions originating in an excited state; peak fitting parameters are found in table 5.3, where the background has been accounted for. Fig. 5.5 (c) presents significant background signal other than the identified peak, however it remains quite unaffected by a change in temperature so it is assumed no other ^{4}He peaks are present in this range.

The rich peak structure seen at 80-150 cm^{-1} for ^{4}He at 100 K (fig. 5.5 (a)) needs a closer look. ^{4}He peaks are shown in the range 80-150 cm^{-1} at 5 K with 0.1 cm^{-1} resolution in fig. 5.6 (a) and at 100 K with 0.1 cm^{-1} resolution in fig. 5.6 (b).

A processed version of the ^{4}He spectrum at 100 K with 0.1 cm^{-1} resolution from fig. 5.6 (b) is shown in fig. 5.6 (c). Where in the range 100-150 cm^{-1} the 5 K spectrum from

TABLE 5.3: Parameters peak fittings for ^{4}He@C$_{60}$ at 5 K and 100 K, from fig. 5.5 (c). Fitting done using Gaussian lineshapes and completely subtracting the background.

Peak	Temperature	Wavenumber / cm^{-1}	Area / cm^{-2}	FWHM / cm^{-1}
α	5 K	283.859 ± 0.019	0.933	2.090 ± 0.051
α	100 K	284.060 ± 0.039	0.453	2.276 ± 0.153
β	5 K	–	–	–
β	100 K	308.602 ± 0.022	0.219	1.218 ± 0.049
γ	5 K	–	–	–
γ	100 K	319.645 ± 0.079	0.064	0.991 ± 0.187

fig. 5.6 (a) was subtracted, in order to eliminate the broad background signal at ~140 cm^{-1}. Afterwards, Savitzky-Golay smoothing (35 points) was applied to improve the spectrum.

TABLE 5.4: Parameters for peak fittings of ^{3}He@C$_{60}$ at 100 K, from fig. 5.6 (c). Fitting done using Gaussian lineshapes.

Peak	Wavenumber / cm^{-1}	Area / cm^{-2}	FWHM / cm^{-1}
1	81.315 ± 0.006	2.187	1.124 ± 0.015
2	88.438 ± 0.007	2.487	1.318 ± 0.017
3	94.791 ± 0.010	1.526	1.222 ± 0.025
4	100.802 ± 0.003	1.637	1.533 ± 0.009
5	105.878 ± 0.012	0.471	1.466 ± 0.029
6	110.382 ± 0.037	0.089	1.044 ± 0.093
7	113.953 ± 0.014	0.395	1.449± 0.037
8a	125.340 ± 0.004	0.161	1.149 ± 0.134
8b	126.544 ± 0.004	0.209	2.497 ± 0.354
9a	132.461 ± 0.005	0.131	1.799 ± 0.195
9b	135.063 ± 0.010	0.223	2.340 ± 0.189

The ^{4}He peaks at 5 K from fig. 5.6 (a) were fitted with Gaussian lineshapes (fig. 5.5 (b)) and the parameters were given in table 5.2. The ^{4}He peaks at 100 K from fig. 5.6 (c) were fitted with Gaussian lineshapes and the parameters are given in table 5.4.

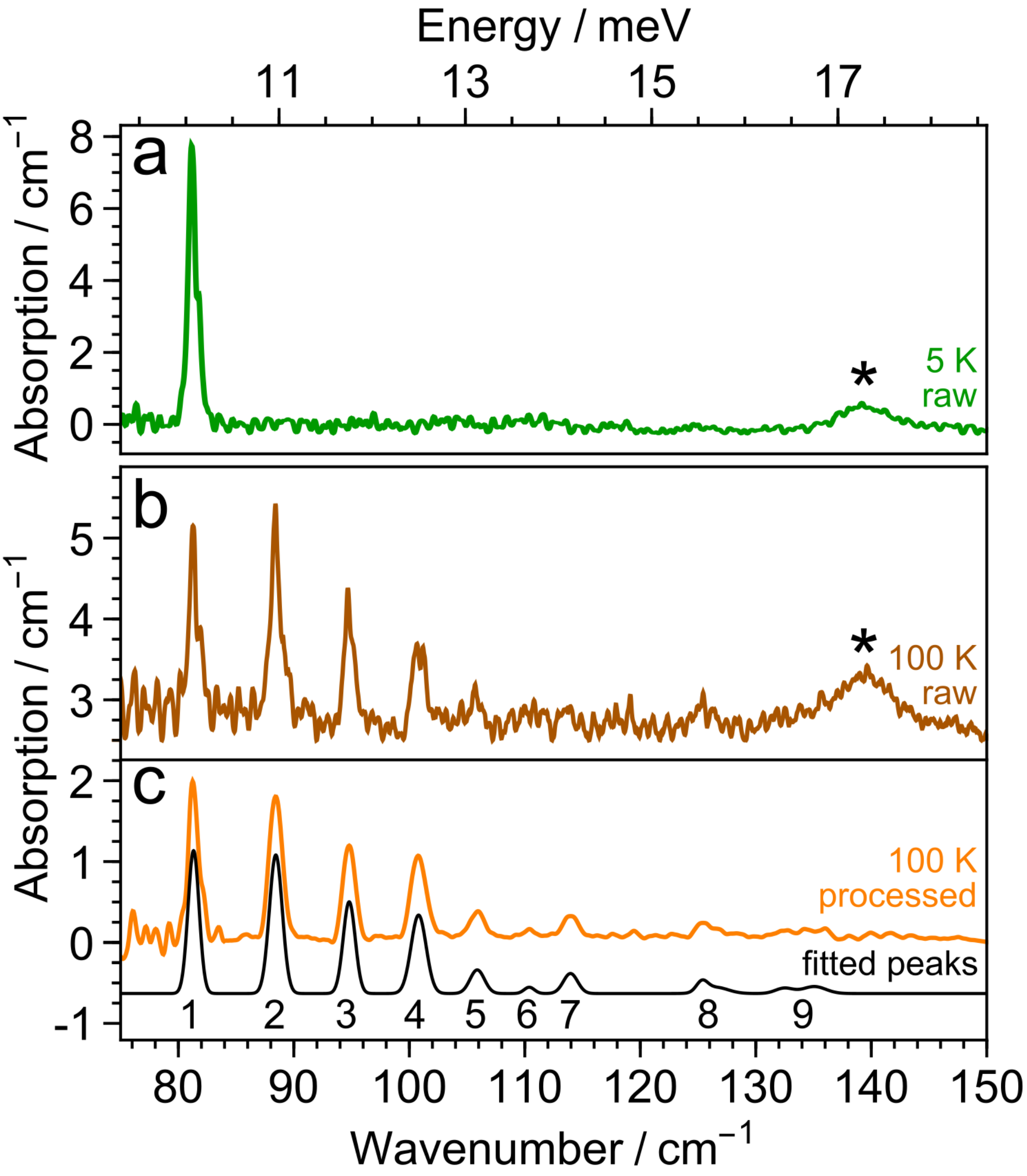

FIGURE 5.6: THz absorption spectra of ^{4}He@C$_{60}$ (f=0.843) at 5 K and 100 K in the 77-150 cm^{-1} region. **(a)** shows the 5 K raw spectrum in green. **(b)** shows the 100 K raw spectrum in dark orange. Broad background peak at ∼ 140 cm^{-1} is marked with an asterisk. **(c)** shows the 100 K processed spectrum in orange, after subtracting the ∼ 140 cm^{-1} broad background peak using the 5 K spectrum (from (a)) and applying Savitzky-Golay smoothing. Peaks fitted with Gaussian lineshapes are shown in black, with fitting parameters in table 5.4.

5.3.2.2 ^{3}He@C$_{60}$ results

The THz (far-IR) spectra at cryogenic temperatures were measured on ^{3}He@C$_{60}$ (95.1±0.7% filled) sublimed powder. In fig. 5.7 (a) the wide THz spectrum of ^{3}He@C$_{60}$ is shown at 5 K and 100 K (with 0.1 cm^{-1} resolution).

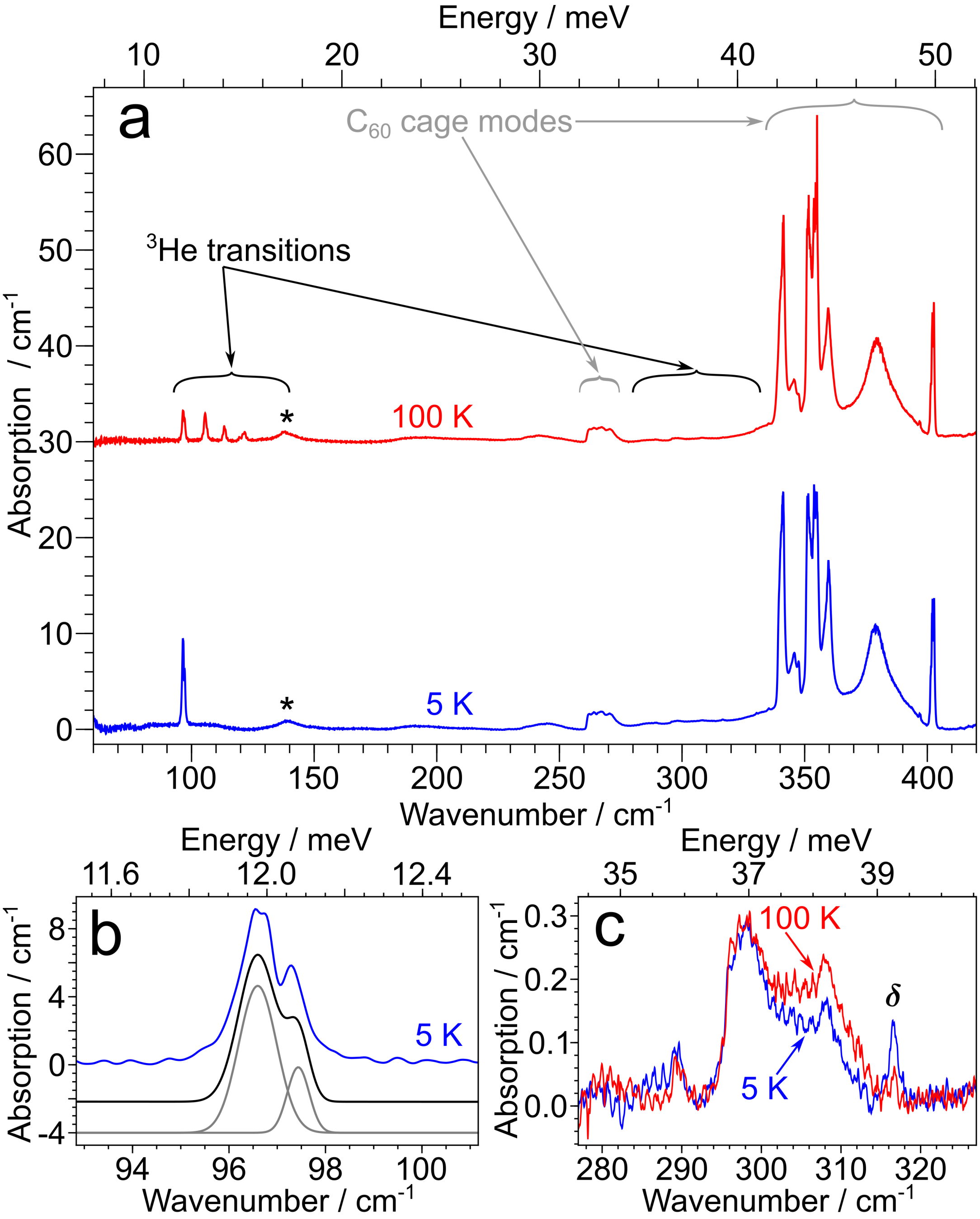

FIGURE 5.7: THz absorption spectra of ^{3}He@C$_{60}$ (f=0.951) at 5 K and 100 K. **(a)** displays the full spectra: blue for 5 K and red for 100 K. **(b)** shows the fundamental peak at 5 K in blue (from (a)), with Gaussian lineshape fitting in black and the two fitted components in gray (fitting parameters in table 5.5). **(c)** shows the spectra from (a) in the 280-320 cm^{-1} region; δ peak fitted with Gaussian lineshape and the parameters are found in table 5.6. Background peaks are marked with an asterisk.

The spectra present discrete peaks for the endohedral ^{3}He and for the C$_{60}$ cage, annotated in fig. 5.7 (a). C$_{60}$ cage modes are seen at ∼265 cm^{-1} and past 330 cm^{-1}. At 140 cm^{-1} there is a broad background feature, marked with an asterisk, which is rather unaffected by temperature (this is used later for background subtraction). Transitions corresponding to ^{3}He are seen between 80-150 cm^{-1} and between 280-320 cm^{-1}.

- ^{3}He **transitions between 80-150** cm^{-1}**:**

At 5 K the fundamental transition of ^{3}He is observed at ∼97 cm^{-1} (fig. 5.7 (a)). A closer look actually reveals two peaks corresponding to this transition, split apart by 0.839 ± 0.008 cm^{-1}, in intensity ratio of approximately 8:2; this fine structure is seen in fig. 5.7 (b) together with two fitted Gaussian lineshapes and the peak fitting parameters are found in table 5.5. The more intense component (1a) seems to have a splitting itself and a fitting using 3 Gaussian lineshapes was attempted but with no success. At high temperature (100 K) the ∼97 cm^{-1} transition decreases in intensity and many hot-band transitions appear at 100-150 cm^{-1} (fig. 5.7 (a) and fig. 5.8). The decrease in intensity with increase in temperature indicates that the ∼97 cm^{-1} transition originates in the ground state. The opposite behaviour for the other peaks indicate they are hot-band transitions, originating in excited states only populated at elevated temperatures.

TABLE 5.5: Parameters for the observed splitting (0.839 ± 0.008 cm^{-1}) of the fundamental ^{3}He@C$_{60}$ transition ∼97 cm^{-1}, at 5 K from fig. 5.7 (b). Fitting done using Gaussian lineshapes.

Peak	Wavenumber / cm^{-1}	Area / cm^{-2}	Ratio	FWHM / cm^{-1}
1a	96.596 ± 0.004	8.514	79.451%	0.926 ± 0.010
1b	97.435 ± 0.006	2.202	20.549%	0.537 ± 0.014

- ^{3}He **transitions between 280-320** cm^{-1}**:**

For ^{3}He at 5 K in the region 280-320 cm^{-1}, a rather weak transition is seen at 316.6 cm^{-1} (fig. 5.7 (c)). This peak decreases in intensity at 100 K, indicating it originates in the ground state; peak fitting parameters found in table 5.6, where the background has been accounted for. Fig. 5.7 (c) presents significant background signal other than the identified peak. However, it remains quite unaffected by a change in temperature so it is assumed no other ^{3}He peaks are present in this range; the slight increase in intensity around 308 cm^{-1} at 100 K is not understood yet, assumed to be just background contribution.

TABLE 5.6: Parameters peak fittings for ^{3}He@C$_{60}$ at 5 K and 100 K, from fig. 5.7 (c). Fitting done using Gaussian lineshapes and completely subtracting the background.

Peak	Temperature	Wavenumber / cm^{-1}	Area / cm^{-2}	FWHM / cm^{-1}
δ	5 K	316.601 ± 0.015	0.165	1.442 ± 0.035
δ	100 K	316.698 ± 0.021	0.027	0.579 ± 0.050

The rich peak structure seen at 80-150 cm^{-1} for ^{3}He at 100 K (fig. 5.7 (a)) needs a closer look. ^{3}He peaks are shown in the range 80-150 cm^{-1} at 5 K with 0.1 cm^{-1} resolution in fig. 5.8 (a) and at 125 K with 0.2 cm^{-1} resolution in fig. 5.8 (b).

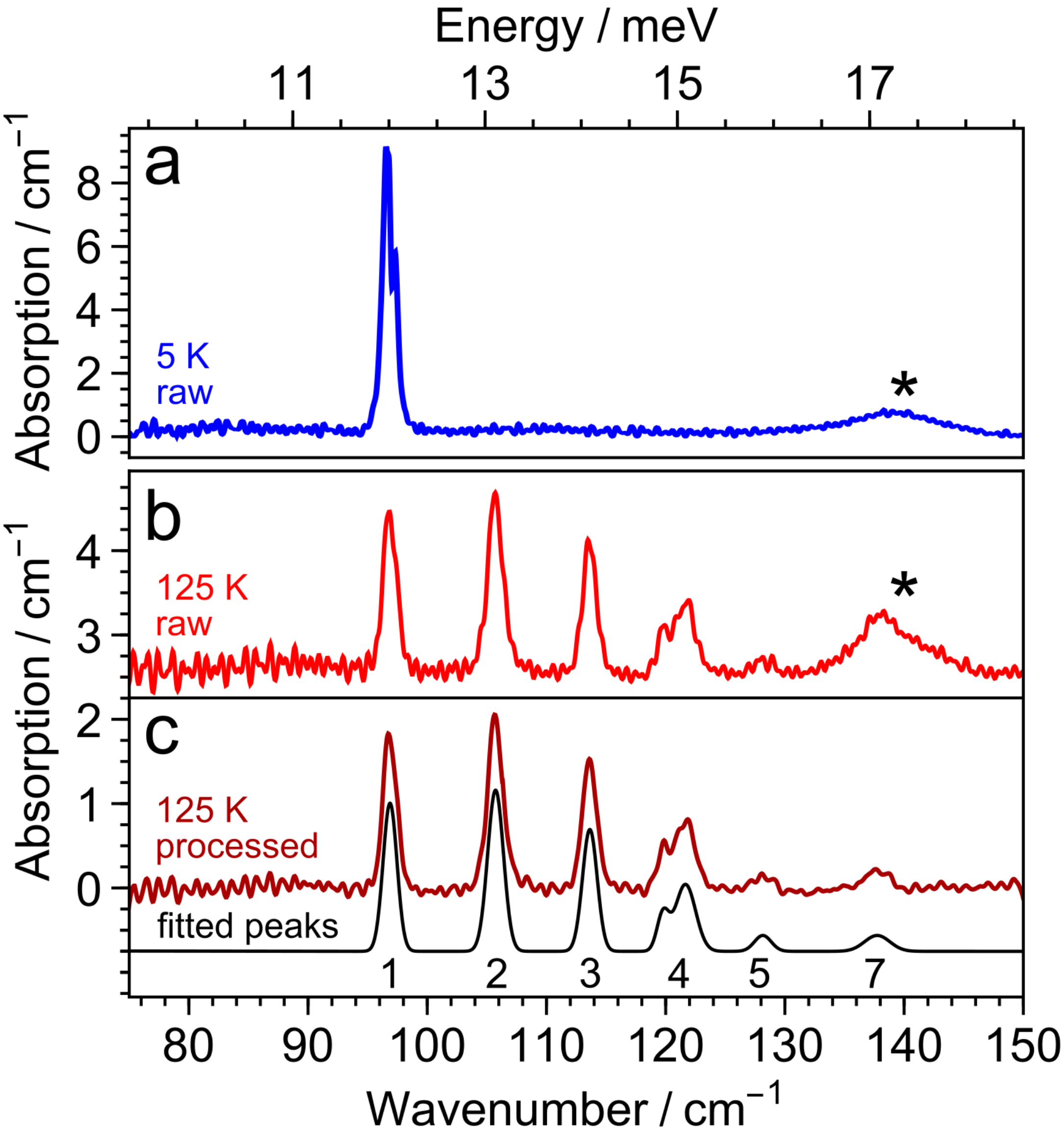

FIGURE 5.8: THz absorption spectra of ^{3}He@C$_{60}$ (f=0.951) at 5 K and 125 K in the 77-150 cm^{-1} region. **(a)** shows the 5 K raw spectrum in blue. **(b)** shows the 100 K raw spectrum in red. Broad background peak at $\sim$ 140 cm^{-1} is marked with an asterisk. **(c)** shows the 125 K processed spectrum in dark red, after subtracting the $\sim$ 140 cm^{-1} broad background peak using the 5 K spectrum (from (a)) and applying Savitzky-Golay smoothing. Peaks fitted with Gaussian lineshapes are shown in black, with fitting parameters in table 5.7.

A processed version of the ^{3}He spectrum at 125 K with 0.2 cm^{-1} resolution from fig. 5.8 (b) is shown in fig. 5.8 (c). Where in the range 100-150 cm^{-1} the 5 K spectrum from fig. 5.8 (a) was subtracted, in order to eliminate the broad background signal at $\sim$140 cm^{-1}. Afterwards, Savitzky-Golay smoothing (20 points) was applied to improve the spectrum.

The ^{3}He peaks at 5 K from fig. 5.8 (a) were fitted with Gaussian lineshapes (fig. 5.7 (b)) and the parameters were given in table 5.5. The ^{3}He peaks at 125 K from fig. 5.8 (c) were fitted with Gaussian lineshapes and the parameters are given in table 5.7.

TABLE 5.7: Parameters for peak fittings of ^{3}He@C$_{60}$ at 125 K, from fig. 5.8 (c). Fitting done using Gaussian lineshapes.

Peak	Wavenumber / cm^{-1}	Area / cm^{-2}	FWHM / cm^{-1}
1	96.855 ± 0.005	2.659	1.374 ± 0.013
2	105.709 ± 0.005	3.289	1.562 ± 0.013
3	113.617 ± 0.007	2.311	1.452 ± 0.017
4a	119.752 ± 0.020	0.561	1.177 ± 0.043
4b	121.636 ± 0.016	1.756	2.008 ± 0.0378
5	128.126 ± 0.036	0.342	1.652 ± 0.075
7	137.719 ± 0.044	0.797	2.496 ± 0.097

5.3.3 Discussion

5.3.3.1 ^{4}He@C$_{60}$ discussion

The THz spectra of ^{4}He@C$_{60}$ were shown in section 5.3.2.1, where two regions were found to contain peaks corresponding to ^{4}He: 80-150 cm^{-1} and 280-320 cm^{-1}.

The fundamental ^{4}He peak appears at ~81 cm^{-1} and it displays a splitting of 0.727 ± 0.011 cm^{-1} (fig. 5.5 (b)). The energy of this transition corresponds well to the ones obtained by INS, using the IN4c instrument in section 4.2.2.2 and the IN1 instrument in section 4.3.2.2. Upon an increase in temperature the fundamental transition decreases in intensity and other hot-band transitions appear between 80-150 cm^{-1}; these are used to determine the potential that the Helium atom experiences when present inside the C$_{60}$ cavity, in section 6.2.

In the high energy region, a ^{4}He peak is found at ~284 cm^{-1}, which originates in the ground state. The hot-band equivalents of this transition are the peaks at 308.602 ± 0.022 cm^{-1} and 319.645 ± 0.079 cm^{-1}. These are found in fig. 5.5 (c) and their interpretation is given in section 6.2.

5.3.3.2 ^{3}He@C$_{60}$ discussion

The THz spectra of ^{3}He@C$_{60}$ were shown in section 5.3.2.2, where two regions were found to contain peaks corresponding to ^{3}He: 80-150 cm^{-1} and 280-320 cm^{-1}.

The fundamental ^{3}He peak appears at ~97 cm^{-1} and it displays a splitting of 0.839 ± 0.008 cm^{-1} (fig. 5.7 (b)). The energy of this transition corresponds well to the ones obtained by INS, using the IN4c instrument in section 4.2.2.1 and the IN1 instrument in section 4.3.2.1. The energy is also the same as in the first THz measurements, performed on a different ^{4}He@C$_{60}$ sample with lower filling factor (section 5.2.2). Upon an increase in temperature the fundamental transition decreases in intensity and other hot-band transitions appear between 80-150 cm^{-1}; these are used to determine the potential that the Helium atom experiences when present inside the C$_{60}$ cavity, in section 6.2.

In the high energy region, a ^{3}He peak is found at 316.601 ± 0.015 cm^{-1}, which originates in the ground state (fig. 5.7 (c)). The energy of this transition corresponds to the INS peak at 39.07 ± 0.14 meV (315.12 ± 1.13 cm^{-1}) from fig. 4.11 (a). This peak is at roughly three times the frequency of the fundamental peak and it is assigned as an overtone transition, see section 6.2 for more details. It is unclear why such a transition is allowed in THz spectroscopy.

5.3.3.3 He@C$_{60}$ fundamental peak splitting

Both fundamental THz transitions of ^{3}He@C$_{60}$ and ^{4}He@C$_{60}$ displayed a small splitting, of 0.839 ± 0.008 cm^{-1} and 0.727 ± 0.011 cm^{-1} respectively. The two components have unequal intensities (peak areas), of ratio 79.5 : 20.5 for ^{3}He@C$_{60}$ and 83.9 : 16.1 for ^{4}He@C$_{60}$. One can see roughly the same 8 : 2 ratio of the peak areas for both compounds, but the splitting is larger for ^{3}He@C$_{60}$ than for ^{4}He@C$_{60}$. This splitting was not observed in the INS measurements. This is because the experimental resolution is significantly reduced in INS compared with THz spectroscopy.

This type of splitting is rather common for endohedral species and it has been seen in other C$_{60}$ molecular endofullerenes.[19,22,26–29] The endofullerenes H$_2$@C$_{60}$, H$_2$O@C$_{60}$ and HF@C$_{60}$ present a splitting between 1-4 cm^{-1} of the J=1 rotational state. This symmetry breaking has been studied computationally by Zlatko Bačić[117] where he showed that this splitting can be explained by considering the nearest neighbours of the endofullerene cage. Essentially the electron-rich HH bonds of the central endofullerene cage can point towards the electron-poor pentagonal faces (P-orientation) or the hexagonal faces (H-orientation) of the nearest neighbours.[54,118] The P-orientation was shown to be lower in energy and more populated at low temperatures (< 90 K) and ambient pressure.[118] It was shown that these orientations lead to a quadrupolar potential which interacts with the quadrupolar moment of the endohedral molecule leading to a splitting of the rotational energy levels. The P-orientation was shown to be mainly responsible for the splitting, whereas the H-orientation would lead to a splitting 30 times smaller. Also, the magnitude of the splitting was shown to scale with the molecular quadrupole moment.[117] In another computational study on the same molecular endofullerenes, the pure translational levels were shown to have a splitting one order of magnitude smaller than the J=1 rotational state.[119] All of these arguments seem to not relate with our He@C$_{60}$ THz results. The helium atom should not have an electric quadrupole moment given that both electrons are paired in a s-orbital. Also, the splittings of the ^{3}He@C$_{60}$ and ^{4}He@C$_{60}$ fundamental transitions (0.727-0.839 cm^{-1}) are a bit smaller than the J=1 rotational splitting and a bit larger than the predicted splittings of the pure translational states, for H_2@C_{60}, H_2O@C_{60} & HF@C_{60}.[22,26–29,120]

The observed He@C_{60} fundamental splittings (0.727-0.839 cm^{-1}) and the component ratios ($\sim 8:2$) are consistent with the merohedral disorder of the P and H orientations mentioned above. Most likely each type of orientation does not split the fundamental transition, but actually generates two distinct P and H populations in the sample. Each population generates a transition with a slightly different frequency; and this frequency difference corresponds to the experimental splitting. This seems like a valid argument, since at low temperatures (< 90 K) and ambient pressure the P : H ratio of the populations in C_{60} is 83.5 : 16.5, from reference 118. The peak ratio for ^{4}He@C_{60} of 83.9 : 16.1 matches almost exactly with the P : H ratio for C_{60} above, whereas for ^{3}He@C_{60} the ratio of 79.5 : 20.5 is close enough. However, the larger splitting seen for the ^{3}He isotope is not fully understood yet.

5.4 Conclusion

To conclude, far-IR measurements of ^{3}He@C_{60} and ^{4}He@C_{60} have been presented. In an initial set of experiments, the THz spectrum of ^{4}He@C_{60} was detected, where the fundamental transition and a couple of hot-band transitions were identified. The ^{4}He fundamental transition was in agreement with the INS results from chapter 4 (section 4.2 and section 4.3). Magnetic field dependent far-IR measurements were performed, at 0-14 T, on the ^{4}He@C_{60} sample, yet no observable change was detected in the spectrum. The ^{3}He@C_{60} THz spectrum was not observed due to the low filling factor of this sample.

A second set of measurements successfully acquired the THz spectra of both ^{3}He@C_{60} and ^{4}He@C_{60}. This was possible since the filling factors were greatly increased through recycling-HPLC. The new ^{4}He@C_{60} THz data was in agreement with previous results from section 5.2. The fundamental ^{3}He@C_{60} THz transition was identified, which is in agreement with the INS measurements from chapter 4 (section 4.2 and section 4.3)

Besides the fundamental peaks of ^{4}He@C_{60} and ^{3}He@C_{60}, at $\sim$81 cm^{-1} and $\sim$97 cm^{-1}, THz hot-band transitions have been identified for both ^{3}He@C_{60} and ^{4}He@C_{60}. Furthermore, another set of THz peaks were identified at higher energies, in the 280-320 cm^{-1} range for both ^{3}He@C_{60} and ^{4}He@C_{60}. The interpretation of these transitions is given in section 6.2.

A splitting of the fundamental transition is observed for both ^{3}He@C_{60} and ^{4}He@C_{60}, of 0.839 ± 0.008 cm^{-1} and 0.727 ± 0.011 cm^{-1} respectively. The relative intensities of the components of $\sim 8:2$ seems to be consistent with the P-orientation and H-orientation merohedral disorder of C_{60}.[118]

The most impressive fact of this chapter is that a noble gas atom such as Helium, with no electric charge or permanent dipole moment, which does not interact with low energy electromagnetic radiation, when enclosed in the C_{60} cage it absorbs THz radiation generating a rich spectrum of peaks in the far-IR.

5.4.1 Future work

The small splitting seen for the fundamental THz transition of $^3He@C_{60}$ and $^4He@C_{60}$ will be investigated further. The larger splitting seen for $^3He@C_{60}$ is not understood yet. Further investigation will be done on the $He@C_{60}$ system, to completely understand this symmetry breaking behaviour of the endohedral Helium atom. The explanation of the symmetry breaking will be attempted using the known merohedral disorder of the C_{60} molecules in the lattice.

After seeing the astonishing THz results of $He@C_{60}$, plans have been made to try and complete the story of noble gas endofullerenes. Far-IR measurements will be attempted on $Ne@C_{60}$, $Ar@C_{60}$, $Kr@C_{60}$, etc..

Chapter 6

Translational quantization of noble gas C_{60} endofullerenes

6.1 Introduction

INS and THz experiments on noble gas endofullerenes were shown in chapter 4 and chapter 5. The measurements demonstrated that when noble gas atoms are translationally confined, they exist in well-defined quantum states, which have transitions between eigenstates observable by INS and THz.

The two techniques INS and THz are ideal to use because of their complementarity, which stems from the selection rules associated with each. INS has almost no selection rules so in principle any transitions can be observed. This is very useful at the lowest temperatures, since only the ground state is populated and all transitions originate from it; which can give an overview of the whole landscape of energy levels. Due to the difficulty associated with using neutrons for spectroscopy, usually INS has an inherent lower spectral resolution than THz. However, THz spectroscopy suffers from the usual selection rules associated with electromagnetic radiation, $\Delta\ell = 0, \pm 1$ and $\Delta m = 0, \pm 1$, where ℓ and m are the usual angular momentum quantum numbers.[43–45]

The benefit of investigating translational quantization is to gain knowledge about the non-covalent interactions at play. Such non-bonded interactions are difficult to measure experimentally, and in general scientists have to rely on high level quantum chemistry calculations. However, without having an experimental result to compare with, the result of various quantum chemistry simulations have questionable validity.

The INS and THz experimental results, from chapter 4 and chapter 5, are theoretically analysed in this chapter. A model is assumed which describes dynamics of the endohedral noble gas atom, and the experimental observations are explained based on this model.

6.1.1 Theory

6.1.1.1 Quantum mechanics for spherically symmetric potentials

Central to quantum mechanics is the time independent Schrödinger equation:[42]

$$\hat{H}(\mathbf{r}_1, \mathbf{r}_2 \ldots)\psi_{\mathbf{q}}(\mathbf{r}_1, \mathbf{r}_2 \ldots) = E_{\mathbf{q}}\psi_{\mathbf{q}}(\mathbf{r}_1, \mathbf{r}_2 \ldots) \tag{6.1}$$

where the vectors $\mathbf{r}_1$, $\mathbf{r}_2 \ldots$ are the coordinates of the particles, the quantum state is described by the eigenfunction $\psi_{\mathbf{q}}(\mathbf{r}_1, \mathbf{r}_2 \ldots)$, $\mathbf{q}$ represents any set of quantum numbers ($\mathbf{q} = \{q_1, q_2 \ldots\}$) and $E_{\mathbf{q}}$ is the eigenvalue (energy) of the eigenfunction $\psi_{\mathbf{q}}$. When applying the Hamiltonian operator $\hat{H}$ (eq. 6.2) to the eigenfunction $\psi_{\mathbf{q}}$, one obtains the eigenfunction back and the eigenvalue $E_{\mathbf{q}}$ associated with it. The Hamiltonian operator $\hat{H}$ is given by:

$$\hat{H}(\mathbf{r}_1, \mathbf{r}_2 \ldots) = -\sum_{i=1}^{N} \frac{\hat{p}_i^2}{2M_i} + V(\mathbf{r}_1, \mathbf{r}_2 \ldots) \tag{6.2}$$

where $\hat{p}_i$ and M_i are the momentum operator and mass for particle i. In the absence of a potential V, eq. 6.2 is the Hamiltonian for a free particle. For the cases studied here the potential is not zero, and for endofullerenes V is the confining potential which keeps the endohedral moiety enclosed. The meaning of V is such that a quantum particle i at coordinates $\mathbf{r}_1$ has potential energy given by $V(\mathbf{r}_1)$.

In the cases of noble gas endofullerenes studied here, there is only one confined particle so the eigenfunction depends only on three spatial variables, so $\psi_{\mathbf{q}}(\mathbf{r}_1, \mathbf{r}_2 \ldots) = \psi_{\mathbf{q}}(r, \theta, \phi)$ in spherical polar coordinates. Usually done in quantum mechanics, in order to solve the Schrödinger equation, we separate the variables of the wavefunction into a radial part and angular part:

$$\psi_{\mathbf{q}}(r, \theta, \phi) = R_{\mathbf{q}}(r)Y_{\mathbf{q}}(\theta, \phi) \tag{6.3}$$

Then we separate the Schrödinger equation into a radial (eq. 6.4) equation and an angular equation (eq. 6.6)[42] , where M is the mass of the particle:

$$-\frac{\hbar}{2M}\frac{\partial^2 u_{\mathbf{q}}}{\partial r^2} + \left[V(r) + \frac{\hbar^2}{2M}\frac{\ell(\ell+1)}{r^2}\right]u_{\mathbf{q}} = E_{\mathbf{q}}u_{\mathbf{q}} \tag{6.4}$$

$$u_{\mathbf{q}}(r) = rR_{\mathbf{q}}(r) \tag{6.5}$$

$$sin(\theta)\frac{\partial}{\partial\theta}\left(sin(\theta)\frac{\partial Y_{\mathbf{q}}}{\partial\theta}\right) + \frac{\partial^2 Y_{\mathbf{q}}}{\partial\phi^2} = -\ell(\ell+1)sin^2(\theta)Y_{\mathbf{q}} \tag{6.6}$$

The wavefunctions which solve the angular equation are called spherical harmonics[42] and are given below:

$$Y_{\ell m}(\theta,\phi) = \sqrt{\frac{(2\ell+1)}{4\pi}\frac{(\ell-m)!}{(\ell+m)!}}e^{im\phi}P_\ell^m(cos(\theta)) \tag{6.7}$$

$$P_\ell^m(x) = (-1)^m(1-x^2)^{m/2}(\frac{d}{dx})^m P_\ell(x) \tag{6.8}$$

$$P_\ell(x) = \frac{1}{2^\ell \ell!}(\frac{d}{dx})^\ell (x^2-1)^\ell \tag{6.9}$$

Where $P_\ell^m(x)$ are the associated Legendre functions and $P_\ell(x)$ are the Legendre polynomials. Thus, for the angular part of the Schrödinger equation the solutions are known.

For the radial part of the Schrödinger equation the solutions are not known in the general case because the wavefunctions strongly depend on the potential $V(r)$.

6.1.1.2 3D quantum harmonic oscillator

The spherically symmetric case of eq. 6.2, where $V(r) = V_2 r^2 = \frac{1}{2}kr^2$, is well known as the 3D quantum Harmonic Oscillator (HO), where $k = M\omega^2$. The Hamiltonian ($\hat{H}_0$) for the spherically symmetric 3D harmonic oscillator is:

$$\hat{H}_0 = -\frac{\hat{p}^2}{2M} + V_2 r^2 = -\frac{\hat{p}^2}{2M} + \frac{k}{2}r^2 \tag{6.10}$$

To find the wavefunctions of the 3D harmonic oscillator (HO), we have to separate them into radial and angular parts:[121,122]

$$\psi_{n_r \ell m}(r,\theta,\phi) = R_{n_r \ell}(r) Y_{\ell m}(\theta,\phi) \tag{6.11}$$

The angular part of the wavefunction are the spherical harmonics Y_ℓ^m given in eq. 6.7. The radial part of the wavefunction for the 3D HO is given below:[121,122]

$$R_{n_r \ell}(r) = \frac{N_\ell^{n_r}}{b^{3/2}}(\frac{r}{b})^\ell e^{-r^2/2b^2} L_{n_r}^{(\ell+\frac{1}{2})}(\frac{r^2}{b^2}) \tag{6.12}$$

$$N_\ell^{n_r} = \sqrt{\frac{2^{n_r+\ell+2} n_r!}{\sqrt{\pi}(2n_r+2\ell+1)!!}} \tag{6.13}$$

$$b = \sqrt{\frac{\hbar}{M\omega}} = \sqrt{\frac{\hbar}{\sqrt{Mk}}} \tag{6.14}$$

$$\omega = \sqrt{\frac{k}{M}} \tag{6.15}$$

Where $N_\ell^{n_r}$ is a normalisation constant and $L_{n_r}^{(\ell+\frac{1}{2})}(x)$ are the generalised Laguerre polynomials. The quantum number n_r represents the number of radial nodes that the wavefunction $R_{n_r\ell}(r)$ posses.

The eigenvalues $E_{n_r\ell}$ of the 3D HO are given by:

$$\begin{aligned} E_{n_r\ell} &= \hbar\omega(\ell + 2n_r + \frac{3}{2}) \\ \ell &= 0,1,2,3... \ and \ n_r = 0,1,2,3... \\ n &= \ell + 2n_r \end{aligned} \tag{6.16}$$

Since the potential is spherically symmetric, the $2\ell + 1$ degeneracy of m substates of each ℓ state is not broken. The usual n quantum number of a harmonic oscillator is given by $n = \ell + 2n_r$, from which the more well-known equation for 3D HO eigenvalues follows; where $E_n = \hbar\omega(n + \frac{3}{2})$.

6.1.1.3 3D polynomial oscillator

The 3D HO quadratic potential ($V(r) = \frac{k}{2}r^2$) is too simple to realistically describe the confining potential of a noble gas atom inside C$_{60}$. Thus, we use a more general polynomial type potential:

$$V(r) = V_2r^2 + V_4r^4 + V_6r^6 \tag{6.17}$$

where $\{V_2, V_4, V_6\}$ are polynomial coefficients, assuming spherical symmetry for the angular part. Unfortunately, there are no analytic solutions of the radial Schrödinger equation (eq. 6.4) for such a polynomial potential. However, we can use numerical linear algebra computations to calculate the result, which converge when given a large enough basis set. In order to use such linear algebra techniques, we need the matrix representation of the corresponding Hamiltonian operators.

A matrix element from the matrix representation of a given Hamiltonian $\hat{H}^{(a)}$ is defined as:[42]

$$\langle\Psi_i|\hat{H}^{(a)}|\Psi_j\rangle = \int_0^\infty \int_0^\pi \int_0^{2\pi} \Psi_i^* \hat{H}^{(a)} \Psi_j \, r^2 \, sin(\theta) \; dr \; d\theta \; d\phi \tag{6.18}$$

The cases discussed here have spherical symmetry so the potential has no angular component. Thus, we can use the ortho-normality of the spherical harmonics below to simplify eq. 6.18 above.[42]

$$\int_0^\pi \int_0^{2\pi} Y_{\ell m}^* \, Y_{\ell' m'} \, sin(\theta) \; d\theta \; d\phi = \delta_{\ell\ell'} \, \delta_{mm'} \tag{6.19}$$

From eq. 6.19 it can be seen that the final Hamiltonian will be block diagonal, with each different ℓ subspace making up the blocks. Also, the spherically symmetric potential does not break the m degeneracy within each ℓ (of $2\ell + 1$).

When using the 3D harmonic oscillator as a basis, with the wavefunctions from eq. 6.11 as basis states, the matrix representation of its Hamiltonian $\hat{H}_0$ from eq. 6.10 is diagonal (see fig. 6.1) with eigenvalues $E_{n_r\ell}$ (eq. 6.16) on its entries.

$$\langle \psi_{n_r\ell m}|\hat{H}_0|\psi_{n_r'\ell' m'}\rangle = E_{n_r\ell}\,\delta_{nn'}\,\delta_{\ell\ell'}\,\delta_{mm'} \tag{6.20}$$

Where the Kronecker delta δ_{ab} = 1 if a=b and = 0 if a$\neq$b.

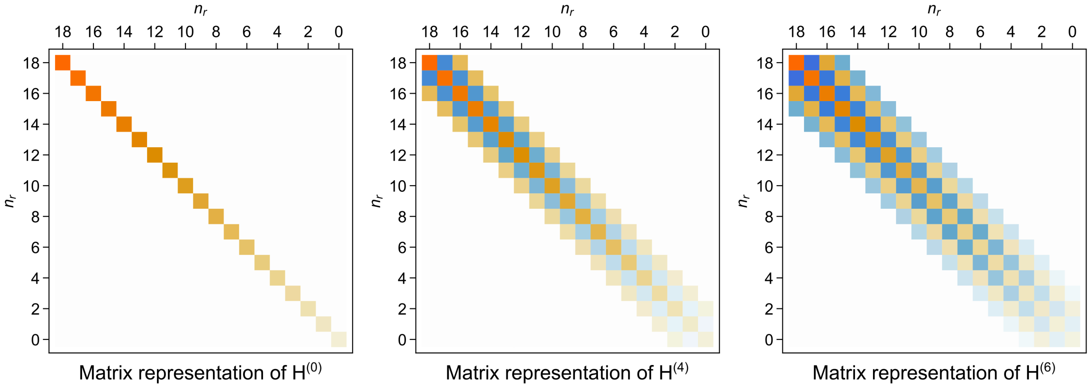

FIGURE 6.1: Matrix plot representations for $\hat{H}_0$, $\hat{H}^{(4)}$, $\hat{H}^{(6)}$ from eq. 6.22, with $n_r = 0, 1, ..., 18$ and $\ell = 0$. Similar plots are obtained for the other ℓ values. The color intensity scales with the magnitude of the matrix element. Orange represents positive matrix elements and blue negative

To obtain the general 3D polynomial oscillator one must compute the matrix representation of the leftover terms in the potential (eq. 6.17), namely $V_4r^4 + V_6r^6$, so we write:

$$\hat{H}^{(4)} = V_4r^4 \textit{ and } \hat{H}^{(6)} = V_6r^6 \tag{6.21}$$

By computing the integral of eq. 6.18 for $\hat{H}^{(4)}$ and $\hat{H}^{(6)}$ analytically, one can calculate all matrix elements of their matrix representation. However, now these matrix representations are not be in diagonal form because we are working in the $\hat{H}_0$ basis (see fig. 6.1).

Thus, the Hamiltonian for the 3D polynomial oscillator discussed here is made up of:

$$\hat{H} = \hat{H}_0 + \hat{H}^{(4)} + \hat{H}^{(6)} \tag{6.22}$$

Writing the matrix representation of $\hat{H}$, in the $\hat{H}_0$ basis, gives a non-diagonal matrix. Performing numerical diagonalisation of this matrix representation gives the final eigenvalues and eigenfunctions which best describe the He@C_{60} system. And subsequently it best describes the interaction between the Helium atom and the inner carbon surface. Transitions between these eigenstates are what is being observed in the THz and INS measurements.

If one could use an infinite basis set to perform the diagonalisation described above the obtained result would be exact for all eigenvalues and eigenfunctions. However, since working with an infinite basis set is currently impossible, we have to truncate the basis at some point. In the computations done here we used ℓ quantum numbers = 0, 1,..., 10 and n_r quantum numbers = 0, 1,..., 18 (see fig. 6.1 for $\ell = 0$ matrix representations). In other words, we used 11 ℓ blocks, each of 19 × 19 dimension ($n_r \times n_r$), since the m degeneracy was ignored. Thus, we ensured convergence for all lower energy eigenvalues (and eigenfunctions), the ones being probed in our measurements. To simplify the calculations only one m value was used, $m = 0$, due to the assumed spherical symmetry.

6.1.1.4 THz Oscillator line strengths

The frequency of the peaks in the THz and INS spectra depend on the difference between the 3D polynomial oscillator eigenvalues. However, it does not say anything about the intensities of these peaks; for this we need to make use of the Fermi golden rule[42] and assume some type of dipole moment operator. The dipole moment associated with the translational motion of the noble gas inside the C_{60} cage is assumed to be linear in the displacement from the cage centre r for simplicity. Written in spherical harmonics it reads:

$$\begin{aligned} d_{1m} &= \sqrt{\frac{4\pi}{3}} A_{1m}\, r\, Y_{1m}(\theta, \phi) \\ \text{where } m &= -1, 0, +1 \end{aligned} \tag{6.23}$$

where A_{1m} is the coefficient for the dipole moment operator. The He@C_{60} cages are randomly oriented, so are the dipoles, and averaging over all orientations gives $|d|^2 = (d_x^2 + d_y^2 + d_z^2)/3$.[123] Spherical symmetry is assumed, therefore the induced dipole moment does not depend on the direction of displacement. Thus, all three components of the induced dipole moment are the same.

The THz absorption line area is written using the Fermi golden rule,[22,42,114] for linearly polarised light in the z direction ($d_z \equiv d_{10}$):

$$\int_{\omega_{fi}} \alpha_{fi}(\omega)\mathrm{d}\omega = Nf\frac{2\pi^2}{h\epsilon_0 c_0 \eta}\left(\frac{\eta^2+2}{3}\right)^2 \omega_{fi}\left(p_i - p_f\right)\sum_{m_i,m_f}\left|\left\langle n_{r_f}, l_f, m_f\right| d_{10}\left|n_{r_i}, l_i, m_i\right\rangle\right|^2, \tag{6.24}$$

each ℓ state is $(2\ell+1)$ is degenerate in m, so summation is done over all m_i and m_f. The integral is taken over the whole frequency range ω_{fi} spanning the THz spectrum. $N = 1.48 \times 10^{27}\mathrm{m}^{-3}$ is the number density of molecules in solid C_{60}, f is the filling factor of the endofullerene, c_0 is the speed of light in vacuum, ϵ_0 is the permittivity of vacuum, η is the index of refraction (for C_{60} $\eta = 2$[115])

In spherical symmetry $d_x = d_y = d_z$, so eq. (6.24) is valid for randomly polarised radiation as well.

The factor $(\eta^2+2)/3$ is the electric field felt by the oscillator being present in a dielectric medium.[124] h is the Planck constant. $\omega_{fi} = (E_f - E_i)/hc_0$, where E_i and E_f are the energies of the initial and final state.

p_i and p_f are the thermal Boltzmann populations of the initial and final states:

$$p_i = \frac{e^{-E_i/k_BT}}{\sum_j(2\ell_j+1)e^{-E_j/k_BT}}. \tag{6.25}$$

where k_B is the Boltzmann constant and T is the temperature in Kelvin.

The sum over m in Eq. (6.24) equals to:[125]

$$\sum_{m_i,m_f}\left|\left\langle n_{r_f}, \ell_f, m_f\right| d_{10}\left|n_{r_i}, \ell_i, m_i\right\rangle\right|^2 = \frac{1}{3}\left|\left\langle n_{r_f}, \ell_f\right| |d_1| \left|n_{r_i}, \ell_i\right\rangle\right|^2, \tag{6.26}$$

where the m dependence has disappeared and $\left|\left\langle n_{r_f}, \ell_f\right| |d_1| \left|n_{r_i}, \ell_i\right\rangle\right|$ is the reduced matrix element of d_{1q}.

The angular part of the reduced matrix element is:[25,44]

$$\left\langle \ell_f \right| |T_k| \left|\ell_i\right\rangle = (-)^{-\ell_f}\sqrt{\frac{(2\ell_f+1)(2k+1)(2\ell_i+1)}{4\pi}}\begin{pmatrix} \ell_f & k & \ell_i \\ 0 & 0 & 0 \end{pmatrix}, \tag{6.27}$$

where T_k is a spherical tensor operator of rank k and the six symbols in the brackets denote Wigner $3j$-symbol.[44] The $3j$-symbol is zero if $|\ell_f - \ell_i| \leq k \leq \ell_f + \ell_i$ is not satisfied. Another property of the $3j$-symbol from eq. (6.27), when $m_f = q = m_i = 0$ the $3j$-symbol is non-zero only if $\ell_f + k + \ell_i$ is even. For the dipole moment $k = 1$, ergo, the selection rule $\Delta\ell = \pm 1$ for THz absorption arises.

6.2 Translational quantization discussion

This section discusses the analysis and interpretation of the INS and THz results. Firstly, a small interpretation of the Ne@C_{60} INS results is shown and secondly an in-depth analysis of the He@C_{60} results are presented.

6.2.1 Neon translational quantization in Ne@C_{60}

The INS spectrum of Ne@C_{60} displayed some peaks, in fig. 4.15 (a). Only the most intense peak at 7.01±0.01 meV could be accurately assigned as the fundamental translational transition of the confined Neon atom. Since only one peak was observed in the spectrum, the same type of analysis done on He@C_{60} in section 6.2.2 was not possible on Ne@C_{60}. However, the 3D harmonic oscillator model can be assumed for Ne@C_{60} and the purely harmonic confining potential calculated, see section 6.1.1.2 for description of the 3D quantum harmonic oscillator.

Equation 6.16 gives the eigenvalues of the 3D harmonic oscillator. The fundamental transition is given by:

$$E_{01} - E_{00} = \hbar\omega = \hbar\sqrt{\frac{k}{M}} \tag{6.28}$$

Where M is the mass of the particle (Neon) and k is the harmonic constant (or force constant). The purely harmonic confining potential $V(r) = \frac{1}{2}kr^2$, so the force constant k is needed to define the Ne@C_{60} potential.

The isotopes of Neon are ^{20}Ne : ^{21}Ne : ^{22}Ne with natural abundances 90.5 : 0.27 : 9.22 and total neutron scattering cross sections 2.71 barn : 5.60 barn : 1.86 barn.[41] From these it can be seen that only the ^{20}Ne isotope can be observed in the INS spectrum. Taking the mass of ^{20}Ne with the fundamental transition of 7.01±0.01 meV gives a harmonic term $V_2 = \frac{1}{2}k = 117.5 \pm 0.3\,\mathrm{meV\,\AA^{-2}}$ ($= 1.883 \pm 0.005\,\mathrm{Jm^{-2}}$). This is much larger than the harmonic term for He@C_{60} confining potential, where $V_2 \simeq 25$ meV (see section 6.2.2). The steeper potential for Ne@C_{60} is expected since the Neon atom has a larger van der Waals radius than Helium and a smaller free volume as a result. This translates to a steeper confining potential for Ne@C_{60}.

Further experiments are planned for Ne@C_{60} to hopefully detect more than one transition and describe the confining potential to the same level of accuracy as done for He@C_{60} in the following section.

6.2.2 Helium translational quantization in He@C_{60}

This section gives an interpretation of the He@C_{60} INS and THz experiments. The focus is on the second round of INS and THz measurements, section 4.3 and section 5.3

respectively; since the new measurements match with the previous ones and bring new information. The analysis was done in collaboration with the group of Toomas Rõõm.

Firstly, a description of the quantum mechanics of the confined Helium atom is required. Two such models are the "particle in a box" and the quantum harmonic oscillator. The eigenvalues of both models are dependent on the mass of the quantum particle and this defines the ratio between the fundamental transitions.[42] For the "particle in a box" the ratio equals the inverse of the masses, for the two Helium isotopes = $\frac{4}{3} = 1.333$. For the quantum harmonic oscillator, the ratio equals the inverse square root of the masses = $\frac{\sqrt{4}}{\sqrt{3}} = 1.155$. From our measurements the ratio of the two transitions is = $\frac{11.90 \pm 0.01 \text{ meV}}{9.86 \pm 0.01 \text{ meV}} = 1.207 \pm 0.002$ from INS and $\frac{\sim 96.8 \text{ cm}^{-1}}{\sim 81.4 \text{ cm}^{-1}} = 1.189$ from THz. This simple argument suggest a model based on the harmonic oscillator is better suited to describe the confined Helium atom.

However, for a harmonic oscillator all transitions between successive eigenvalues have the same energy, so only one peak should be observed. This is different from the comb of THz peaks observed in the spectra of both ^{3}He@C$_{60}$ and ^{4}He@C$_{60}$. The spacing between the THz peaks probe the an-harmonicity of the potential. This suggest a deviation from the quadratic potential of a harmonic oscillator. To account for this, an-harmonic terms are added to the potential confining the Helium atom. The quantum mechanics of the three-dimensional harmonic oscillator together with the 3D an-harmonic (polynomial) oscillator are given in section 6.1.1.

The potential energy of a Helium atom inside C$_{60}$ is in general given by $V(r, \theta, \phi)$, where r is the distance of the Helium atom from the cage centre. We assume spherical symmetry of the potential given the high degree of symmetry of the C$_{60}$ molecule. This means the potential has no angular dependence and can be simplified $V(r, \theta, \phi) \simeq V(r)$. The 3D polynomial oscillator used here has the potential given by the superposition of three terms:

$$V(r) = V_2 r^2 + V_4 r^4 + V_6 r^6 \tag{6.29}$$

where $\{V_2, V_4, V_6\}$ are the polynomial coefficients which set the dependence on even powers of r. This produces a more realistic potential, which describes the dynamics of confined Helium more accurately.

The eigenvalues of the polynomial oscillator depend quite strongly on the polynomial coefficients and the mass of the confined particle. Transitions between such eigenvalues are being probed in the INS and THz experiments. By matching the transitions probed by our measurements, the coefficients of the confining potential can be found with great precision. There are essentially no selection rules for INS,[41] whereas THz has the usual selection rule for electromagnetic radiation $\Delta\ell = 0, \pm 1$.[43,44]

Since the experimental resolution is higher for THz and more peaks were identified than in the INS measurements, the THz spectra were mainly used in the analysis. The THz spectrum can be simulated using eq. 6.24, as described in section 6.1.1. A best fit match of the simulation with the experimental spectrum determines the coefficients of the potential and the dipole moment operator.

The peaks in the experimental THz spectra were fitted with Gaussian lineshapes in section 5.3. A synthetic spectrum $y(\omega)$ of resolution 0.25 cm^{-1} was generated by using the frequencies and areas of the fitted peaks and using a constant FWHM of 1 cm^{-1} for all synthetic peaks. For a given set of parameters $\kappa = \{V_2, V_4, V_6, A_{10}\}$ of the potential with the dipole moment coefficient, at a given temperature, the THz spectrum was simulated ($f(\omega, \{\kappa\})$) using eq. 6.24, in its analytic form using the Wolfram Mathematica software. The parameters were varied in order to minimise the sum of least squares $\chi^2 = \sum[y(\omega) - f(\omega, \{\kappa\})]^2$. The confidence limits for each parameter κ_i were calculated using the second derivatives of χ^2 as shown below:[126]

$$\Delta\kappa_i = \sqrt{2\chi^2 \left(\frac{\partial^2\chi^2}{\partial\kappa_i^2}\right)^{-1}}. \tag{6.30}$$

The THz spectra were fitted this way in the region 77-150 cm^{-1} and the simulated spectra together with experimental spectra are shown in fig. 6.2 (a) and (b) for $^3\mathrm{He@C}_{60}$ and $^4\mathrm{He@C}_{60}$ respectively. The potential and dipole moment parameters which resulted from the fitting are given in table 6.1. The coefficients for the two isotopes are slightly different, however, when plotting them there is no observable difference. The interaction potential is expected to be the same for the two isotopes since the electronic structures of $^3\mathrm{He}$ and $^4\mathrm{He}$ are the same.

TABLE 6.1: Best fit coefficients, with confidence limits, for the radial potential function $V(r) = V_2r^2 + V_4r^4 + V_6r^6$ and induced dipole moment $d_{10} = \sqrt{\frac{4\pi}{3}}A_{10}\, r\, Y_{10}(\theta,\phi)$ for $^3\mathrm{He@C}_{60}$ and $^4\mathrm{He@C}_{60}$. Parameters obtained by fitting the experimental THz spectra, 125 K $^3\mathrm{He@C}_{60}$ and 100 K $^4\mathrm{He@C}_{60}$ from fig. 6.2, in the 77-150 cm^{-1} range.

Parameter	$^3\mathrm{He@C}_{60}$	$^4\mathrm{He@C}_{60}$
V_2 / meV Å^{-2}	25.80 ± 0.11	24.998 ± 0.016
V_4 / meV Å^{-4}	33.7 ± 0.6	36.1 ± 0.6
V_6 / meV Å^{-6}	27.86 ± 0.05	26.34 ± 0.21
A_{10} / D Å^{-1}	$(4.20 \pm 0.05) \times 10^{-2}$	$(4.44 \pm 0.07) \times 10^{-2}$

The experimental spectra shown are the processed ones from fig. 5.8 for $^3\mathrm{He@C}_{60}$ and from fig. 5.6 for $^4\mathrm{He@C}_{60}$. The black curves represent simulations done using eq. 6.24 with the best fit parameters of the potential and dipole moment from table 6.1. The vertical bars on the spectrum indicate the frequencies and amplitudes for each individual

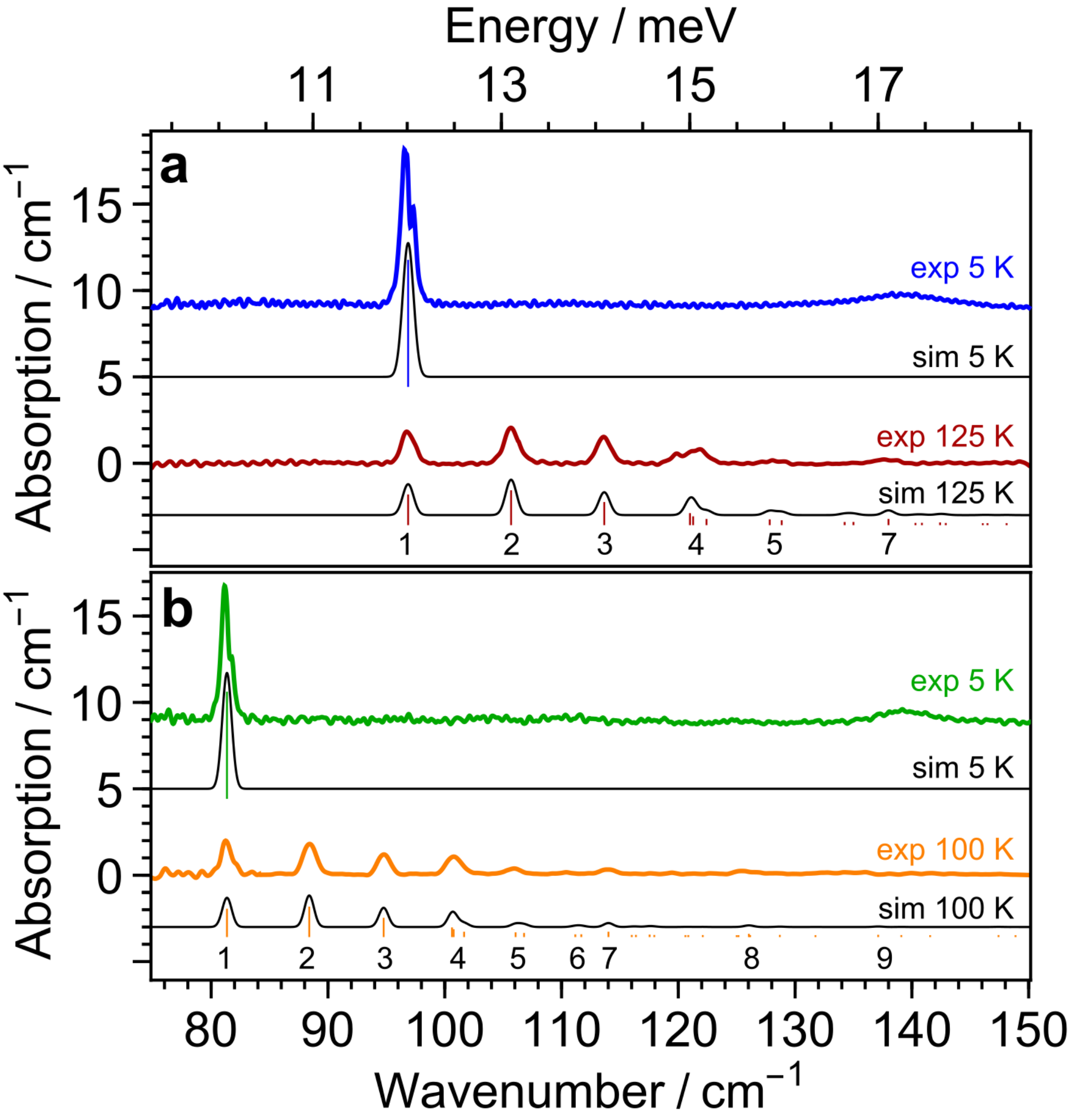

FIGURE 6.2: **(a)** THz spectra of ^{3}He@C$_{60}$ at 5 K in blue and 125 K in dark red, from fig 5.8 (a) and (c). **(b)** THz spectra of ^{4}He@C$_{60}$ at 5 K in green and 100 K in orange, from fig 5.6 (a) and c. Underneath each experimental spectrum the result of the simulation at the same temperature, using the potential parameters from table 6.1, is shown in black. The vertical bars indicate the simulated frequencies and amplitudes of each transition, which summed up give the black curve. Transitions are labelled according to the assignment from the energy level diagram from figure 6.3 (b).

simulated transition, which also shows that some peaks are composed of more than one transition. The annotation of the peaks is the same as shown in section 5.3, and it is done according to the assignment of the transitions from the energy level diagram shown in fig. 6.3, where some peaks are shown to correspond to more than one transition. On the energy diagram all levels with the same ℓ quantum number have the same color: $\ell = 0$ in black, $\ell = 1$ in red, $\ell = 2$ in orange, $\ell = 3$ in yellow, $\ell = 4$ in green, $\ell = 5$ in blue and $\ell = 6$ in purple. The levels on the same column have the same n_r quantum number; and thin black lines crossing the levels span the horizontal length for clarity.

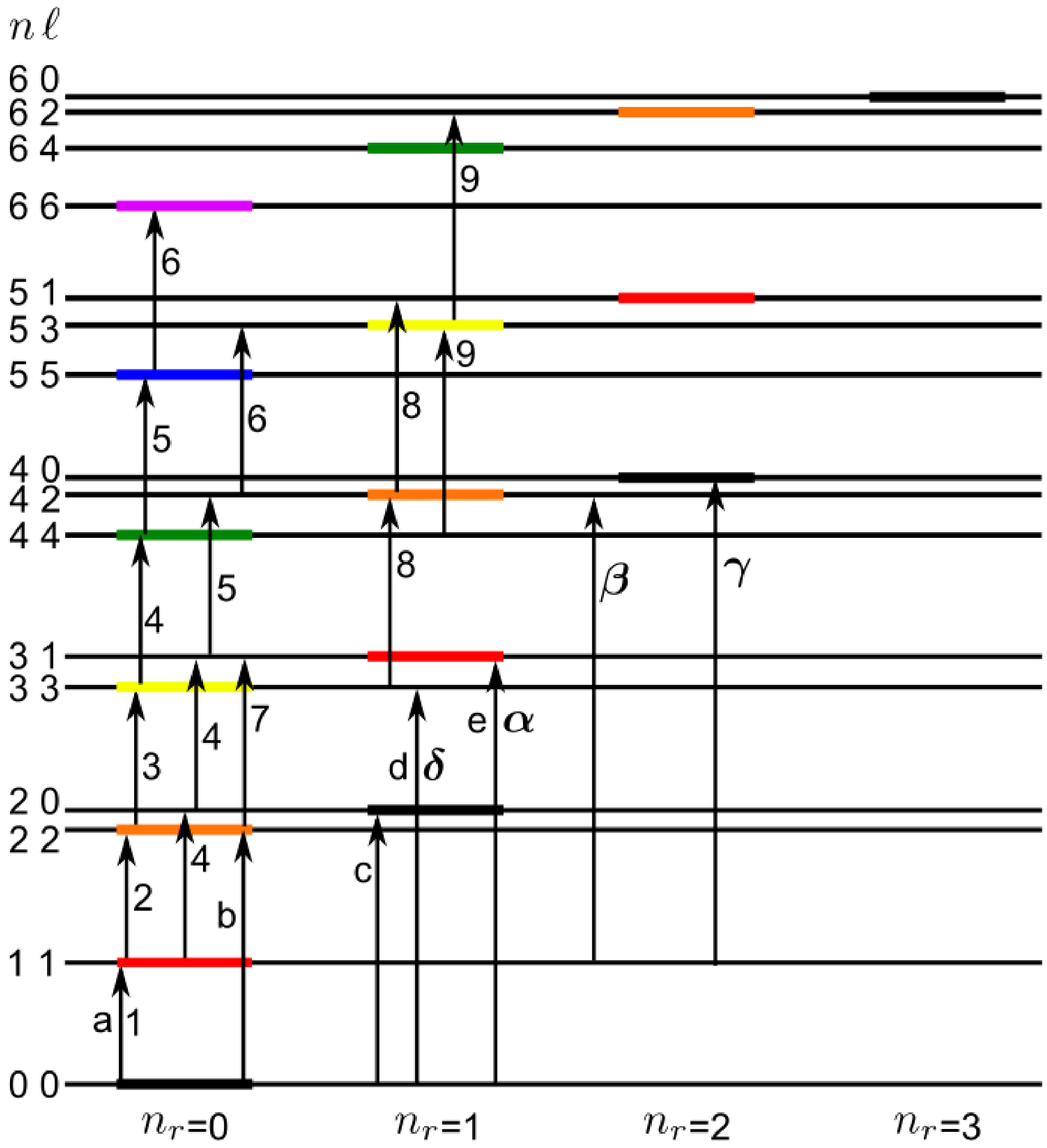

FIGURE 6.3: Energy level diagram of Helium confined in C_{60}. Levels with the same ℓ quantum number are $(2\ell + 1)$-fold degenerate and have the same color. The states with the same n_r quantum number are placed on the same column. The quantum number $n = (\ell + 2n_r)$. Arrows represent observed transitions and the label depicts which experimental peak it corresponds to. The label placed on the left of the arrow stands for THz peaks and the label placed on the right stands for INS. THz transitions in the range 77-150 cm^{-1} are labelled as numbers (1-9) and the ones in the range 280-320 cm^{-1} are labelled as Greek letters (α, β, γ, δ). The INS transitions are labelled with letters (a-e). Some experimental peaks correspond to more than one transition.

The label placed on the left of the arrow stands for THz peaks and the label placed on the right stands for INS. THz transitions in the range 77-150 cm^{-1} are labelled with numbers 1-9 (for $\Delta\ell = \pm 1$ & $\Delta n_r = 0$) and the ones in the range 280-320 cm^{-1} are labelled with Greek letters α, β, γ for $\Delta\ell = \pm 1$ & $\Delta n_r = +1$ and with δ for the $^3\text{He@C}_{60}$ THz transition with $\Delta\ell = +3$ & $\Delta n_r = 0$. The INS transitions are labelled with letters (a-e).

The parameter fitting was done only considering THz region 77-150 cm^{-1}. However, some Helium peaks were also observed at 280-320 cm^{-1}. The simulation done using the parameters from table 6.1 does predict absorption peaks in this range. The simulated spectra of $^4\mathrm{He@C_{60}}$ at 5 K and 100 K in the 280-320 cm^{-1} region are shown in fig. 6.4. The experimental spectra in fig. 6.4 were taken from fig 5.5 (c) after subtracting the broad baseline. There are three peaks in the spectrum, one from the ground state and two from excited states, labelled according to the energy diagram from fig. 6.3. The frequency and the initial state of the transitions are simulated correctly, yet the amplitudes are not. The simulation predicts a much weaker intensity for these transitions than it is actually observed. The experimental peaks are more than an order of magnitude more intense than predicted, indicated by the extra $\times 15$ scaling of the simulated peaks. The α, β, γ transitions have the usual change in the ℓ quantum number $\Delta\ell = +1$, together

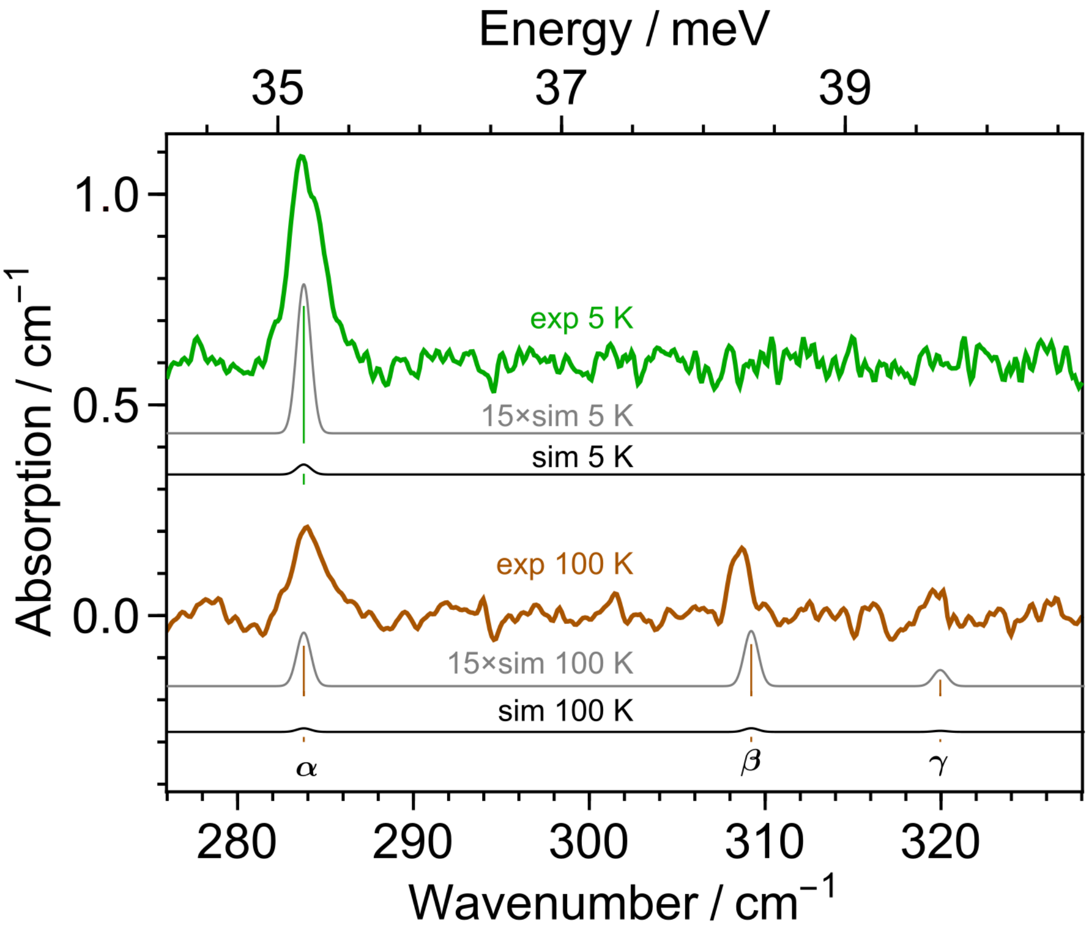

FIGURE 6.4: Experimental THz spectra of $^4\mathrm{He@C_{60}}$ at 5 K shown in green and 100 K in dark orange, in the range 277-327 cm^{-1}. Spectra are taken from fig 5.5 (c) after subtracting the broad baseline. Underneath each experimental spectrum the result of the simulation at the same temperature, using the parameters from table 6.1, is shown in black. In gray, the simulated spectra are scaled by a factor of 15 for clarity. The vertical bars indicate the simulated frequencies and amplitudes of each transition. Transitions are labelled according to the assignment from the energy level diagram from figure 6.3.

with a $+1$ change in the n_r quantum number, $\Delta n_r = +1$ which is allowed for THz transitions. At moment it is still a mystery why these transitions are a lot more intense than predicted. Using a different power for the radial displacement r when defining the induced dipole moment operator (like r^3, r^5,... in eq. 6.23) made these transitions more intense relative to the fundamental. Suggesting the dipole moment for He@C_{60} is more complex and defining it accurately requires more than a linear term in r. Further investigations will be done in this regard.

The corresponding α, β, γ peaks for ^{3}He are shifted to higher frequencies due to the mass difference and overlap with the strong vibrational peaks of the cage (at $>$ 330 cm^{-1}), so they could not be identified in the spectrum. However, the ^{3}He@C_{60} THz spectrum displayed one peak in the 280-320 cm^{-1} region (fig. 5.7 (c)) at 316.6 cm^{-1} labelled δ. This originates in the ground state due to the temperature dependence and its energy matches with the ^{3}He@C_{60} INS peak labelled d (fig. 6.5 (a) or fig. 4.11 (a)). This transition corresponds to $\Delta n_r = 0$ and $\Delta\ell = +3$, which is allowed for INS but strictly forbidden for THz. At the moment the reason why this transition is allowed in THz spectroscopy is a mystery. A possible explanation might involve the non-zero nuclear spin of ^{3}He ($I = 1/2$), in a spin-orbit type coupling. However, this might relax the selection rule to $\Delta\ell = \pm 2$ and not $\Delta\ell = \pm 3$. The equivalent transition for ^{4}He would be at 264.516 cm^{-1}, where it overlaps with C_{60} cage peaks at $\sim$ 265 cm^{-1}; yet there is no clear sign of a ^{4}He peak in this range.

The eigenvalues obtained by fitting the THz data were used to calculate the energy of the INS transitions. This is shown by the vertical bars in fig. 6.5 (a) and (b) for ^{3}He@C_{60} and ^{4}He@C_{60} respectively, where the transitions are labelled (a-e) according to the energy level diagram from fig. 6.3. All INS measurements were done at low temperature (2.7 K) so all transitions are from the ground state only. There is a good correspondence between the energies of the simulated transitions and the experimental spectra. Since INS has essentially no selection rules, the low temperature INS spectra shows overtone peaks which give a nice overview of the energy level diagram. Peak a is the fundamental transitions, peaks b & c are overtone transitions with $\Delta\ell = \pm 2$ and peaks d & e are overtones with $\Delta\ell = \pm 3$. For ^{4}He@C_{60} only the a-c peaks were observed, where b and c were weak and at the limit of detection, which is due to smaller sample amounts of ^{4}He@C_{60}. Peaks d and e for ^{4}He@C_{60} have energies overlapping with the first C_{60} vibration at 33 meV. Daggers (†) mark the positions of the C_{60} vibrational peaks, which in the difference spectra shown give rise to dispersion shapes because the cage vibrational modes are slightly shifted by the presence of the endohedral atom.

The correspondence between simulations and all experimental results is good. Thus, the confining potential for the ^{3}He atom in ^{3}He@C_{60} is shown in fig. 6.6 (a); the ^{4}He@C_{60} confining potential is extremely similar. The energy levels from the diagram in fig. 6.3 are shown for the ^{3}He@C_{60} eigenvalues on the same plot as the confining potential.

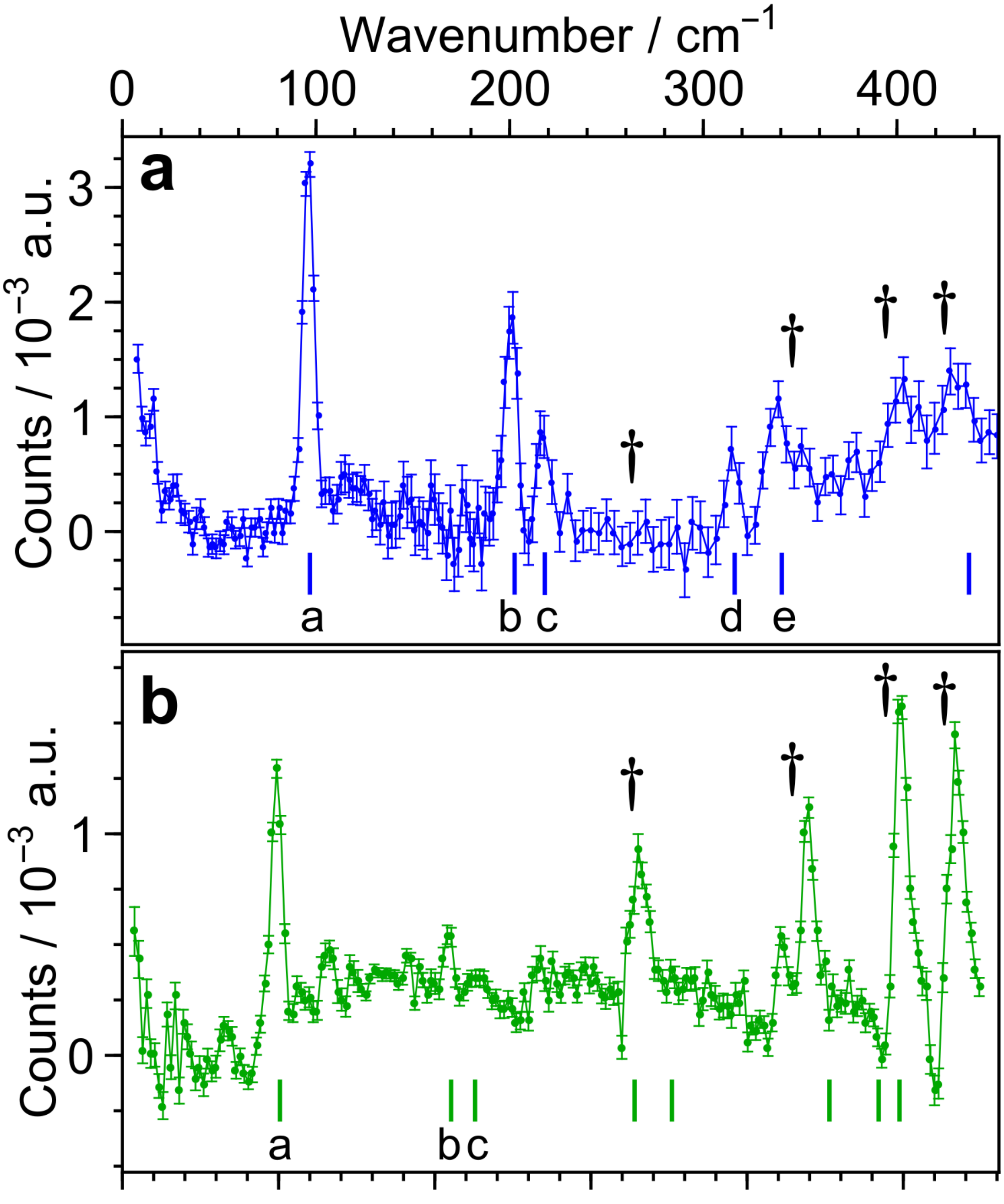

FIGURE 6.5: INS difference spectra of: **(a)** ^{3}He@C$_{60}$ at 2.7 K in blue (from fig 4.10 **(b)**) and **(b)** ^{4}He@C$_{60}$ at 2.7 K in green (from fig 4.12 **(b)**). The short vertical bars indicate the energies of the predicted translational transitions from the ground state; defined by the potential from table 6.1. Transitions are labelled according to the assignment from the energy level diagram from figure 6.3. Positions of C$_{60}$ cage peaks are marked with daggers (†).

6.2.2.1 Comparison with empirical potentials

The confining potential of He@C_{60} obtained experimentally above is compared with ones obtained from He-C semi-empirical two-body potentials.[2,127] The two-body potentials shown here are: Lennard-Jones[2] (LJ) and modified Buckingham[127](mB).

To obtain the confining potential, first a 3D structure of C_{60} is generated with a given radius and HP:HH bond lengths ratio. An interaction potential between the carbon atoms of the cage and the endohedral Helium atom is chosen (LJ or mB in this case). The confining potential at any one point is obtained by summing all the 60 two-body interactions between the helium atom, at that point, and all 60 carbon atoms in the cage. To get the confining potential along an axis, the position of the helium atom is moved along that axis and then the potential is computed for each position.

For both computed He@C_{60} confining potentials, a radius of 3.586 Å was used for the C_{60} cage, of computational origin, as specified in references 2,127. This radius was used since currently there is no experimental value for the radius of He@C_{60} endofullerenes. The radius here means the distance from the centre of the cage to the centre of the carbon atoms. The C-C HP & HH bond lengths were not specified in references 2,127, but we chose the HP:HH bond ratio to match the experimentally known values.[7,55] The exact bond lengths used were: HP bond = 1.4688 Å and HH bond = 1.4085 Å.

The He-C two-body Lennard-Jones interaction potential[2] is defined in eq. 6.31 below, with parameters given in table 6.2.

$$V_{LJ} = 4\epsilon\left[\left(\frac{\sigma}{r}\right)^{12} - \left(\frac{\sigma}{r}\right)^{6}\right] \tag{6.31}$$

TABLE 6.2: Parameters for the Lennard-Jones potential (eq. 6.31) between carbon and helium.[2]

Carbon-Atom	σ (Å)	ϵ (kJ/mol)
Helium	2.971	0.1554

This Lennard-Jones semi-empirical two-body potential between Helium and Carbon is defined in references 2,128. These two-body parameters are given as an approximation of three-body LJ parameters between aromatic molecules and noble gas atoms;[128] where they show that the three-body terms involving two carbon atoms and one noble gas atom can be important. The relevance of the three-body terms for the dispersion interaction is seen when the noble gas atom is located in the plane of the aromatic molecule; because in this case the simpler two-body potential gives wrong predictions.[128] When the noble gas atom is located above the plane of carbon atoms in aromatic molecules, there is almost no difference between using a two-body or a three-body potential. Since inside a fullerene molecule the Helium atom can only be above a plane of carbon atoms and cannot sit in the plane, using a two-body potential is appropriate.

The other two-body He-C interaction potential is the modified Buckingham potential (mB),[127] defined in eq. 6.32, with parameters given in table 6.3.

$$V_{mB} = \epsilon' \left[2.9 * 10^5 * exp\left(\frac{-12.5}{\rho}\right) - 2.25 * \rho^6 \right] \ (if\ \rho \leq 3.311) \tag{6.32}$$

$$= 336.176 * \epsilon' * \rho^2 \ (if\ \rho \geq 3.311) \tag{6.33}$$

Where $\rho = \frac{r_i + r_j}{r}$ and $\epsilon' = \sqrt{\epsilon_i \epsilon_j}$ and the parameters for the modified Buckingham potential are found in table 6.3

TABLE 6.3: Modified Buckingham potential (eq. 6.32) parameters.

Atom	r_i (Å)	ϵ_i (kJ/mol)
C	1.96	0.234
He	1.53	0.109

The He-C modified Buckingham potential used here is obtained from the MM3 molecular mechanics program.[129] The program defines the interaction parameters in order to agree with thousands of known cases; which are well defined for common organic molecules with numerous studied examples. Because there are not many examples of noble gas atoms interacting with organic molecules, the parameters involving noble gases might not be very accurate.

For both He@C_{60} confining potentials obtained from LJ or mB, rotating the cage to obtain the confining potential along different orientations made a very small difference. In the lower part there was essentially no difference between different C_{60} orientations, which is the region probed by the INS and THz measurements. Both He@C_{60} confining potentials computed here were done by moving the Helium atom along the centre of a HH bond. The comparison between the He@C_{60} confining potential obtained experimentally in this study and the two computed from LJ or mB two-body potentials is shown in figure 6.6 (b). Where the experimental potential is shown in black, the LJ one in orange and the mB one in blue.

A really good match is seen between the LJ potential and the experimental one, within the probed energy range. There are some small variations compared with the experimental potential but the agreement is good. We believe this is because the LJ parameters[2,128] used here were optimised for the interaction of carbon atoms *in aromatic molecules* with noble gas atoms. Furthermore, the He-C interatomic LJ parameters can be defined as a two-body potential if the noble gas is located above a plane of carbon

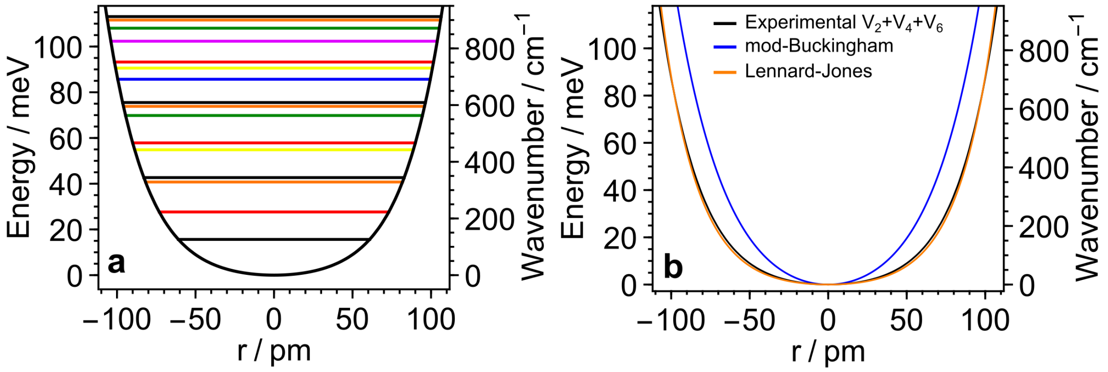

FIGURE 6.6: **(a)** ^{3}He@C_{60} confining potential $V(r)$ using the parameters from table 6.1. The ^{3}He@C_{60} eigenstates are also shown as horizontal lines, with the coloring scheme from the energy level diagram in fig.6.3. **(b)** Experimental confining potential $V(r)$ from (a) is shown in black; the semi-empirical confining potentials obtained from two-body interaction potentials are shown in orange for Lennard-Jones (LJ)[2] and in blue for modified Buckingham (mB).[127]

atoms and not in the plane[128] (which is always the case for noble gas endofullerenes). The more empirical mB confining potential gives a worse fit with the experimental, it is predicted to be steeper than actually observed. The reason for the poor fit is probably because the interatomic He-C two-body mB potential comes from the MM3 molecular mechanics program, which has the noble gas parameters less accurately defined as compared with usual intermolecular interactions in organic molecules. Point to note is that at larger displacement from the cage centre ($>$ 100 pm), at potential energies $>$ 800 cm^{-1} which go above the plot shown in figure 6.6 (b), the LJ confining potential deviates from the experimental one, it gets steeper than observed. Furthermore, the mB confining potential actually starts to match the experimental better than the LJ one as displacement & energy are increased. These high energies were not probed in our measurements, so the confining potential is only extrapolated in this range, yet it serves to support the need for further experimental intermolecular interaction potentials required to benchmark computational studies.

6.2.2.2 Comparison with Quantum chemistry potentials

The He@C_{60} confining potential has been simulated using quantum chemistry techniques. The simulations were done by Jyrki Rantaharju from University of Southampton. The calculations were done by displacing the Helium atom away from the centre of the cage and calculating the energy at every point. The C_{60} radius used was 3.586 Å, the same as for the semi-empirical LJ and mB above.

All quantum chemistry calculations were done using Psi4.[130] The confining potential was calculated with density-fitting (DF) second-order Møller-Plesset perturbation theory (DF-MP2). Density functional theory (DFT) methods were also used to calculate the confining potential. The hybrid DFT-functionals used are: ωB97X-V,[131,132] LC-VV10,[132,133] B3LYP (20% exact exchange),[134–137] PBE0 (25% exact exchange).[109,110] ωB97X-V and LC-VV10 have VV10 correlation functional contribution in order to better deal with non-covalent interactions. For B3LYP and PBE0, the Grimme D3 empirical dispersion correction with Beck-Johnson Damping[138,139] was added to better handle dispersion interactions.

The simulations converged to a good approximation when using the correlation-consistent cc-pVXZ (X=D, T, Q, 5) basis sets.[140,141] The resulting simulated He@C_{60} confining potentials at the cc-pV5Z level are shown in figure 6.7 (a, b). The experimental potential is shown in black and the ones obtained through quantum chemistry are shown as individual points, as specified in the legend. Panel (b) shows a scaled up version of (a), with data points joined by straight lines, to display the different potentials more clearly.

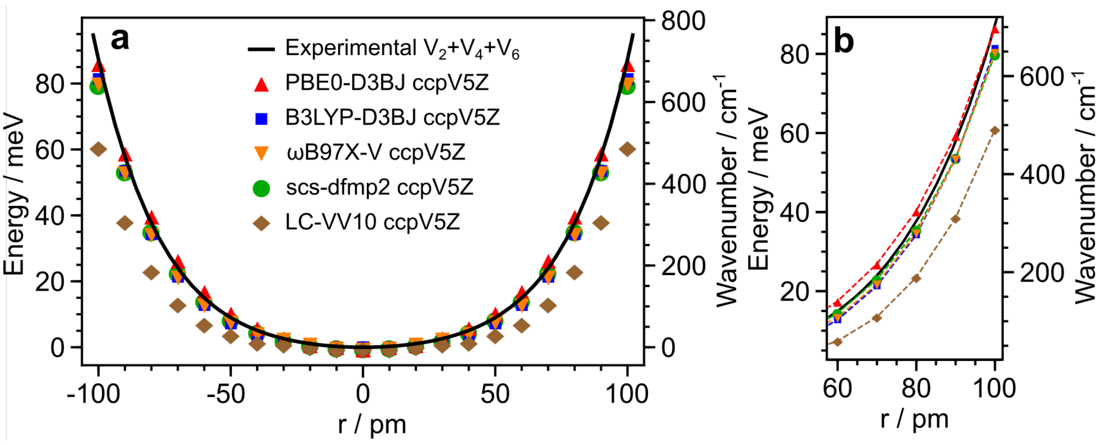

FIGURE 6.7: **(a)** Experimentally determined He@C_{60} confining potential is shown as a black curve. Confining potentials obtained through quantum chemistry calculations are shown using DFT (triangles, square and diamond) and MP2 (circle). **(b)** Is a scaled version of (a), to allow for better comparison, where the points have been joined by straight dashed lines.

The correspondence between the simulated and experimental potentials is good, some matching better than others. If one has a close look at fig. 6.7 (b), small differences can be seen between all algorithms used. Generally, the simulated potentials seem to match the experimental one on a given range and then they diverge. There is not one simulated confining potential which perfectly matches the experimental one. This serves to further strengthen the need of accurate experimental non-covalent interaction potentials, to be used for benchmarking computational chemistry algorithms.

6.3 Conclusion

To conclude, this chapter was dedicated to the analysis of atomic translational quantization, observed for the noble gas atoms enclosed in C_{60} fullerenes. ^{3}He@C_{60}, ^{4}He@C_{60} and Ne@C_{60} endofullerenes have been studied using Inelastic Neutron Scattering (INS) and THz (far-IR) spectroscopy. The quantized translational states of He and Ne have been shown to display observable transitions in the INS and THz spectra, in chapters 4 and 5. These experimental spectra provide valuable information about the interaction potential between the noble gas atom and the carbon atoms constituting the C_{60} cage.

INS measurements were performed on Ne@C_{60}, and a spectrum for the confined Neon atom was observed. This was composed of the fundamental transition for ^{20}Ne at 7.01 ± 0.01 meV and a couple of peaks at higher energies with unclear assignment. Assuming a purely Harmonic model for the Ne@C_{60} confining potential, using the fundamental transition, the harmonic potential term was calculated to be $V_2 = \frac{1}{2}k = 117.5 \pm 0.3\ \text{meV}\ \text{Å}^{-2}$ ($1.883 \pm 0.005\ \text{Jm}^{-2}$). This term is much larger than the harmonic term of He@C_{60}, expected since the larger size of Neon reduces the free volume available for translation, effectively making the confining potential steeper.

INS measurements of ^{3}He@C_{60} and ^{4}He@C_{60} revealed some peaks in the spectra due to the translational quantization of the Helium isotopes, in chapter 4. The transitions are sensitive to the mass of the isotope, the lighter ^{3}He generating higher energy transitions than ^{4}He. The most intense INS peaks, at 11.90 ± 0.01 meV for ^{3}He@C_{60} and 9.86 ± 0.01 meV for ^{4}He@C_{60}, were assigned to fundamental translational transitions of the confined He isotopes. Furthermore, overtone transitions were observed for the two isotopes, which offered a nice outline of the energy level structure of the atomic confinement.

THz measurements of ^{3}He@C_{60} and ^{4}He@C_{60} displayed a rich structure of peaks in the spectrum, with some fundamental and hot-band peaks, in chapter 5. The fundamental transitions, at $\sim$97 cm^{-1} for ^{3}He@C_{60} and $\sim$81 cm^{-1} for ^{4}He@C_{60}, matched with the same ones detected by INS on these compounds, from chapter 4. Two regions were found in the THz spectra to give rise to Helium peaks: at $77 - 150\ \text{cm}^{-1}$ and at $277 - 327\ \text{cm}^{-1}$. In the first region the fundamental peaks are found, together with hot-band transitions with the usual selection rule $\Delta\ell = \pm 1$. This region was used to find the potential function which best describes the confinement of Helium inside C_{60}. The model used was the 3D an-Harmonic Oscillator, or 3D polynomial oscillator, and the results of fitting the experimental peaks in order to define the confining potential are found in table 6.1. Surprisingly, the peaks in the second region ($277 - 327\ \text{cm}^{-1}$) were predicted by the model but with incorrect absorption amplitudes. These peaks for ^{4}He@C_{60} were found to correspond to $\Delta\ell = \pm 1$ and $\Delta n_r = \pm 1$ transitions, where both quantum numbers change by 1 at the same time. These peaks seem to provide useful insight into the induced dipole moment that He acquires when confined inside C_{60}. For ^{3}He@C_{60} a THz peak was found at $316.601 \pm 0.015\ \text{cm}^{-1}$ which corresponded to the 39.07 ± 0.14 meV peak in the INS spectrum. This transition is assigned to an overtone transition with $\Delta\ell = +3$ (and $\Delta n_r = 0$) which is allowed for INS but strictly forbidden for THz. The reason why this transition is allowed in the THz is unclear, the nuclear spin 1/2 of ^{3}He might be responsible, yet it is too early to say this with certainty.

6.3.1 Future work

In the Ne@C$_{60}$ INS measurements, only the fundamental translational transition was observed. Further experiments are planned, in order to identify other overtone or hot-band transitions to better describe the Ne@C$_{60}$ confining potential experimentally.

Plans are in motion to complete the study of noble gas C$_{60}$ endofullerenes. The aim will be to investigate Ne@C$_{60}$, Ar@C$_{60}$, Kr@C$_{60}$, using INS and THz spectroscopy. This will determine the confining potentials for the other noble gas endofullerenes, hopefully to the same level of detail as accomplished for He@C$_{60}$.

A better description of the He@C$_{60}$ confining potential will be attempted; by using higher order terms in the $V(r)$ potential, such as $V_8 r^8$ and/or $V_{10} r^{10}$, and fit the experimental INS and THz spectra. This should give an even better match of the simulated peaks with the experimental spectra, resulting in a more accurate confining potential.

A better simulation of the ^{4}He@C$_{60}$ THz peaks in the region 280-320 cm^{-1} will be attempted. This will involve adding higher order powers of the displacement r for the dipole moment operator to better match the ^{4}He@C$_{60}$ THz spectrum in the 280-320 cm^{-1} region. The results of such simulations should define more accurately the induced dipole moment of a He atom when confined in C$_{60}$.

The strictly forbidden ($\Delta\ell = +3$) THz transition at 316.601 ± 0.015 meV of ^{3}He@C$_{60}$ will be further studied. The $I = 1/2$ nuclear spin of ^{3}He will be added in the simulations, by including a spin-orbit coupling term in the Hamiltonian. This might shed some light on why such a forbidden transition is observed in the THz spectrum of ^{3}He@C$_{60}$.

Chapter 7

Conclusions

The purpose of this PhD thesis is to describe spectroscopic investigations of C_{60} fullerenes and endofullerenes. The techniques used are Nuclear Magnetic Resonance (NMR), Inelastic Neutron Scattering (INS) and far-Infrared (far-IR or THz) spectroscopy. The main conclusions of this study are given below.

The ^{13}C solution NMR spectrum of C_{60} displays two extra peaks, of weak intensity in relative ratio 2:1. These are labelled HP with amplitude $1.63 \pm 0.15\,\%$ of the main C_{60} peak and HH with amplitude $0.81 \pm 0.08\,\%$ of the main C_{60} peak. The labelling comes from the two types of C-C bonds present in C_{60}: Hexagon-Pentagon bond (HP) and Hexagon-Hexagon bond (HH). These side peaks are on the deshielded side of the main C_{60} peak, shifted by $^{1}\Delta_{\mathrm{HP}} = 12.56 \pm 0.01$ ppb and $^{1}\Delta_{\mathrm{HH}} = 19.98 \pm 0.02$ ppb with respect to it, at 298 K. These shifts decrease linearly in magnitude as temperature is increased. The HH peak is more strongly influenced by a change in temperature than the HP peak, having a steeper slope with respect to temperature.

Endofullerene samples also exhibit the HP & HH side peaks, with the same pattern as for C_{60}. The only difference being the shifts are slightly decreased in magnitude by the presence of an endohedral molecule and this effect scales with the size of the endohedral molecule. The HH shift seems to be more strongly affected by the presence of an endohedral molecule than the HP shift.

The origin of the HP & HH shifts is shown to be due to the one-bond secondary NMR isotope shift effect. These arise when $^{13}C_2$ isotopomers of C_{60} have the ^{13}C's adjacent along a HP bond ($[\mathrm{HP}\text{-}^{13}C_2]\text{-}C_{60}$) or a HH bond ($[\mathrm{HH}\text{-}^{13}C_2]\text{-}C_{60}$). The fine structure seen in the natural abundance C_{60} ^{13}C NMR spectrum is *not* due to ^{13}C-^{13}C J-couplings. The relative amplitudes of the two side peaks is 2:1, identical to the HP:HH bond ratio in C_{60} of 2:1. The amplitudes of the side peaks with respect to the main C_{60} peak are described through a purely statistical argument and a Monte-Carlo type simulation.

The solution ^{13}C NMR spectrum of 20-30% ^{13}C enriched C_{60} is broader than that of natural abundance C_{60}, and the fine structure is absent. An algorithm is developed, based on a Monte-Carlo type approach, to simulate C_{60} spectra of arbitrary levels of ^{13}C. Firstly, the ^{13}C spin systems in C_{60} are decoupled based on a cluster identification method which uses the magnitudes of ^{13}C-^{13}C J-couplings relative to the experimentally observed isotope shifts in C_{60}. Then the spectra of each cluster are approximated by their second moment and added up in a Monte-Carlo fashion to simulate the C_{60} spectrum. The simulation using this method matches quite well with the experimental result, even for natural abundance C_{60}. Multiple spectra of C_{60}, with various ^{13}C contents, are shown after being computed using this method. This method of approximating the spectrum evaluates rapidly for large number of J-coupled spins and may be adapted to other problems in solution and solid-state NMR.

The ^{13}C solution NMR spectrum of ^{3}He@C_{60} displays a small splitting of the main peak into a 1:1 doublet, of $77.5 \pm 0.2\,\mathrm{mHz}$ at 340 K. The HP & HH side peaks of ^{3}He@C_{60} show the same splitting as the main ^{13}C peak. The splitting is assigned to an internuclear J-coupling between ^{3}He and ^{13}C, in the absence of a formal covalent chemical bond between them. This leads to the notation $^{0}J_{HeC}$, where the superscript zero indicates the number of chemical bonds between ^{3}He and ^{13}C. The $^{0}J_{HeC}$-coupling displays an increase in magnitude as temperature is increased. This is consistent with the ^{3}He nucleus coming closer to ^{13}C on average at elevated temperatures. Quantum chemistry DFT calculations predict a negative $^{0}J_{HeC}$, with a magnitude close to the experimental $^{0}J_{HeC}$ extrapolated at 0 K. The long spin lattice relaxation times of ^{3}He and ^{13}C enable the direct observation of such a ^{0}J-coupling.

A similar type of ^{0}J-coupling is observed in CH_4@C_{60}, between ^{1}H and a ^{13}C (C_{60}) within the cage. Unfortunately, the ^{1}H spin lattice relaxation time is short ($\sim$1.5 s), so direct observation of the $^{0}J_{HC}$ splitting was not possible. However, $^{0}J_{HC}$ leads to a significant broadening of the ^{13}C (C_{60}) peak of CH_4@C_{60}, as compared with empty C_{60}. This is not caused by faster relaxation of the ^{13}C (C_{60}) spin induced by the endohedral CH_4 (e.g. $^{1}\mathrm{H} - {}^{13}\mathrm{C}$ dipolar relaxation). The broadening was shown to disappear when applying ^{1}H decoupling on the endohedral CH_4. For CH_4@C_{60} all is consistent with a $^{0}J_{HC}$-coupling between endohedral ^{1}H and a ^{13}C within the enclosing C_{60} cage.

^{3}He@C_{60}, ^{4}He@C_{60} and Ne@C_{60} endofullerenes are studied using Inelastic Neutron Scattering (INS). The measurements of ^{3}He@C_{60} and ^{4}He@C_{60} reveal some peaks in the spectra due to the translational quantization of the Helium isotopes. The transitions are sensitive to the mass of the isotope, the lighter ^{3}He having higher energy transitions than ^{4}He. Two different INS instruments detected the same fundamental peaks of ^{3}He@C_{60} and ^{4}He@C_{60}. Some overtone transitions are also observed in a second set of measurements, after the sample preparation was improved. The most intense INS peaks at 11.90 ± 0.01 meV for ^{3}He@C_{60} and 9.86 ± 0.01 meV for ^{4}He@C_{60} are assigned to fundamental translational transitions of the confined He isotopes. Furthermore, the

overtone transitions observed for the two isotopes offer a nice outline of the energy level structure due to the atomic confinement.
INS measurements of Ne@C_{60} reveal the fundamental translational transition for ^{20}Ne at 7.01 $\pm$ 0.01 meV and a couple of peaks at higher energies with unclear assignment.

Far-IR (THz) measurements of ^{3}He@C_{60} and ^{4}He@C_{60} display a rich structure of peaks in the spectrum, with some fundamental and hot-band peaks. Two regions were found in the THz spectra to give rise to Helium peaks: at $77-150$ cm^{-1} and at $277-327$ cm^{-1}. The fundamental transitions, found in the $77-150$ cm^{-1} region, match with the same ones detected by INS on these compounds. The THz fundamental transition is shown to be composed of two peaks in ratio $\sim 8:2$ separated by: 0.727 ± 0.011 cm^{-1} for ^{4}He@C_{60} and by 0.839 ± 0.008 cm^{-1} for ^{3}He@C_{60}. The reason for this splitting is not fully understood yet; it likely originates from merohedral disorder of the C_{60} lattice. A ^{3}He@C_{60} THz peak, from the second region, at 316.601 ± 0.015 cm^{-1} matches with an overtone transition detected by INS.

The INS and THz results on translational quantization of noble gases inside C_{60} are theoretically interpreted as a 3D spherical quantum oscillator, with a confining potential function given by even power polynomials, up to 6^{th} order.
A purely Harmonic model is assumed for the Ne@C_{60} confining potential, since only the fundamental peak is observed. Using the fundamental transition, the harmonic potential term is calculated to be 117.5 ± 0.3 meV Å^{-2}.
For ^{3}He@C_{60} and ^{4}He@C_{60}, the peaks in the region $77-150$ cm^{-1} are used to characterise the confining potential (up to 6^{th} order) and the induced dipole moment the Helium atom acquires inside the C_{60} cage. The fundamental and hot-band peaks from this region correspond to transitions with the usual selection rule $\Delta\ell = \pm 1$. The peaks in the second region ($277-327$ cm^{-1}) are predicted by the model but with incorrect absorption amplitudes. These peaks for ^{4}He@C_{60} are found to correspond to $\Delta\ell = \pm 1$ and $\Delta n_r = \pm 1$ transitions, where both quantum numbers change by 1. These peaks appear to provide useful insight into the induced dipole moment that the He atom acquires when confined inside C_{60}. For ^{3}He@C_{60}, the THz peak at 316.601 ± 0.015 cm^{-1} corresponds to an overtone transition with $\Delta\ell = +3$ and $\Delta n_r = 0$, which is allowed for INS but strictly forbidden for THz. The reason why this transition is allowed in the THz spectrum is unclear; the nuclear spin 1/2 of ^{3}He might be responsible, yet at the moment this is just a hypothesis.

References

[1] G. R. Bacanu, G. Hoffman, M. Amponsah, M. Concistrè, R. J. Whitby and M. H. Levitt, *Physical Chemistry Chemical Physics*, 2020, **22**, 11850–11860.

[2] L. Pang and F. Brisse, *The Journal of Physical Chemistry*, 1993, **97**, 8562–8563.

[3] H. W. Kroto, J. R. Heath, S. C. O'Brien, R. F. Curl and R. E. Smalley, *Nature*, 1985, **318**, 162–163.

[4] M. S. Dresselhaus, G. Dresselhaus and P. C. Eklund, *Science of Fullerenes and Carbon Nanotubes*, Academic Press, 1996.

[5] G. Meijer, D. S. Bethune, W. C. Tang, H. J. Rosen, R. D. Johnson, R. J. Wilson, D. D. Chambliss, W. G. Golden, H. Seki, M. S. De Vries, C. A. Brown, J. R. Salem, H. E. Hunziker and H. R. Wendt, *MRS Proceedings*, 1990, **206**, 619.

[6] R. D. Johnson, C. S. Yannoni, J. Salem, G. Meijer and D. S. Bethune, *MRS Online Proceedings Library (OPL)*, 1990/ed, **206**, year.

[7] C. S. Yannoni, P. P. Bernier, D. S. Bethune, G. Meijer and J. R. Salem, *Journal of the American Chemical Society*, 1991, **113**, 3190–3192.

[8] J. M. Hawkins, A. Meyer, T. A. Lewis, S. Loren and F. J. Hollander, *Science*, 1991, **252**, 312–313.

[9] C. J. Bruns and F. J. Stoddart, *The Nature of the Mechanical Bond: From Molecules to Machines*, John Wiley & Sons, 2017.

[10] Y. Chai, T. Guo, C. Jin, R. E. Haufler, L. P. F. Chibante, J. Fure, L. Wang, J. M. Alford and R. E. Smalley, *The Journal of Physical Chemistry*, 1991, **95**, 7564–7568.

[11] M. Saunders, H. A. Jiménez-Vázquez, R. J. Cross and R. J. Poreda, *Science*, 1993, **259**, 1428–1430.

[12] M. Saunders, R. J. Cross, H. A. Jiménez-Vázquez, R. Shimshi and A. Khong, *Science*, 1996, **271**, 1693–1697.

[13] M. Saunders, H. A. Jiménez-Vázquez, R. J. Cross, S. Mroczkowski, D. I. Freedberg and F. A. L. Anet, *Nature*, 1994, **367**, 256–258.

[14] M. Saunders, H. A. Jimenez-Vazquez, B. W. Bangerter, R. J. Cross, S. Mroczkowski, D. I. Freedberg and F. A. L. Anet, *Journal of the American Chemical Society*, 1994, **116**, 3621–3622.

[15] G.-W. Wang, B. R. Weedon, M. S. Meier, M. Saunders and R. J. Cross, *Organic Letters*, 2000, **2**, 2241–2243.

[16] K. Komatsu, M. Murata and Y. Murata, *Science*, 2005, **307**, 238–240.

[17] Y. Morinaka, F. Tanabe, M. Murata, Y. Murata and K. Komatsu, *Chemical Communications*, 2010, **46**, 4532–4534.

[18] K. Kurotobi and Y. Murata, *Science*, 2011, **333**, 613–616.

[19] A. Krachmalnicoff, R. Bounds, S. Mamone, S. Alom, M. Concistrè, B. Meier, K. Kouřil, M. E. Light, M. R. Johnson, S. Rols, A. J. Horsewill, A. Shugai, U. Nagel, T. Rõõm, M. Carravetta, M. H. Levitt and R. J. Whitby, *Nature Chemistry*, 2016, **8**, 953–957.

[20] S. Bloodworth, G. Sitinova, S. Alom, S. Vidal, G. R. Bacanu, S. J. Elliott, M. E. Light, J. M. Herniman, G. J. Langley, M. H. Levitt and R. J. Whitby, *Angewandte Chemie International Edition*, 2019, **58**, 5038–5043.

[21] S. Bloodworth, G. Hoffman, M. C. Walkey, G. R. Bacanu, J. M. Herniman, M. H. Levitt and R. J. Whitby, *Chemical Communications*, 2020.

[22] S. Mamone, M. Ge, D. Hüvonen, U. Nagel, A. Danquigny, F. Cuda, M. C. Grossel, Y. Murata, K. Komatsu, M. H. Levitt, T. Rõõm and M. Carravetta, *The Journal of Chemical Physics*, 2009, **130**, 081103.

[23] A. J. Horsewill, S. Rols, M. R. Johnson, Y. Murata, M. Murata, K. Komatsu, M. Carravetta, S. Mamone, M. H. Levitt, J. Y.-C. Chen, J. A. Johnson, X. Lei and N. J. Turro, *Physical Review B*, 2010, **82**, 081410.

[24] A. J. Horsewill, K. S. Panesar, S. Rols, J. Ollivier, M. R. Johnson, M. Carravetta, S. Mamone, M. H. Levitt, Y. Murata, K. Komatsu, J. Y.-C. Chen, J. A. Johnson, X. Lei and N. J. Turro, *Physical Review B*, 2012, **85**, 205440.

[25] S. Mamone, M. Jiménez-Ruiz, M. R. Johnson, S. Rols and A. J. Horsewill, *Physical Chemistry Chemical Physics*, 2016, **18**, 29369–29380.

[26] S. Mamone, J. Y. C. Chen, R. Bhattacharyya, M. H. Levitt, R. G. Lawler, A. J. Horsewill, T. Rõõm, Z. Bačić and N. J. Turro, *Coordination Chemistry Reviews*, 2011, **255**, 938–948.

[27] A. J. Horsewill, K. Goh, S. Rols, J. Ollivier, M. R. Johnson, M. H. Levitt, M. Carravetta, S. Mamone, Y. Murata, J. Y.-C. Chen, J. A. Johnson, X. Lei and N. J. Turro, *Philosophical Transactions of the Royal Society A: Mathematical, Physical and Engineering Sciences*, 2013, **371**, 20110627.

[28] S. Mamone, M. R. Johnson, J. Ollivier, S. Rols, M. H. Levitt and A. J. Horsewill, *Physical Chemistry Chemical Physics*, 2016, **18**, 1998–2005.

[29] K. S. K. Goh, M. Jiménez-Ruiz, M. R. Johnson, S. Rols, J. Ollivier, M. S. Denning, S. Mamone, M. H. Levitt, X. Lei, Y. Li, N. J. Turro, Y. Murata and A. J. Horsewill, *Physical Chemistry Chemical Physics*, 2014, **16**, 21330–21339.

[30] C. Beduz, M. Carravetta, J. Y.-C. Chen, M. Concistrè, M. Denning, M. Frunzi, A. J. Horsewill, O. G. Johannessen, R. Lawler, X. Lei, M. H. Levitt, Y. Li, S. Mamone, Y. Murata, U. Nagel, T. Nishida, J. Ollivier, S. Rols, T. Rõõm, R. Sarkar, N. J. Turro and Y. Yang, *Proceedings of the National Academy of Sciences*, 2012, **109**, 12894–12898.

[31] S. S. Zhukov, V. Balos, G. Hoffman, S. Alom, M. Belyanchikov, M. Nebioglu, S. Roh, A. Pronin, G. R. Bacanu, P. Abramov, M. Wolf, M. Dressel, M. H. Levitt, R. J. Whitby, B. Gorshunov and M. Sajadi, *Scientific Reports*, 2020, **10**, 18329.

[32] T. Rõõm, L. Peedu, M. Ge, D. Hüvonen, U. Nagel, S. Ye, M. Xu, Z. Bačić, S. Mamone, M. H. Levitt, M. Carravetta, J.-C. Chen, X. Lei, N. J. Turro, Y. Murata and K. Komatsu, *Philosophical Transactions of the Royal Society A: Mathematical, Physical and Engineering Sciences*, 2013, **371**, 20110631.

[33] M. Ge, U. Nagel, D. Hüvonen, T. Rõõm, S. Mamone, M. H. Levitt, M. Carravetta, Y. Murata, K. Komatsu, X. Lei and N. J. Turro, *The Journal of Chemical Physics*, 2011, **135**, 114511.

[34] G. Tabacchi, *ChemPhysChem*, 2018, **19**, 1249–1297.

[35] B. F. Henson, G. V. Hartland, V. A. Venturo, R. A. Hertz and P. M. Felker, *Chemical Physics Letters*, 1991, **176**, 91–98.

[36] K. Müller-Dethlefs, M. Sander and E. W. Schlag, *Chemical Physics Letters*, 1984, **112**, 291–294.

[37] M. Takahashi, H. Ozeki and K. Kimura, *The Journal of Chemical Physics*, 1992, **96**, 6399–6406.

[38] P. Hobza and K. Muller-Dethlefs, *Non-Covalent Interactions*, 2009.

[39] L. Zhu and P. Johnson, *The Journal of Chemical Physics*, 1991, **94**, 5769–5771.

[40] H. Krause and H. J. Neusser, *The Journal of Chemical Physics*, 1993, **99**, 6278–6286.

[41] S. W. Lovesey, *Theory of Neutron Scattering from Condensed Matter: Volume I: Nuclear Scattering*, Oxford University Press, Oxford, New York, 1986.

[42] D. J. Griffiths and D. F. Schroeter, *Introduction to Quantum Mechanics*, Cambridge University Press, Cambridge, 3rd edn., 2018.

[43] G. Herzberg, *Molecular Spectra and Molecular Structure: Spectra of Diatomic Molecules*, Van Nostrand, 2nd edn., 1950, vol. 1.

[44] R. N. Zare, *Angular Momentum: Understanding Spatial Aspects in Chemistry and Physics*, John Wiley & Sons, 1988.

[45] P. R. Bunker and P. Jensen, *Molecular Symmetry and Spectroscopy*, NRC Research Press, 2nd edn., 2006.

[46] M. H. Levitt, *Spin Dynamics: Basics of Nuclear Magnetic Resonance*, John Wiley & Sons, 2nd edn., 2007.

[47] C. J. Jameson, *The Journal of Chemical Physics*, 1977, **66**, 4983–4988.

[48] P. E. Hansen, *Progress in Nuclear Magnetic Resonance Spectroscopy*, 1988, **20**, 207–255.

[49] O. W. Sørensen, G. W. Eich, M. H. Levitt, G. Bodenhausen and R. R. Ernst, *Progress in Nuclear Magnetic Resonance Spectroscopy*, 1984, **16**, 163–192.

[50] C. Bengs and M. H. Levitt, *Magnetic Resonance in Chemistry*, 2018, **56**, 374–414.

[51] J. Jeener, in *Advances in Magnetic and Optical Resonance*, ed. J. S. Waugh, Academic Press, 1982, vol. 10, pp. 1–51.

[52] R. Taylor, J. P. Hare, A. K. Abdul-Sada and H. W. Kroto, *Journal of the Chemical Society, Chemical Communications*, 1990, 1423–1425.

[53] H. W. Kroto, A. W. Allaf and S. P. Balm, *Chemical Reviews*, 1991, **91**, 1213–1235.

[54] W. I. F. David, R. M. Ibberson, J. C. Matthewman, K. Prassides, T. J. S. Dennis, J. P. Hare, H. W. Kroto, R. Taylor and D. R. M. Walton, *Nature*, 1991, **353**, 147–149.

[55] K. Hedberg, L. Hedberg, D. S. Bethune, C. A. Brown, H. C. Dorn, R. D. Johnson and M. D. Vries, *Science*, 1991, **254**, 410–412.

[56] F. Leclercq, P. Damay, M. Foukani, P. Chieux, M. C. Bellissent-Funel, A. Rassat and C. Fabre, *Physical Review B*, 1993, **48**, 2748–2758.

[57] H. Batiz-Hernandez and R. A. Bernheim, *Progress in Nuclear Magnetic Resonance Spectroscopy*, 1967, **3**, 63–85.

[58] W. T. Raynes, A. M. Davies and D. B. Cook, *Molecular Physics*, 1971, **21**, 123–133.

[59] M. Saunders, K. E. Laidig and M. Wolfsberg, *Journal of the American Chemical Society*, 1989, **111**, 8989–8994.

[60] A. Krachmalnicoff, M. H. Levitt and R. J. Whitby, *Chemical Communications*, 2014, **50**, 13037–13040.

[61] S. Budavari, *The Merck Index: An Encyclopedia of Chemicals, Drugs, and Biologicals*, Merck, Rahway, N.J., U.S.A., 1989.

[62] M. S. Syamala, R. J. Cross and M. Saunders, *Journal of the American Chemical Society*, 2002, **124**, 6216–6219.

[63] M. Mehring, *Principles of High Resolution NMR in Solids*, Springer-Verlag, Berlin Heidelberg, 2nd edn., 1983.

[64] B. Masenelli, F. Tournus, P. Mélinon, A. Pérez and X. Blase, *The Journal of Chemical Physics*, 2002, **117**, 10627–10634.

[65] S. Díaz-Tendero, F. Martín and M. Alcamí, *Computational Materials Science*, 2006, **35**, 203–209.

[66] P. Vujanić, Z. Meić and D. Vikić-Topić, *Spectroscopy Letters*, 1995, **28**, 395–405.

[67] P. S. Nielsen, R. S. Hansen and H. J. Jakobsen, *Journal of Organometallic Chemistry*, 1976, **114**, 145–155.

[68] F. Cimpoesu, S. Ito, H. Shimotani, H. Takagi and N. Dragoe, *Physical Chemistry Chemical Physics*, 2011, **13**, 9609–9615.

[69] L. B. Krivdin and R. H. Contreras, in *Annual Reports on NMR Spectroscopy*, ed. G. A. Webb, Academic Press, 2007, vol. 61, pp. 133–245.

[70] S. Wolfram, *Mathematica: A System for Doing Mathematics by Computer*, Addison-Wesley, 2nd edn., 1991.

[71] M. JASZUŃSKI, K. RUUD and T. HELGAKER, *Molecular Physics*, 2003, **101**, 1997–2002.

[72] R. N. Bracewell, *The Fourier Transform and Its Applications*, McGraw-Hill, 3rd edn., 2000.

[73] P. L. Corio, *Structure of High-Resolution NMR Spectra*, Academic Press, 1967.

[74] R. R. Ernst, G. Bodenhausen and A. Wokaun, *Principles of Nuclear Magnetic Resonance in One and Two Dimensions*, Clarendon Press ; Oxford University Press, Oxford [Oxfordshire]; New York, 1987.

[75] M. Karplus, *Journal of the American Chemical Society*, 1963, **85**, 2870–2871.

[76] J. Cavanagh, W. J. Fairbrother, A. G. Palmer III, M. Rance and N. J. Skelton, *Protein NMR Spectroscopy. Principles and Practice*, Elsevier Academic Press, Amsterdam, 2nd edn., 2007.

[77] A. J. Dingley and S. Grzesiek, *Journal of the American Chemical Society*, 1998, **120**, 8293–8297.

[78] K. Pervushin, A. Ono, C. Fernández, T. Szyperski, M. Kainosho and K. Wüthrich, *Proceedings of the National Academy of Sciences*, 1998, **95**, 14147–14151.

[79] F. Cordier and S. Grzesiek, *Journal of the American Chemical Society*, 1999, **121**, 1601–1602.

[80] S. P. Brown, M. Pérez-Torralba, D. Sanz, R. M. Claramunt and L. Emsley, *Journal of the American Chemical Society*, 2002, **124**, 1152–1153.

[81] D. R. Davis, R. P. Lutz and J. D. Roberts, *Journal of the American Chemical Society*, 1961, **83**, 246–247.

[82] J.-C. Hierso, *Chemical Reviews*, 2014, **114**, 4838–4867.

[83] J. M. Griffin, J. R. Yates, A. J. Berry, S. Wimperis and S. E. Ashbrook, *Journal of the American Chemical Society*, 2010, **132**, 15651–15660.

[84] M. J. Plevin, D. L. Bryce and J. Boisbouvier, *Nature Chemistry*, 2010, **2**, 466–471.

[85] F. R. SALSBURY Jr. and R. A. HARRIS, *Molecular Physics*, 1998, **94**, 307–312.

[86] M. Pecul, *The Journal of Chemical Physics*, 2000, **113**, 10835–10836.

[87] D. L. Bryce and R. E. Wasylishen, *Journal of Molecular Structure*, 2002, **602-603**, 463–472.

[88] J. Vaara, M. Hanni and J. Jokisaari, *The Journal of Chemical Physics*, 2013, **138**, 104313.

[89] J. Jokisaari and J. Vaara, *Physical Chemistry Chemical Physics*, 2013, **15**, 11427.

[90] J. Vaara and M. V. Romalis, *Physical Review A*, 2019, **99**, 060501.

[91] M. P. Ledbetter, G. Saielli, A. Bagno, N. Tran and M. V. Romalis, *Proceedings of the National Academy of Sciences*, 2012, **109**, 12393–12397.

[92] M. E. Limes, N. Dural, M. V. Romalis, E. L. Foley, T. W. Kornack, A. Nelson, L. R. Grisham and J. Vaara, *Physical Review A*, 2019, **100**, 010501.

[93] D. H. Brouwer, S. Alavi and J. A. Ripmeester, *Physical Chemistry Chemical Physics*, 2007, **9**, 1093.

[94] T. Akasaka and S. Nagase, *Endofullerenes : A New Family of Carbon Clusters*, Kluwer Academic Publishers, Dordrecht; Boston, 2002.

[95] G. R. Bacanu, J. Rantaharju, G. Hoffman, M. C. Walkey, S. Bloodworth, M. Concistrè, R. J. Whitby and M. H. Levitt, *Journal of the American Chemical Society*, 2020, **142**, 16926–16929.

[96] G. Hoffman, M. C. Walkey, J. Gräsvik, G. R. Bacanu, S. Alom, S. Bloodworth, M. E. Light, M. H. Levitt and R. J. Whitby, *Angewandte Chemie International Edition*, 2021.

[97] G. A. Morris, H. Barjat and T. J. Home, *Progress in Nuclear Magnetic Resonance Spectroscopy*, 1997, **31**, 197–257.

[98] G. A. Morris and R. Freeman, *Journal of the American Chemical Society*, 1979, **101**, 760–762.

[99] J. F. Stoddart, *Chemical Society Reviews*, 2009, **38**, 1802–1820.

[100] L. Becker, R. J. Poreda and T. E. Bunch, *Proceedings of the National Academy of Sciences*, 2000, **97**, 2979–2983.

[101] M. Goldman, *Journal of Magnetic Resonance (1969)*, 1984, **60**, 437–452.

[102] R. D. Johnson, C. S. Yannoni, H. C. Dorn, J. R. Salem and D. S. Bethune, *Science*, 1992, **255**, 1235–1238.

[103] W. Even, J. Smith and M. W. Roth, *Molecular Simulation*, 2005, **31**, 207–213.

[104] F. Cordier and S. Grzesiek, *Journal of Molecular Biology*, 2002, **317**, 739–752.

[105] F. Jensen, *Introduction to Computational Chemistry*, Wiley, Chichester, 3rd edn., 2017.

[106] M. Straka, P. Lantto and J. Vaara, *The Journal of Physical Chemistry A*, 2008, **112**, 2658–2668.

[107] U. Benedikt, A. A. Auer and F. Jensen, *The Journal of Chemical Physics*, 2008, **129**, 064111.

[108] F. Jensen, *Journal of Chemical Theory and Computation*, 2006, **2**, 1360–1369.

[109] C. Adamo and V. Barone, *Chemical Physics Letters*, 1998, **298**, 113–119.

[110] C. Adamo and V. Barone, *The Journal of Chemical Physics*, 1999, **110**, 6158–6170.

[111] L. Schröder, T. J. Lowery, C. Hilty, D. E. Wemmer and A. Pines, *Science*, 2006, **314**, 446–449.

[112] H. Molin, *Magnetic Resonance in Chemistry*, 1987, **25**, 606–608.

[113] K. Heinloth, *Zeitschrift für Physik*, 1961, **163**, 218–229.

[114] M. Ge, U. Nagel, D. Hüvonen, T. Rõõm, S. Mamone, M. H. Levitt, M. Carravetta, Y. Murata, K. Komatsu, J. Y.-C. Chen and N. J. Turro, *The Journal of Chemical Physics*, 2011, **134**, 054507.

[115] J. Hora, P. Pánek, K. Navrátil, B. Handlířová, J. Humlíček, H. Sitter and D. Stifter, *Physical Review B*, 1996, **54**, 5106–5113.

[116] M. Young, *Optics and Lasers: Including Fibers and Optical Waveguides*, Springer-Verlag, Berlin Heidelberg, 5th edn., 2000.

[117] P. M. Felker, V. Vlček, I. Hietanen, S. FitzGerald, D. Neuhauser and Z. Bačić, *Physical Chemistry Chemical Physics*, 2017, **19**, 31274–31283.

[118] W. I. F. David, R. M. Ibberson, T. J. S. Dennis, J. P. Hare and K. Prassides, *Europhysics Letters (EPL)*, 1992, **18**, 219–225.

[119] Z. Bačić, V. Vlček, D. Neuhauser and P. M. Felker, *Faraday Discussions*, 2018, **212**, 547–567.

[120] M. Concistrè, S. Mamone, M. Denning, G. Pileio, X. Lei, Y. Li, M. Carravetta, N. J. Turro and M. H. Levitt, *Philosophical Transactions of the Royal Society A: Mathematical, Physical and Engineering Sciences*, 2013, **371**, 20120102.

[121] S. Flügge, *Practical Quantum Mechanics*, Springer-Verlag, Berlin Heidelberg, 1999.

[122] B. H. Bransden and C. J. Joachain, *Quantum Mechanics*, Pearson Prentice Hall, 2nd edn., 2000.

[123] R. Loudon, *The Quantum Theory of Light*, Oxford University Press, Oxford, New York, Third Edition edn., 2000.

[124] D. L. Dexter, *Physical Review*, 1956, **101**, 48–55.

[125] W. Gordy and R. L. Cook, *Microwave molecular spectra*, John Wiley & Sons, New York, 3rd edn., 1984.

[126] P. R. Bevington and D. K. Robinson, *Data Reduction and Error Analysis for the Physical Sciences*, McGraw-Hill Education, 3rd edn., 2003.

[127] H. A. Jiménez-Vázquez and R. J. Cross, *The Journal of Chemical Physics*, 1996, **104**, 5589–5593.

[128] A. Terry Amos, T. Frank Palmer, A. Walters and B. L. Burrows, *Chemical Physics Letters*, 1990, **172**, 503–508.

[129] J. H. Lii and N. L. Allinger, *Journal of the American Chemical Society*, 1989, **111**, 8576–8582.

[130] R. M. Parrish, L. A. Burns, D. G. A. Smith, A. C. Simmonett, A. E. DePrince, E. G. Hohenstein, U. Bozkaya, A. Y. Sokolov, R. Di Remigio, R. M. Richard, J. F. Gonthier, A. M. James, H. R. McAlexander, A. Kumar, M. Saitow, X. Wang, B. P. Pritchard, P. Verma, H. F. Schaefer, K. Patkowski, R. A. King, E. F. Valeev, F. A. Evangelista, J. M. Turney, T. D. Crawford and C. D. Sherrill, *Journal of Chemical Theory and Computation*, 2017, **13**, 3185–3197.

[131] N. Mardirossian and M. Head-Gordon, *Physical Chemistry Chemical Physics*, 2014, **16**, 9904–9924.

[132] N. Mardirossian and M. Head-Gordon, *Molecular Physics*, 2017, **115**, 2315–2372.

[133] O. A. Vydrov and T. Van Voorhis, *The Journal of Chemical Physics*, 2010, **133**, 244103.

[134] C. Lee, W. Yang and R. G. Parr, *Physical Review B*, 1988, **37**, 785–789.

[135] S. H. Vosko, L. Wilk and M. Nusair, *Canadian Journal of Physics*, 1980, **58**, 1200–1211.

[136] A. D. Becke, *The Journal of Chemical Physics*, 1993, **98**, 5648–5652.

[137] P. J. Stephens, F. J. Devlin, C. F. Chabalowski and M. J. Frisch, *The Journal of Physical Chemistry*, 1994, **98**, 11623–11627.

[138] S. Grimme, J. Antony, S. Ehrlich and H. Krieg, *The Journal of Chemical Physics*, 2010, **132**, 154104.

[139] S. Grimme, S. Ehrlich and L. Goerigk, *Journal of Computational Chemistry*, 2011, **32**, 1456–1465.

[140] T. H. Dunning, *The Journal of Chemical Physics*, 1989, **90**, 1007–1023.

[141] D. E. Woon and T. H. Dunning, *The Journal of Chemical Physics*, 1994, **100**, 2975–2988.